The Canterbury University ST Atmospheric Radar Development: Design and Feasibility

A thesis

submitted in partial fufillment

of the requirements for the Degree of

Doctor of Philosophy

in Physics

at the

University of Canterbury

by

Adam J. Dunford

University of Canterbury

1998

Abstract

This thesis describes the design of several components of a proposed VHF radar system for the Department of Physics and Astronomy of the University of Canterbury, New Zealand. A suite of software for implementing the full correlation analysis (FCA) of Briggs [1984] has been developed and its operation tested using data from the MU radar of the University of Kyoto.

An examination of the spatiotemporal variation in signal power of the MU data revealed two distinct features. The first, short duration regions of high power were considered to be aircraft flying above the radar. The second structures observed were thin horizontal layers of low reflected power. Profiles of potential refractive index squared were calculated from radiosonde data and these showed good agreement with profiles of reflected echo power.

The FCA velocities are shown to be dependant on both triangle size and FCA algorithm. Failure to exclude the zero-lag covariance datum led to larger velocity differences between different receiving triangles in agreement with the modelling results of Holdsworth and Reid [1995]. Comparison of the FCA algorithms of Briggs [1984] and Brown and Chapman [1972] (B&C) show that the B&C method gives both smaller velocities and larger variances than the Briggs method. Comparisons are presented between FCA and DBS velocities on both 10 and 50 minute timescales and these show good agreement. FCA momentum fluxes are obtained by combining the FCA winds with vertical winds and these were compared with momentum fluxes calculated using the symmetric-beam method of Vincent and Reid [1983] and the 'five-beam' method of Worthington and Thomas [1996]. On the short timescales available here the FCA method showed only moderate agreement with the two DBS techniques, which had good agreement with each other.

The operation of the radar controller and integrating A/D converter hardware designed for the Canterbury radar is discussed and a procedure is described for measuring the pointing angle of the transmitting array using cosmic radio sources. Finally, modifications to the transmitting array are described to allow the radar to measure winds using a multi-beam method similar to Doppler beam-swinging thus providing an alternative to the spaced antenna mode of operation.

Acknowledgements

I wish to express my appreciation of a number of people who have helped me during the course of my Ph.D. Firstly, thanks must go to both Dr. Grahame Fraser and Dr. Bryan Lawrence for their supervision and encouragement. Thanks also to the late Dr. C. Harvey Cummack, for his friendship, the many interesting discussions we had and for trying to teach me the trade. Other members of the atmospheric research group have also been of great assistance. Dr. Bob Bennett for his ideas for the multi-beam modifications to the VHF array, Dr. Don Grainger for pointing out an error in my statistical analysis and many of the research students in the group for their helpful discussions. I am also grateful to Geoff Graham and Ross Ritchie of the electronics workshop for their help with the analogue-to-digital converter. The Department of Physics and Astronomy provided me with a teaching assistantship for a part of this thesis for which I am grateful.

A large portion of this work has involved the analysis of data collected on the MU radar of Kyoto University and the assistance of Professor Shoichiro Fukao and Dr. Mamoru Yamamoto in this regard is gratefully acknowledged. In addition, the prompt fashion in which extra data and synoptic weather maps were obtained was very helpful.

Finally it remains to thank my friends and family. Thanks must go to both the Dunford and McConnell families for their support in too many ways to mention. Thanks also to Alan Grant for his continual willingness to take me away from my work for long talks and sticky buns. To Melissa, Renee and Hannah and all the other children, thank you for making the world a little bit brighter. Last, and most definitely not least, I owe a debt of gratitude to my wife, Cara, and my Lord, Jesus Christ, for caring for me and believing in me.

Table of Contents

List of Figures

List of Tables

Chapter 1
Introduction

The atmosphere is essential to life on earth, and changes in it can have a dramatic impact upon our environment. The interactions between the atmosphere and the environment are complicated and a thorough knowledge of atmospheric dynamics is necessary for a full understanding of the problem. Wind-profiling radars are useful for studying dynamics as they have good vertical and temporal resolution and can provide continuous observations.

This thesis describes the design of a VHF radar system for measuring winds in the lower atmosphere and the analysis of the operation of such systems using data from an existing radar. The proposed radar will complement the middle atmosphere MF radar and the meteor radar currently operated by the Department of Physics and Astronomy at the University of Canterbury, New Zealand. Chapter 1 introduces some basic concepts about the atmosphere and radar systems. Chapter 2 then describes the methods of analysis for measuring winds and momentum flux which will be employed on the Canterbury VHF radar. Chapter 3 investigates these methods using data from the Middle and Upper atmosphere (MU) radar which is operated by the Radio Atmospheric Science Center of Kyoto University, Japan. Finally, Chapter 4 presents detailed information about several aspects of the proposed radar system.

1.1 Regions of the atmosphere

The atmosphere is considered to be made up of various layers, based upon the vertical temperature profile. Individual layers are called *spheres* and are bounded by the extrema in the profile, which are known as *pauses*. A typical atmospheric temperature profile is shown in figure 1.1. The height and depth of each layer vary with latitude and longitude and also throughout the year. The region of interest in this work is the lowest *sphere*, the troposphere.

The troposphere is the region from ground level up to the tropopause. The altitude of the tropopause varies with latitude, from about 16 km near the equator to 9 km near the poles [Holton, 1979]. By considering a simple model of the atmosphere (in which scattering is neglected and absorption is independent of wavelength,

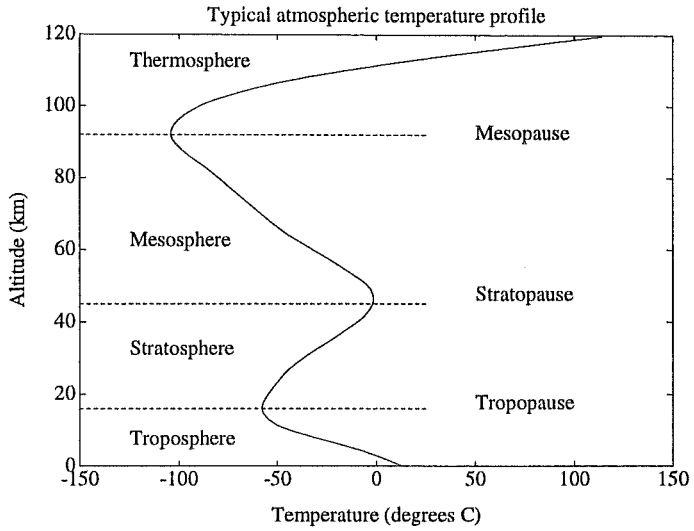

Figure 1.1. A typical mid-latitude temperature profile showing the atmospheric layers, called *spheres* and the regions that separate them, called *pauses*.

pressure, and temperature) it can be shown that the temperature in the troposphere will decrease linearly with height [Houghton, 1977], as can be seen in figure 1.1.

1.2 Observing techniques

With the exception of certain techniques, most observations of the atmosphere are indirect. This is especially true in the stratosphere and mesosphere which are logistically challenging to sample directly. In-situ measurements in these regions are normally made using rocket-boosted payloads or stratospheric balloons. In the troposphere and lower stratosphere aircraft, kite, tethered balloon and radiosonde measurements are able to be employed.

Indirect, or remote, measurement techniques generally make use of electromagnetic or acoustic radiation to determine the state of the atmosphere. Radar, acoustic radar, lidar and satellite observations fall into this category. Although remote measurements are in some sense less 'real' than direct in-situ sampling, they have the advantage of much greater spatial and/or temporal coverage.

1.2.1 Atmospheric radar systems

Radar is an acronym for RAdio Detection And Ranging. Radar systems have a wide range of applications, many more than will be described here. All radar systems

use the reflection of electromagnetic radiation from various objects to determine information about those objects. Radar systems can be categorised depending on the frequency of radiation used and the type of object of interest. They are used in situations as diverse as satellite determination of the ground cover over a large region and measurement of atmospheric wind velocities. It is this latter case which is of interest here. The operation of one type of wind-profiling radar, known as a Stratosphere - Troposphere (ST) or Mesosphere - Stratosphere - Troposphere (MST) radar, is described in detail in section 1.3.

Radars which observe the atmosphere are distinguished from other types of radars by being concerned with reflections or scatter off 'sky', i.e. a transparent target with no obvious fixed boundaries. The general procedure is for periodic pulses to be transmitted and the returned signal sampled and analysed to determine quantities such as wind velocities, momentum fluxes, temperatures and information about the nature of the scattering medium.

When probing the atmosphere it is important to know the height from which the signal is being received. This is determined by measuring the time delay of the echo with respect to the transmitted signal and using the known speed of the electromagnetic wave to calculate a height of reflection. It is assumed here that the radio waves propagate through the atmosphere at the same speed as light travels in a vacuum, i.e. c. Distances based on this assumption are referred to as virtual ranges, and hence the virtual range of a stationary target is $c\tau/2$, where τ is the propagation time. In vertical sounding it is further assumed that the radar beam is directed straight up and thus the distance being measured is in the vertical; in the case of off-zenith scatter or inaccurately directed beams this may not be true. Hereafter in this work virtual range in the vertical direction will simply be referred to as either range or height unless otherwise specified.

If a pulse has a length Δt then an echo is received for a time Δt after a delay period τ has passed. Thus the range resolution is $\Delta r = c\Delta t/2$. Reducing the length of the pulse increases the range resolution, but also decreases the signal-to-noise ratio. The bandwidth of the transmitted pulse is inversely proportional to the pulse length and hence, since the receiver should match this bandwidth, the noise power,

which has an essentially flat frequency spectrum, will increase with decreasing pulse width.

The inverse relationship between noise power and pulse width is problematical. On one hand good height resolution necessitates use of the smallest possible pulse length, while on the other the need for high returned-signal power requires the use of the largest possible pulse length. A short pulse would therefore give a low signal-to-noise ratio, which is not desirable. One solution, described in more detail in section 1.3.2.2, is to use phase coding which allows the use of a long pulse without loss of resolution. Extra 'features', phase or frequency codes, are put into a long pulse so that each subpulse can be identified.

Having calculated the height of reflection it remains to determine the required atmospheric variables. In this work the radar signal characteristics, discussed in section 3.2, the wind velocities (sections 3.3 and 3.4) and momentum fluxes (section 3.5) are considered. There are two different methods for measuring horizontal velocities. The first, known as full correlation analysis, uses correlation methods on the signals from three or more non-collinear spaced antennae, while the other, Doppler beam swinging, uses radial velocities measured with several slightly off-zenith beams. Both methods are used in this work and will be described more fully in sections 2.1 and 2.3. Measurement of the vertical velocity, (and, by the latter method, of the horizontal components as well) is made by using the Doppler shift of the received signal to calculate a radial velocity along each direction of the antenna beam, as described in section 2.2.

1.2.2 Radiosondes

Although major advances have been made in observing the atmosphere, the radiosonde still remains the main operational measuring instrument for direct profiling of parameters such as temperature and pressure. In its basic form, a radiosonde consists of a payload of sensors and transmitting equipment suspended below a balloon. Conventional radiosondes measure pressure, temperature and humidity, although more exotic radiosondes are also flown to measure quantities such as ozone concentration and stratospheric-aerosol properties. The instrument used in this work is described in section 3.1.2.

Data from the various radiosonde sensors are transmitted by radiowaves to an antenna on the ground where they are processed to produce useful information. The radiosonde may have a radar-reflecting target attached to allow its height and position to be monitored by radar or be equipped with a Global Positioning System (GPS) device. In the absence of such devices 'geopotential heights' are used. The geopotential height is defined as the work required to raise a unit mass from sea level to a height z, divided by the global average of gravity at mean sea level, and can be calculated from the measured pressure and temperature. In the lower regions of the atmosphere the difference between the true height and the geopotential height is negligible, however the error becomes increasingly significant above the stratosphere due to the decrease in gravity with height.

1.3 ST radars

Stratosphere-Troposphere (ST) radars typically operate at around 50 MHz, with vertically-directed antenna beams. They can make measurements between 1 and 20 km with height resolution on the order of 100-1000 m. A good overview of the operation of these radars is given by Rottger [1988] and reviews of the measurement techniques by Hocking et al. [1989] and Hocking [1997a]. A recent discussion of some of the strengths and limitations of the ST/MST technique may be found in Hocking [1997b].

In the lower atmosphere the coherence time of a ST radar signal (determined principally by turbulent fluctuations) is generally much longer than the time between successive pulses [Rottger, 1988]. Since the phase and amplitude of the echoes vary little from pulse to pulse, the ST radar is oversampling, and the coherence of the radar echo allows the signal-to-noise ratio to be improved by use of coherent integration (section 1.3.2.1). A general ST radar system is shown in figure 1.2.

1.3.1 Hardware components

The various components of the radar system are sequenced by an electronic 'radar controller' which is in turn controlled by a host computer which processes the data. In some systems the radar controller is part of the host computer while in

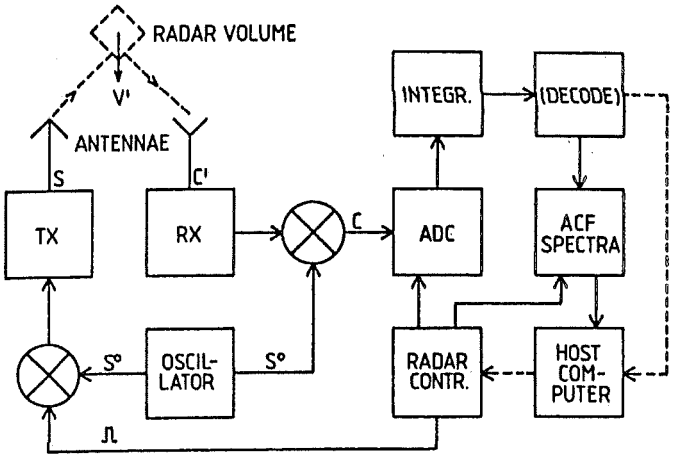

Figure 1.2. A schematic of a generalised ST radar system. The system comprises a transmitter (TX), antennae, control hardware and software and receivers (RX). The signals from the receivers are sampled by the analogue-to-digital converters (ADC), coherently integrated (INTEGR) and phase decoded (DECODE). These, and/or the correlation functions or power spectra, are then stored for further processing. Based on Figure 6a in Rottger [1988]

others it is a separate component. The operation of the controller for the proposed Canterbury VHF radar is described in section 4.2

1.3.1.1 Radar antennae

Antennae for atmospheric radars must be carefully designed so as to minimise unwanted signals such as ground scatter, sea scatter, aeroplane echoes and cosmic noise. Reduction of these requires small angular beam width, and hence high gain. This in turn implies a large size for the antenna. The angular beam width, gain and physical area of a general antenna are related by [Rottger, 1988],

$$G = \frac{4\pi A_e}{\lambda^2} \approx \frac{4\pi}{\theta_b^2}$$

where G, θ_b, A_e and λ are the gain, half-power beam width, effective area and wavelength of the antenna respectively.

The requirement for a large antenna is most easily satisfied by use of an array of elements which, if necessary, can then be individually phased to change the beam direction. These elements are often Yagi-Uda or half-wave dipole antennae which are linked by a cascading network of either open wire or coaxial cable feeders. The half-wave dipole antenna is simply a wire whose length is half the radar wavelength while

the Yagi-Uda is more complicated, having reflector, director and driven elements, and has a higher gain than the half-wave dipole.

The two methods for measuring wind velocities mentioned in section 1.2.1 require different antennae. The spaced-antenna method (SA) uses a large, and hence narrow-beam transmitting antenna and at least three smaller spaced receiving antennae which are generally distinct from and located close to the transmitting antenna. In theory the SA method does not actually require a large antenna, in fact MF systems normally have quite large beamwidths due to the large wavelengths involved (the exception to this is the magnificent Buckland Park array in Adelaide, Australia [Briggs et al., 1969]), although a narrow beam is more efficient as more power is directed vertically. However Royrvik [1983] has suggested that too large an antenna can degrade the performance of a SA system. The other method, often referred to as Doppler beam swinging (DBS), requires a narrow-beam transmitting antenna and one narrow-beam receiving antenna to allow it to be accurately directed. In DBS systems it is common for the transmitting and receiving antenna to be the same physical array. For the proposed VHF system both the SA and a modified-DBS method will be used, with the SA technique being the primary method. The design of an antenna system capable of operating in both modes is discussed in section 4.4.

1.3.1.2 Transmitters, oscillators and receivers

A radar transmitter is simply a powerful multi-stage amplifier whose input is a continuous signal from an oscillator modulated by an on-off pulse and possibly a coding pattern from the radar controller. This input signal is amplified in the driver stage and again in the final stage to give a peak power on the order of $1 - 1000$kW [Rottger, 1988]. The peak power for the Canterbury VHF radar is 100kW (G. Fraser pers com). A block diagram of a transmitter is shown in figure 1.3a.

The output from the oscillator is a continuous sinusoidal signal at the radar frequency. It is split into signals for transmission and phase reference in the receivers. The signal to the transmitter often has phase flips of 0° or 180° inserted to allow for phase coding. The signal to the receivers is split and has phases of 0° and 90° inserted to allow for in-phase and quadrature detection. When the same antenna is used for both transmission and reception a transmit/receive duplexer (switch) is added which protects the sensitive receivers from the high-power signals emitted

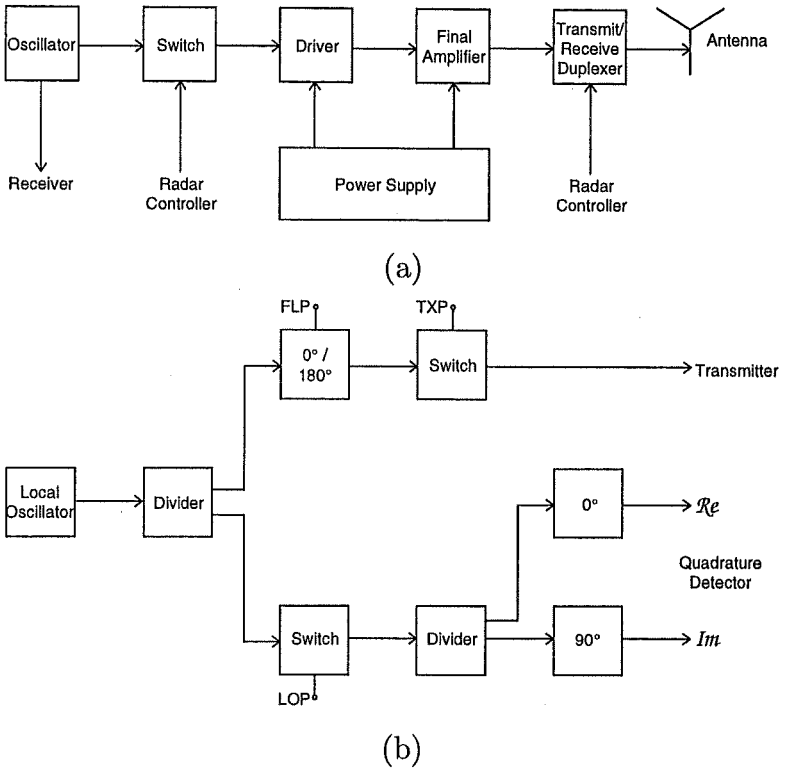

Figure 1.3. Schematics of radar system components. The transmitter, (a), amplifies a signal from the local oscillator, (b), and radiates this through an antenna. The local oscillator produces a sine wave of the appropriate radio frequency and this is used to phase-lock the receivers (Figure 1.4) to the transmitted pulse. The control signals for phase-coding (FLP), transmit on and off (TXP), and for protecting the local oscillator from any feedback of signal through the receivers during transmission (LOP) are generated by the radar controller. From Rottger [1988].

from the transmitter during transmission. A block diagram of an oscillator is shown in figure 1.3b.

Radio-frequency receivers take a low-power signal from an antenna which is mixed with a signal from the local oscillator to lower the frequency. It is then split and mixed with the 0° and 90° signals from the local oscillator to give real (in-phase) and imaginary (quadrature) components, before being sampled by analogue-to-digital converters (A/D). A block diagram of a receiver is shown in figure 1.4.

1.3.2 Data processing

The signal processing carried out prior to the correlation analysis will now be considered in more detail. Let the output of a receiver, $c(t)$, be sampled by the A/D converter at times $t_k = k\Delta t_s$, where Δt_s is the sampling interval, to produce a time series $c_k, k = 0, 1, 2...K$. This digital series is the record of one radar echo and the discrete values c_k represent the signal received from different ranges. It is

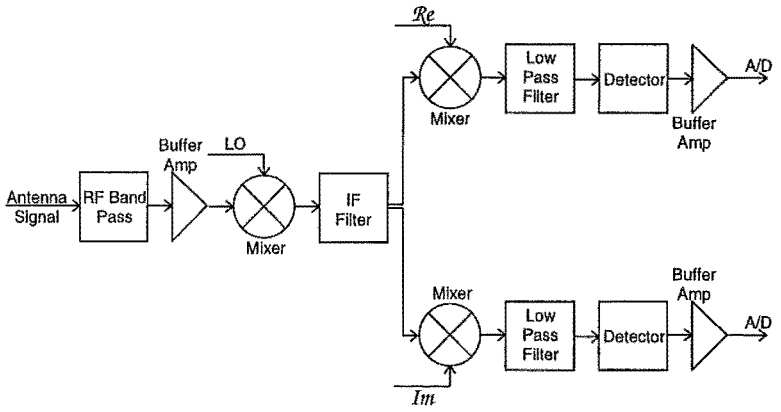

Figure 1.4. Schematic of a radar receiver. In reception the radio-frequency (RF) signal from the antenna is mixed with a local oscillator signal (LO) to give an intermediate-frequency (IF) signal. This is then split and mixed with signals from the local oscillator ($\mathcal{R}e$ and $\mathcal{I}m$), Figure 1.3b, to give real and imaginary components and is then sampled by the A/D.

convenient to flip the phase of the transmitted signal from one pulse to the next, giving a pair of time series c_k and $c_{k'}$, which together are known as a radar cycle. One radar cycle thus takes $2T_{ipp}$, where T_{ipp} is the interpulse period. N radar cycles constitutes a radar burst.

1.3.2.1 Coherent integration

The relatively low vertical velocities in the atmosphere mean that the Doppler shift of a vertically directed reflected pulse is relatively small. Thus the echo contains mostly high-frequency noise with the signal power being confined to low frequencies. Low-pass filtering will reduce the noise while leaving the signal largely unchanged. The simplest low-pass filter is complex addition of N samples over a period $t_i << \tau_c$, where τ_c is the coherence time of the signal. This process is known as coherent integration and the hardware required for its implementation is described in section 4.2. A different approach to this problem is to digitise large amounts of data and then use filtering to obtain the required signal as is done by Hocking [1997c] on the CLOVAR system.

The total complex signal, c_{k_n}, can be expressed as

$$c_{k_n} = c^r_{k_n} + c^s_{k_n} + c^c_{k_n} + c^{instr}_{k_n}$$

where the superscripts r and s represent the random noise and signal respectively, and c and $instr$ the radar clutter and a DC offset due to instrumental effects

respectively. The subscript k refers to the range index, and n to the sample number. Radar clutter may be due to reflections from a fixed target, such as a cliff or tall building or from non-stationary targets such as moving tree branches or ocean waves [Woodman, 1988].

When the phase is flipped in the second pulse of each radar cycle the sign of the signal and the radar clutter will change. Thus the instrumental DC offset can be removed by subtracting the two pulses, i.e.

$$\begin{aligned} c_{j_n} &= c_{k_n} - c_{k'_n} \\ &= 2(c^r_{k_n} + c^s_{k_n} + c^c_{k_n}) \end{aligned}$$

since $c^s_{k_n} = -c^s_{k'_n}$, $c^c_{k_n} = -c^c_{k'_n}$, $c^i_{k_n} = c^i_{k'_n}$ and it is assumed that $c^r_{k_n}$ has the same statistical properties as $-c^r_{k'_n}$.

The signal has now been preprocessed sufficiently for coherent addition to take place. The coherently integrated samples are given by

$$c_j = \frac{1}{N}\sum_{n=1}^{N} c_{j_n} = \frac{2}{N}\sum_{n=1}^{N} c^r_{k_n} + c^s_{k_n} + c^c_{k_n}$$

This gives integrated data samples c_j at range j for $j = 1, ..., J$. It is these samples which are used in the subsequent correlation analysis.

The fixed clutter contribution can found by coherently integrating for a sufficiently long period ($>> \tau_c$) so that the atmospheric component becomes negligible due to its finite coherence time. Since the fixed clutter contribution is by definition constant, it can then be determined and subtracted from the signal. For the removal of clutter from non-stationary targets more sophisticated techniques must be employed [Woodman, 1988].

1.3.2.2 Phase coding

Phase coding allows a high average transmitted power, i.e. a long duration pulse, while maintaining height resolution for which a short pulse is required. This is achieved by periodically altering the phase of the carrier wave by 0° or 180°. An example of a four-element pulse is shown in figure 1.5a. Numerically, phase changes of 0° and 180° can represented by 1 and -1 respectively. Thus the code in figure 1.5a is $1, 1, -1, 1$. The received signal is processed by crosscorrelation with

the transmitted code. Phase coding is described in Woodman et al. [1984], Rastogi [1986] and Sulzer and Woodman [1986].

Let $s_{h,i}$ be the complex signal from range h and transmitter pulse i, in a sequence of coded transmitter pulses. Decoding requires the crosscorrelation of this sequence with the transmitted code c_m, where c_m is either 1 or -1 for $m = 1, 2, ..., M$ and M is the length of the code. If $s'_{h,i}$ is the decoded signal then

$$s'_{h,i} = \sum_{m=1}^{M} s_{h+m,i} c_m \tag{1.1}$$

This process is essentially a correlation and hence codes are required whose autocorrelation function (acf) resembles a delta function. Such a code, for reflection from a single target, will give a decoded echo at a single height and at no others.

For reflection from a single hard target the echo, $s_{h,i}$, will be c_m and the decoded signal, $s'_{h,i}$, will be the acf of c_m padded before and after with zeros. If the acf of c_m, and hence the decoded signal, is a delta function then the correct reflection height of the target will have been determined. In practice it is not possible to find such perfect codes and so it is necessary to use those whose acfs have minimum sidelobes. For reflection from a single target, such a code will produce spurious echoes at heights either side of the correct height due to the decoding process.

An improvement on this situation is to find a pair of codes whose small acf sidelobes are of opposite signs. Addition of the acfs from each pulse will then exactly cancel out any sidelobes present, leaving a single signal at the correct height. Such pairs of codes are known as complementary codes and are often used in ST-radar systems. An example of a complementary code pair is shown in figure 1.5.

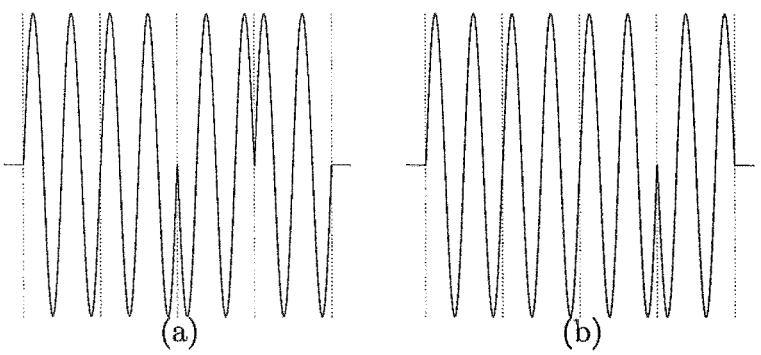

Figure 1.5. Two examples of a phase-coded transmitter pulse; each code is four subpulses, or bits, long. The coding is done by changing the carrier phase by 0° , (1), or 180°, (−1). Thus code (a) is $1, 1, -1, 1$ and code (b) is $1, 1, 1, -1$. Together (a) and (b) form a complementary code pair.

Given the overwhelming trend of 'reviews' to discuss the general methodology of a given technique without an accompanying simple example it is now time to redress the balance. Consider the reflection of the four-bit codes in figure 1.5 from a single target. These are $c_{m,1} = 1, 1, -1, 1$ and $c_{m,2} = 1, 1, 1, -1$. The received signals, $s_{h,1}$ and $s_{h,2}$, are replicas of the transmitted pulse, and hence

$$\begin{aligned} s_{h,1} &= 0,0,0,0,0,0,0,0,1,1,-1,1,0,0,0,0,0,0,0,0 \\ s_{h,2} &= 0,0,0,0,0,0,0,0,1,1,1,-1,0,0,0,0,0,0,0,0 \end{aligned}$$

Decoding using equation (1.1) gives,

$$\begin{aligned} s'_{h,1} &= 0,0,0,0,1,0,-1,4,-1,0,1,0,0,0,0,0 \\ s'_{h,2} &= 0,0,0,0,-1,0,1,4,1,0,-1,0,0,0,0,0 \end{aligned}$$

which are the acfs of the coded pulses. Note the spurious echoes, corresponding to the side lobes in the acf, at ranges above and below the true height, which corresponds to the peak of the acf. Adding the decoded pulses together gives,

$$s'_{h,1} + s'_{h,2} = 0,0,0,0,0,0,0,8,0,0,0,0,0,0,0,0$$

It should be noted that the echo strength has increased by a factor of $2M$ over a single unit-strength pulse, where M is the length of the pulse. ST radars typically have code lengths of 16 or more bits giving a useful signal gain. If there are two reflectors spaced one 'bit' apart in height then although the reflected pulse does not contain two separate peaks, the decoded pulse does. It is these two processes; increased signal strength and range resolution, which make phase coding a valuable tool in ST-radar systems.

Chapter 2
ST radars - Methods of analysis

The first indication that radio waves could be used to determine atmospheric wind velocities came in 1933 when Ratcliffe and Pawsey [1933] observed that records of downcoming B.B.C. wireless waves from spatially separated antennae were similar, but not identical, and faded with time. This was attributed to diffraction from moving ionospheric irregularities, and was used by Pawsey [1935] to estimate ionospheric wind velocity. The Canterbury VHF radar is intended to measure horizontal and vertical winds in the troposphere and lower stratosphere and this chapter describes the analysis methods that will be used to accomplish this.

The spaced antenna (SA) method, which provides horizontal winds, is discussed in section 2.1 and results, using data from the MU radar, are presented in section 3.3. The other major method of wind measurement, Doppler beam-swinging (DBS), is described in section 2.3 and comparisons between the SA and DBS method are presented in section 3.4. Finally, methods of calculating momentum fluxes using a combination of SA horizontal winds and vertical winds (section 2.2) and DBS winds will be covered in section 2.4 and results of a comparison between the various techniques are discussed in section 3.5.

2.1 Full Correlation Analysis

One of the earliest applications of spaced-antenna techniques to the measurement of atmospheric velocities was by Mitra [1949], who used a dedicated transmitter rather than B.B.C. radio transmissions. The velocity was calculated by finding the time delays between similar peaks in the signals from separated antennae. The effects of random changes in the reflecting surface and possible anisotropies in the structure of the surface were neglected. This method was refined by Briggs et al. [1950] to include random changes, and by Phillips and Spencer [1955] for the case where the surface structure is anisotropic. These improved techniques used correlation functions, and may therefore be described as correlation analysis methods, in contrast to the 'similar fades' techniques. Initially measurements of ionospheric velocities were obtained using total reflections from the E-region, while observation

of the lower D-region commenced when Gardner and Pawsey [1953] made the first measurements using partial reflections. Early radar systems often used a right-angled triangle of receiving aerials as the full correlation analysis was analytically more simple in this case. Brown and Chapman [1972] treated the case for a general triangle and this method is described in section 2.1.2.

With the advent of ST radars full correlation analysis (FCA), formerly used only at mesospheric heights, came closer to the ground. For a thorough and understandable treatment of the method of FCA the reader is referred to Briggs [1984]. This gives a method of analysis for an arbitrary number of receivers in any geometrical configuration.

2.1.1 Conceptual ideas behind FCA

One of the most basic concepts upon which FCA is based is that atmospheric velocities can be determined by studying the motion of a 'pattern' as it moves across spatially separated sensors. In the case of a radar, the backscattered radio waves form fluctuating Fresnel diffraction patterns on the ground and the sensors are aerials, either single or in arrays.

Such a pattern can be represented by its contours, i.e. lines of constant value. If the measured quantity is real and random in nature then a three-dimensional representation would look like a contorted surface, with hills and valleys. Figure 2.1 shows a hill moving at a velocity V in a direction ϕ to the y axis. The variation of the measured quantity with time is recorded by three sensors at o, x and y which form a right-angled triangle with side lengths ξ_0 and η_0 in the x and y directions respectively.

If the pattern moves over the sensors without changing and with constant velocity, then the records from o, x and y will be a section through the hill along lines $o' - o''$,$x' - x''$ and $y' - y''$ respectively. The records from the three sensors are shown in figure 2.2. The maxima correspond to the points labeled o_m, x_m and y_m in figure 2.1. If the hill size is large compared to the sensor spacing then the line joining o_m, x_m and y_m, known as a line of maximum, will be approximately straight and perpendicular to the direction of motion.

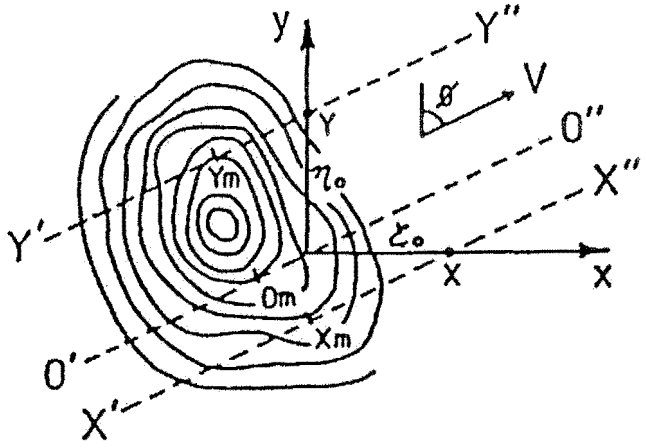

Figure 2.1. Schematic of signal pattern moving over three spaced sensors. From Briggs [1984].

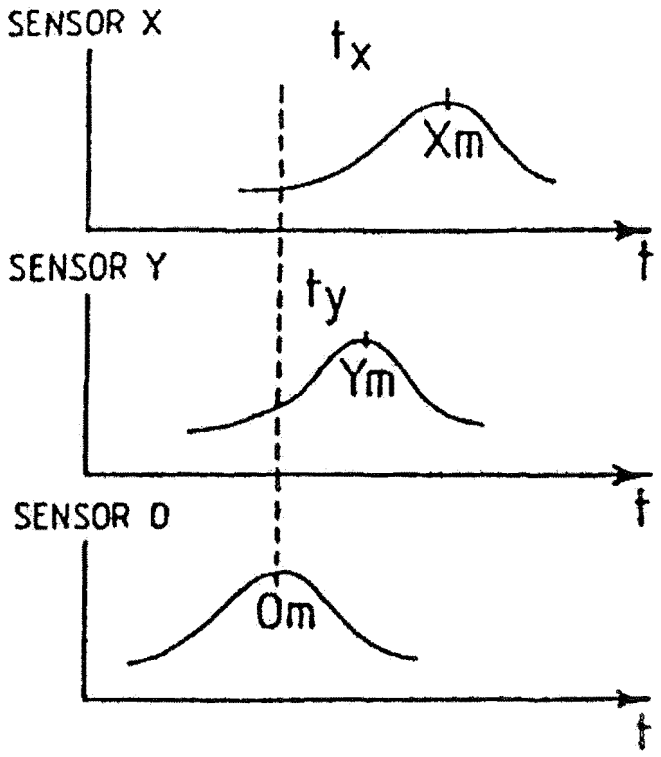

Figure 2.2. Examples of signals received from the three spaced sensors of Figure 2.1. From Briggs [1984].

Figure 2.1 can now be replaced by the simpler figure 2.3 which has a single line of maximum moving across the sensors. From the time displacements t_x and t_y in figure 2.2 it is found that

$$t_x = \frac{\xi_0 \sin\phi}{V}, \; t_y = \frac{\eta_0 \cos\phi}{V}$$

Defining

$$v'_x = \frac{\xi_0}{t_x}, \; v'_y = \frac{\eta_0}{t_y}$$

leads to

$$v'_x = \frac{V}{\sin\phi}, \; v'_y = \frac{V}{\cos\phi}$$

V may be found by geometrically connecting a perpendicular line from the origin to a line joining the v'_x and v'_y values.

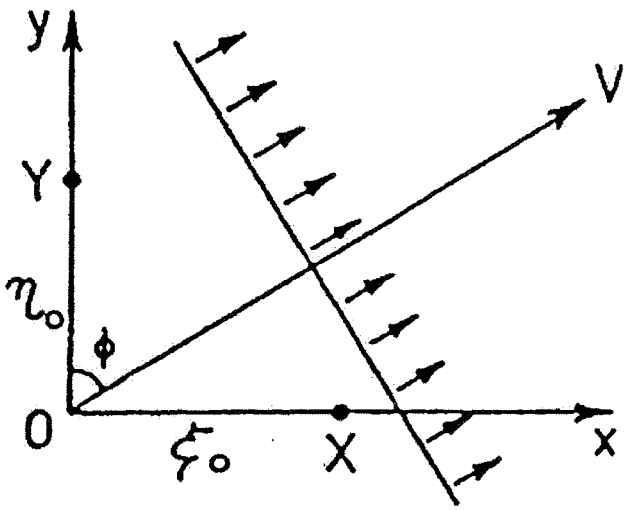

Figure 2.3. A 'line of maximum' moving over the three sensors of Figure 2.1. From Briggs [1984].

In a real case there would be many such hills and valleys moving past the sensors and it would be necessary to calculate average time displacements $\overline{t_x}$ and $\overline{t_y}$. The lines of maxima, although lying at a variety of angles to the direction of motion, will not deviate greatly from the perpendicular to the direction of motion and will be symmetrically distributed around this perpendicular provided the pattern is isometric.

There are two important reasons why this simple method must be refined. Firstly, the pattern may be systematically elongated, or anisometric, which will tend to tilt the lines of maxima along the major axis of elongation. This will produce errors in the calculated direction of motion. Secondly, if the pattern changes as it moves then the magnitude of the calculated velocity will also be in error. In the extreme case where there is no systematic motion the records will still show similarities (due to random fluctuations) if the sensors are separated by less than the pattern scale. The average time displacement will now be zero, and the velocity, V, infinite. If the systematic motion is combined with random changes then the calculated velocity will in general be too large. It is now desirable to use a more sophisticated method; that of full correlation analysis.

2.1.1.1 A stationary and time invariant pattern

Define a correlation function, $\rho(\xi, \eta)$, as

$$\rho(\xi, \eta) = \frac{< f(x,y)\ f^*(x+\xi, y+\eta) >}{< [f(x,y)]^2 >}$$

where f is a function of zero mean and * denotes complex conjugation. The spatial averaging, denoted by $\langle\rangle$, may be carried out by fixing ξ and η and averaging over all points (x, y), in the pattern. As this is logistically difficult it is assumed that the same result can be obtained by fixing (x, y) and (ξ, η) and averaging over time. To completely describe ρ would require averaging over all possible values of ξ and η and would still be time consuming; so to proceed further a number of assumptions are made about the form of ρ.

If the pattern is isometric then ρ should depend only on the magnitude of displacement and not the direction, i.e. $\rho(\xi, \eta) = \rho(\sqrt{\xi^2 + \eta^2})$. In this case, contours of constant correlation will be circles centered on the origin. If the form of ρ in any direction is known, then ρ is completely fixed. Such a pattern and its corresponding correlation function are shown in figure 2.4a and figure 2.4b.

Inclusion of anisotropy in the pattern is simply a matter of stretching the isometric pattern. This requires two parameters; a scale of stretch and an orientation relative to the (x, y) axes. This transformation converts the contours of ρ to a family of concentric ellipses. The axial ratio and orientation of these ellipses define the amount and direction of pattern stretch. The ellipse for a certain value of ρ,

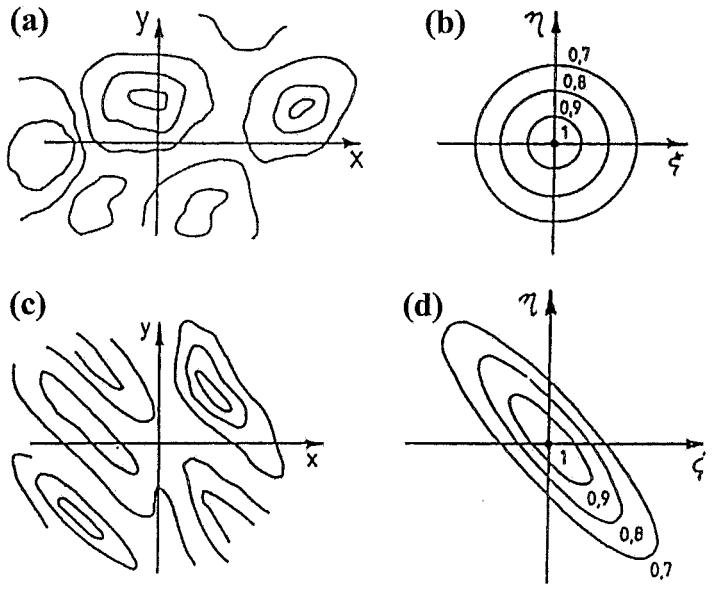

Figure 2.4. An example of a stationary non-changing random pattern and its corresponding correlation contours. (a) and (b) show the case for an isometric pattern and (c) and (d) show an anisometric pattern. From Briggs [1984].

say $\rho(\xi, \eta) = \frac{1}{2}$, is called the characteristic ellipse and sets the scale of the pattern irregularities in each direction in the (x, y) plane. An example of an anisometric pattern and its corresponding correlation function are shown in figure 2.4c and 2.4d.

The assumption of elliptical contours constrains the form of ρ. The variables ξ and η can only occur in linear combinations of ξ^2, η^2 and $\xi\eta$. Thus,

$$\rho(\xi, \eta) = \rho(A\xi^2 + B\eta^2 + 2H\xi\eta)$$

where A, B and H are constants. It should be noted that the functional form of ρ is still arbitrary, the assumption constrains only the forms in which the variables ξ and η may appear.

2.1.1.2 A stationary and randomly changing pattern

The assumption of a time-invariant pattern will now be relaxed. Consider instead, a pattern that changes randomly with time but has no tendency to move in any particular direction - rather like the surface of a boiling cauldron of porridge. The pattern will now be a function of time, i.e. $f(x, y) \rightarrow f(x, y, t)$.

The sensor at the origin records $f(0, 0, t)$ which could be described by a temporal autocorrelation function. More generally, a spatio-temporal correlation

function can be defined as

$$\rho(\xi,\eta,\tau) = \frac{< f(x,y,t)\ f^*(x+\xi, y+\eta, t+\tau) >}{< [f(x,y,t)]^2 >}$$

by making time displacements of records from different sensors. The contours of constant correlation are now concentric surfaces, in (ξ,η,τ) space, about the origin.

Assumptions are again made about the form of these surfaces. There can be no systematic tilt of the surfaces relative to the τ axis as this would imply a non-stationary pattern. Following Briggs [1984], it is assumed that the surfaces form a family of concentric ellipsoids with one axis in the τ direction. Thus the form of ρ is now

$$\rho(\xi,\eta,\tau) = \rho(A\xi^2 + B\eta^2 + K\tau^2 + 2H\xi\eta)$$

This implies that the temporal autocorrelation functions have the same functional form as the spatial correlation functions. This assumption is somewhat justified by the fact that any function with a maximum at the origin can be expressed, to second order, in this form.

2.1.1.3 A moving and randomly changing pattern

Consider the case where the pattern of section 2.1.1.2 moves with a speed V in a direction ϕ clockwise from the y axis. The surfaces of constant correlation will now acquire a tilt relative to the τ axis.

This added sophistication is readily achieved by considering an observer moving with the pattern. Such an observer would simply see the pattern of section 2.1.1.2. A coordinate transformation must made to convert quantities calculated in a frame moving with the pattern to a stationary frame, which would be the real world.

Let x, y, t be coordinates in a stationary frame and x', y', t' be those in a frame moving with the pattern. Thus the necessary transformations are

$$\begin{aligned} x &= x' + v_x t \\ y &= y' + v_y t \\ t &= t' \\ \xi &= \xi' + v_x \tau \end{aligned}$$

$$\eta = \eta' + v_y\tau$$
$$\tau = \tau'$$

where $v_x = V\sin\phi$ and $v_y = V\cos\phi$ are components of V. Note that v_x and v_y are the true components, in contrast to the pseudo-components, v'_x, v'_y, of section 2.1.1.

For the observer moving with the pattern the correlation function, ρ, is given by

$$\begin{aligned}\rho(\xi',\eta',\tau') &= \rho(A\xi'^2 + B\eta'^2 + K\tau'^2 + 2H\xi'\eta') \\ &= \rho(A(\xi - v_x\tau)^2 + B(\eta - v_y\tau)^2 + K\tau^2 \\ &\quad +2H(\xi - v_x\tau)(\eta - v_y\tau)\end{aligned} \tag{2.1}$$

A stationary observer would see

$$\rho(\xi,\eta,\tau) = \rho(A\xi^2 + B\eta^2 + C\tau^2 + 2F\xi\tau + 2G\eta\tau + 2H\xi\eta) \tag{2.2}$$

Deferring for the moment any experimental determination of the parameters A, B, C, F, G and H of equation (2.2), it will now be shown that a knowledge of these allows the calculation of all the quantities of interest.

2.1.1.4 Determination of useful quantities

It will be assumed that the parameters A, B, C, F, G and H of equation (2.2) have been obtained. This equation fully describes the situation. It now remains to determine practically useful quantities.

Calculation of 'true' velocity

By comparing the coefficients in equations (2.1) and (2.2) it is seen that

$$AV_x + HV_y = -F \tag{2.3}$$
$$BV_y + HV_x = -G \tag{2.4}$$

These simultaneous equations can be solved to give the velocity components. In practice the coefficients in equations (2.3) and (2.4) are divided though by C, as the resulting coefficients are more easily determined experimentally. This velocity is known as the 'true' velocity, as calculated by FCA.

Calculation of apparent velocity

The time delays for maximum correlation are closely related to the time delays mentioned in section 2.1.1. In an entirely similar way an 'apparent' velocity, V_a, may be calculated using these maximum correlation delays. In general this will be too large and in the wrong direction due to the neglection of random changes and anisotropy. Nevertheless it provides an independent check on the assumptions of FCA. If V and V_a are very different then caution may be required in the use of the 'true' velocity. The calculation of apparent velocities is described by Brown and Chapman [1972].

Calculation of spatial properties of the pattern

The next step is to describe the scale and degree of anisotropy in the pattern. Define $\tau_{\frac{1}{2}}$ as the time when the autocorrelation function, as measured by a stationary observer, has the value $\frac{1}{2}$. Thus, from equation (2.2),

$$\rho(0,0,\tau_{\frac{1}{2}}) = \rho(C\tau_{\frac{1}{2}}) = \frac{1}{2}$$

Contours of constant correlation in the (ξ,η) plane are ellipses, as stated in section 2.1.1.1. The 'characteristic ellipse'; that for which $\rho(\xi,\eta) = \frac{1}{2}$, is given by

$$\rho(\xi,\eta,0) = \rho(A\xi^2 + B\eta^2 + 2H\xi\eta) = \frac{1}{2} = \rho(C\tau_{\frac{1}{2}})$$

Thus,

$$\frac{A}{C}\xi^2 + \frac{B}{C}\eta^2 + \frac{2H}{C}\xi\eta = \tau_{\frac{1}{2}}$$

describes the characteristic ellipse in terms of measurable parameters. It is usual to calculate the minor axis, axial ratio and orientation of major axis of the characteristic ellipse.

Calculation of random changes

Finally, consider the random changes in the pattern as it moves along. To an observer moving with the pattern, the pattern evolution would be due only to the random changes and could be described by the temporal autocorrelation,

$$\rho(0,0,\tau) = \rho(K\tau^2)$$

A 'mean lifetime', $t_{\frac{1}{2}}$, as measured by this observer will be defined, for which the autocorrelation function equals $\frac{1}{2}$. By comparison of the coefficients in equations (2.1) and (2.2) it is seen that

$$t_{\frac{1}{2}}^2 = \frac{C}{K}\tau_{\frac{1}{2}}^2$$

and

$$C = Av_x^2 + Bv_y^2 + K + 2Hv_xv_y$$

If the pattern is anisometric then the pattern scale will depend on direction. Thus a spacing, $d_{\frac{1}{2}}$, can be defined in the direction of motion such that sensors spaced a distance $d_{\frac{1}{2}}$ apart record a correlation of $\frac{1}{2}$, i.e. $\rho(0, d_{\frac{1}{2}}) = \frac{1}{2}$. It can be shown [Briggs, 1984] that $d_{\frac{1}{2}}$ is given by

$$d_{\frac{1}{2}}^2 = \frac{v_x^2 + v_y^2}{\frac{A}{C}v_x^2 + \frac{B}{C}v_y^2 + \frac{2H}{C}v_xv_y}\tau_{\frac{1}{2}}^2$$

2.1.1.5 Determination of the parameters needed for FCA

As was shown in the preceding sections, all necessary quantities can be evaluated once the values $\frac{A}{C}, \frac{B}{C}, \frac{F}{C}, \frac{G}{C}$ and $\frac{H}{C}$ have been experimentally determined. The calculation of these parameters will now be described.

Consider a pair of sensors, (i, j), with a vectorial separation (ξ_{ij}, η_{ij}). The signals are recorded at each location and used to calculate the correlation function ρ at various values of time shift τ. If the pattern is moving ρ will have a maximum at some value of $\tau = \tau'_{ij}$, given by

$$\frac{\partial\rho}{\partial\tau}|_{\tau'_{ij}} = 0$$

It can be seen from equation (2.2) that

$$\tau'_{ij} = -\frac{F}{C}\xi_{ij} - \frac{G}{C}\eta_{ij} \tag{2.5}$$

For a certain time-shift τ_{ij} the autocorrelation function, $\rho(0, 0, \tau)$, will take the value of the crosscorrelation function between the pair of sensors. Algebraically,

$$\rho(0, 0, \tau_{ij}) = \rho(\xi_{ij}, \eta_{ij}, 0)$$

and hence, from equation (2.2),

$$\rho(C\tau_{ij}^2) = \rho(A\xi_{ij}^2 + B\eta_{ij}^2 + 2H\xi_{ij}\eta_{ij})$$

Thus it is found that

$$\tau_{ij}^2 = \frac{A}{C}\xi_{ij}^2 + \frac{B}{C}\eta_{ij}^2 + \frac{2H}{C}\xi_{ij}\eta_{ij} \tag{2.6}$$

Equations (2.5) and (2.6) are the starting point for the determination of the FCA parameters. From the measured signal the auto- and crosscorrelation functions are calculated. The τ_{ij} and τ'_{ij} can then be obtained from these. If there are three or more non-collinear sensors then equations (2.5) and (2.6) give systems of equations which can be solved to give the required parameters.

2.1.2 The method of Brown and Chapman

Another important method of FCA is due to Brown and Chapman [1972] which, although it has many similarities to the Briggs [1984] procedure, is ideologically distinct. Whereas Briggs' approach starts from a moving pattern to calculate true velocities and can utilise an arbitrary number and configuration of receivers the Brown and Chapman technique proceeds by calculating the true velocity as a correction to the apparent velocity and uses only three receivers. Nevertheless up to the stage of calculating the parameters $\frac{A}{C}, \frac{B}{C}, \frac{F}{C}, \frac{G}{C}$ and $\frac{H}{C}$ the methods are essentially identical. Beyond this point, however, it is extremely difficult to formally prove their equivalence and thus the two methods must be examined by comparing the velocities produced. Results of a comparison using data from the MU radar are shown in section 3.3.2.

2.1.3 Experimental implementation of FCA

The method of implementing the outline of section 2.1.1.5 will now be discussed. The computational requirements of FCA mean that it is most easily achieved by using purpose-written software. All important program modules were written in Fortran 90 by the author, unless otherwise acknowledged.

Consider having three or more time series of digitally-sampled complex data on which it is wished to perform FCA. These data series are denoted by c_{ijk} where i,j and k refer to the sensor, sample number and height respectively. For simplicity

it is assumed that no coherent integration or phase decoding are necessary and that the data have been read into the analysis program. As the FCA is the same for all heights the subscript k will be dropped. However in practice the program would repeat the analysis at all heights.

First, the correlation functions are calculated. For N sensors there are N autocorrelation functions and $\frac{1}{2}N(N+1)$ crosscorrelation functions. Given two data series c_{ij} and $c_{i'j}$, where $j = 1, 2, ..., J$, the correlation function, $\rho_{ii'}(l)$, is

$$\rho_{ii'}(l) = \left| \frac{1}{J-l} \sum_{j'=1+l}^{J-l} c_{ij'} c^*_{i',j'+l} \right|$$

for $l = 0, 1, 2, ..., L$, and

$$\rho_{ii'}(l) = \left| \frac{1}{J+l} \sum_{js'=1-l}^{J} c_{ij'} c^*_{i',j'+l} \right|$$

for $l = -1, -2, ..., -L$, where * denotes complex conjugation. The N individual autocorrelation functions are averaged to give a mean autocorrelation function. The correlation functions are often left as complex variables, with the modulus being used in FCA and the phase used in calculation of vertical velocities. The functions can, if desired, be smoothed; however this is largely unnecessary. Examples of experimental autocorrelation and crosscorrelation functions are shown in figure 2.5.

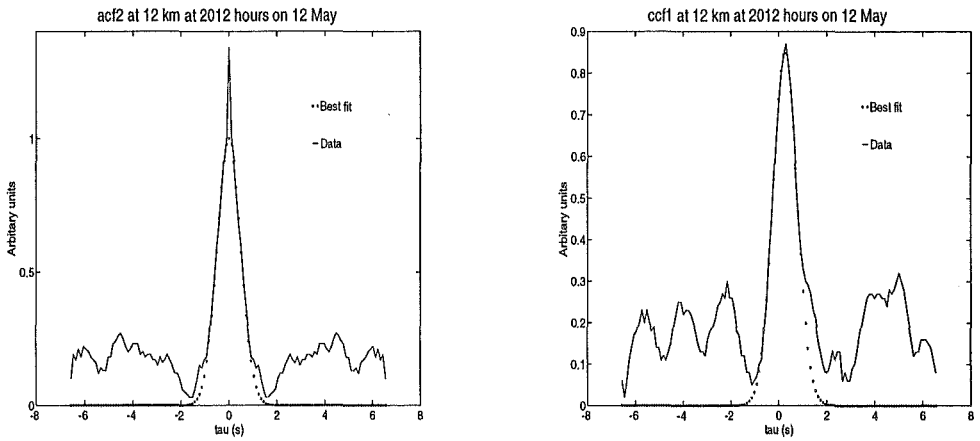

(a) (b)

Figure 2.5. Examples of experimental correlation functions; (a) is an autocorrelation function (acf) and (b) is a crosscorrelation function (ccf).

To find the τ and τ' values for FCA, the times at which the correlation functions take on certain values must be determined. This is done by fitting an analytic form

to the experimental correlation functions. In this work the Gaussian form

$$y(x) = ae^{-\left(\frac{x-b}{c}\right)^2} \tag{2.7}$$

was used. It is then algebraically straightforward to find the values at which this functional form has, say, a maximum. To obtain a normalised autocorrelation function the values obtained from, say, ρ_{ii} are divided by a_{ii} and the crosscorrelation values, ρ_{ij}, by $\sqrt{a_{ii}a_{jj}}$.

In practice, the fitting of a Gaussian shape is a numerically intensive procedure. Equation (2.7) is non-linear in the coefficients a, b and c and thus a non-linear fitting routine must be used. As FORTRAN 77 code was available for the Levenberg-Marquardt non-linear fitting method [Press et al., 1992] it was decided to adapt this code into Fortran 90 and use it. A significant improvement on the original code was the substitution of singular-value decomposition for Gauss-Jordan elimination at a particular step in the algorithm. This allowed much improved error trapping, a feature of great importance in software which must successfully handle anything the atmosphere can throw at it.

It may also be necessary to scale the correlation functions before attempting to fit a functional form to them. Typical values of the unscaled correlation-function are on the order of 10^{10} and these may cause underflow or overflow errors in the Gaussian fitting routines or subsequent analysis if no scaling is used. The large real numbers, as opposed to, say, 16-bit integer values which might be expected from a digital device such as the integrating A/D converter of section 4.2, are due to the use of a signal preprocessor (G. Fraser pers com). Thus, it is generally advisable to scale the correlation functions before fitting, as was done in this work.

The correlation functions will often have a 'spike' at the origin due to the presence of uncorrelated random noise. Including this point in the fit would introduce serious error and so it was ignored. The ratio between the fitted value at the origin and the spike value is useful as an indication of the signal-to-noise ratio [Briggs, 1984]. The correlation functions may also have an offset, i.e. they may not go down to zero within the finite number of time shifts computed, despite removal of the average value from the data; indicating the presence of slowly varying components. Finally, the tail ends of the correlation functions, large positive and

negative lags, often contain very little information and can be fairly noisy. For these reasons it is advisable to fit to only a section of the correlation function. The method followed in this work was to find the maximum value of the correlation function and then to include points either side of this value, down to $\frac{1}{e}$ of the maximum. This portion of the computed correlation function, less the datum at zero time shift, was then fitted.

In calculating the τ values (the point at which the autocorrelation function takes the origin value of the crosscorrelation function) the method of Fooks [1965] was used. A similar method has been used by Holdsworth and Reid [1995] although there appears to be an error of sign in equation 9 of Holdsworth and Reid's [1995] paper, by comparison with equation 1 of Fooks [1965] and also equation 29 of Briggs et al. [1950]. Fooks derives the result that

$$\tau^2 = \tau'^2 + \tau''^2$$

where τ'' is the time at which the autocorrelation function takes the value of the maximum of the crosscorrelation function. This has the advantage of using higher values of correlation which are less likely to be affected by noise [Fooks, 1965] although there is the difficulty that, as correlation values must be less than or equal to unity, this procedure may produce biased statistics [Awe, 1964].

Having fitted equation (2.7) to the data, the required quantities are easily obtained. The maximum value is a, occurring at a time b, and the point x at which the correlation function takes a value y is given by

$$x = c \ln(\frac{a}{y}) + b$$

Once the τ and τ' values have been obtained, equations (2.5) and (2.6) can then be used to determine the FCA parameters. With N sensors, these give 2 by $\frac{1}{2}N(N+1)$ and 3 by $\frac{1}{2}N(N+1)$ systems of linear equations to be solved. The `svdfit` routine of Numerical Recipes [Press et al., 1992] was used to perform this.

Before using the FCA parameters to calculate velocities they should first be tested to see if they are physically reasonable. If $H^2 - AB = 0$, i.e. contours of constant correlation are parabolas or straight lines, then it is impossible to calculate a velocity as the solution of equations (2.3) and (2.4) would involve division by zero.

$H^2 - AB > 0$ corresponds to hyperbolic contours of constant correlation and it is therefore reasonable to exclude both these of cases from further analysis.

Once velocities have been calculated they are then tested against acceptance criteria. Data are rejected either due to their low quality, e.g. low signal-to-noise ratio, or because they do not satisfy the assumptions of the analysis, e.g. the contours of constant correlation are hyperbolic rather than elliptical. Data which have been 'accepted' have a greatly reduced number of outlying points. These criteria, based upon those in Briggs [1984], are listed here:

- The mean signal to noise ratio must be greater than -3dB; $\frac{S}{N} > 1$.
- The analysis must not fail numerically at any stage. Failure could occur, for instance, by being unable to fit a Gaussian form to the correlation functions.
- The correlation contours may not be highly elongated. Axial ratios less than 3 are required.
- The correlation contours must be elliptical or circular. That is, H^2 must be less than AB.
- $\frac{d^2_{\frac{1}{2}}}{t^2_{\frac{1}{2}}}$ must be greater than zero. Note that the analysis involves the calculation of $d^2_{\frac{1}{2}}$, $t^2_{\frac{1}{2}}$, rather than $d_{\frac{1}{2}}$,$t_{\frac{1}{2}}$, and the analysis may, due to numeric instabilities, assign negative values to these quantities.
- The sum of τ' around a closed loop must be greater than zero. In practice

$$\frac{\left|\sum_{closed\ loop} \tau'\right|}{\sum_{closed\ loop} |\tau'|} < .2$$

  was used.

- The apparent and FCA velocities must be reasonably similar. The conditions

$$\frac{1}{3} |V_{apparent}| < |V_{FCA}| < 2 |V_{apparent}|$$

  and

$$|\phi_{FCA} - \phi_{apparent}| < \frac{\pi}{4}$$

  have been used on the data analysed in this work.

- The FCA velocity must be subsonic, i.e. $|V_{FCA}| < 300$ ms^{-1}.

2.2 Vertical velocities

Although the full correlation analysis of section 2.1 allows calculation of the horizontal velocity components, a different technique must be used to find the vertical component. If an electromagnetic wave is reflected by a moving reflector then the reflected wave has a different frequency to the incident wave. This frequency difference, or Doppler shift, is proportional to the velocity of the reflector.

Once the Doppler shift is measured, the velocity may be easily calculated. If, in addition, the electromagnetic wave is incident in the vertical direction then the velocity measured will be the vertical velocity. In the case of the MU radar this is readily achieved as the beam is precisely steerable. It would thus seem that the most straightforward approach would be to calculate the Fourier transform of the data series and measure the Doppler shift directly from this.

Calculating the Fourier transform of the data is a numerically intensive process on the same order as calculating the correlation functions used in FCA. It is fortunate that these tasks can be combined, and the Doppler shifts calculated from the correlation functions, thus removing the necessity of performing Fourier transforms.

When the correlation functions are computed from complex data, i.e. real and imaginary data series, the correlation functions are complex. While the magnitude is needed for FCA, the phase of the correlation function can be used to determine the Doppler shift. It will be shown subsequently that when there is a non-zero vertical velocity the phase of the correlation function varies linearly with the time shift, τ. This phase slope is proportional to the Doppler shift. This procedure of calculating Doppler shifts from correlation function phase slopes is commonly used [e.g. Woodman and Guillen, 1974; Vincent et al., 1987].

2.2.1 Theoretical development

Consider a random pattern of complex amplitude, $E(x,t)$, moving along the x axis with velocity V and changing as it moves. The pattern is due to radar reflections from atmospheric scatterers whose velocity is $v = \frac{1}{2}V$ due to the 'point source effect' [Briggs and Vincent, 1992]. The method used here follows that of Briggs and Vincent [1992]. It is assumed that any phase changes in the reflected signal are due to atmospheric effects and are not instrumental in origin.

Initially, it is assumed that there is no mean vertical velocity, and hence no mean Doppler shift, that the motion is one dimensional and that the scattering is centered on the zenith. These restrictions will subsequently be relaxed one by one. In this simple case the signals $E_1(t)$ and $E_2(t)$ received at two antennae separated by ξ_0 have a mean frequency equal to the transmitted frequency. If the reflected energy has a symmetrical distribution about the zenith it can be shown [e.g. Bracewell, 1965; May, 1988] that the correlation functions are real, or equivalently, complex but with a zero phase, even though computed from complex variables.

As in section 2.1.1.2 it is assumed that the contours of constant correlation are ellipses. First consider the situation for zero vertical velocity. For the case where the horizontal velocity, V, is also zero the correlation function, ρ, is given by

$$\rho(\xi,\tau) = \rho\left(\frac{\xi^2}{\xi_1^2} + \frac{\tau^2}{\tau_1^2}\right)$$

where ξ_1 and τ_1 are the pattern scale and pattern lifetime measured at the correlation value of $\frac{1}{e}$. When V is non-zero the correlation function becomes

$$\rho(\xi,\tau) = \rho\left(\frac{(\xi - V\tau)^2}{\xi_1^2} + \frac{\tau^2}{\tau_1^2}\right)$$

If a Gaussian form is assumed for the correlation functions then

$$\rho(\xi,\tau) = \exp -\left(\frac{(\xi - V\tau)^2}{\xi_1^2} + \frac{\tau^2}{\tau_1^2}\right)$$

Now a non-zero vertical velocity which is uniform over the radar volume is included. From elementary theory the Doppler shift for a moving source, Δf, is given by

$$\Delta f = \frac{\Delta v}{\lambda}$$

where Δv is the relative velocity and λ is the wavelength of the wave. For reflections off an atmospheric scatterer

$$\Delta f = -\frac{2w}{\lambda}$$

where the vertical velocity w is positive upwards. The factor of two arises from the fact that the path difference of the reflected wave is twice the distance moved by the scatterer in a certain time.

The Doppler shift introduced by the vertical motion will move the power spectrum and the cross spectrum of the signal along the frequency axis. Since the correlation functions are Fourier transforms of the frequency spectra [Ratcliffe, 1956] these will now have a non-zero phase, i.e. they will be complex. From the shift theorem of Fourier transforms, if $f(t)$ and $F(f)$ are Fourier transforms of each other then so are $f(x-a)$ and $\exp(-2\pi iaf)F(f)$, and $\exp(2\pi iax)f(x)$ and $F(f-a)$ [Bracewell, 1965]. Therefore with a non-zero vertical velocity the correlation function will be

$$\rho(\xi,\tau) = \exp\left(-\frac{i4\pi w}{\lambda}\tau\right)\exp-\left(\frac{(\xi - V\tau)^2}{\xi_1^2} + \frac{\tau^2}{\tau_1^2}\right)$$

The phase, ψ, of the auto and cross-correlation functions is thus given by

$$\psi(\tau) = -\frac{4\pi w}{\lambda}\tau$$

Next, consider the case of zero vertical velocity but with the scattered power being centered off-zenith at an angle θ_0. This can occur from inclined aspect-sensitive layers or from non-vertically directed beams. The spatial autocorrelation function, $\rho(\xi,\tau)$, is the Fourier transform of the angular power spectrum, $W\left(\frac{s}{\lambda}\right)$ where $s = \sin\theta$. If this is re-centered on $s_0 = \sin\theta_0$ then $W\left(\frac{(s-s_0)}{\lambda}\right)$ represents the angular power spectrum. Thus from the shift theorem of Fourier transforms the spatial autocorrelation is now

$$\exp\left(\frac{i2\pi s_0}{\lambda}\xi\right)\rho(\xi,0)$$

Therefore in the presence of a non-zero horizontal velocity and off-zenith scattered power the spatio-temporal correlation function is given by

$$\exp\left(\frac{i2\pi s_0}{\lambda}(\xi - V\tau)\right)\rho(\xi,\tau)$$

and the phases of the auto and cross-correlation functions are

$$\begin{aligned}\psi_{auto}(\tau) &= -\frac{4\pi v s_0}{\lambda}\tau \\ \psi_{cross}(\tau) &= -\frac{4\pi v s_0}{\lambda}\tau + \frac{2\pi\xi_0 s_0}{\lambda}\end{aligned}$$

The introduction of a factor of two is due to the 'point source effect' i.e. $V = 2v$.

Note that there are two distinct Fourier transform relations being used here. In one a $\tau \leftrightarrow f$ pair is used to transform between the temporal autocorrelation

function and the frequency power spectrum. In the other a $\xi \leftrightarrow \theta$, or equivalently $\xi \leftrightarrow s = \sin\theta$, pair is used to transform between the spatial correlation function and the angular power spectrum.

The next refinement is to re-include the effect of a vertical velocity. Since the scatter from an angle of θ_0 is now being considered, there will be an additional Doppler shift of

$$\Delta f = -\frac{2wc_0}{\lambda}$$

where $c_0 = \cos\theta_0$, due to the radial component of the vertical velocity. Thus the spatio-temporal correlation function is now given by

$$\exp\left(-\frac{i4\pi wc_0}{\lambda}\tau\right)\exp\left(\frac{i2\pi\left(\xi - V\tau\right)s_o}{\lambda}\right)\rho\left(\xi,\tau\right)$$

and the phases of the auto and cross-correlation functions are

$$\begin{aligned}\psi_{auto}\left(\tau\right) &= -\frac{4\pi\left(vs_0 + wc_0\right)}{\lambda}\tau \\ \psi_{cross}\left(\tau\right) &= -\frac{4\pi\left(vs_0 + wc_0\right)}{\lambda}\tau + \frac{2\pi\xi_0 s_0}{\lambda}\end{aligned}$$

Some points about these last two equations should be noted. Firstly, the term $vs_0 + wc_0$ is simply the total radial velocity. Secondly, various other works obtain $-vs_0 + wc_0$ for the radial velocity due to a difference in the definition of θ. It should also be noted that although being concerned here with vertical velocities the theory is also used in radar interferometry [e.g. Pfister, 1971; Farley et al., 1981; Rottger and Ierkic, 1985; Brown, 1992; Brown et al., 1995a] to determine horizontal velocities and angles of arrival.

The final sophistication is to allow a two-dimensional horizontal velocity, i.e. a velocity in both the x and y directions, in addition to the off-zenith scatter and vertical velocity. Let the direction cosines of the scattering region be (l_0, m_0, j_0). Briggs [1992] has shown that the correlation function is given by

$$\exp\left(\frac{i2\pi l_o}{\lambda}\left(\xi - V_x\tau\right)\right)\exp\left(\frac{i2\pi m_o}{\lambda}\left(\eta - V_y\tau\right)\right)\exp\left(-\frac{i4\pi\left(1 - l_0^2 - m_0^2\right)}{\lambda}w\tau\right)\rho\left(\xi,\eta,\tau\right)$$

where $\rho\left(\xi,\eta,\tau\right)$ is the correlation function in the absence of either vertical velocity or off-zenith scatter. Therefore the phase of the autocorrelation function is

$$\psi_{auto}\left(\tau\right) = -\frac{4\pi}{\lambda}\left(v_x l_0 + v_y m_0 + w\left(1 - l_0^2 - m_0^2\right)\right)\tau \qquad (2.8)$$

and for the crosscorrelation function calculated from signals from a receiver pair (ξ_{ij}, η_{ij}) the phase is

$$\psi_{cross_{ij}}(\tau) = -\frac{4\pi}{\lambda}\left(v_x l_0 + v_y m_0 + w\left(1 - l_0^2 - m_0^2\right)\right)\tau + \frac{2\pi}{\lambda}\left(\xi_{ij} l_0 + \eta_{ij} m_0\right) \quad (2.9)$$

which is seen to be proportional to the vertical velocity.

2.2.2 Practical implementation

In using equations (2.8) and (2.9) of the previous section care must be taken that there are not more unknowns than can be solved for. Although v_x and v_y are known from FCA, l_0 and m_0 need to be determined, in addition to the required vertical velocity v_z.

Firstly, lines of best fit must be obtained for the phase of the autocorrelation function and each of the crosscorrelation functions. Next, the intercept of the line fitted to the crosscorrelation phase is used to determine the direction cosines l_0 and m_0. From equation (2.9) it is seen that the intercept is given by

$$\psi_{cross_{ij}}(0) = \frac{2\pi}{\lambda}\left(\xi_{ij} l_0 + \eta_{ij} m_0\right)$$

With more than one pair of receivers this gives simultaneous equations that can be solved for l_0 and m_0. Equation (2.8) can now be used to calculate the vertical velocity.

2.2.2.1 The problem of 'phase jumps'

The implementation of the algorithm described above is relatively simple in comparison to FCA. The major problem that occurs is that of 'phase jumps' in the phase of the correlation functions; these must be removed if a meaningful linear fit is to be determined.

When correlation functions are calculated from complex data the resulting variable is complex, as has been shown above. To calculate the phase a function such as arctangent must be used to convert the real and imaginary components to an angle. The inverse trigonometric functions are, however, many-to-one in form and this means that the phases of the correlation functions will be the 'true value' modulo 2π. This process produces discontinuities of $2n\pi$ in the calculated phases, where n is an integer.

The method used in this work is, firstly, to test whether a point differs from the preceding one in phase by a multiple of 2π. In addition to this the quadrant in which each phase angle lies is calculated. If a quadrant change of ± 1 occurs in the region of a phase change then appropriate multiples of 2π are introduced to remove the phase jump.

2.3 Doppler Beam Swinging

As mentioned in section 1.2.1 an alternative method of wind vector determination, known as Doppler beam swinging (DBS), exists which uses several off-zenith beams to obtain radial velocities and hence u, v and w. A discussion of the DBS method can be found in Sato [1988] and Rottger [1988]. DBS has been shown to be fundamentally identical to the full correlation analysis (FCA) used in this thesis [Briggs, 1980; May, 1990] although the experimental details are different. In both cases irregularities in the refractive index give rise to scattering which in one case leads to a Doppler shift and in the other to a time-shift in the correlation functions [Larsen and Rottger, 1989]. DBS uses a single narrow-beam antenna which is electronically steered in various directions while the FCA requires one transmitting aerial and three or more spatially separated receiving antennae which may have relatively large beamwidths. Computational differences also exist. The FCA method uses time displacements calculated from correlation functions to determine the motion of a ground diffraction pattern, while DBS obtains the radial velocity by calculating the Doppler shift of measured frequency spectra.

2.3.1 Method of analysis

Although expressions which obtain the velocity components from beams with arbitrary directions can be derived [Sato, 1988], it is possible to use a choice of beams which simplifies the analysis. Consider the beam directions shown in figure 2.6. By measuring the Doppler shift, Δf, on the central beam and using

$$\Delta f = \frac{2\Delta v_r}{\lambda}$$

where λ is the radar wavelength, it is possible to calculate the radial velocity, Δv_r, which in this case is the vertical velocity component, w.

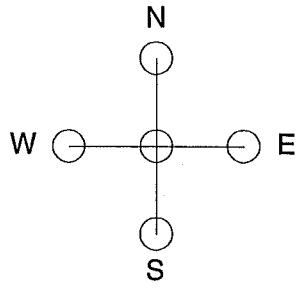

Figure 2.6. Example of beam directions used in a DBS system. The vertical component, w, is obtained using the central beam and the horizontal components, u and v, are obtained using pairs of beams along the compass axes as described in the text.

To calculate the horizontal components consider figure 2.7 which shows the pair of beams along the east-west axis. The radial velocities in each beam are given by

$$\begin{aligned} V_{r,\theta} &= u_1 \sin\theta + w_1 \cos\theta \\ V_{r,-\theta} &= -u_2 \sin\theta + w_2 \cos\theta \end{aligned}$$

Assuming that the wind is the same in both radar volumes, i.e. $u_1 = u_2 = u$ and $w_1 = w_2$, then [Rottger, 1988]

$$u = \frac{V_{r,\theta} - V_{r,-\theta}}{2 \sin\theta}$$

A similar expression can be derived for the other horizontal component using the north-south pair of beams.

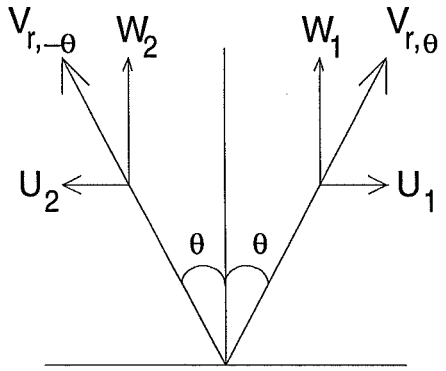

Figure 2.7. Geometry of a pair of off-zenith beams used to calculate the horizontal velocity.

2.4 Momentum flux measurements

It is now recognised that the transport of momentum throughout the atmosphere plays a vital role in balancing the general circulation. This was not always the case and there were several apparent 'anomalies' which were not easily explained by considering the atmosphere as simply a 'turbulent' fluid. Two of these, the cold summer mesopause and the quasi-biennial oscillation, can now be accounted for more readily by wave-transported momentum [McIntyre, 1993].

The determination of momentum fluxes can be performed with aircraft mounted systems, radiosondes and wind-profiling radars [Worthington and Thomas, 1996]. While each system has its individual merits the radar alone can provide continuous height and time coverage, albeit at a single place. Momentum flux measurements are important as input to numerical models [Larsen, 1988], in addition to providing information on smaller scale dynamics such as those inside frontal zones.

Before discussing the methods of measuring momentum fluxes the physical significance of the velocity covariances $\overline{u'w'}$ and $\overline{v'w'}$ will be presented. The treatment given follows that of Murphy [1990]. The theory may be applied to total velocity components (u, v, w) but only perturbation velocities, i.e. those which have had the mean value subtracted (hereafter denoted by primes), will be discussed here.

Consider the two dimensional perturbation velocity vector, $\mathbf{V}'$, shown in figure 2.8. For an atmospheric density of ρ the horizontal momentum per unit volume associated with the motion is $\rho u'$. Under a vertical velocity w' the rate of transport of some quantity through a horizontal plane of area A is $w'A$. Thus the amount of horizontal momentum per unit volume crossing unit area in unit time, i.e. the vertical flux of horizontal momentum per unit volume, is $\rho u'w'$. Hence the vertical flux of horizontal momentum per unit mass is $u'w'$.

2.4.1 Methods of analysis

In this section three different methods of calculating $\overline{u'w'}$ and $\overline{v'w'}$, the momentum flux per unit mass, will be presented. These are the symmetric beam technique of Vincent and Reid [1983], the 5-beam method of Worthington and Thomas [1996] and a combination of FCA horizontal winds with Doppler vertical winds. This latter method will be denoted by FCAW.

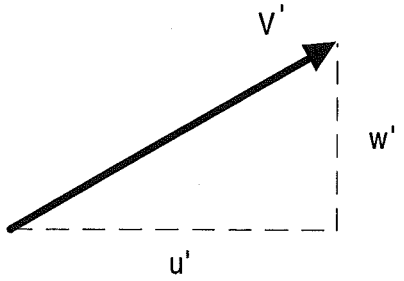

Figure 2.8. Components of a perturbation velocity vector.

2.4.1.1 Symmetric beam method

Consider figure 2.7 of section 2.3.1 which shows a pair of beams symmetrically offset from the zenith. If the mean radial velocities over the observing period are subtracted from the instantaneous values in each beam then the resulting perturbation velocities are

$$\begin{aligned} V'_{r,\theta} &= u'_1 \sin\theta + w'_1 \cos\theta \\ V'_{r,-\theta} &= -u'_2 \sin\theta + w'_2 \cos\theta \end{aligned}$$

Squaring these, subtracting the values from each beam and averaging gives [Fukao et al., 1988]

$$\begin{aligned} \overline{V'^2_{r,\theta}} - \overline{V'^2_{r,-\theta}} &= \overline{\left(u'_1 \sin\theta + w'_1 \cos\theta\right)^2} - \overline{\left(-u'_2 \sin\theta + w'_2 \cos\theta\right)^2} \\ &= \left(\overline{u'^2_1} - \overline{u'^2_2}\right) \sin^2\theta + \left(\overline{w'^2_1} - \overline{w'^2_2}\right) \cos^2\theta + 2\left(\overline{u'_1 w'_1} + \overline{u'_2 w'_2}\right) \sin\theta \cos\theta \end{aligned}$$

Assuming that $\overline{u'^2_1} = \overline{u'^2_2}$, $\overline{w'^2_1} = \overline{w'^2_2}$ and $\overline{u'_1 w'_1} = \overline{u'_2 w'_2}$, i.e. that the statistical properties are spatially invariant, then

$$\overline{V'^2_{r,\theta}} - \overline{V'^2_{r,-\theta}} = 2\overline{u'w'} \sin 2\theta$$

and hence

$$\overline{u'w'} = \frac{\overline{V'^2_{r,\theta}} - \overline{V'^2_{r,-\theta}}}{2 \sin 2\theta}$$

2.4.1.2 Five beam and FCAW methods

The 5-beam and FCAW methods have many similarities. Both use the velocity components u, v, w rather than the variances of the radial velocities as does the symmetric beam method. By subtracting the mean to obtain perturbation velocities

u', v', w', forming the products of these and then averaging, it is possible to obtain the required momentum fluxes.

Although the methods are similar they have different experimental arrangements. The 5-beam method uses Doppler beam swinging (section 2.3) to measure the velocity components. FCAW, on the other hand, uses FCA (section 2.1) to obtain the horizontal velocities, thus requiring a spaced antenna system, and calculates the phase of the autocorrelation function, which is equivalent to the radial Doppler shift, to get the vertical component (section 2.2).

Chapter 3
ST radars - MU radar results

This chapter presents the results of application of the methods of Chapter 2 to real data. This application has a twofold purpose, allowing the design and testing of software to be carried on independently of the actual progress of the VHF radar as well as facilitating the investigation of the techniques themselves. Section 3.1 deals with the experimental arrangements used on the MU radar to collect the data. Section 3.2 investigates the information obtained by studying the variation of received power with height and time. Section 3.3 compares horizontal FCA velocities. In particular, studies of the triangle size effect and comparisons between the algorithms of Briggs [1984] and Brown and Chapman [1972] are presented. Section 3.4 shows comparisons between the FCA of Briggs [1984] and Doppler beam-swinging data on both 10 and 50 minute timescales. Finally, section 3.5 uses the vertical and horizontal velocities from both FCA and DBS to investigate momentum fluxes.

3.1 Experimental details

3.1.1 The MU radar

The radar used to collect the data for this work is known as the Middle and Upper atmosphere (MU) radar and is located in Shigaraki ($35°N, 136°E$), Japan. It is operated by the Radio Atmospheric Science Center (RASC) of Kyoto University.

The data were collected on the 12th and 13th of May 1994 by Drs. Mamoru Yamamoto, of RASC, and Grahame Fraser, of the University of Canterbury. Phase decoding and coherent integration were performed at Shigaraki. The preprocessed data were stored on magnetic tape and brought back to New Zealand for analysis.

To determine if any significant meteorological events occurred during the experiments, surface analysis and 700, 500 and 300HPa maps (corresponding to approximately 3, 5.5 and 9km [Holton, 1979]) were obtained from the Japanese Meteorological Service. These maps show that at 1200 hours on the 12th of May 1994 a cold front was situated $\approx$ 1000km to the east moving eastward away from Japan and

a high pressure system was situated ≈ 300km to the northwest which over the next 24 hours moved eastward over Japan. During the time period covered no frontal systems passed over the radar site. Thus it may be concluded, considering the short (two day) time scale of the experiments, that the weather had no substantial effect on the wind or momentum flux measurements made.

A map of the location of the MU radar is shown in figure 3.1 and a photograph of the site is shown in figure 3.2.

Figure 3.1. Map showing the location of the Middle and Upper atmosphere (MU) radar operated by the University of Kyoto. The radar is located near Shigaraki (centre of figure).

3.1.1.1 System configuration

The MU radar is a sophisticated instrument and was designed to be flexible enough to carry out a wide range of experiments. A full discussion of the radar system can be found in articles by Fukao et. al. [1985a; 1985b]. Some of the parameters of the radar are given in Table 3.1.

The system uses the same antenna for transmission and reception and is thus not typical of most SA radars. This is to allow the facility to be used in both DBS and SA modes.

When used in the SA mode, up to four sections of the main antenna may be used to receive. These sections are comprised of hexagonal units of 19 crossed Yagi dipole elements, and may range in size from one unit to the entire aerial. The

Figure 3.2. A photograph of the MU radar site, at Shigaraki, Japan. The large circle at the bottom left is the aerial of 475 crossed Yagi antennae. The five boxes on the perimeter of the aerial contain the transmit/receive modules. The large building above this houses the control and processing equipment and accomodation. On the right is a helipad and tennis court and in the center top is an ionosonde aerial.

Parameter	**Value**
Frequency	46.5 MHz
Antenna diameter	103 m
Half power beam width	3.6°
Peak transmitter power	1 MW
Pulse length	$1 - 512$ μs
Pulse repetition rate	400 μs $-$ 65 ms
Pulse coding	up to 32 code elements

Table 3.1. Parameters of the MU radar

crossed Yagi aerial is essentially two Yagi elements at right angles and allows the antenna to use linear or circular polarisation. An example of the use of the main aerial for reception is shown in figure 3.3. For transmission all or part of the aerial may be used.

The system uses parallel processing to allow the fastest possible operation. Thus, for instance, operation does not have to cease while data is being processed as this is done by a separate unit.

3.1.1.2 Experimental configurations

FCA experiments

The data to be analysed in this work are from six experiments run by Drs. Yamamoto and Fraser on May 12 and May 13, 1994. Two aerial configurations were used. In both cases the entire aerial was used for transmission and four sections were used for reception. The aerials used for reception are shown in figure 3.3 and the times and configurations of the six experiments are shown in Table 3.2. Three of the six experiments used a quadrilateral array of receiving aerials and the other three used one with larger spacings.

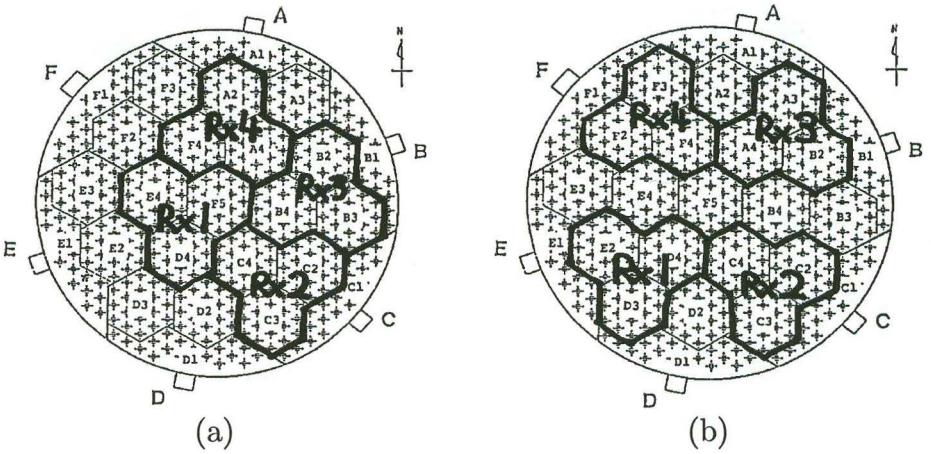

Figure 3.3. The two receiver aerial configurations used in the six FCA experiments analysed in this work. Experiments 1, 3 and 5 used configuration (a) and experiments 2, 4 and 6 used configuration (b). The portion of the main aerial used by each of the four receivers is indicated by the solid outline.

During each experimental run the same operational parameters were used. These are listed in Table 3.3. One data file was produced approximately every 26 seconds. The files contain the raw signals from each receiver; the only preprocessing done being 256 coherent integrations per sample and 16-bit phase decoding on each pulse.

DBS Experiments

When FCA experiments were not being performed the MU radar was used for DBS operation and thus DBS velocities are available immediately prior to and after some experiments in table 3.2. These are listed in table 3.4. The DBS experiments used the entire array for both transmission and reception, and a 10° zenith angle was used for reception. Similar operational parameters were used as for the FCA runs

Expt no.	Date	Start time	End time	Receiver config.	Number of radar runs
1	12 May 1994	5:47 pm	6:54 pm	a	154
2	12 May 1994	6:56 pm	8:19 pm	b	191
3	13 May 1994	10:06 am	11:16 am	a	160
4	13 May 1994	11:18 am	12:23 pm	b	150
5	13 May 1994	12:27 pm	2:35 pm	a	294
6	13 May 1994	2:37 pm	3:29 pm	b	119

Table 3.2. Details of the six FCA experiments performed using the MU radar. The receiver configuration used in each experiment is shown in Figure 3.3a or 3.3b. The number of complete radar runs is the number of output files containing 256 coherently integrated samples at all 64 heights.

Parameter	Value
Minimum height	5100 m
Maximum height	14550 m
Height resolution	150 m
Number of heights	64
Number of coherent integrations	256
Number of incoherent integrations	0
Interpulse period	400 μs
Number of coherently integrated samples	256
Complementary code length	16 bits
Code bit length	1 μs
Phase flipping	yes
Transmission polarisation	Right circularly polarised

Table 3.3. Further operational parameters used in the FCA experiments.

and these are given in table 3.5. Two notable differences are the greater maximum height and the reduced time resolution (24.15km and 58.3s for DBS as compared to 14.55km and 26.2s for FCA). The latter is due to the different numbers of coherent and incoherent integrations performed and also the fact that DBS must sample 5 separate beams.

As the primary focus of this thesis is the investigation of the SA method of wind determination it was not considered necessary to develop a suite of DBS analysis software. To this end programs written by Dr. W. Brown, who was at that time at RASC, were used to obtain both Cartesian and radial velocities from the raw data files. Minor modifications were made to the programs supplied by Dr. Brown to allow execution on the Canterbury University computer systems. The operation of these programs is described in section 3.4.1.

Expt no.	Date	Start time	End time	Number of radar runs
1	12 May 1994	4:25 pm	5:27 pm	57
2	12 May 1994	8:37 pm	9:30 pm	50
3	13 May 1994	8:41 am	9:34 am	50
4	13 May 1994	3:37 pm	4:31 pm	50

Table 3.4. Details of the DBS experiments performed using the MU radar.

Parameter	Value
Minimum height	5100 m
Maximum height	24150 m
Height resolution	150 m
Number of heights	128
Number of coherent integrations	38
Number of incoherent integrations	6
Interpulse period	400 μs
Number of coherently integrated samples	128
Complementary code length	16 bits
Code bit length	1 μs
Phase flipping	yes
Transmission polarisation	Right circularly polarised
Number of beams	5
Beam directions	N, E, S, W and vertical
Zenith angle	10°

Table 3.5. Further operational parameters used in the DBS experiments.

3.1.1.3 Data format

Data were collected continuously using a newly installed preprocessing and data-collection system which allows the radar to continue operation without the need to stop and write data to tape. These data were brought back from Japan by Dr. Fraser on Exabyte tape and were written onto zip files on a cd-rom by the University of Canterbury Computer Services Centre. While allowing the files to be read without an Exabyte drive, this meant that a large temporary storage space was needed to unzip the files. This difficulty was eventually solved by writing the unzipped files to cd-rom.

The data files are in binary form and contain a header followed by the pre-processed signals from the receivers. The header contains such information as the time of the experiment, the number of samples taken and the number of ranges sampled. The data from the receivers are real numbers stored in 4-byte big endian

Variable	Sensor Type	Range	Resolution
Pressure	Capacitive aneroid	1060 to 3 hPa	0.1 hPa
Temperature	Capacitive bead	+60 to -90 °C	0.1 °C
Relative humidity	Thin-film capacitor	0% to 100% RH	1% RH

Table 3.6. Specifications for a Vaisala RS80 radiosonde.

format, i.e. the most significant byte is leftmost. The FCA data are stored in ascending height and ascending receiver-number order; i.e. the real and imaginary data for receiver one from the minimum to the maximum height followed by the real and imaginary data for receiver two from all heights and so on.

When the DBS data were being analysed it was realised that some files had not been brought back to New Zealand and this was rectified by applying to RASC for the remaining data. The prompt fashion in which these were produced was most commendable. These new files were initially in a native VMS binary format, with a non I.E.E.E. bit ordering for the real numbered data, however, once this was realised, a small program was written to convert the data to I.E.E.E. format.

3.1.2 The Vaisala RS80 radiosonde

The radiosonde data analysed in this work are from a Vaisala RS80 radiosonde. A Vaisala sonde is connected to a helium-filled meteorological balloon and may ascend to altitudes of around 35km. Temperature, pressure and relative humidity data are recorded. The sonde is not tracked by radar and hence geopotential heights are calculated. The outputs from the various radiosonde sensors are used to modulate a radio signal in a predetermined sequence (e.g. pressure-temperature-pressure-humidity ...) This signal is then electronically decoded and further processed by a computer program to produce the required information. The specifications of the Vaisala RS80 are given in Table 3.6.

3.2 Signal characteristics

3.2.1 Introduction

Consideration of calculated wind velocities will not always expose all facets of an atmospheric phenomenon. Often, as is the case here, other characteristics of the

radar signal may be highly revealing. In this section, the nature of the returned signal power, correlation functions and Gaussian fitting failures are investigated. Figures 3.4 to 3.9 show these characteristics for each of the six experimental runs. Similar plots are obtained regardless of which receivers are chosen.

Part (a) of each figure shows the signal power measured by receiver 1 as a height-time-intensity (RTI) plot. The corresponding (b) figures show RTI plots of the 'raw' (i.e. prior to Gaussian fitting) crosscovariances between receivers 1 and 2. These are plotted, in preference to the fitted correlation values, so as to provide information on the correlation between the aerials in the regions where the FCA software fails. The values are in decibels, i.e. $value_{dB} = 10 \log value$, where *value* is an intensity or power level. Note that all decibel values given in this work are relative to a value of unity. A colour scale is given below each graph. Part (c) of figures 3.4 to 3.9 shows Boolean-type height-time plots of failures in the Gaussian fitting procedure. This procedure is necessary for calculation of the τ and τ' values of the full correlation analysis. Failure in the fitting of one or more of the auto or crosscorrelation functions is indicated by a blue square. If failure occurs in the fitting routines it is impossible to calculate a wind velocity or any other FCA parameter.

Two main features may be observed in figures 3.4 to 3.9. The first is the sporadic vertical stripes of high reflected power with a region of very high power near the center of the stripe. These can be seen in all figures and are usually found above 10 km. Such events appear to correspond to high values of crosscorrelation, as well as to failures in the Gaussian fitting routine. The second feature is the presence of layered structures. These can be seen most obviously in figures 3.4 and 3.5 although a single layer near 11.5 km is observable in most figures. The low-powered layers often show quite fine detail and are highly correlated with layered structure in both the crosscorrelations and the failure plots. Each of these features will now be considered in more detail.

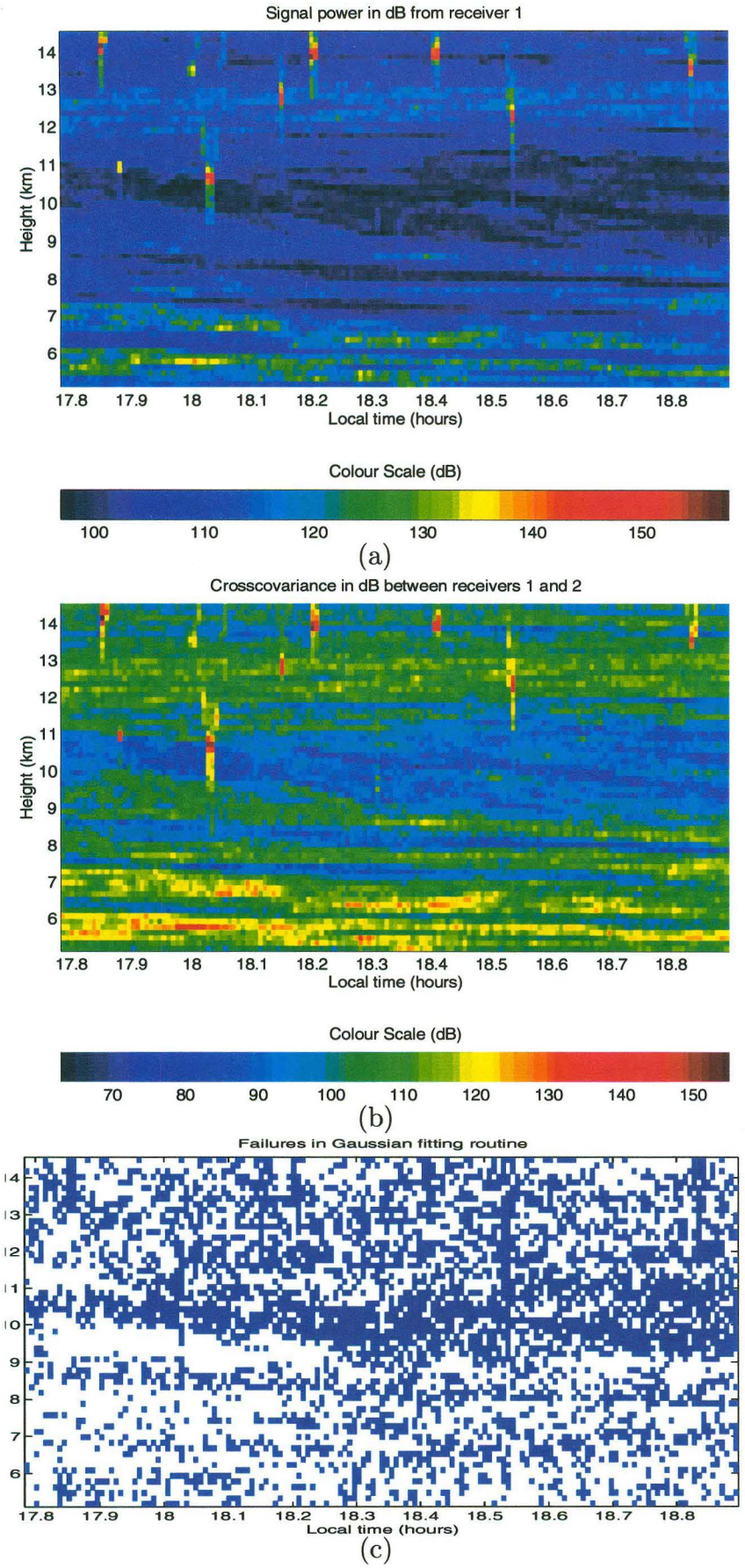

Figure 3.4. Height-time-intensity and height-time-failure plots of the data from experiment 1. (a) shows the average signal power (dB) over the 256 samples in each radar run from receiver 1, (b) shows the calculated cross-covariance (dB) between receivers 1 and 2 and (c) shows the points (in blue) at which the correlation function fitting routine failed.

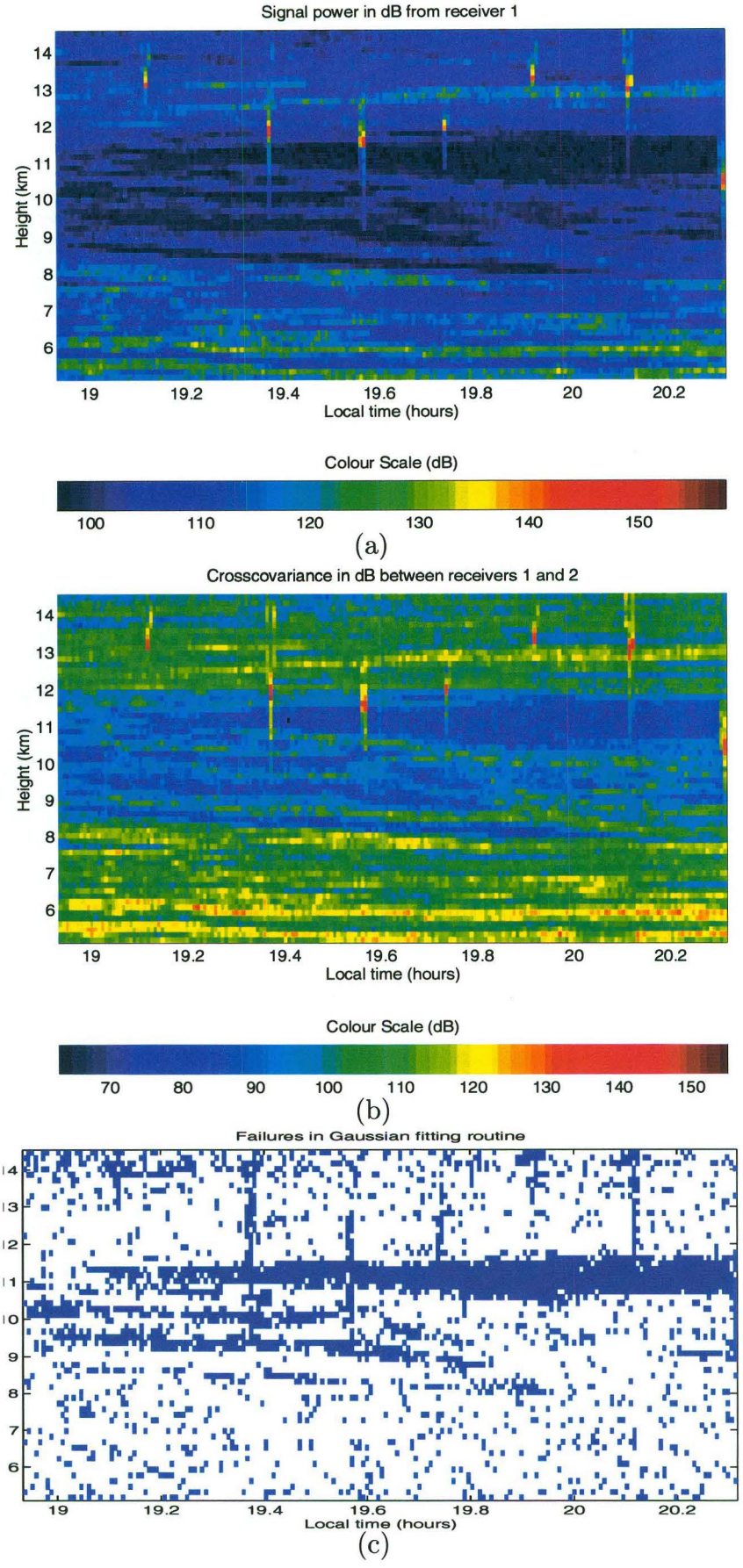

Figure 3.5. Height-time-intensity and height-time-failure plots of the data from experiment 2. (a) shows the average signal power (dB) over the 256 samples in each radar run from receiver 1, (b) shows the calculated cross-covariance (dB) between receivers 1 and 2 and (c) shows the points (in blue) at which the correlation function fitting routine failed.

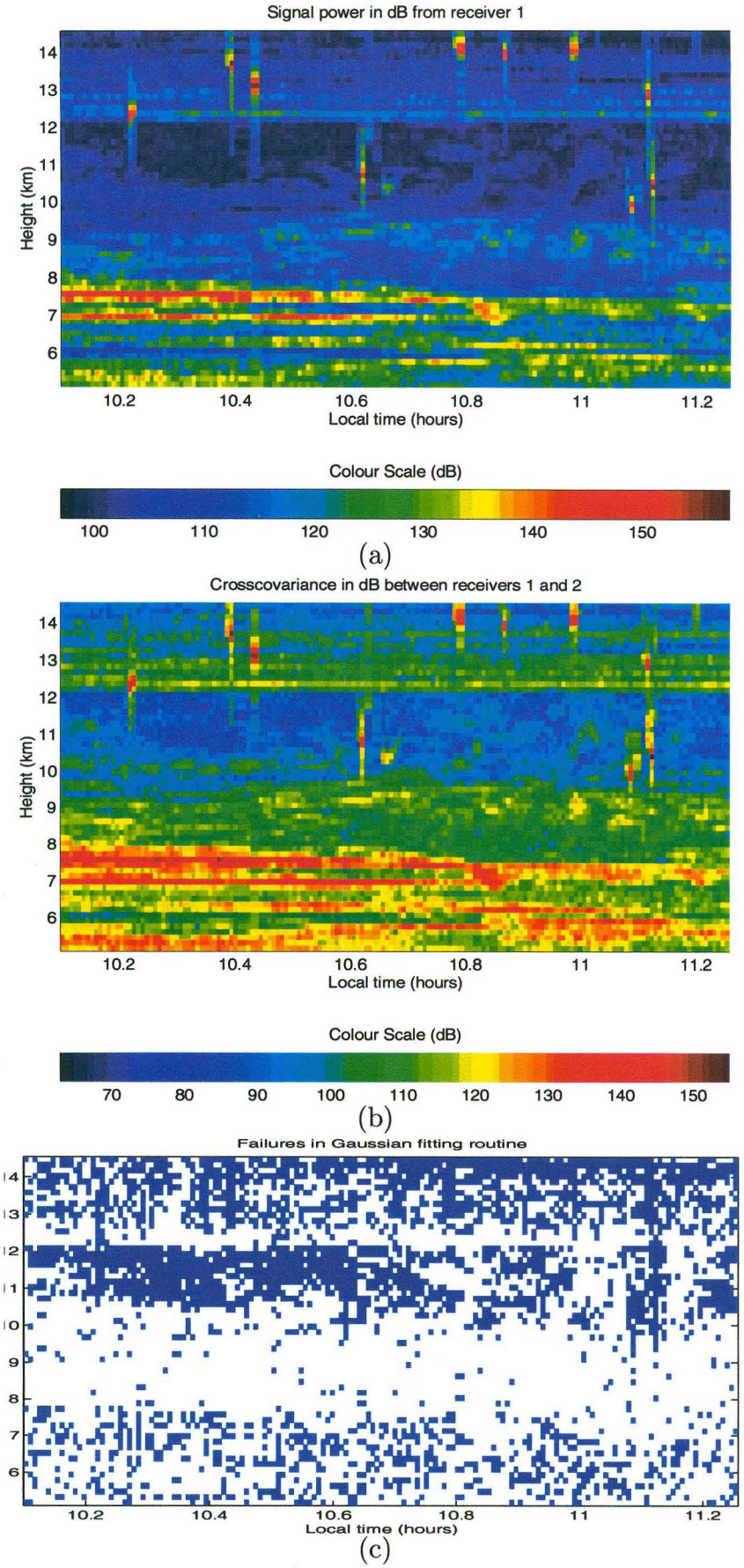

Figure 3.6. Height-time-intensity and height-time-failure plots of the data from experiment 3. (a) shows the average signal power (dB) over the 256 samples in each radar run from receiver 1, (b) shows the calculated cross-covariance (dB) between receivers 1 and 2 and (c) shows the points (in blue) at which the correlation function fitting routine failed.

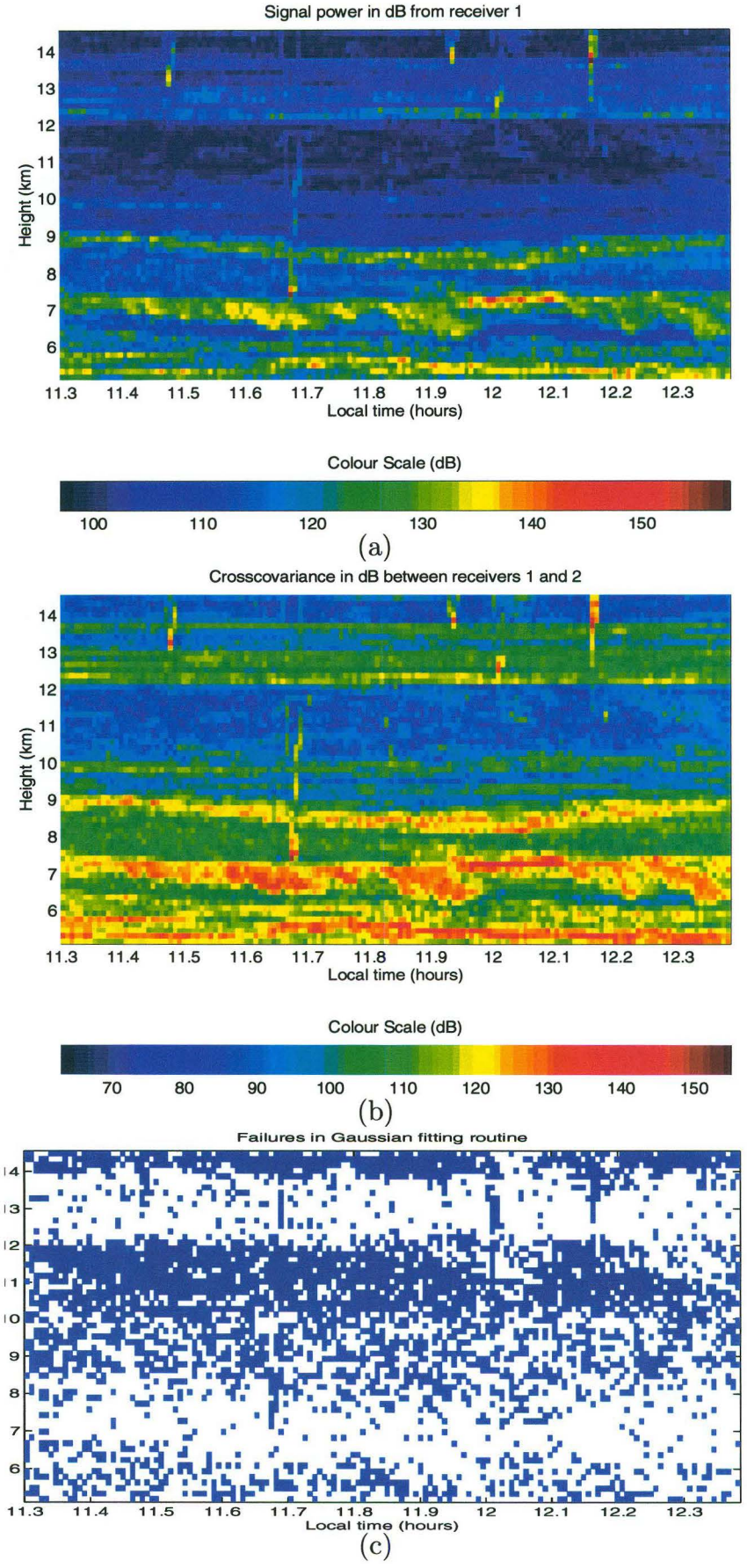

Figure 3.7. Height-time-intensity and height-time-failure plots of the data from experiment 4. (a) shows the average signal power (dB) over the 256 samples in each radar run from receiver 1, (b) shows the calculated cross-covariance (dB) between receivers 1 and 2 and (c) shows the points (in blue) at which the correlation function fitting routine failed.

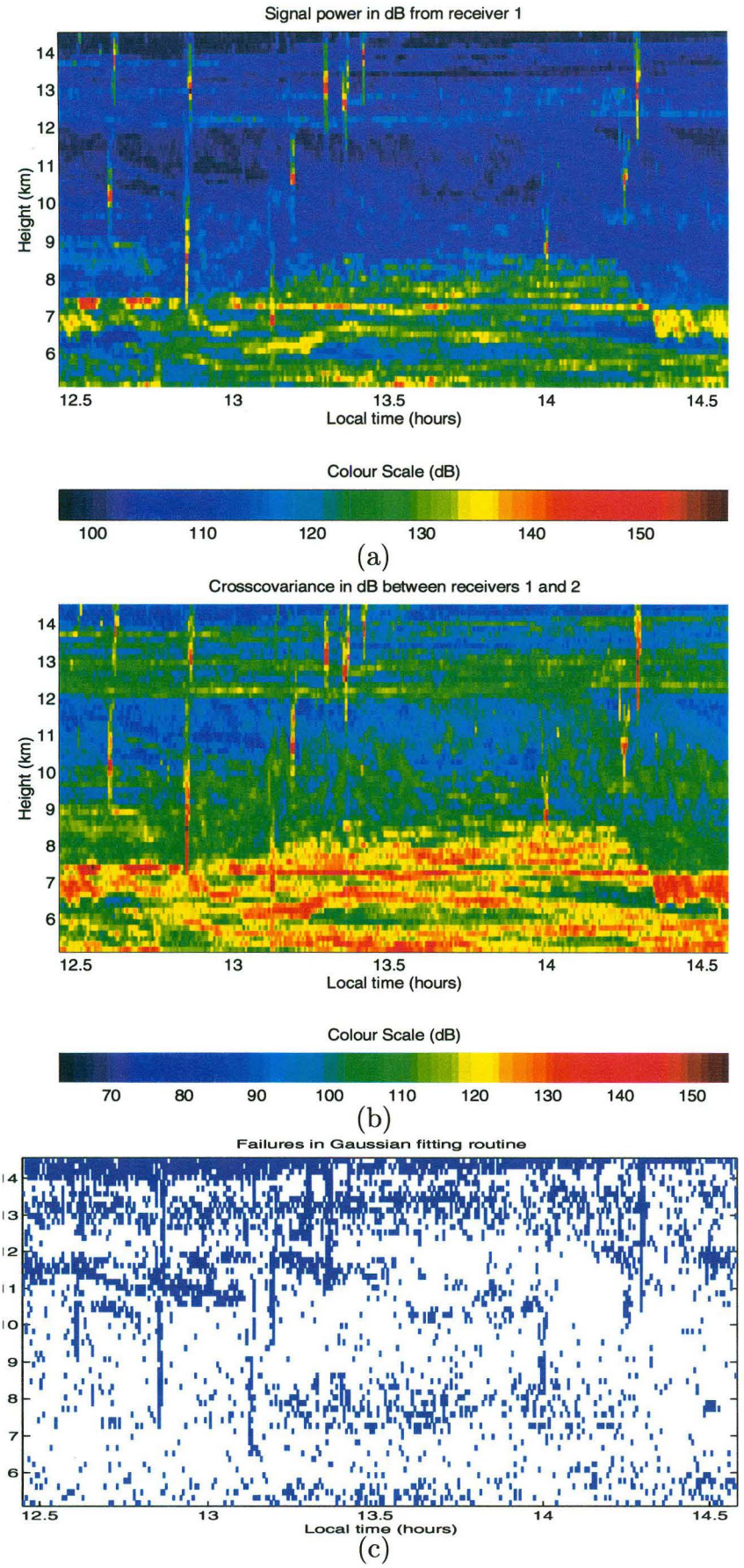

Figure 3.8. Height-time-intensity and height-time-failure plots of the data from experiment 5. (a) shows the average signal power (dB) over the 256 samples in each radar run from receiver 1, (b) shows the calculated cross-covariance (dB) between receivers 1 and 2 and (c) shows the points (in blue) at which the correlation function fitting routine failed.

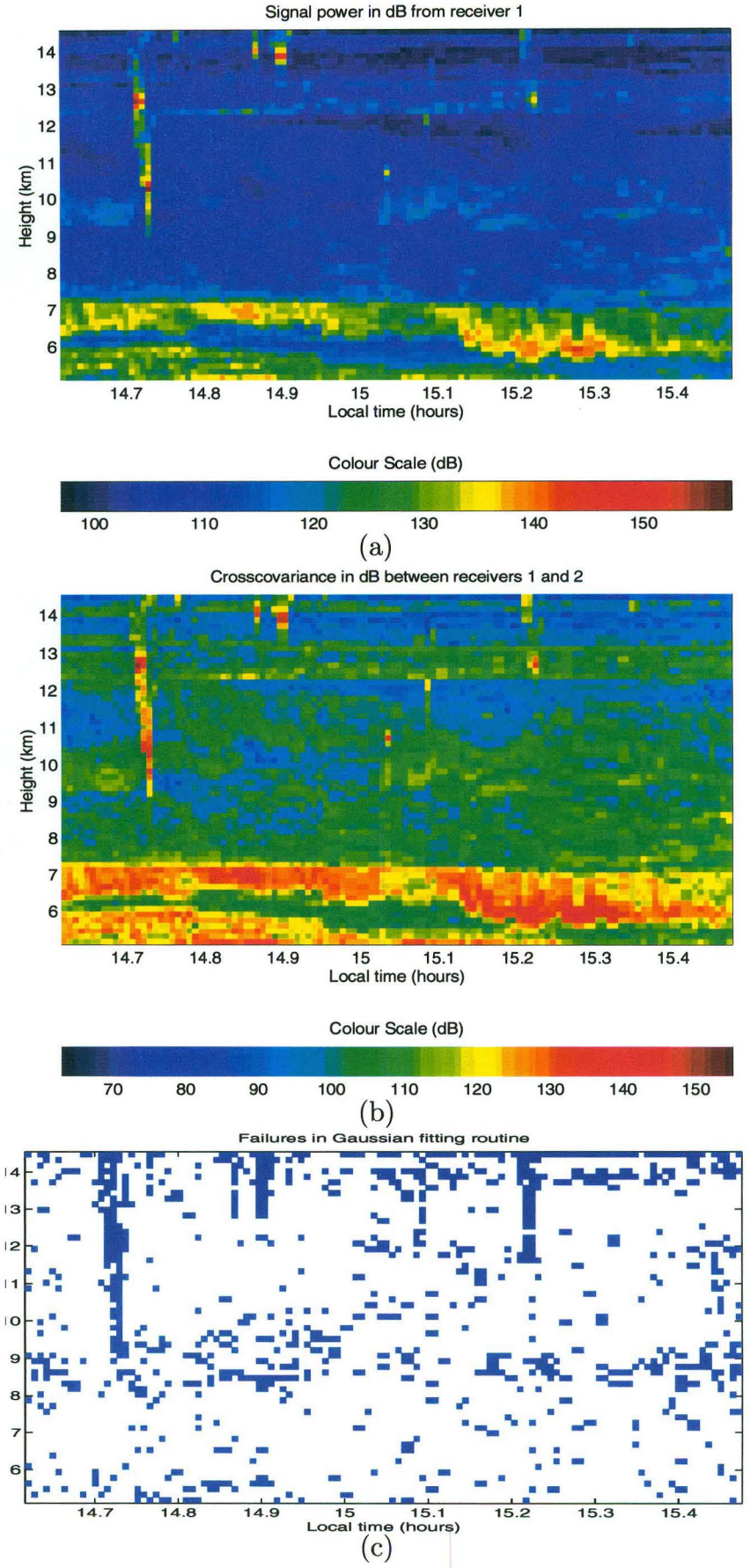

Figure 3.9. Height-time-intensity and height-time-failure plots of the data from experiment 6. (a) shows the average signal power (dB) over the 256 samples in each radar run from receiver 1, (b) shows the calculated cross-covariance (dB) between receivers 1 and 2 and (c) shows the points (in blue) at which the correlation function fitting routine failed.

3.2.2 High-powered events

It can be seen from figures 3.4 to 3.9 that the sharp vertical stripes of high power (part (a)) correlate with the failures of the Gaussian fitting routine shown in part (c). Since such failures make it impossible to determine wind velocities, their cause is of some interest. Recall from section 2.1.3 that the fitting routine takes a portion of the calculated correlation function and seeks to minimise the difference between these points and a Gaussian function. Fitting failures are thus likely to be due to the form of the correlation functions. In this and subsequent sections all fitted correlation functions have been normalised as described in section 2.1.3 and thus the raw correlation data may be greater than unity.

Analysis shows that there is in fact a major difference between the calculated correlation functions in regions of fitting failure, and those from which the analysis proceeds successfully to a velocity. Figures 3.10 and 3.11 show horizontal sections, i.e. data from the same heights but different times, through two of these events - each from a different experimental run. As can be seen in figures 3.10d-f and 3.11g-i the correlation functions, and hence the frequency-power spectrum (which is the Fourier transform of the autocorrelation function), during the event are markedly different to the same functions before and after. The former calculated correlation functions become almost delta-function-like in shape and usually show large sidelobes. Note that the crosscorrelations measured during the events are very large, indicating that all receivers are observing essentially the same signal, i.e. that the ground-echo pattern has no spatial variation. The frequency-power spectra show aliasing, as there is a large amount of power near the Nyquist frequency. Since this can not instantaneously fall to zero it follows that the non-zero power beyond the Nyquist frequency will be aliased back into the region of interest.

The signal powers of the high-power events are also markedly different to the those from 'normal' regions. The power shown in the RTI plots (figure 3.4 to 3.9) is the average of the 256 samples in each radar run. Figures 3.12a and b show the signal power of each individual sample for the two events displayed in figures 3.10 and 3.11. It can be seen that rather than a continuous high-power signal throughout the entire sample or a single isolated spike of very high power, there is a gradual rise up to a maximum followed by a gradual decrease back to the ambient level.

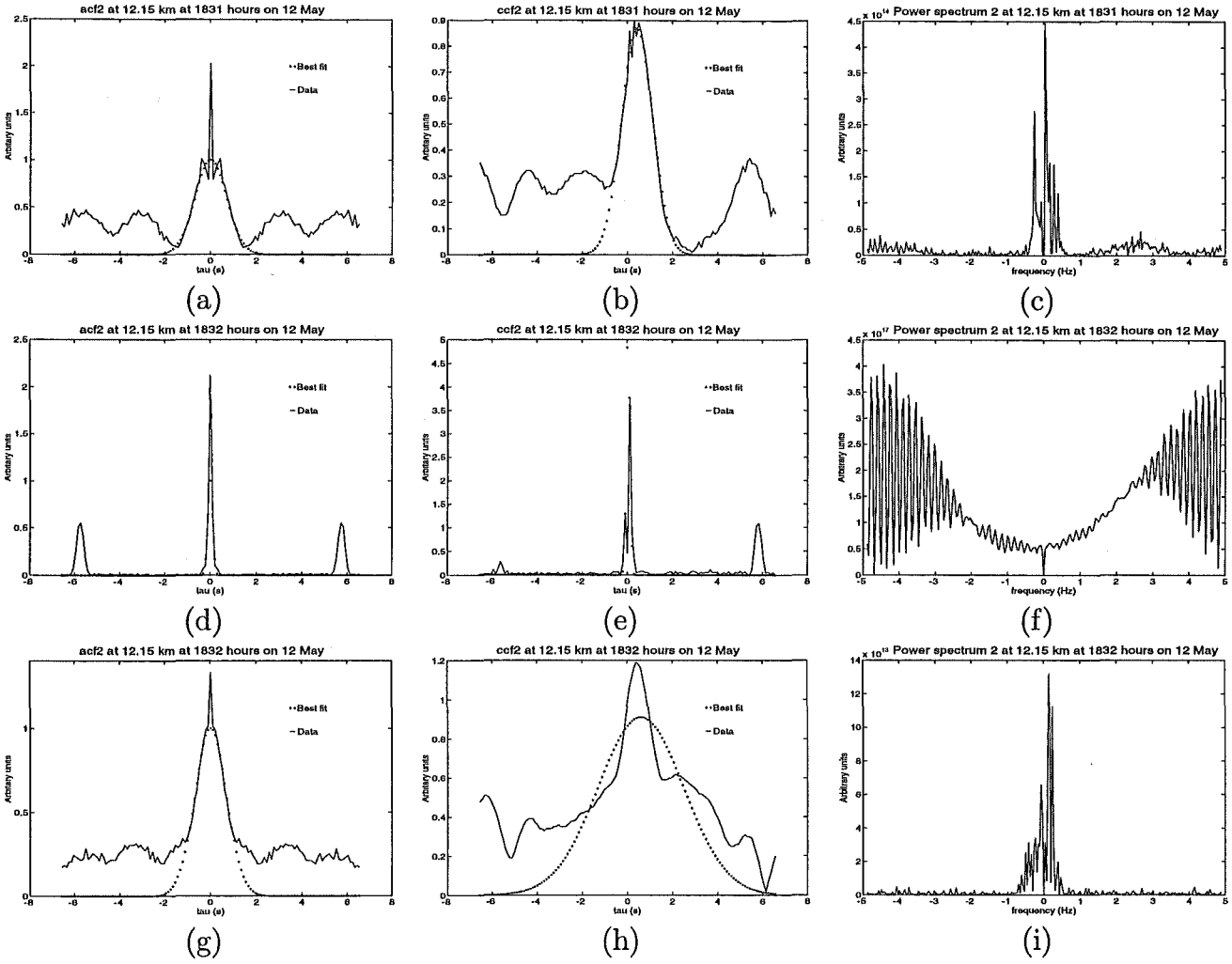

Figure 3.10. Auto- (acf) and cross- (ccf) correlation functions and power spectra for a high-power event in experiment 1. Figures (a)-(c) are before the event, (d)-(f) are during the event and (g)-(i) are after the event.

These signal characteristics can also be seen in figures 3.13 and 3.14 which display the same type of plot for a number of other high-power events. In these figures the signals from each of the four receivers are successively offset by 40dB for clarity. This signal shape is strongly suggestive of a highly reflective object passing through the aerial beam. Two explanations are presented as to the source of these echoes. The first, suggested by Dr. W. Brown (pers com), is that they are range- and frequency-aliased meteor echoes. The second is that they are due to aircraft.

Range aliasing refers to a phenomenon whereby echoes from heights above a certain level are observed to come from a lower level. Such aliasing occurs because the radar, as mentioned in Section 1.2.1, determines range from the time lag measured from the *immediately preceding* transmitter pulse. Thus an echo which takes longer to return than the period between successive transmitted pulses would

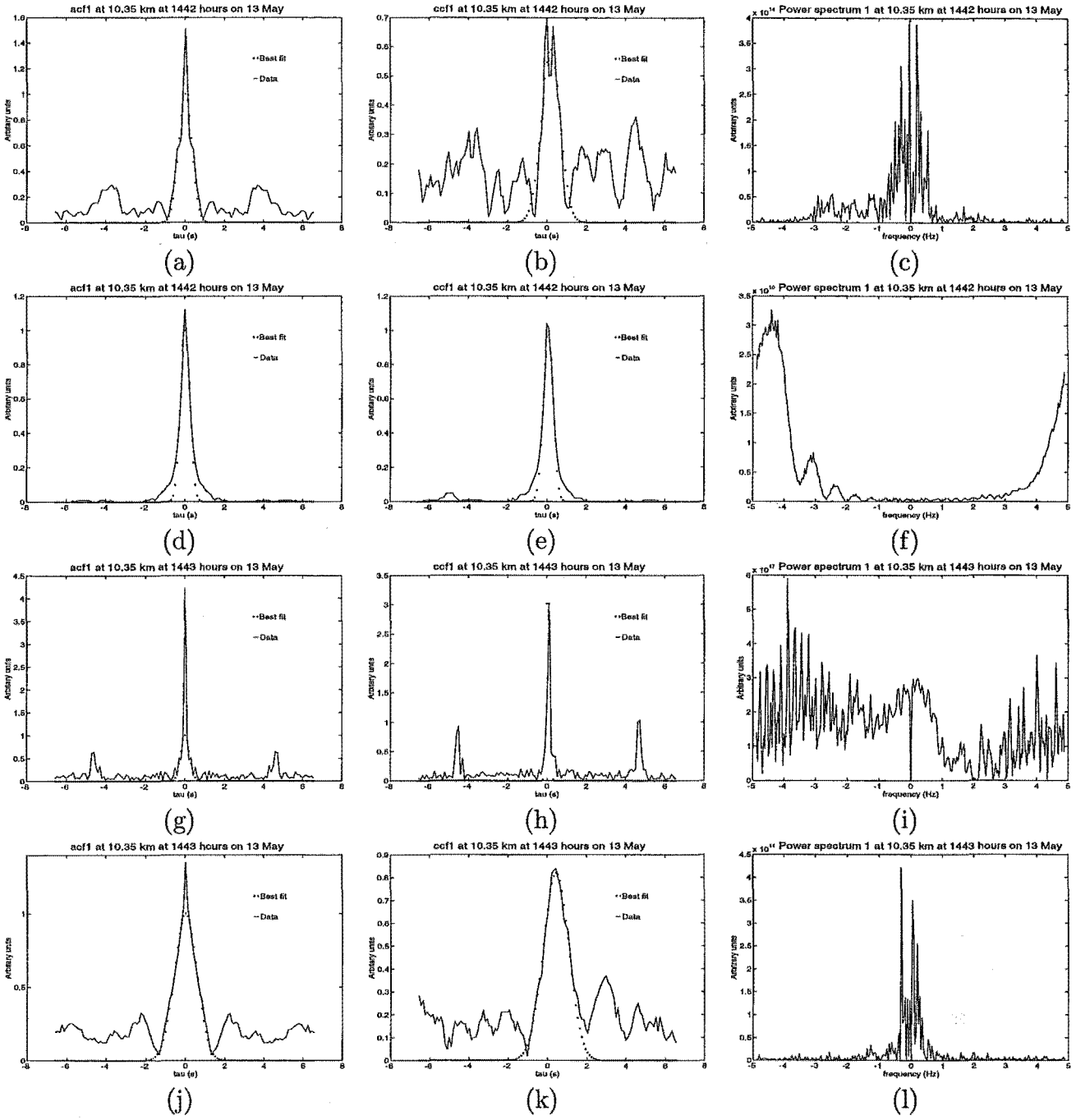

Figure 3.11. Auto- (acf) and cross- (ccf) correlation functions and power spectra for a high-power event in experiment 6. Figures (a)-(c) are before the event, (d)-(f) are immediately before the event, (g)-(i) are during the event and (j)-(l) are after the event.

appear to come from a lower height. This would certainly be the case for meteors which are observed in a layer with a height of maximum occurrence of approximately 95km (S. Marsh pers com).

It is unlikely however that the events are due to meteors as the signal powers shown in figures 3.12, 3.13 and 3.14 do not have the form expected for a meteor echo.

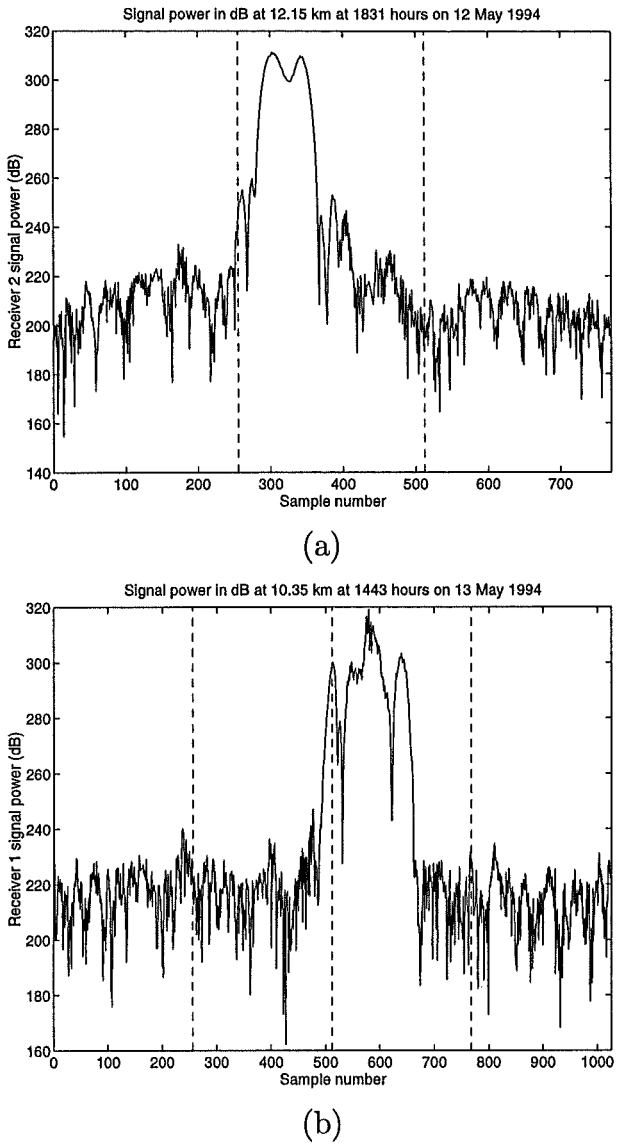

Figure 3.12. Signal power (dB) for the 256 individual samples in each of the runs shown in Figure 3.10 and 3.11. As the MU radar has no delay between runs the data may be concatenated. Dashed lines indicate the end of each run and the commencement of the next.

In such a case, the power should increase sharply up to some maximum and then decrease exponentially as the trail of ionisation produced by the meteor diffuses. This is definitely not observed in the radar experiments. In addition the interpulse period of section 3.1.1.2 translates to a height of 60km and thus most of the 'meteors', which appear to occur between 10-15km, would be coming from heights of 70-85km which is rather lower than the height of maximum meteor occurrence.

Aircraft have much greater reflectivity than the surrounding air and are likely to be found at heights observed with the radar. Each radar run involves 256 samples spaced at intervals of 0.1024 seconds and is thus approximately 26 seconds long. For

an object to produce a high reflected power it must be within the radar sampling volume (or main beam) for some portion of the radar run. The MU radar has a total beam width of 3.6° which, at the heights shown (assuming a vertical direction and no range aliasing) in figures 3.10 and 3.11, gives a spatial width of 750m and 650m respectively. The speed of these objects can be estimated by considering how long they take to pass through the main aerial lobe. If the time for the power in figure 3.12 to rise and fall back to normal levels is taken as one third of the total run an estimate for the horizontal velocity on the order of 300ms^{-1} is obtained. This agrees well with the approximate cruising speed of a typical passenger jet aircraft of 260ms^{-1} (A. Grant pers com).

A high-power event is present in the radar data approximately every 5min. Attributing these events to aircraft would require a relatively high flow of air traffic over the radar. However the radar site *is* on a line between Osaka and Nagoya, two major cities in Japan, and it is possible that the site does lie under major domestic and/or international routes.

Aircraft-clutter removal has been discussed by several workers. Hocking [1993] has used Fourier transformations of very long data series with no coherent integration. Since the aircraft echoes occur at different frequency shifts to the atmospheric signal they can then be removed [Hocking, 1997c]. Bowhill [1986] has used a Tukey algorithm to remove aircraft echoes from data. The Tukey algorithm, applied to a data array, compares each data point with the two on either side. If the three points form a monotonically increasing or decreasing sequence, the original point is copied without change. However, if the central data point is remote from the other two, it is replaced by whichever of the two surrounding points is closest to it in value. Carter [1983] discusses an on-line system in which sudden large changes in the data are not included in the coherent integration. Perhaps, though, the final word should go to Rottger [1983] who suggests not siting the radar under an aircraft flight route.

In conclusion, the high-powered events discussed here have been found to have very different signal characteristics to the surrounding regions. The signal power during the events does not appear to have the form required for a meteor echo, and it therefore seems likely that they are due to the passage of aircraft through the antenna beam.

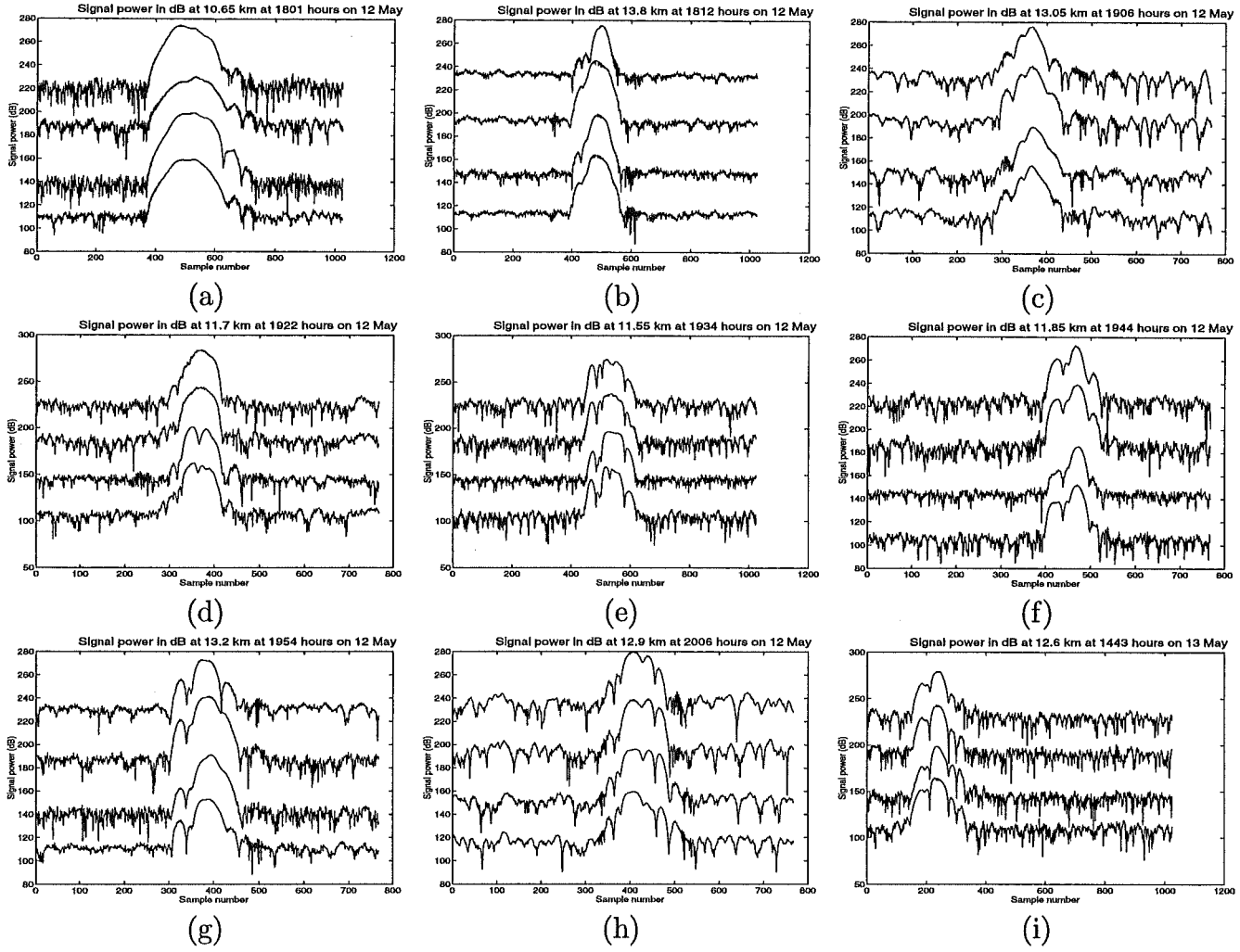

Figure 3.13. Signal power (dB) during several high-power events. Data from all four receivers are shown on each graph and are successively offset by 40dB for clarity. Figures (a) and (b) are from experiment 1, (c) - (h) are from experiment 2 and figure (i) is from experiment 6.

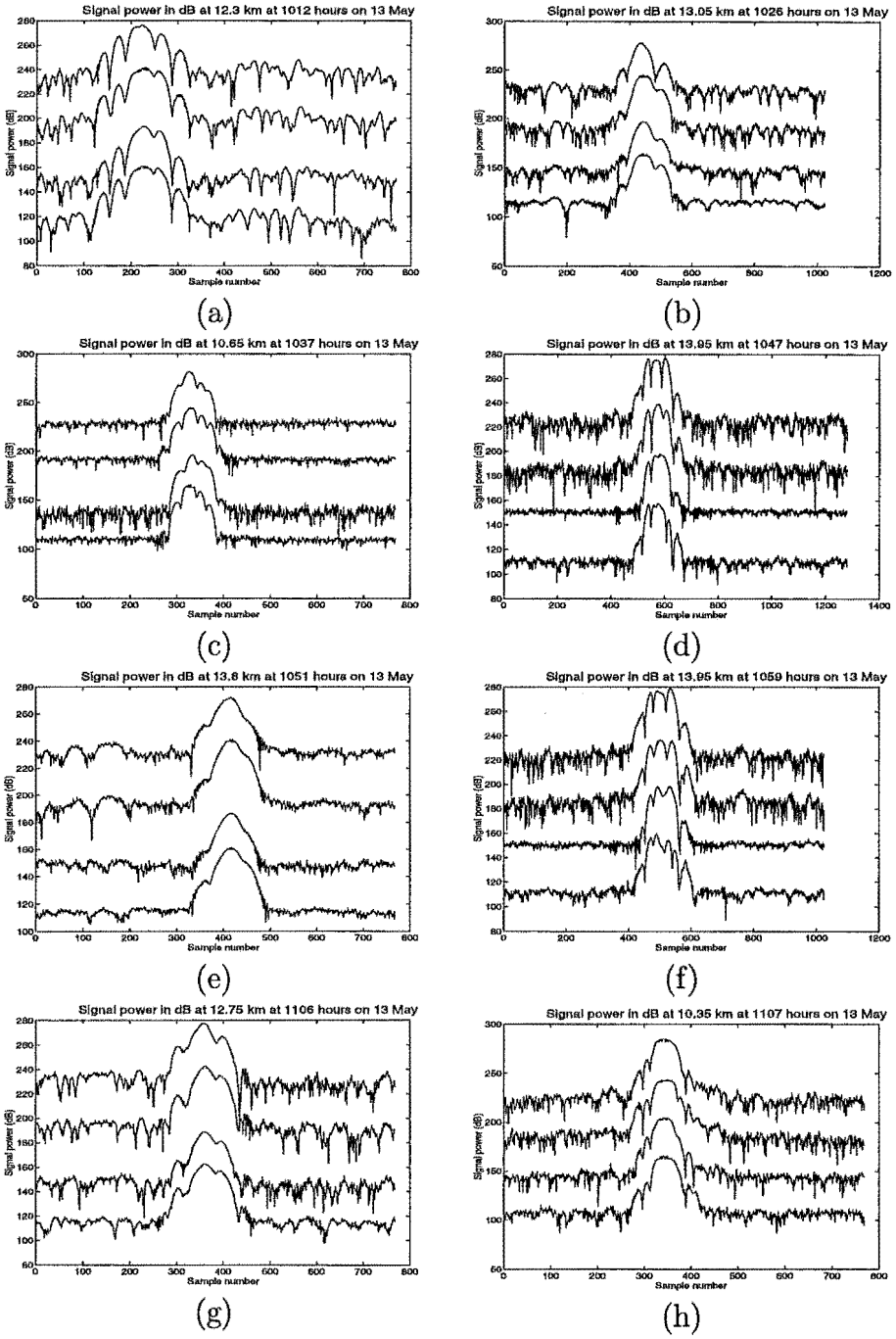

Figure 3.14. Signal power (dB) during high-power events in experiment 3. The data show the signal power of the 256 samples in each run. As the MU radar has no time delay between runs the data from sucessive runs have been concatenated. Data from all four receivers are shown on each graph and are successively offset by 40dB for clarity.

3.2.3 Low-power layer structure

Horizontal atmospheric layers have been reported by a number of workers [e.g. Green and Gage, 1980; Kumar et al., 1994; Rao et al., 1994; Brown et al., 1995b; Hooper and Thomas, 1998]. These features are usually persistent events found over narrow height ranges, and show enhanced scatter. Similar layers can be seen in the lower tropospheric region of the RTI plots (figures 3.4 to 3.9) presented here. In this section, however, it is the regions of low reflected power that are of interest. These features can be clearly seen in part (a) of figures 3.4 and 3.5 with corresponding layers of low cross-covariance shown in part (b), and layers of failure in the Gaussian fitting routines in part (c) of these figures.

The first step in investigating these low-power layers will be to consider the cause of the failures in the fitting routines. Low signal power does not necessarily imply fitting failure, although a very low signal-to-noise ratio may make the fit less plausible. If the received signal contains only noise or uncorrelated signal then this will produce correlation functions to which it is meaningless to fit any analytical form.

Figures 3.15a-u and 3.16a-aa show the calculated auto- and crosscorrelation functions and the corresponding power spectra for vertical slices through two different regions of low-power layers in experiments 1 and 2. The signal characteristics of slices within and between the layers are shown, as described in the figure captions. Note that the vertical scales on the crosscorrelation function plots are different to those on the autocorrelation functions.

Most of the autocorrelation functions of the low-power layers show the presence of a high level of random noise in the signal, as indicated by the large noise spike at zero time shift. Some layers have such a noisy signal that the autocorrelation function essentially becomes a delta function. The crosscorrelation functions are also noisy and there is no evidence for the correlation of the random noise between receivers - this would produce a noise spike on the crosscorrelation functions.

It is useful, as a comparison, to consider the auto- and crosscorrelation functions that would be calculated from a series of random numbers. The autocorrelation of a noise series with itself would be negligible, except at the origin where correlation

would be complete. The crosscorrelation of two different random series would also, except for random fluctuations, be essentially zero.

With this in mind, a close consideration of the correlation functions in figures 3.15 and 3.16 reveals that while in some cases there are layers with correlated signals in the presence of noise, e.g. figures 3.15d-e, in the majority of low-power layers the reflected signal is essentially uncorrelated. This can also be seen in figures 3.4b and 3.5b where the crosscorrelation in the layers is over 20 dB less than the surrounding regions.

The signal power of such a layer is often several orders of magnitude less than that in the intervening regions. This can be seen in figures 3.17a and 3.17b which show the signal-power profiles of the features under consideration. It was noted by Sheppard et al. [1993] that the failure rate of FCA was highest in regions of low signal-to-noise ratio. Their analysis of approximately 60 hours of data recorded on the MU radar found the highest number of failures to be from 11 to 13 km which is in general agreement with the heights at which Gaussian fitting failure occurs in the experiments discussed here.

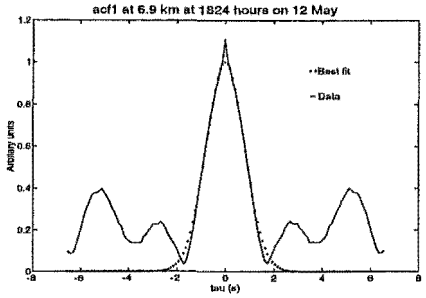

(a)

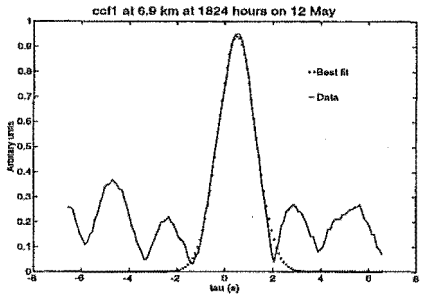

(b)

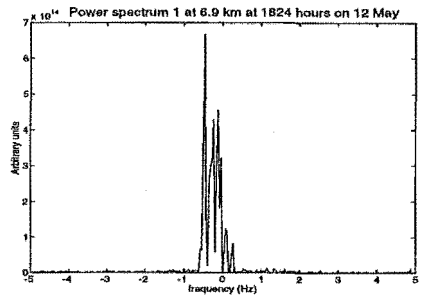

(c)

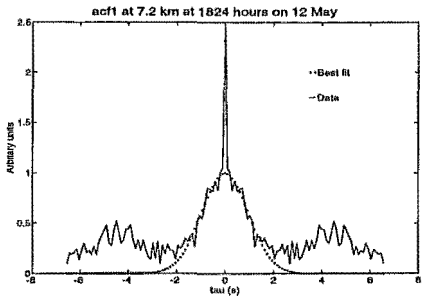

(d)

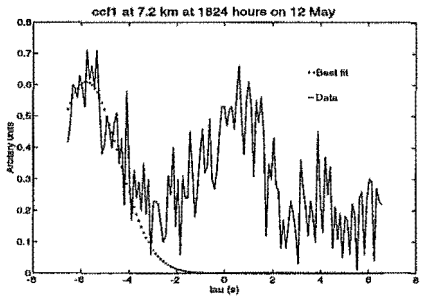

(e)

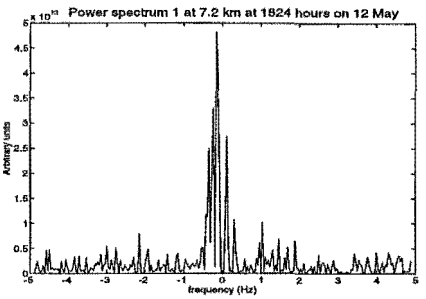

(f)

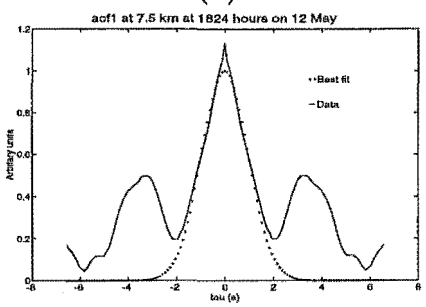

(g)

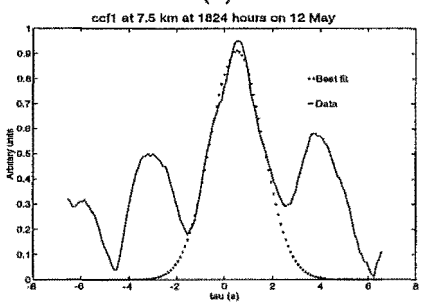

(h)

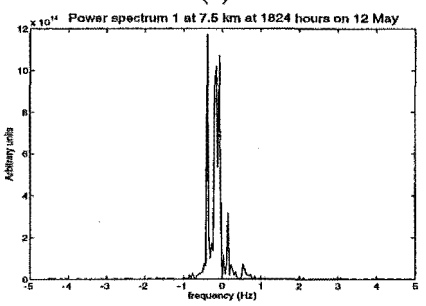

(i)

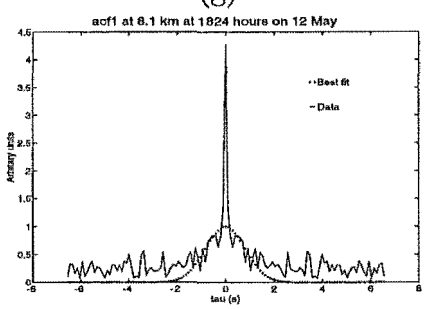

(j)

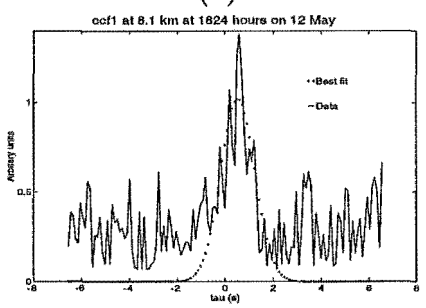

(k)

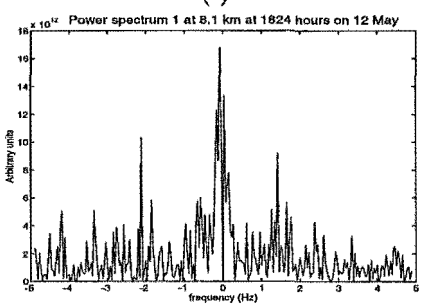

(l)

Continued over page

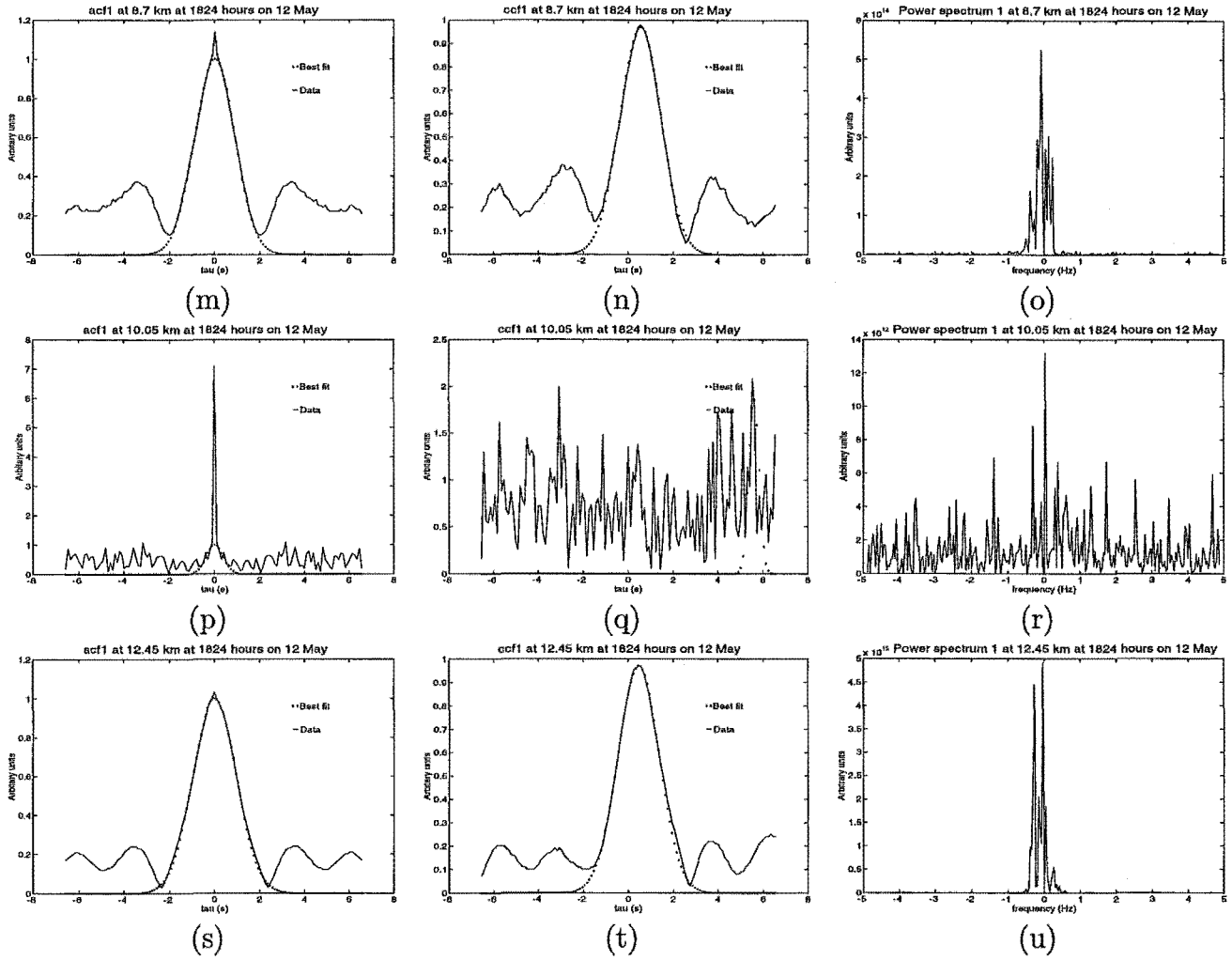

Figure 3.15. Correlation functions and power spectra for low-power layers in experiment 1. Figures (a)-(c) are below the layers, (d)-(f) are in the lowest layer, (g)-(i) are between the first and second layers and (j)-(l) are in the second layer. Figures (m)-(o), (p)-(r) and (s)-(u) are respectively below, in and above the main layer near 10.5 km.

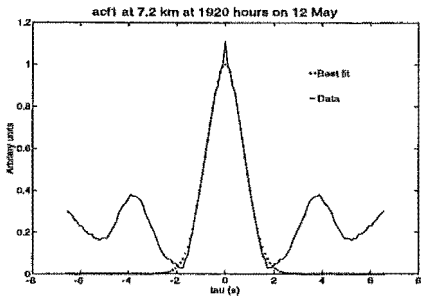

(a)

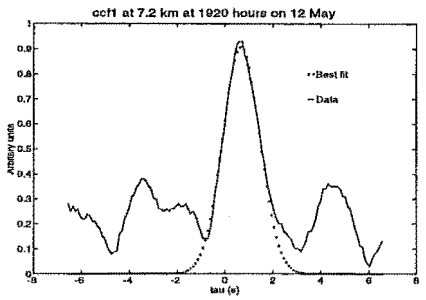

(b)

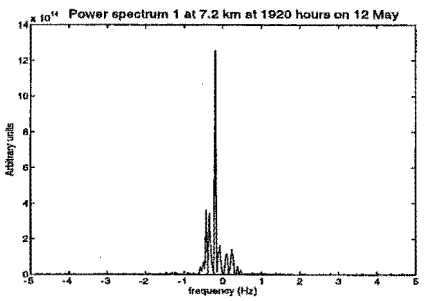

(c)

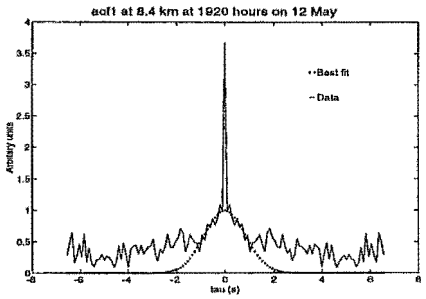

(d)

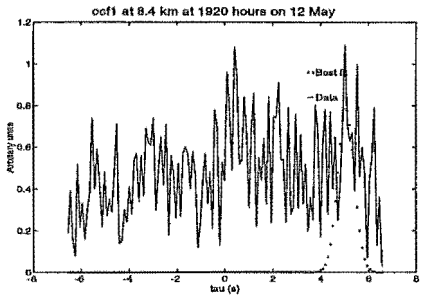

(e)

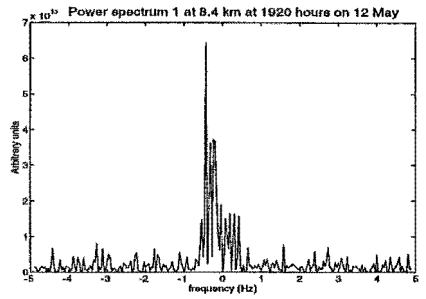

(f)

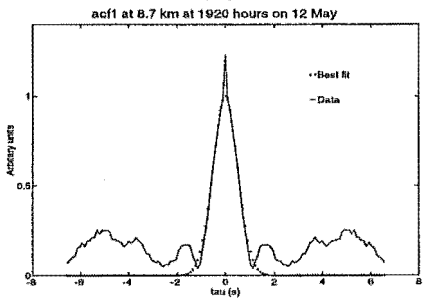

(g)

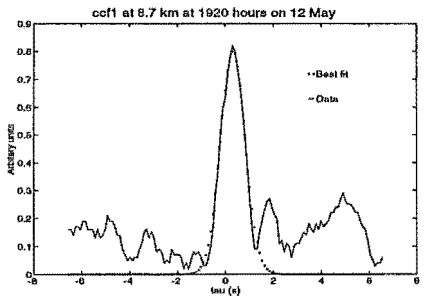

(h)

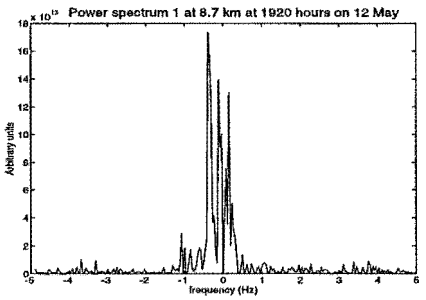

(i)

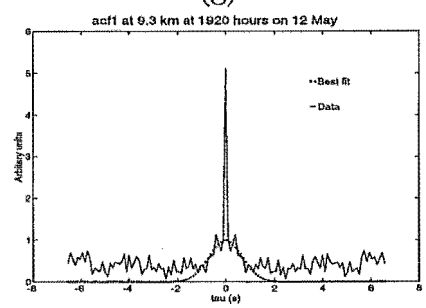

(j)

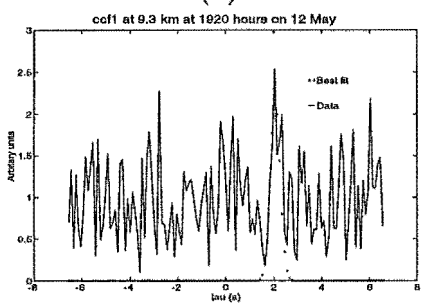

(k)

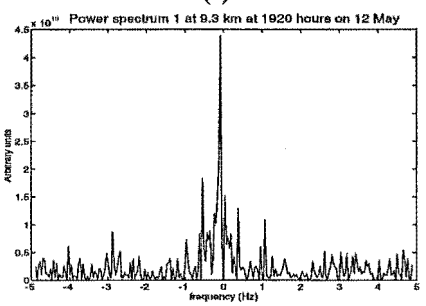

(l)

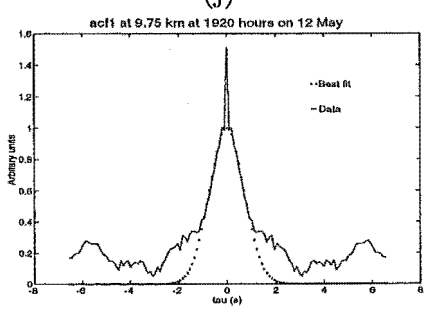

(m)

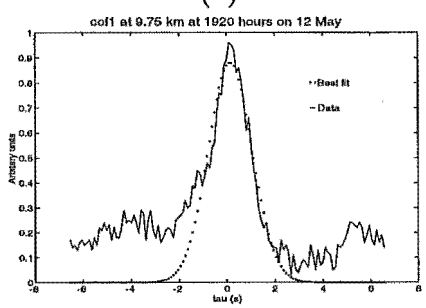

(n)

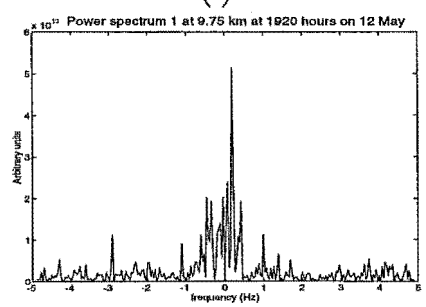

(o)

Continued over page

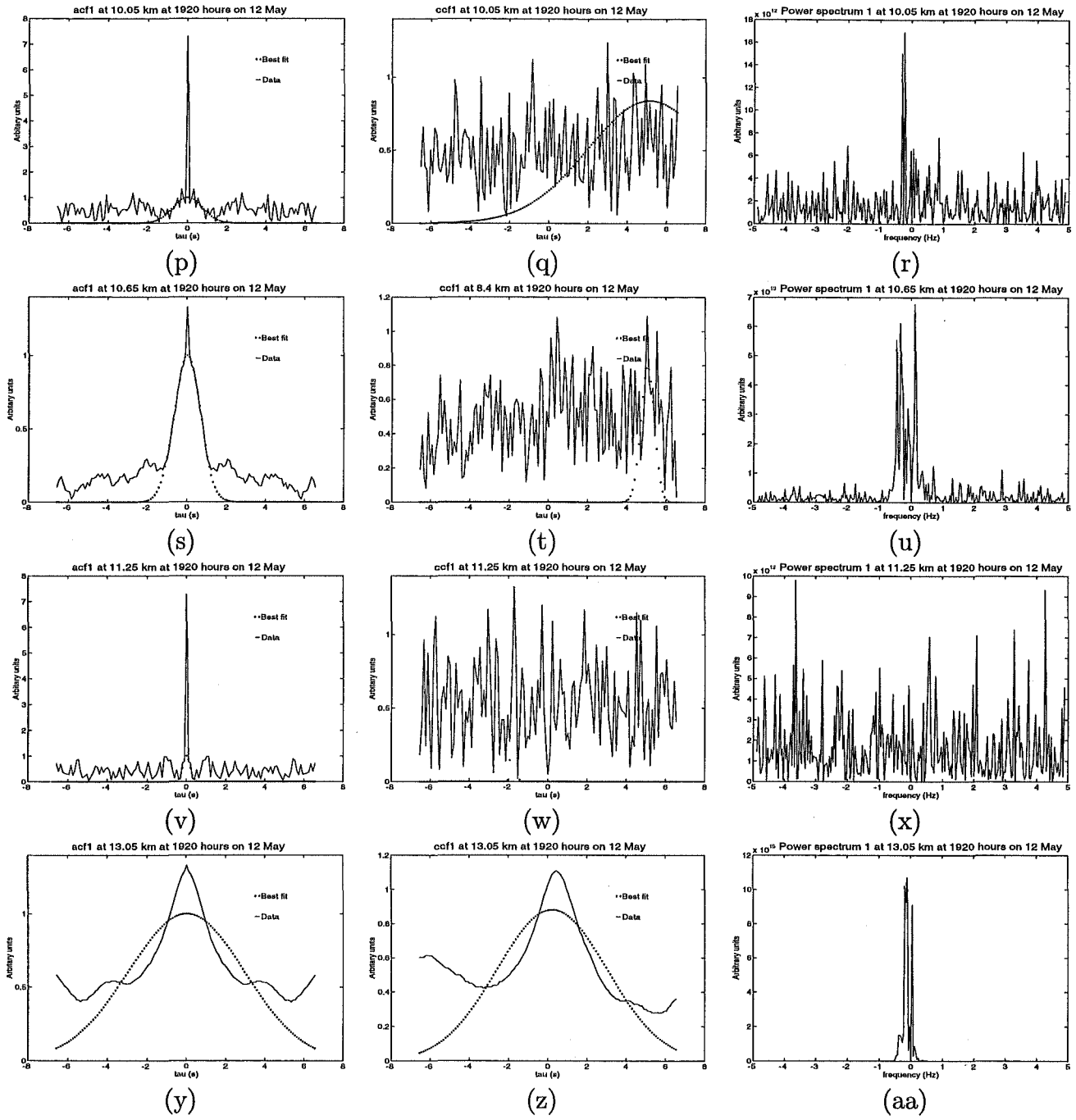

Figure 3.16. Correlation functions and power spectra for low-power layers in experiment 2. Figures (a)-(c) are below the layers, (d)-(f) are in the lowest layer, (g)-(i) are between the first and second layers and (j)-(l) are in the second layer. Figures (m)-(o), are above this layer and (p)-(r) are in the third layer. Finally, (s)-(u), (v)-(x) and (y)-(aa) are respectively below, in and above the main layer near 11 km.

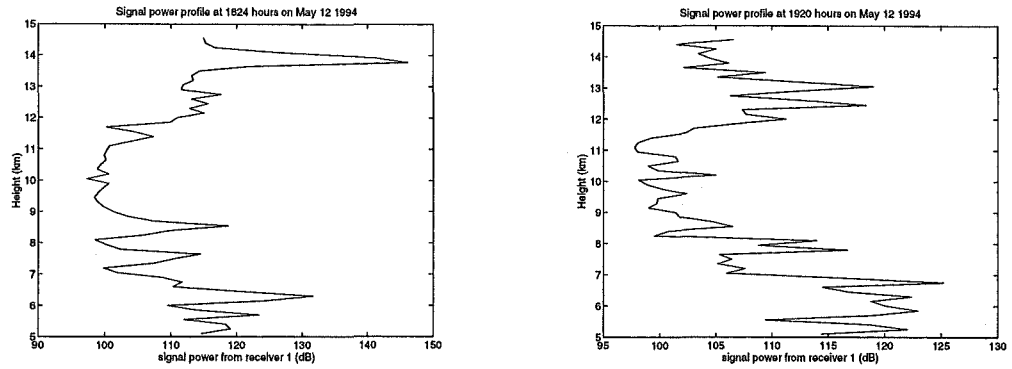

Figure 3.17. Signal power through two regions of layered structure. Figure (a) shows the profile through the region of the three main low-power layers in experiment 1 at 7, 8 and 9-11 km. Figure (b) shows the profile through four layers in experiment 2 at 8.25, 9, 10 and 11 km. The high-power region at 14 km in (a) is due to a high-power event.

Another feature noted by Sheppard et al. [1993], and visible in most of the colour RTI plots (figures 3.4 to 3.9), is the increase in signal-to-noise ratio and corresponding decrease in failure rate above the highest low-power layer. This increase has been used by Gage and Green [1979] to determine the height of the tropopause and the technique is now commonly used for tropopausal investigations [e.g. Nastrom et al., 1989; Vaughan et al., 1995; Devara et al., 1997]. If the decrease in signal-to-noise ratio is to be ascribed to the $\frac{1}{r^2}$ dependence of echo power, then an explanation must also be found for the increase above 13 km. Possible causes for the variation in reflected power with height will now be considered.

3.2.3.1 Radiosonde observations

It is shown in basic radar theory that the reflected power is proportional to the square of the gradient of the potential refractive index. The latter can be calculated from radiosonde data.

The refractive index, n, is given by, [Tsuda et al., 1988],

$$n - 1 = 77.6 \times 10^{-6} \frac{p}{T} + 0.37 \frac{e}{T^2}$$

where p is the atmospheric pressure (hPa), T is the temperature (K) and e is the partial pressure of water vapor (hPa). The gradient of potential refractive index, M, is essentially the rate of change of n where n is expressed in terms of potential

temperature. M is given by, [Tsuda et al., 1988],

$$M = -77.6 \times 10^{-6} \left(\frac{P}{T} \frac{\partial \ln \theta}{\partial z} + 15500 \frac{pq}{T^2} \frac{\partial \ln \theta}{\partial z} - 7750 \frac{pq}{T^2} \frac{\partial \ln q}{\partial z} \right) \qquad (3.1)$$

where θ is the potential temperature and q is the specific humidity. To a reasonable approximation

$$\theta = T \left(\frac{p_0}{p} \right)^{0.286}$$

where p_0 is the pressure (in hPa) at some reference level [Andrews et al., 1987], say $p_0 = 1000$ hPa, and, [Washington and Parkinson, 1986],

$$q = \frac{0.622e}{p}$$

Pressure, temperature and relative humidity can all be measured with a radiosonde. Relative humidity, u, may be converted to partial pressure of water vapour using, [Washington and Parkinson, 1986],

$$e = u \times e_s$$

where e_s is the saturation vapor pressure of water vapour. The vapour pressure e_s at a temperature T is related to the vapour pressure e_{s_0} at a temperature T_0 by

$$e_s = e_{s_0} \exp \left(\frac{-45050}{8.314} \left(\frac{1}{T} - \frac{1}{T_0} \right) \right)$$

where $e_{s_0} = 6.107hPa$ at $T_0 = 0°C$ [Atkins, 1988]. Hence the saturation vapour pressure can be calculated, and e and q found from u. This allows determination of the profile of M, and hence M^2, which is proportional to the reflected power. M^2 profiles from the two radiosonde flights are shown in figure 3.18.

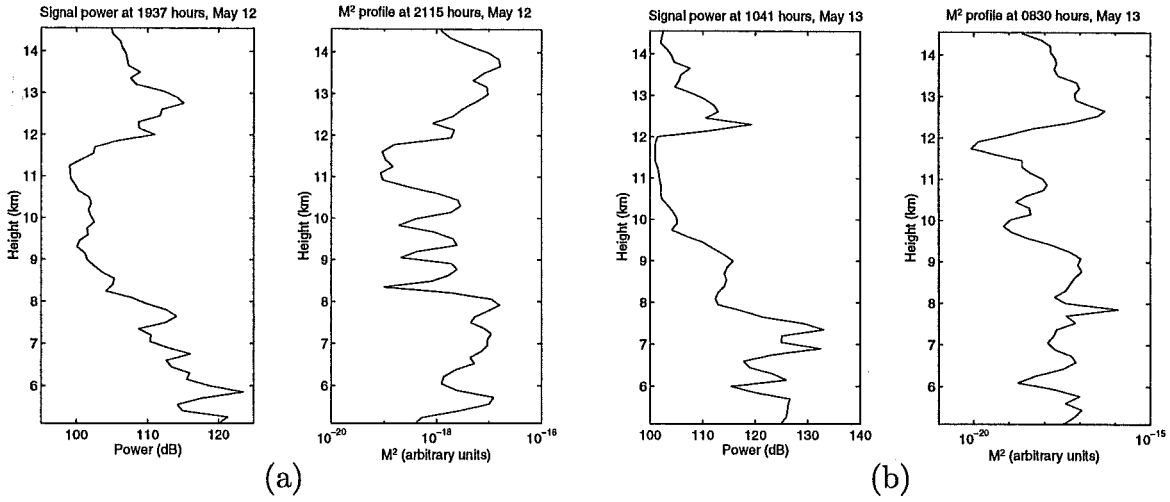

Figure 3.18. Profiles of the square of the potential refractive index gradient, M^2, calculated from radiosonde data. Figure (a) shows the profile for May 12 and figure (b) shows May 13. Also shown for comparison are the average power profiles from the immeadiately preceeding and suceeding radar experiments. Both M^2 profiles have been averaged to give a height resolution of 150 m, i.e. the same as the radar range resolution.

It is unfortunate that neither of the radiosonde flights occurred during a period of radar observation. The flight on May 12th was approximately 1 h after the end of the observing period and the flight on May 13th occurred about $1\frac{3}{4}$ h before the start of the observations. However even if a radiosonde had been launched during one of the experiments there is no guarantee that it would have stayed above the radar, as a radiosonde flight path follows the background wind.

To make the M^2 profiles more comparable with the radar data, the radiosonde data has been averaged. The radiosonde data has a sampling rate of approximately 1 Hz, and this combined with the rate of ascent produces a geopotential height approximately every 10 m. This resolution is considerably greater than the radar range resolution of 150 m and for this reason the averages of groups of 15 data points in the May 12 radiosonde record and 16 points in the May 13 record have been used to give a height resolution approximately equal to that of the radar.

To enable a reasonable comparison to be made the signal power profiles from the immediately preceding and succeeding radar experiments (2 and 3) have been averaged and these are displayed in figure 3.18. The decrease near 11.5 km in both M^2 profiles is at a similar height to the largest low-power layer in figures 3.5 and 3.6 and also with the decrease visible in the average power profiles. Both plots of

radiosonde data also show an increase in M^2 above approximately 12 km. This increase in the potential refractive index gradient agrees with the increase in echo power above 12 km which is visible in the RTI plots and also with the average power profiles.

Although the detail of the other low-power layers has been averaged out in the power profile in 3.18a there is evidence for the existence of layers in the M^2 profile. From figure 3.5 it can be seen that the layers are weakening near the end of the experiment and also that they are not perfectly horizontal and thus it is not possible to make quantitative comparisons with the layer heights in the M^2 profile. The RTI plots do show, however, that the layers are present for several hours during May 12 and it is probable that they are present during the radiosonde ascent. In addition, the low values of M^2 occur at approximately the same heights, $8-10$km, as the low-power layers in figures 3.4 and 3.5 and hence it is not unreasonable to assume that the low-power layers do correspond to regions of low M^2. Simultaneous radar and radiosonde measurements made by other workers [e.g. Green and Gage, 1980; Tsuda et al., 1988; Chu et al., 1990] have also found the same strong correlation between M^2 and signal strength. Therefore it seems likely that the structure of the low-powered layers, and of the signal power structure in general, is determined by the structure in the potential refractive index.

It is also necessary to consider the nature of the signal in the layers. From consideration of the observed correlation functions it can be seen that the signal has negligible coherence. Thus, either the signal is pure noise, in the sense of having no information content, or it contains meaningful signal which has in some way been 'scrambled'. A method for determination of which is the case would be to measure the signal power from regions known to contain simply noise, e.g. in the stratosphere. Assuming that these signals have the lowest power level detectable by the receivers and that the noise level is constant with height, a comparison of the signal power in the low-power layers with the known noise level would allow determination of the significance of the former. It may also be possible to use power spectra to investigate this lower noise level [e.g. Hildebrand and Sekhon, 1974] however this is complicated by the fact that it is possible for a 'scrambled' signal to have the same statistical properties as noise [Slack, 1945].

A discussion of layered structures, either low- or high-power, must consider the physical mechanisms by which the observed variation in power could be produced. The profile of refractive index, or equivalently $n - 1$, does not show the large variations visible in M^2 and it is perhaps surprising to see large changes in the gradient of potential refractive index when the refractive index itself is relatively smooth. This can be explained by the fact that whereas $n - 1$ is on the order of $10^{-4} - 10^{-3}$ the values of M^2 are very much smaller, being on the order of 10^{-16}. To determine the cause of these variations each of the parameters in equation (3.1) must be considered. Profiles of pressure, temperature, and potential temperature (p, T, and θ) vary relatively slowly throughout the height range under consideration and it is unlikely that the rapid variation in M^2 is solely due to these 'dry' terms. The humidity terms, q and $\frac{dq}{dz}$, however display quite abrupt changes with height and it is these 'wet' variables which contribute largely to the structure of M^2 in the troposphere. This is in agreement with the findings of Tsuda et al. [1988], also using the MU radar, who found that in the lower troposphere (below 12km) the dry terms determine the general shape of the M^2 profile while the wet terms determine the fine structure. An alternative mechanism for obtaining an increase in echo power is a region of strong wind shear which produces intense turbulence and hence enhanced scattering. The effect of these shears may not be resolvable in the radiosonde data, and hence the M^2 values, due to the low spatio-temporal resolution of the sonde.

3.2.4 Conclusion

It has been shown that studying the spatiotemporal variation of the backscattered power received by the radar can yield useful information. In this section two distinct phenomena were investigated. Firstly, regions of very high power were found to correspond to regions where the FCA was unable to calculate a velocity. In these regions the computed correlation functions often took the form of a large spike at the origin with smaller side lobes at higher and lower time shifts and the frequency power spectra often showed considerable aliasing. The high power was not due to a single spike nor to a constant high power throughout the entire run, but rather showed the appearance of an object of high reflectivity passing through the aerial beam.

It was hypothesised that these events might be caused either by aircraft or by range-aliased meteors. The characteristics of the reflected power were not of the expected form for a meteor echo, which should show a linear increase up to some maximum value and then an exponential decrease as the ionisation trail diffused away. Also the high power events appear to occur between $70-85$km, after allowing for range aliasing, which is somewhat lower than the height of maximum meteor occurrence ($\approx$ 95km). Thus the aircraft hypothesis was considered to be more plausible.

The second feature observed was the presence of thin horizontally stratified regions of very low power which, again, corresponded to areas where the FCA method failed. The correlation functions showed similar characteristics to those which would be obtained from either random noise or uncorrelated signal. Suggestions were made as to a method of determination of the true signal-to-noise ratio, which would allow discrimination between these two cases.

To investigate the cause of the low signal power, profiles of potential refractive index (M) squared, which is proportional to the reflected echo power, were calculated from radiosonde data and it was shown that these layers corresponded to regions of low M^2. Although the times of the radiosonde flights were not coincident with radar observations these profiles also showed layered structure, which matched the heights of the layers in the radar data thus providing evidence of the persistence of the phenomena.

3.3 Tropospheric velocities

Both horizontal and vertical wind velocities have been calculated using the methods described in sections 2.1 and 2.2. The dependence of the horizontal velocities upon the method of calculation, using the algorithms of Briggs [1984] and Brown and Chapman [1972], are presented in section 3.3.2. The horizontal velocities were also found to differ depending on the sets of receiving aerials used and this is discussed in section 3.3.1. Vertical velocities are shown, and compared to the signal characteristics described in section 3.2.

3.3.1 Comparison of receiving triangles

3.3.1.1 Introduction

The discussion of FCA theory in section 2.1 mentioned that early work often used a right-angled triangle of receiving aerials. However it was noticed that this was not the most desirable configuration. Barber [1957] showed that for the simplified analysis where only time delays between similar records are used an equilateral triangle of receivers is best. Kelleher [1966] and Beynon and Wright [1969] studying total reflections from the E layer noted a tendency for the characteristic ellipse to align along the longest side of the triangle. Kelleher [1966] and Sastri and Rao [1971] found that the true velocity increased with increasing aerial separation. Golley and Rossiter [1970], also using total reflections, have made a comprehensive study of these effects. Their results are summarised below.

- The magnitude of V_t increases with increasing triangle size with an upper limit which is assumed to be the correct value.
- The average directions of V_t and V_a are good estimates of the direction of ground-pattern drift for all triangle sizes
- The magnitude of V_a is independent of triangle size
- The radius of the correlation ellipse, in the direction of drift, increases with triangle size
- The correlation ellipse tend to align with the hypotenuse and this effect decreases with increasing triangle size.

All these effects were attributed to the same cause, namely the triangle size being smaller than the pattern scale and thus were grouped together as the 'triangle size effect'. A study by Golley and Rossiter [1971] using partial reflections from the D region found no evidence of these effects and this was attributed to the pattern scale being approximately the same size as the smallest triangle size available. The triangle size effect has, in recent years, been observed at VHF by several workers [Van Baelen et al., 1990; Chang et al., 1993]. Vincent and Rottger [1980] found no evidence for the effect in their VHF study, a result attributed to having maximised receiving antenna isolation and using a single receiver which was switched between aerials.

Various causes for the triangle size effect have been proposed. Although filtering can be invoked to explain the effect it has been rejected by Chandra and Briggs [1978]. They showed that

> 'the effects of filtering must occur even if all the assumptions of FCA are satisfied. However it is not possible for the derived velocity (V_t) to be a function of receiver separation within the framework of these assumptions' [Chandra and Briggs, 1978].

So the triangle size effect must either be a failure of the FCA assumptions or instrumental [Chandra and Briggs, 1978]. Fedor and Plywaski [1972] have suggested coupling between antennas, however their analysis predicts an increase of V_a with increasing aerial spacing. It was considered that

> 'the apparent absence of a variation of V_a with antenna spacing (in Golley and Rossiter [1970]) is largely due to the statistical errors in determining this quantity' [Fedor and Plywaski, 1972].

The conclusions of Fedor and Plywaski [1972] are supported by the results of Vincent and Rottger [1980] who, by minimising antenna coupling, found no evidence for the triangle size effect in their study. Meek [1990] has proposed that not properly correcting for the presence of random noise could lead to a reduction in V_t and used this to explain the triangle size effect.

Modelling has also been done to try to reproduce the effect. Burke [1987] used a model that gave a decrease in V_t with decreasing receiver separation for the case of random spatial changes in the direction of motion. Tahara et al. [1997] have used a one-dimensional model which gives the expected variation in velocity; however the model also predicts a variation in V_a. This variation in both V_a and V_t has also been observed in a model by Van Baelen et al. [1989]. Recently Holdsworth and Reid [1995] used a model that reproduces many of the triangle size effect phenomena. They found that not correcting for noise led to an underestimation of V_t as in Meek's [1990] analysis. When noise correction was done there was only a small variation in velocity with receiver separation which was attributed to the effect of FCA acceptance criteria. A slight variation was found in the apparent velocities, in contrast to Golley and Rossiter [1970]. Holdsworth and Reid [1995] claim that this result is supported by figure 7b of Van Baelen et al.'s [1990] paper, which shows little variation between apparent velocities measured on the two available spacings. This

section will present results which provide stronger evidence of variation in apparent velocities between different receiver configurations.

In this section results are presented which support the modelling work of Holdsworth and Reid [1995]. It will be shown that failure to correctly account for noise in the correlation function fitting procedure can lead to erroneous values of wind velocity. In particular, velocities perpendicular to the longest side of the receiving triangle are found to be underestimated. In addition, some sets of receiving triangles show differences which are insensitive to the treatment of noise. This latter effect is considered to be due to anisotropy in the ground diffraction pattern, as evidenced by differences between correlation functions from aerial pairs with parallel baselines.

3.3.1.2 Comparisons of true velocities

The general implementation of Briggs' method requires choice of a receiver origin and of the order of the receivers. While these choices should not affect the calculated velocities, the possibility exists that an error in the program will cause such a dependence. Figure 3.19 shows the east-west and north-south velocities from various aerial configurations, with a $y = x$ line for comparison. The number code refers to the ordering of the receivers with the first number being the origin. The layout of a given set of receivers may be found by reference to figure 3.3. In each case the same data is being analysed, the only difference being the change in order of the receivers, and in some cases the origin. The velocities are from all heights and all times in experiment 3. It can be seen that, as expected, the velocities lie along the $y = x$ line. This agreement gives confidence that both the FCA and its practical implementation are performing as expected.

Figure 3.20, however, shows a comparison of the velocities from two different triangles, 134 and 234, in experimental run 5. There is a marked deviation from the $y = x$ relationship that could be expected in the absence of any triangle effect, particularly in the east-west direction. The comparisons show data from all heights throughout the run.

Velocity profiles of the data in figure 3.20 are shown in figure 3.21 and an additional comparison is shown in figure 3.22 (triangles 123 and 234). The profiles

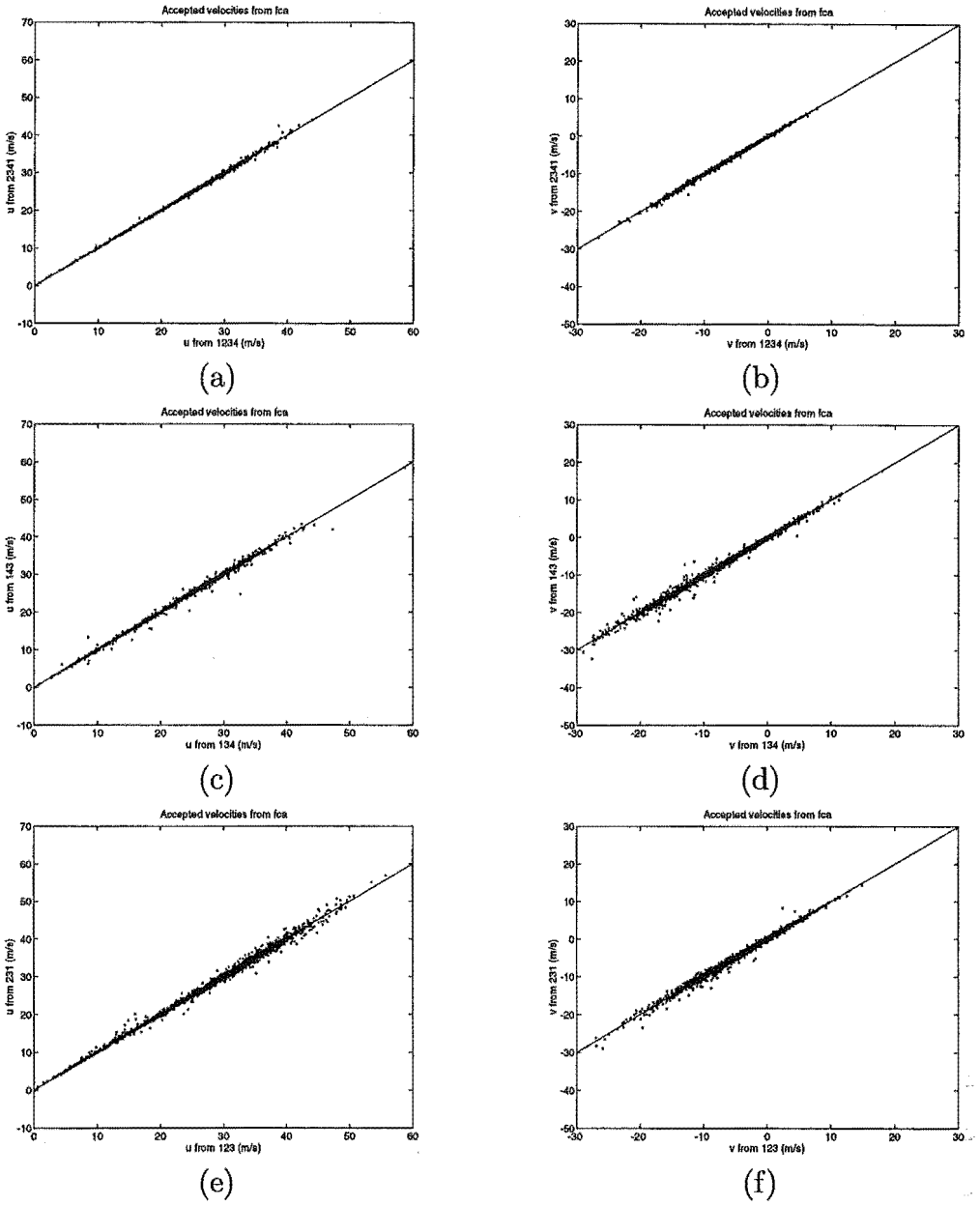

Figure 3.19. Comparison of velocities calculated using the same data but with the aerials in different orderings. The quartets or triplets of numbers in the axis labels refer to the aerials used in the calculation, the first number being the origin. The expected $y = x$ relationship is shown as a solid line. (a), (c) and (e) show east-west velocities, and (b), (d) and (f) show north-south velocities. The data are from experiment 3.

are averages of results from the 294 25-second runs in experiment 5. Only data which pass the acceptance criteria (section 2.1.3) are included in the average. There are obvious differences between the west-east (u) velocities of the two triangles, while less difference is visible between the south-north (v) velocities. Figures 3.21 and 3.22 also show profiles of mean differences. Samples from the two triangles are statistically dependent and thus the standard deviation is approximately the

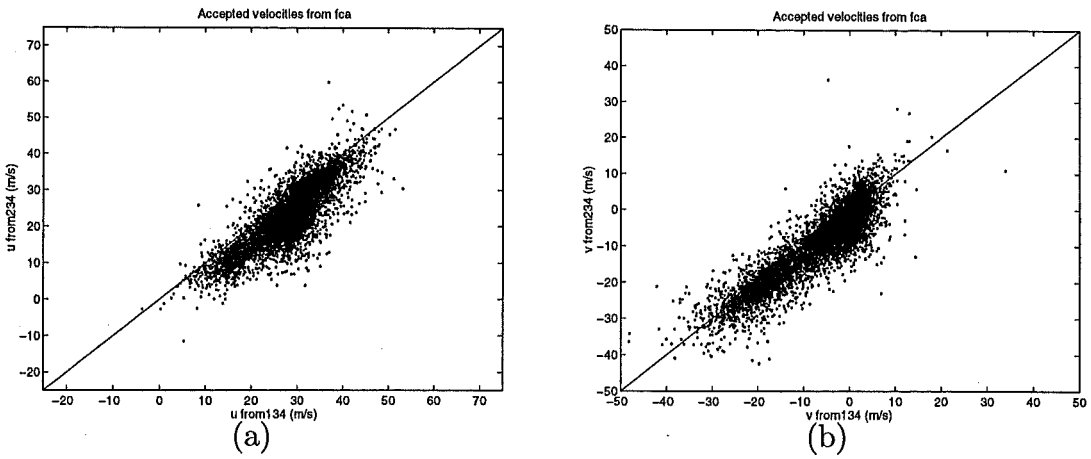

Figure 3.20. Scatter plots of east-west and north-south velocities from different triangles for all heights during experiment 5. The solid line is y=x.

standard deviation of the individual differences. Regions where the differences are statistically significant, at the 99% level of confidence, are indicated.

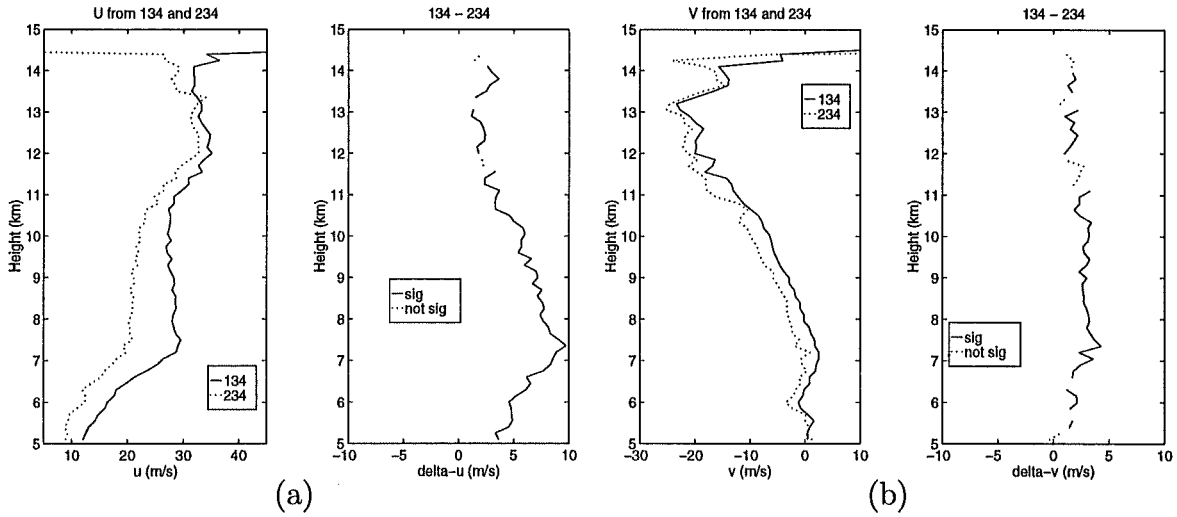

Figure 3.21. Accepted velocity profiles from triangles 134 and 234 using data from experiment 5. Also shown are profiles of the velocity difference. These profiles are averages of the difference between the samples whose average is shown in the velocity profiles. The solid line indicates differences which are statistically significant at the 99% level.

The prevailing wind direction during the experiment was westerly and thus the smaller differences in the north-south direction, in figures 3.21b and 3.22b, may be explained as follows. Triangle 234 in figure 3.3a has its longest side perpendicular to the wind direction and thus would be expected to underestimate the velocity in this direction. In the north-south direction, however, the wind velocity is much smaller and though triangles 123 and 134 have their longest side perpendicular to the north-south axis the small velocity along this axis leads to a smaller difference

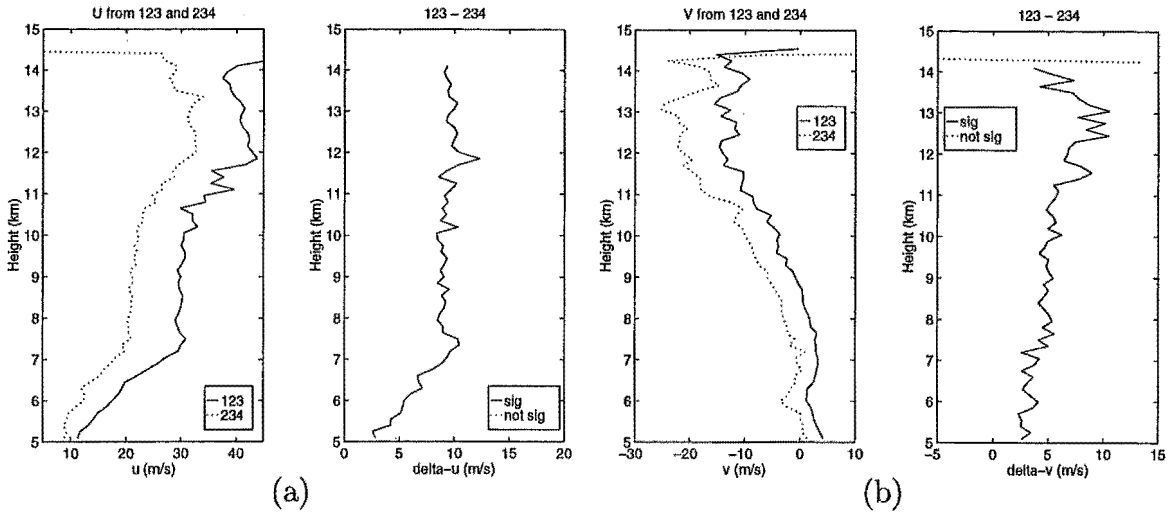

Figure 3.22. Accepted velocity profiles from triangles 123 and 234 using data from experiment 5. Also shown are profiles of the velocity difference. These profiles are averages of the difference between the samples whose average is shown in the velocity profiles. The solid line indicates differences which are statistically significant at the 99% level.

between the triangles. Comparisons of different triangles with the same longest side (e.g. 123 and 134, and 124 and 234) have shown no major differences.

3.3.1.3 Comparisons of apparent velocities

From section 3.3.1.1 it is possible that the apparent velocities may also show some variation with changing receiver spacing. Comparison of apparent velocities from the same triangles used in figure 3.21 and 3.22 are shown in figures 3.23 and 3.24. There are differences between the profiles which are statistically significant at the 99% level of confidence thus providing evidence to support the modelling results discussed earlier. Comparisons of apparent velocities from other triangles also show differences.

3.3.1.4 Effect of noise

Several papers have considered that one of the major causes of the triangle size effect has been the failure to properly account for random noise in the FCA, in particular, in the fitting of some analytic form to the auto- and cross-correlation functions. In the presence of random noise the autocorrelation function will show a large 'spike' at zero time shift. The noise has a frequency spectrum much wider than that of the signal, or, equivalently, has a time scale much shorter than the sampling period, and thus the noise is only correlated at the zero lag point. Inclusion of this

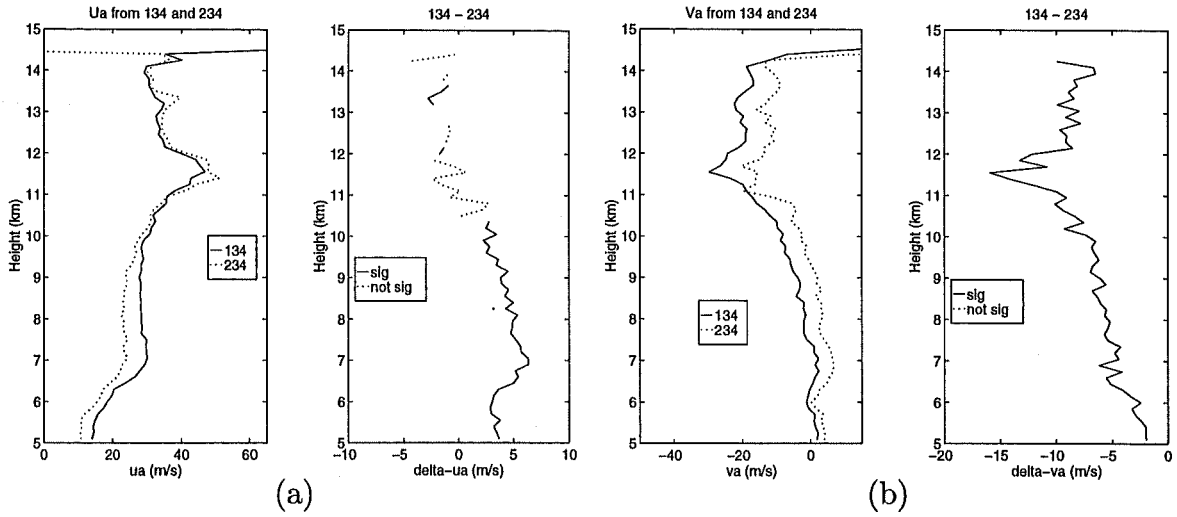

Figure 3.23. Accepted apparent velocity profiles from triangles 134 and 234 using data from experiment 5. Also shown are profiles of the velocity difference. These profiles are averages of the difference between the samples whose average is shown in the velocity profiles. The solid line indicates differences which are statistically significant at the 99% level.

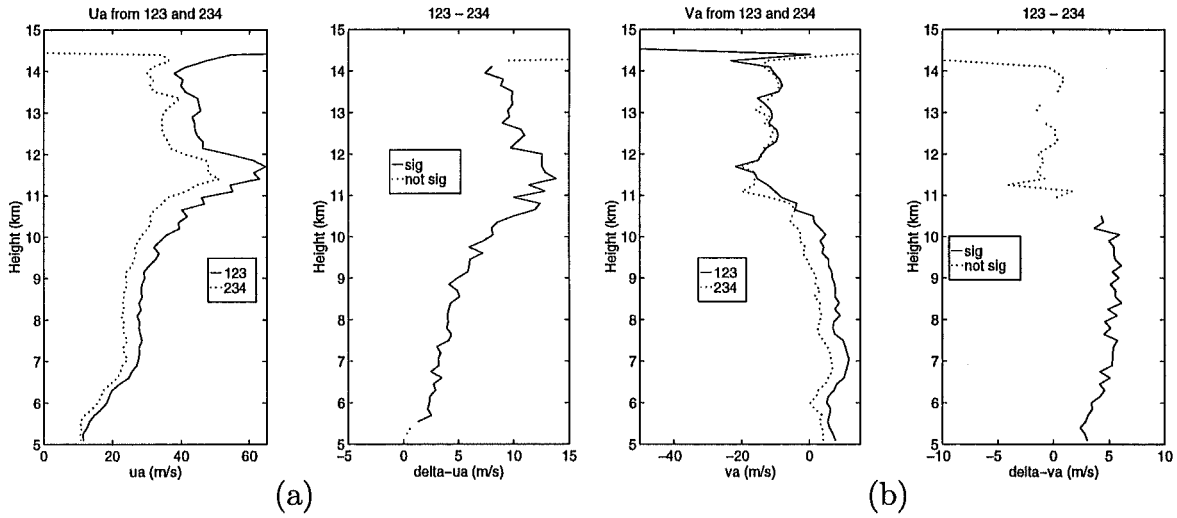

Figure 3.24. Accepted apparent velocity profiles from triangles 123 and 234 using data from experiment 5. Also shown are profiles of the velocity difference. These profiles are averages of the difference between the samples whose average is shown in the velocity profiles. The solid line indicates differences which are statistically significant at the 99% level.

point in the subsequent fitting will lead to erroneous values for the parameters used in the FCA [e.g. Meek, 1990]. Holdsworth and Reid [1995] have used model data to show that the addition of increasing levels of noise can lead to an increasing triangle effect when the zero-lag point is used.

This is not the case for the analysis presented here which follows a similar method to that of Briggs [1984] in excluding the zero lag value as a datum from the fits. The ratio of this value to the fitted zero lag value then gives a measure of the

signal-to-noise ratio. This is slightly different to 'despiking' which fits to a small number of points either side of the zero lag point to obtain a revised zero lag value. To determine the effect of inclusion of the zero-lag point as a fitting datum the data were re-analysed and the zero-lag point included.

The procedure used to fit a Gaussian function to the covariance data is as follows. Let n_{max} be the maximum number of lags for which the covariance function is calculated and let n_{spike} be some (small) integer. The data is first scanned over the range $-n_{max}, \ldots, -n_{spike}, n_{spike}, \ldots, n_{max}$ for the maximum value. Then a Gaussian function is fitted to points either side of this value, excluding those in the range $-n_{spike}, \ldots, n_{spike}$, down to $\frac{1}{e}$ of the maximum. The fitted value from the auto-covariance function is used to scale the cross-covariances prior to fitting [Briggs, 1984]. The τ and τ' values used in the FCA are then found from the fitted Gaussian functions.

Figures 3.25 and 3.26 show comparisons of triangles for which the data have been reanalysed to include the zero lag point i.e. $n_{spike} = 0$. Figures 3.27 and 3.28 show the same triangles, using $n_{spike} = 1$. It can be seen that there are larger differences between the triangles for the case where noise is not corrected for, in agreement with the results of Holdsworth and Reid [1995]. Profiles of the differences for the cases $n_{spike} = 1$ and $n_{spike} = 0$ are shown together in figure 3.29 which shows that the difference, i.e. the triangle size effect, is larger when the central noise spike is included as a datum in the FCA. Differences between the two analyses are most apparent near 11km where the signal-to-noise ratio is low. The inclusion of the zero-lag point also produces a larger difference between triangles with a common longest side e.g. 124 and 234, a further reason for its rejection as a valid datum.

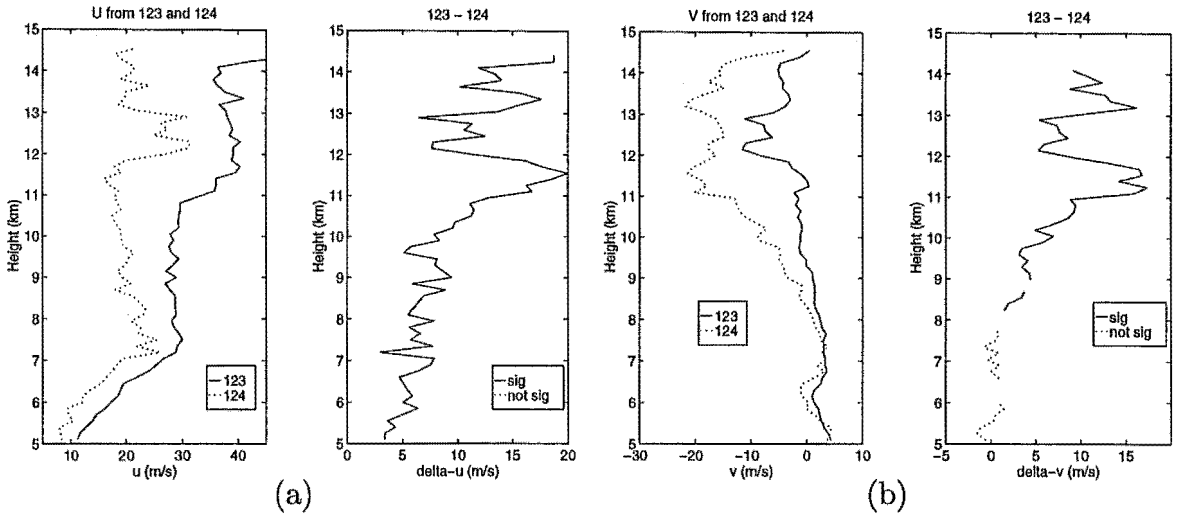

Figure 3.25. Accepted velocity profiles from triangles 123 and 124 calculated using the zero-lag covariance value as a datum. The data are from experiment 5. Also shown are profiles of the velocity difference. These profiles are averages of the difference between the samples whose average is shown in the velocity profiles. The solid line indicates differences which are statistically significant at the 99% level.

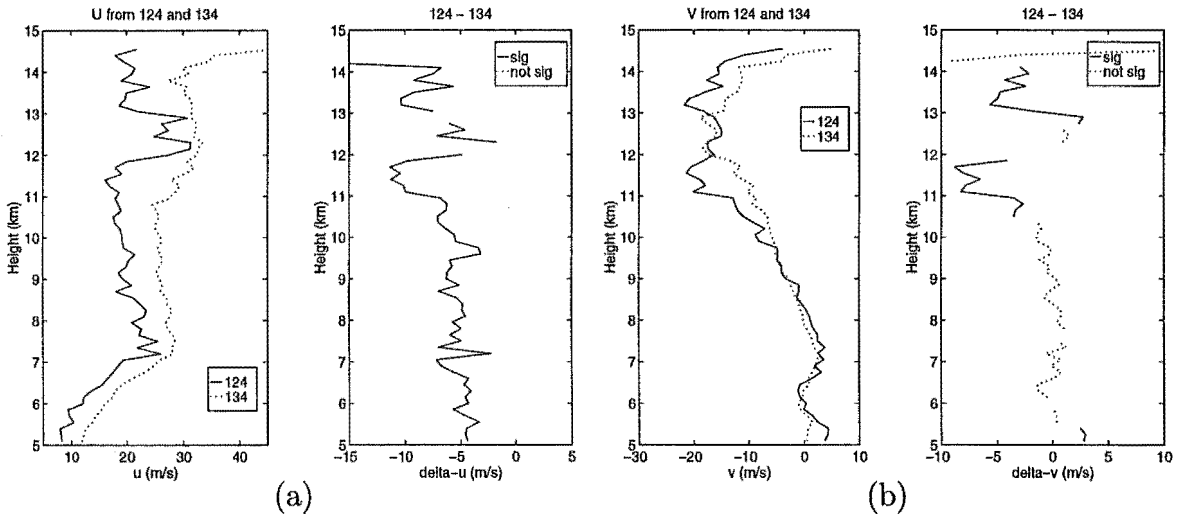

Figure 3.26. Accepted velocity profiles from triangles 124 and 134 calculated using the zero-lag covariance value as a datum. The data are from experiment 5. Also shown are profiles of the velocity difference. These profiles are averages of the difference between the samples whose average is shown in the velocity profiles. The solid line indicates differences which are statistically significant at the 99% level.

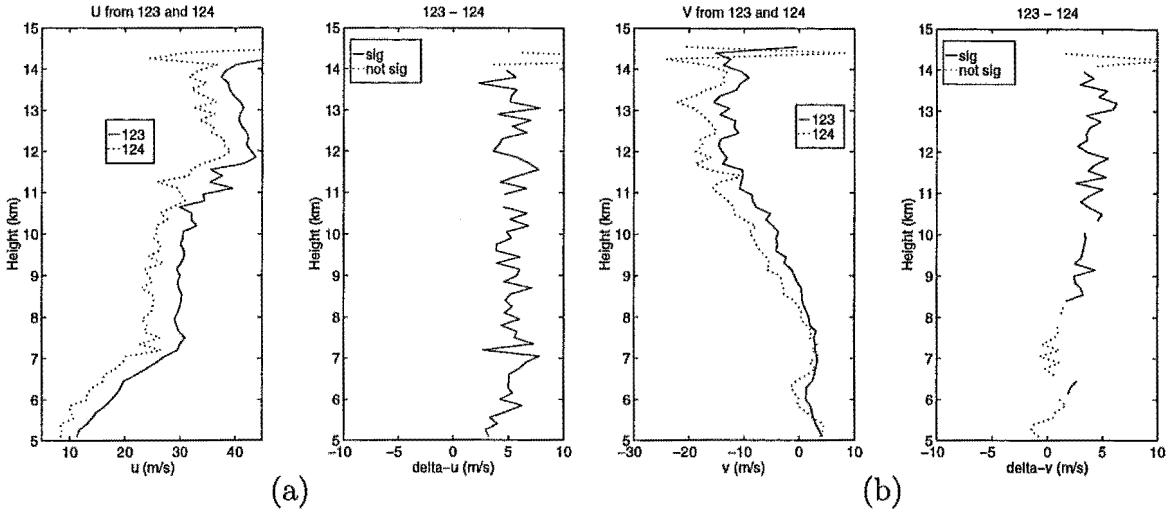

Figure 3.27. Accepted velocity profiles from triangles 123 and 124 calculated excluding the zero-lag covariance value as a datum. The data are from experiment 5. Also shown are profiles of the velocity difference. These profiles are averages of the difference between the samples whose average is shown in the velocity profiles. The solid line indicates differences which are statistically significant at the 99% level.

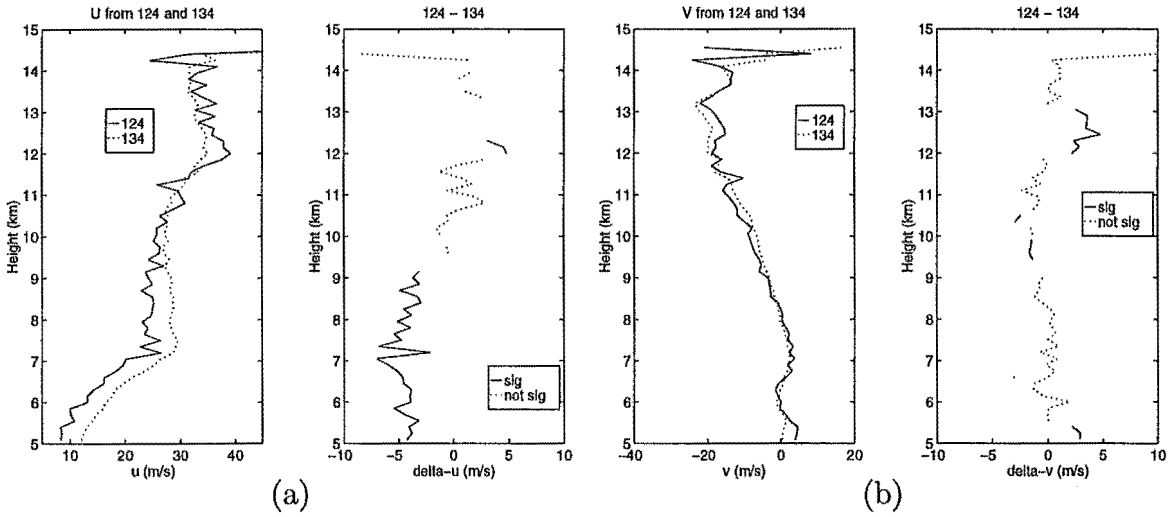

Figure 3.28. Accepted velocity profiles from triangles 124 and 134 calculated excluding the zero-lag covariance value as a datum. The data are from experiment 5. Also shown are profiles of the velocity difference. These profiles are averages of the difference between the samples whose average is shown in the velocity profiles. The solid line indicates differences which are statistically significant at the 99% level.

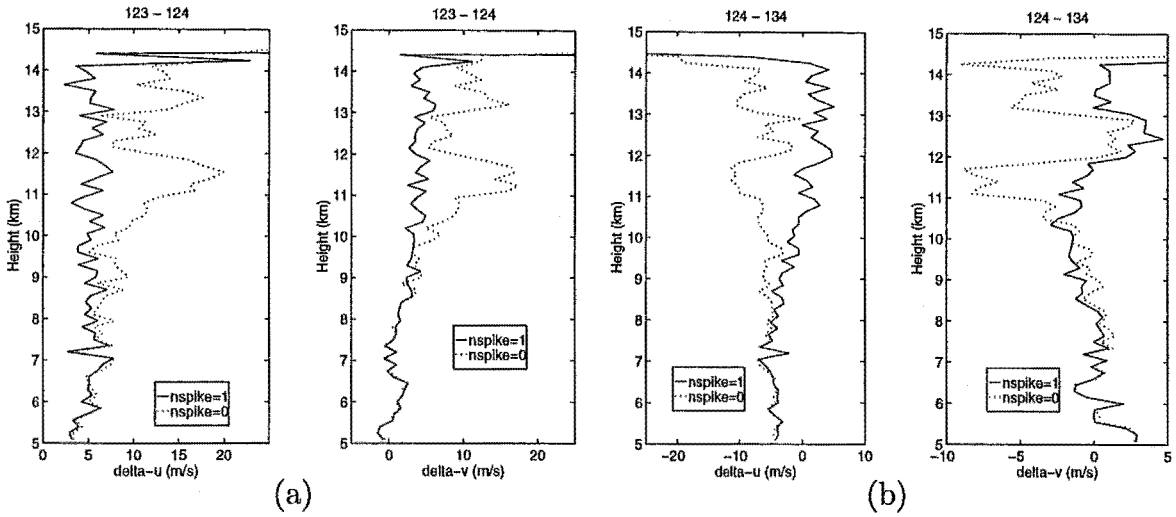

Figure 3.29. Profiles of mean accepted velocity differences of triangles 123,124 and 124,134 with the zero-lag covariance both included (nspike=0) and excluded (nspike=1) as a datum. All data are from experiment 5.

A possible weakness in the fitting procedure is the exclusion of only the zero lag datum. Assuming the noise is random it should only be correlated at zero lag and thus only the zero lag point need be rejected. This assumption will now be investigated. Figure 3.30 shows a comparison of the mean difference profiles for $n_{spike} = 1$ (the default) and $n_{spike} = 3$, i.e. excluding the 5 central points of the covariance data, for the same triangles shown in figure 3.29. Although the variation is small it can be seen that using $n_{spike} = 3$ decreases the difference between the triangles slightly.

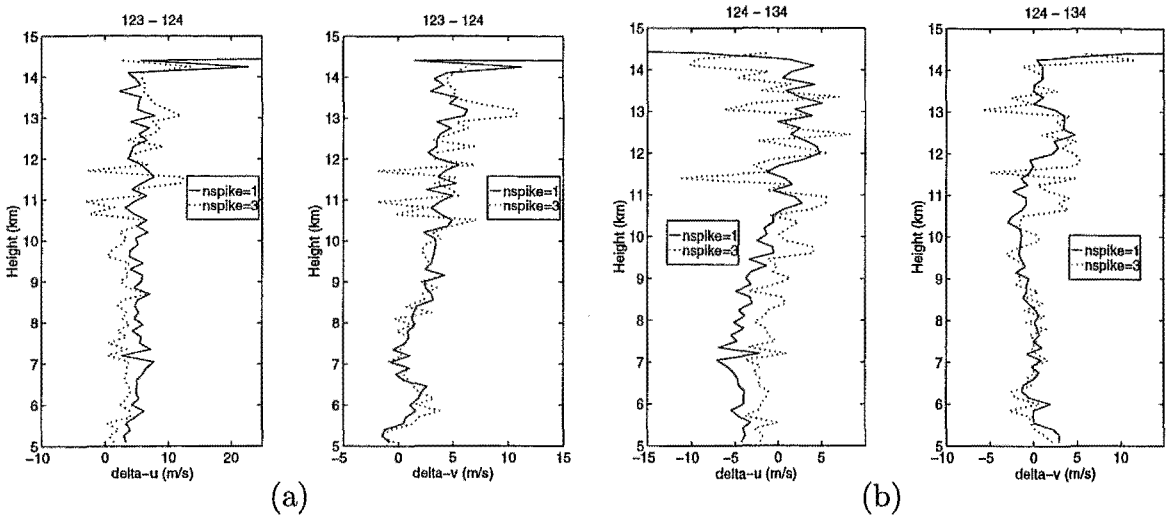

Figure 3.30. Profiles of mean accepted velocity differences with the central 5 points of the covariance (nspike=3) and the zero-lag point excluded (nspike=1) as data. All data are from experiment 5.

The cross-covariance maximum is generally close to zero lag and hence the exclusion of the central 5 points is somewhat drastic, especially as the points used for the fitting procedure are selected in the manner described above. This, and the fact that $n_{spike} = 3$ does not always produce smaller differences, does not allow firm conclusions to be drawn as to the preferability of this method over $n_{spike} = 1$. However the results at least indicate that the velocity obtained by FCA is dependant, to some extent, on the method used to handle the central points of the covariance functions.

3.3.1.5 Other effects

Although correcting for noise leads to a reduction of the triangle size effect there are cases where differences persist even after corrections for noise have been performed. Figures 3.31 and 3.32 show data from the triangles in figures 3.21 and 3.22 of section 3.3.1.2, reanalysed to include the effects of noise, as in section 3.3.1.4. The inclusion or exclusion of the zero lag covariance datum in the FCA would seem to cause little change in this case as there are few obvious differences between the figures with $n_{spike} = 1$ and those with $n_{spike} = 0$. This can be seen clearly in figure 3.33 which shows the two profiles of differences between the triangles for $n_{spike} = 1$ and $n_{spike} = 0$.

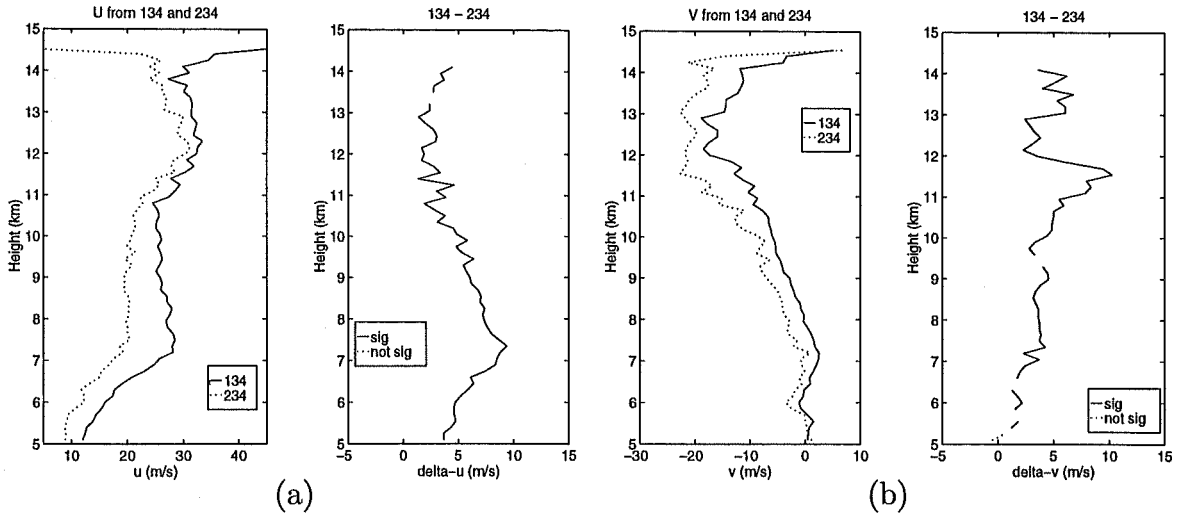

Figure 3.31. Accepted velocity profiles from triangles 134 and 234 calculated using the zero-lag covariance value as a datum. The data are from experiment 5. Also shown are profiles of the velocity difference. These profiles are averages of the difference between the samples whose average is shown in the velocity profiles. The solid line indicates differences which are statistically significant at the 99% level.

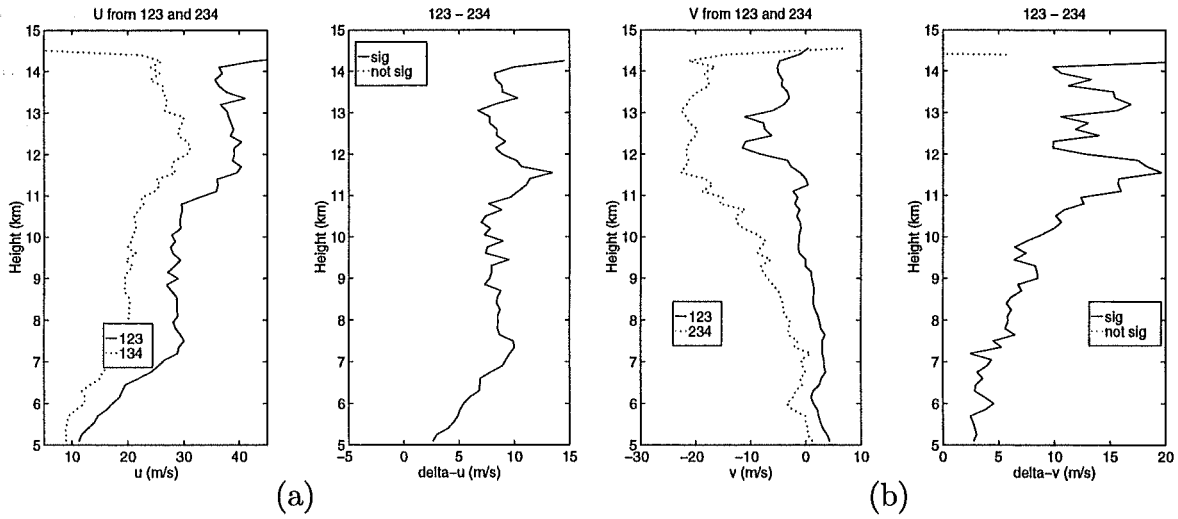

Figure 3.32. Accepted velocity profiles from triangles 123 and 234 calculated using the zero-lag covariance value as a datum. The data are from experiment 5. Also shown are profiles of the velocity difference. These profiles are averages of the difference between the samples whose average is shown in the velocity profiles. The solid line indicates differences which are statistically significant at the 99% level.

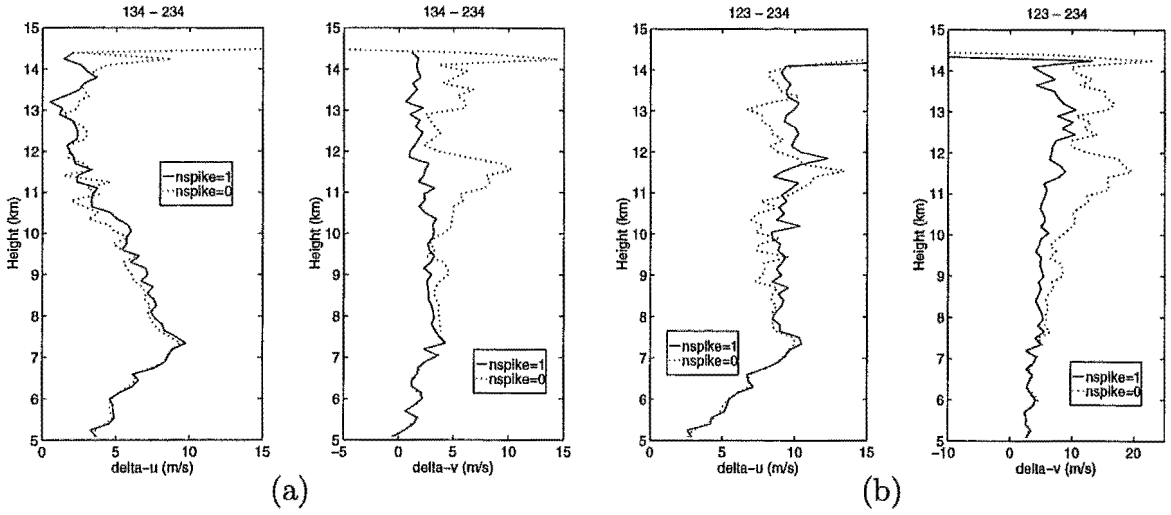

Figure 3.33. Profiles of mean accepted velocity differences of triangles 134,234 and 123,234 with the zero-lag covariance both included (nspike=0) and excluded (nspike=1) as a datum. All data are from experiment 5.

Any explanation of this behaviour must account for the fact that not all of the triangles are insensitive to the inclusion or exclusion of the zero lag data. The hypothesis used here is that anisotropy in the ground diffraction pattern, over and above the elliptical anisotropy allowed for in Briggs' [1984] analysis, is responsible for this selective insensitivity.

Using all four receivers it is possible to calculate two sets of correlation functions along parallel pairs of aerials. One pair would be aerials 1,2 and 4,3 of figure 3.3 and the other would be aerials 1,4 and 2,3. It is expected that each member of the set would see, on average, the same correlation function however figure 3.34 shows that there are differences in the τ and τ' values and in the zero-lag crosscorrelations. These differences will now be explored further.

Consider first, the differences between the crosscorrelation values. Table 3.7 shows the mean differences between the zero lag crosscorrelation values for the two sets of parallel baseline aerial pairs. It can be seen that there are differences for all of the 6 experiments particularly 1, 3 and 5 where the difference between aerial pairs 1-4 and 2-3 is large. To evaluate the mean of ρ, which has a non-normal probability distribution, it is necessary to use the Fisher z-transformation to convert ρ to z which does have a normal distribution. The transformation is [Berenson et al., 1988]

$$z = \frac{1}{2} \ln \frac{1+\rho}{1-\rho} \tag{3.2}$$

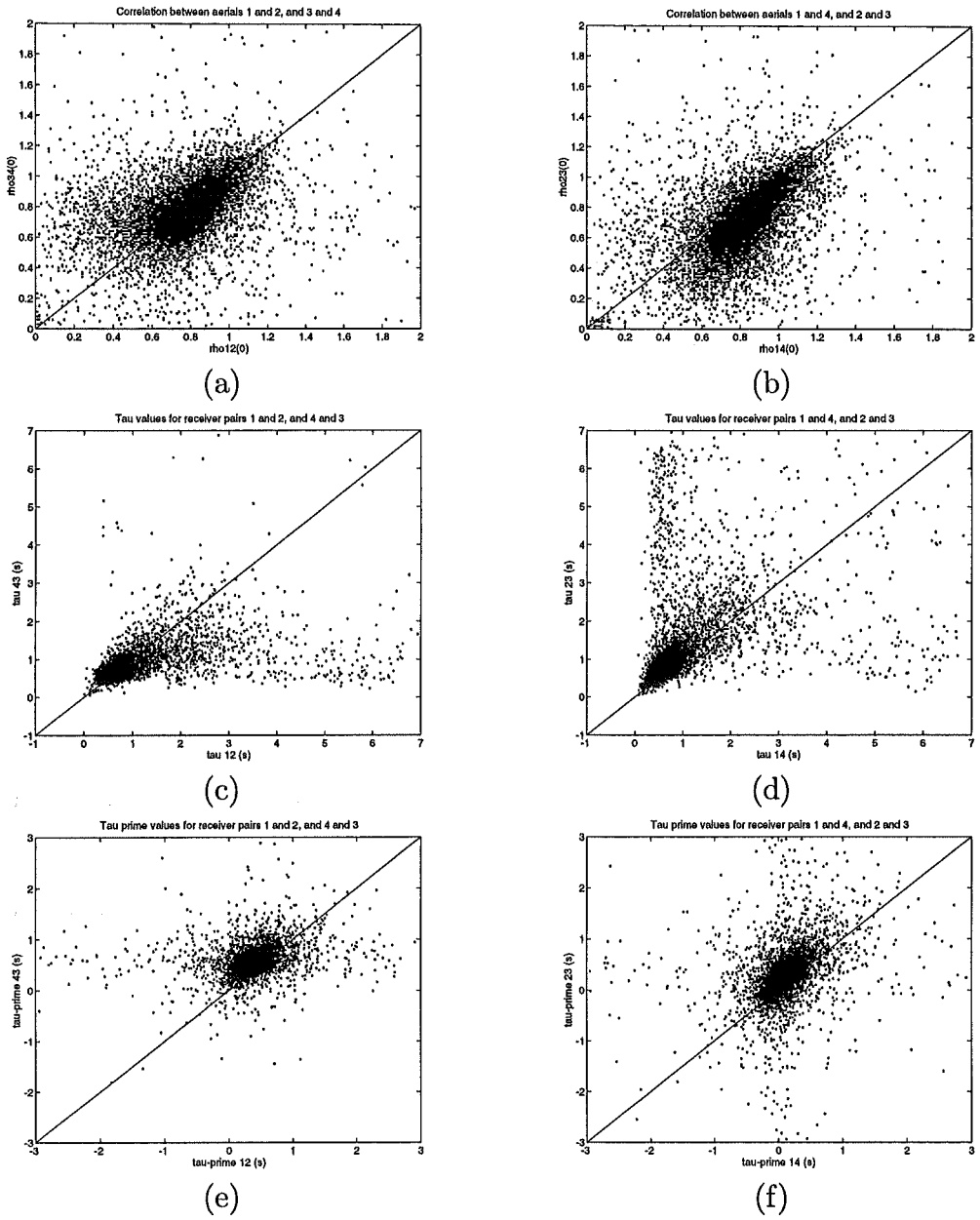

Figure 3.34. Comparison of crosscorrelation, τ and τ' from aerial pairs with parallel baselines using data from all heights in experiment 3. (a), (c) and (e) show the comparison of pairs 1,2 and 4,3 and (b), (d) and (f) show pairs 1,4 and 2,3. The solid line is $y = x$.

and thus the inverse transform is

$$\rho = \frac{e^{2z} - 1}{e^{2z} + 1} \tag{3.3}$$

To obtain the values in table 3.7 the values of ρ_0 from all heights in each experiment which passed the FCA acceptance criteria are first transformed using equation (3.2). An average is taken of these transformed values and the mean z values are transformed back using equation (3.3) and then subtracted. By taking the standard deviation and average of the difference of the z values it is also possible

Expt No.	$\rho_{0_{12}} - \rho_{0_{43}}$	$\rho_{0_{14}} - \rho_{0_{23}}$
1	0.02	0.11
2	0.02	0.06
3	0.04	0.10
4	0.03	0.06
5	0.04	0.11
6	0.05	0.06

Table 3.7. Differences in crosscorrelation between aerial pairs with parallel baselines. For each experiment zero-lag values of crosscorrelation functions were transformed using Fisher's Z-transform for correlation values. These transformed variables were averaged and then inverse-transformed. The differences between these means for each aerial pair are shown.

to determine whether the differences in ρ_0 are statistically significant. All of the values in table 3.7 are significant at the 99% level and thus there is clearly some anisotropy in the ground pattern. It may further be stated that the difference in correlations between aerial pairs is in itself direction dependent and also depends on the antenna spacing.

The τ,τ' values are what is actually used in the full correlation analysis and since the τ values are dependant on ρ_0 it is necessary to investigate the possibility of variation in them. It is conceivable that the τ' values also vary even though they are not directly dependant on the values of ρ_0. Table 3.8 shows the mean differences between the τ,τ' values on parallel aerial pairs for all heights in experiment 5 which pass the acceptance criteria.

$\tau'_{0_{12}} - \tau'_{0_{43}}$ (lags)	$\tau'_{0_{14}} - \tau'_{0_{23}}$ (lags)	$\tau_{0_{12}} - \tau_{0_{43}}$ (lags)	$\tau_{0_{14}} - \tau_{0_{23}}$ (lags)
-1.55	-1.50	-0.42	-1.33

Table 3.8. Mean differences in τ, τ' between aerial pairs with parallel baselines.

The difference in the τ' values in table 3.8 indicates that the correlation functions are shifted along the time axis relative to each other, while the variation in τ values indicates a difference in the magnitude of the correlation function, as do the values in table 3.7. In the implementation of the FCA used in this thesis a Gaussian function of the form

$$y(x) = ae^{-\left(\frac{x-b}{c}\right)^2} \tag{3.4}$$

is fitted to the calculated correlation function. By obtaining values of the three Gaussian parameters a, b and c it is therefore possible to calculate an average correlation function for each of the aerial pairs. Table 3.9 shows mean values of a, b and c from all heights in experiment 5 which passed the FCA acceptance criteria and figure 3.35 shows the average fitted correlation functions obtained from these values.

	ρ_{12}	ρ_{43}	ρ_{14}	ρ_{23}
$\overline{a}$	0.852	0.896	0.808	0.761
$\overline{b}$	2.93	4.20	0.10	3.13
$\overline{c}$	13.2	13.4	13.9	13.9

Table 3.9. Average values of the Gaussian parameters a, b and c of equation (3.4). The averages are of fitted values in experiment 5 for which the calculated velocities passed the acceptance criteria of Briggs [1984] and which have ρ_{max}, the peak crosscorrelation value, less than 1 for all crosscorrelation functions. $\overline{a}$ is the inverse-transform of the mean of the Fisher transformed values of ρ_{max}. $\overline{b}$ is found by taking the mode of the τ' values and $\overline{c}$ is the mean of all fitted widths.

The differences in ρ_0 between the aerial pairs in figure 3.35 are -0.001 for $\rho_{12} - \rho_{43}$ and 0.084 for $\rho_{14} - \rho_{23}$. These differences are based on averages of fitted correlation coefficients and thus are not expected to be identical to those in table 3.7 for experiment 5. Nevertheless they are similar, with ρ_{14} and ρ_{23} showing a larger difference than ρ_{12} and ρ_{43}. These systematic differences in the average correlation functions may also provide an explanation for the insensitivity to noise displayed by some triangles. Each triangle is a subset of the four receivers being used here to determine anisotropy and thus taking different subsets could be expected to lead to different behaviour. The fact that some triangle comparisons are sensitive to noise while others appear to be insensitive may be due to the triangles being in different regions of the anisotropic ground pattern.

The correlation functions are essentially sections through the ground diffraction pattern. This pattern is the convolution of the radar aerial polar diagram and the aspect sensitivity of the scattering medium and either of these are possible causes of the observed anisotropy in the correlation functions. Consideration of the signal characteristics during a high-power event may provide information supporting the former. Figure 3.14 shows the signal power during several of these events and it can be seen that there are often asymmetries in the central lobe. If these events are due

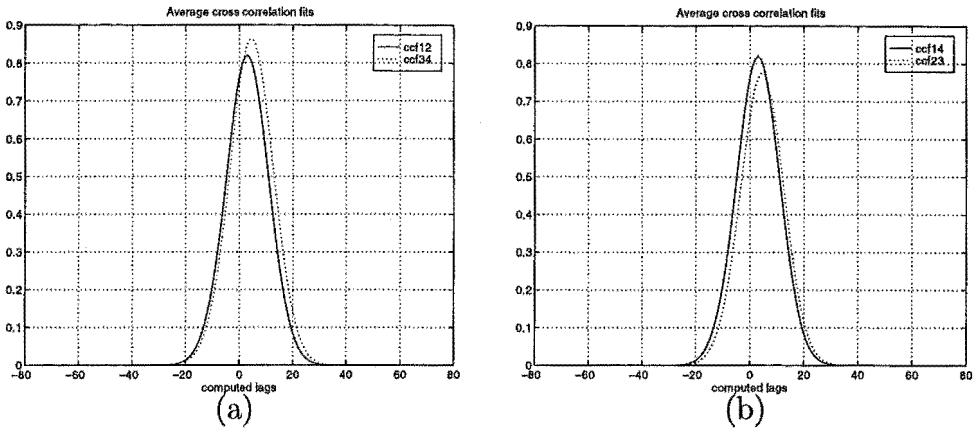

Figure 3.35. Cross correlation functions from pairs of aerials with parallel baselines. The functions are plots of equation (3.4) using the values in table 3.9. (a) shows the average correlation functions for receiver pairs 1-2 and 4-3 and (b) shows the correlation functions for pairs 1-4 and 2-3 .

to a high-reflectivity object passing through the aerial beam then figure 3.14 gives an estimate of the antenna polar diagram and its degree of anisotropy.

3.3.1.6 Conclusion

From the results presented above it would seem advisable to either remove the zero lag covariance as a datum, as is done here, or to use some points near zero-lag to calculate a revised zero-lag value for use in subsequent fitting. This latter method is known as 'de-spiking', as it removes the effect of the random noise spike at zero-lag. If the noise, in the sense of any unwanted signal, is not merely at zero-lag then it is preferable to exclude these points from the fit as well, or not to use them in forming a revised zero-lag value.

It has been shown that the choice of observing triangle can have an effect on the velocities obtained by full correlation analysis. Analysis of data recorded on four receivers was analysed using various triangles taken from the set of four receivers. The analysis was found to underestimate the wind velocity when the wind direction was perpendicular to the longest side of the triangle, in agreement with the results of Chang et al. [1993]. Failure to exclude the zero-lag point value of the covariance data prior to fitting led to a larger difference between velocities calculated using different receiving triangles, a manifestation of the 'triangle size effect', in agreement with the modelling results of Holdsworth and Reid [1995].

Another effect observed in this study is a triangle effect which is insensitive to the inclusion of the zero lag data, i.e. the exclusion of this data produced no reduction in the velocity difference between triangles. This effect was attributed to anisotropies in the ground diffraction pattern due to systematic differences observed in the correlation functions from parallel pairs of receivers.

3.3.2 Comparison of FCA algorithms

The primary operational aim for the Canterbury VHF radar will be the measurement of wind profiles using spaced-receiver techniques. To allow some measure of confidence in the particular method being used it is prudent to make comparisons with other FCA procedures. There are a number of variations on the spaced-antenna method that could be used for such a comparison. Some of these include other versions of FCA [e.g. Meek, 1980], a frequency-domain analogue of FCA [e.g. Briggs and Vincent, 1992; Holdsworth et al., 1992; Holdsworth, 1997], a spaced-antenna method using oblique beams, rather than vertical as is normally the case, [e.g. Liu et al., 1990; Liu et al., 1991; Pan and Liu, 1992; Liu and Pan, 1993] and techniques using cross-spectral analysis [e.g, Doviak et al., 1996; Holloway et al., 1997] and crosscorrelation amplitude slopes [e.g. Lataitis et al., 1995].

Other non-FCA techniques which may also be used for comparison, for instance the Doppler beam swinging method which is discussed in more detail in section 3.4, interferometry techniques [e.g. Pfister, 1971; Farley et al., 1981; Rottger and Ierkic, 1985; Brown, 1992; Brown et al., 1995a], and the meteor radar technique, which uses backscatter from mesospheric meteor ionisation trails, [e.g. Stubbs and Vincent, 1973; Cervera and Reid, 1995; Valentic et al., 1997; Hocking and Thayaparan, 1997]. The reviews of Hocking et al. [1989] and Hocking [1997a], and references therein, provide a good description of the various comparisons done between the FCA/SA method and other techniques. In the stratosphere and troposphere it is possible to make comparisons with balloon measurements [e.g. Rottger and Vincent, 1978; Vincent and Rottger, 1980; Vincent et al., 1987] which also show good agreement. In summary it may be said that the extensive tests of the spaced-antenna method have shown that it is reliable and provides good measurement of the wind direction and magnitude [Briggs, 1977; Costa et al., 1992].

In this section a comparison of two FCA algorithms will be presented. The first, used by the author, is due to Briggs [1984] and can utilise three or more non-collinear receivers. The second is due to Brown and Chapman [1972] and was used by Dr. G. Fraser to analyse a section of data from experiment 1. This latter algorithm is also used on the medium frequency radars at Birdlings Flat, New Zealand and Scott Base, Antarctica, which are operated by the University of Canterbury. The Brown and Chapman (BC) algorithm is discussed in section 2.1.2. The algebraic equivalence of the two algorithms cannot be readily proven, and will thus be tested by comparing velocities calculated by Fraser with those calculated by the author. The same three receivers (1,3 and 4) were used for both algorithms.

There are few comparisons between these two algorithms in the literature and this section has the twofold aim of validating the FCA algorithm to be used on the Canterbury VHF system and also of investigating the algorithm currently used on the MF radars. Lawrence [1990] has found that the two methods gave similar results with the Briggs technique being better for small amplitude winds while Brown [1992] again found good agreement with the Briggs technique having a slightly higher acceptance rate. It was felt that this was due to the Briggs method using extra information to the Brown and Chapman method, a point which is discussed further below.

This section will present an analysis of data from the VHF MU radar and show that while the two methods do agree there are statistically significant differences. In particular, the Brown and Chapman velocity magnitudes are shown to be smaller than the Briggs magnitudes. It will also be shown that the BC method has a larger variance than the Briggs method, particularly in regions of low signal strength.

Before presenting the results of the comparison it is necessary to discuss some of the finer points of difference between the two techniques. Firstly, the implementations to be studied employ different interpolation methods to find the τ and τ' values. The first, used by Fraser and denoted τ_{Fraser}, is to fit a parabola over a small number of correlation values in the region that contains the sought-after τ and τ' values. This region will be different for different τ and τ'. The second technique, used by the author and denoted $\tau_{Dunford}$, is to take almost all of the correlation values and fit a Gaussian function to the data as described in section

2.1.3. From this function the necessary values can then be obtained. It should be noted that neither algorithm specifies a unique method to be used for calculation of these values. While suggestions are given, the actual implementation is left up to the programmer.

Another important difference is that in his implementation of the Brown and Chapman method Fraser uses only two of the three sides of the receiving triangle to obtain the apparent velocity, and hence the true velocity, whereas the Briggs analysis utilises all three sides thereby using extra information which is discarded by the former approach. The Brown and Chapman method does use all three sides to calculate the characteristic ellipse which is then used to correct the apparent velocity to give the true velocity. This underutilisation of information has implications for the velocities obtained by the two methods and will be discussed in more detail later. It should perhaps be pointed out that in their discussion of the practical implementation of the theory Brown and Chapman [1972] do suggest using all possible pairs of receiving triangle sides to obtain an average apparent velocity. For historical reasons this was not implemented as it would have lead to a significant increase in the computational time needed to obtain a wind measurement and required more memory which was, at that time, severely limited.

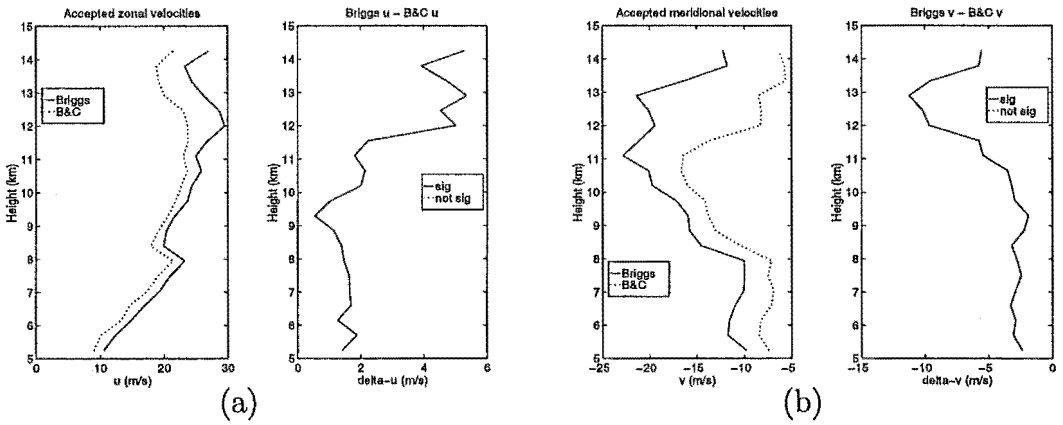

Figure 3.36. Comparison of (a) east-west and (b) north-south velocity components calculated using the algorithms of Briggs [1984], as implemented by Dunford, and Brown and Chapman [1972], as implemented by Fraser. The data shown includes all heights and the first 143 runs from experiment 1.

Figure 3.36 shows a comparison of the east-west and north-south velocities calculated by the two methods using data from 143 of the 154 runs in experiment 1, this being the number analysed by Fraser. It may be observed that the Briggs algo-

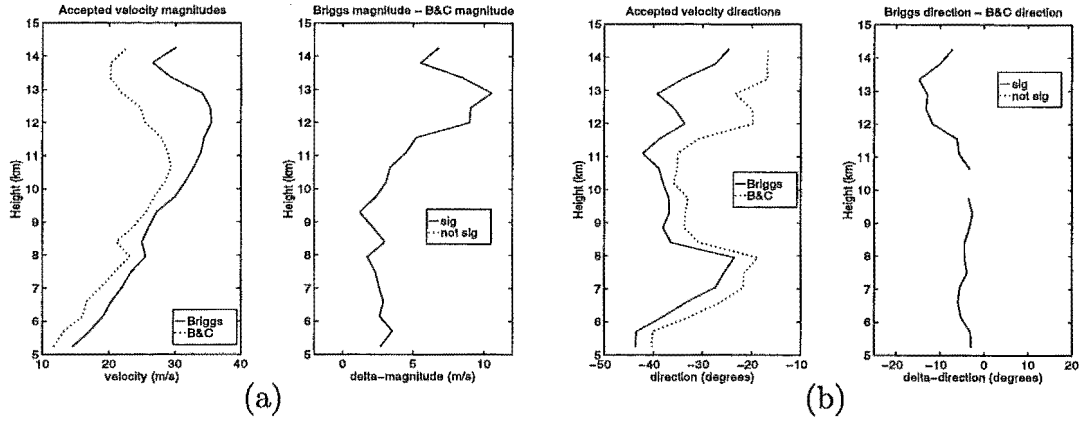

Figure 3.37. Comparison of velocity magnitudes (a) and velocity directions (b) calculated using the algorithms of Briggs [1984], as implemented by Dunford, and Brown and Chapman [1972], as implemented by Fraser. The data shown includes all heights and the first 143 runs from experiment 1.

rithm, which uses the $\tau_{Dunford}$ method, gives larger values than the BC algorithm, which uses the τ_{Fraser} method. This is also seen in figure 3.37a, which shows that the Briggs velocity magnitudes are consistently larger than the BC magnitudes. It should be noted that the directions are also different, on the order of 5°. All velocities have been passed through both the acceptance criteria and the outlier removal procedure of section 3.4.2. In addition, the velocities have been processed in groups of three heights, giving a resolution of 450m. Regions where differences are statistically significant at the 99% level are indicated.

There are two mechanisms by which the observed variations in the velocities may be produced. These are the methods used to find the τ and τ' values, and the different algorithms used to calculate velocities from those values. These two effects will now be considered separately.

3.3.2.1 Variation of velocity with tau and tau-prime

To determine the influence of the $\tau_{Dunford}$ and τ_{Fraser} methods on the velocities, the section of Fraser's program code which implements the BC algorithm was incorporated into the author's FCA program in place of the existing Briggs code. Comparison of velocities from the two programs will then show the effect of using different τ and τ' values on the BC algorithm. Because of the different programming languages used it would be much more difficult to perform a similar comparison using the Briggs algorithm. Figures 3.38a and 3.38b show a comparison of the velocities from 143 runs in experiment 1.

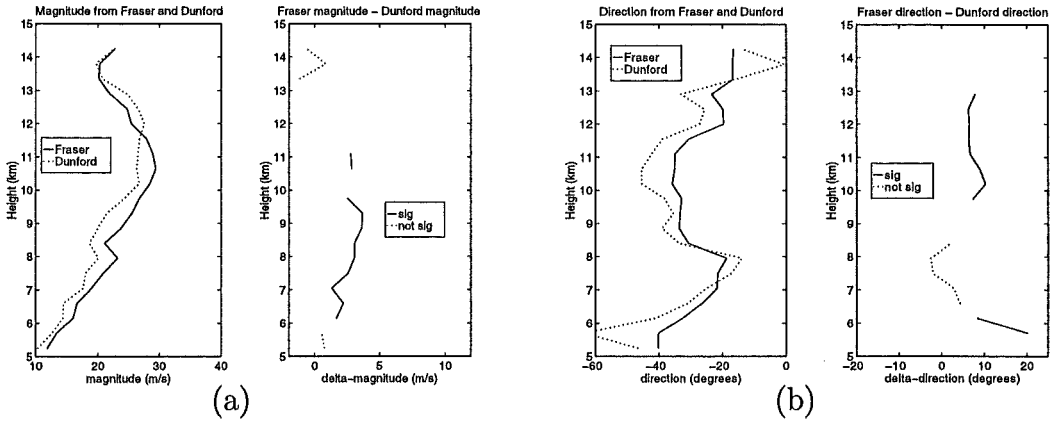

Figure 3.38. Comparison of (a) magnitudes and (b) directions based on tau and tau-prime values calculated by Dunford and Fraser and the algorithm of Brown and Chapman [1972]. The data shown includes all heights and the first 143 runs from experiment 1.

It can be seen that the difference between the magnitudes is generally less than for figure 3.37a, in some cases being statistically insignificant. In addition the directions show little systematic difference being both positive and negative. Thus it would seem that the differences in figures 3.36 and 3.37 can not be due solely to the method of finding τ, τ' especially as the magnitudes of Fraser in figure 3.38a are larger than those of Dunford, while in figure 3.37a Briggs is larger than Brown and Chapman.

3.3.2.2 Variation of velocity with FCA algorithm

To determine the effect of different FCA algorithms on the velocity, a comparison of results using the Briggs and BC algorithms and the $\tau_{Dunford}$ fitting method was carried out. As mentioned above this was a far less complex programming task than recoding the Briggs algorithm in Fortran 77 to use the τ_{Fraser} method. Figure 3.39 shows the magnitudes and directions from all 154 runs in experiment 1 and it can be seen that the Briggs magnitudes are consistently bigger than the BC magnitudes while the directions do not show any systematic differences. Thus it would seem that the variations seen in figures 3.36 and 3.37 are a combination of the effect of the FCA algorithm and the τ,τ' fitting method with the FCA algorithm being dominant.

To further investigate this difference in FCA algorithms, data from experiments other than 1 will now be considered. It should be noted that as the Brown and Chapman code has been written to use triangle 134 of experiment 1, to allow comparison

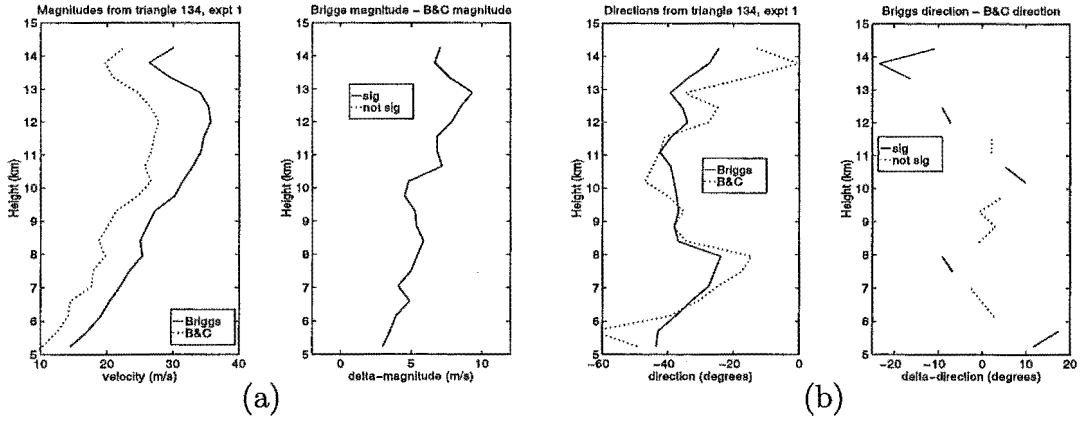

Figure 3.39. Comparison of (a) velocity magnitudes and (b) velocity directions calculated using the algorithms of Briggs [1984] and Brown and Chapman [1972]. The data shown includes all heights and runs runs from experiment 1.

with Fraser's results, it is only possible to analyse data from experiments that share this configuration. This therefore precludes analysis of data from experiments 2,4 and 6 and from any other triangle configurations. With this caveat, data will now be presented from experiments 3 and 5.

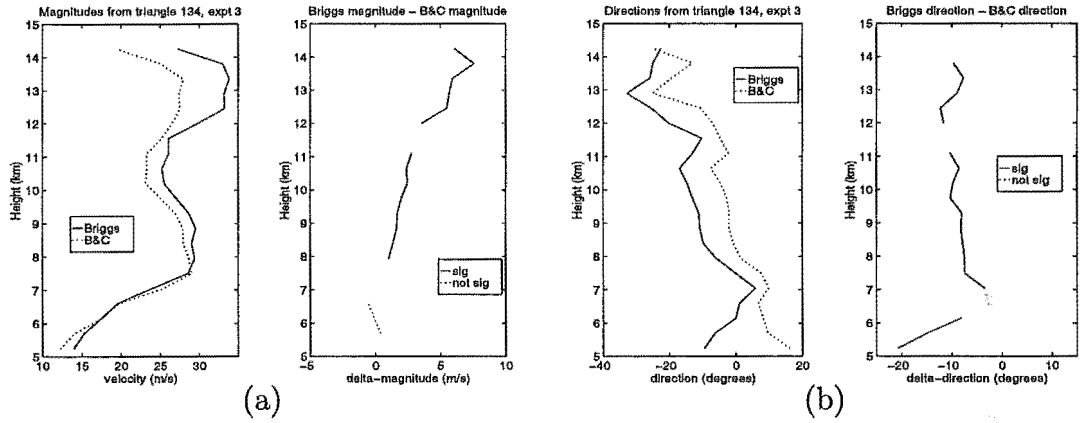

Figure 3.40. Comparison of (a) velocity magnitudes and (b) velocity directions calculated using the algorithms of Briggs [1984] and Brown and Chapman [1972]. The data shown includes all heights and runs runs from experiment 3.

Figures 3.40 and 3.41 show the velocity magnitudes and directions from experiments 3 and 5. As before, the velocities have passed both the FCA acceptance criteria and the outlier rejection procedure. It can be seen that, as in figure 3.39, the Briggs magnitudes are generally larger than the BC magnitudes. A source of minor concern is the difference in directions between the two methods in figures 3.40b and 3.41b. Although small, in agreement with Briggs [1977] and Costa et al. [1992], it might be expected that the methods would show no systematic difference.

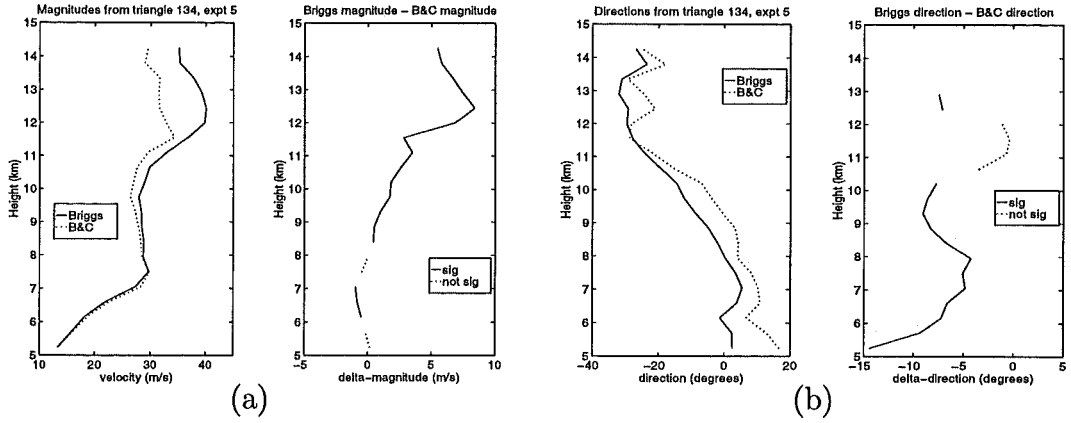

Figure 3.41. Comparison of (a) velocity magnitudes and (b) velocity directions calculated using the algorithms of Briggs [1984] and Brown and Chapman [1972]. The data shown includes all heights and runs runs from experiment 5.

For the methods to show variations in direction, they must be treating the velocity components u and v differently. That this is in fact the case can be seen in figures 3.42 and 3.43 where the meridional velocities exhibit larger differences than the zonal velocities.

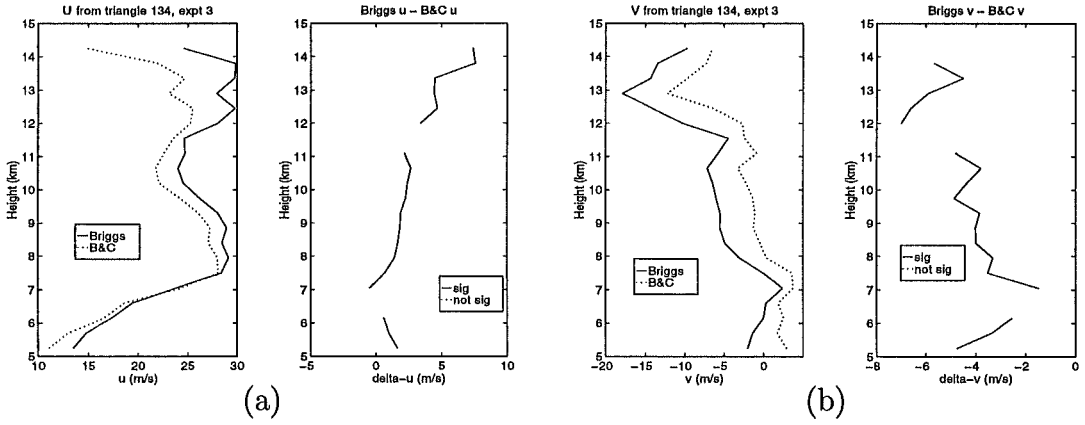

Figure 3.42. Comparison of (a) east-west and (b) north-south velocity components calculated using the algorithms of Briggs [1984] and Brown and Chapman [1972]. The data shown includes all heights and runs runs from experiment 3.

As was mentioned above the implementation of the BC method used here uses only two of the three receiving triangle sides, in contrast to the Briggs algorithm. It is possible that the variation between velocity components is a manifestation of the triangle size effect of section 3.3.1 and that the difference between the two methods is related to the different averaging used. It would be an interesting extension of this work to employ the BC method using different triangles, different choices of the two sides used and the average suggested by Brown and Chapman [1972] to see

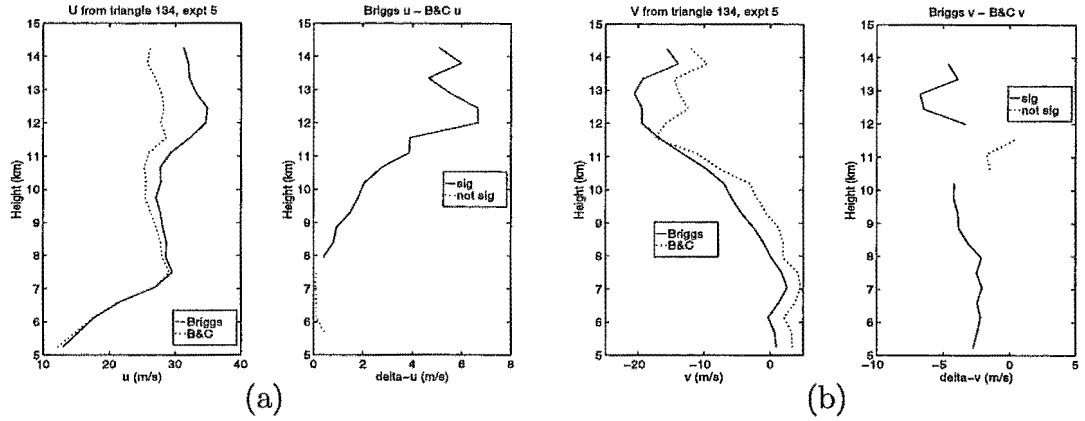

Figure 3.43. Comparison of (a) east-west and (b) north-south velocity components calculated using the algorithms of Briggs [1984] and Brown and Chapman [1972]. The data shown includes all heights and runs runs from experiment 5.

if this changes the differences between the two algorithms. However, for reasons discussed above, this would involve a substantial amount of re-programming and has thus been left for future work.

3.3.2.3 Variation of variance with FCA algorithm

It may be noted from the figures in the previous sections that the differences between Briggs and Brown and Chapman are generally larger at the top of the height range. This is a region of lower signal strength and thus one, or both, of the methods may have poor performance in these regions. This, in addition to the fact that the methods use different averaging, motivates a study of the variances of the velocities calculated using the two techniques.

Figure 3.44 shows the variances of the zonal and meridional velocities from experiments 1, 3 and 5 using accepted data with outliers removed and 3 height range bins. It is immediately apparent that the Brown and Chapman algorithm, as implemented here, has a much larger variance. In particular in figures 3.44e,f near $10 - 11$km where the signal power is low the BC method does not perform as well as the Briggs method. It seems reasonable that this is due to the lesser averaging used by the technique, as compared to the Briggs method. Again, re-coding of the BC algorithm to use the averaging suggested by Brown and Chapman [1972] would allow a more definitive conclusion to be drawn.

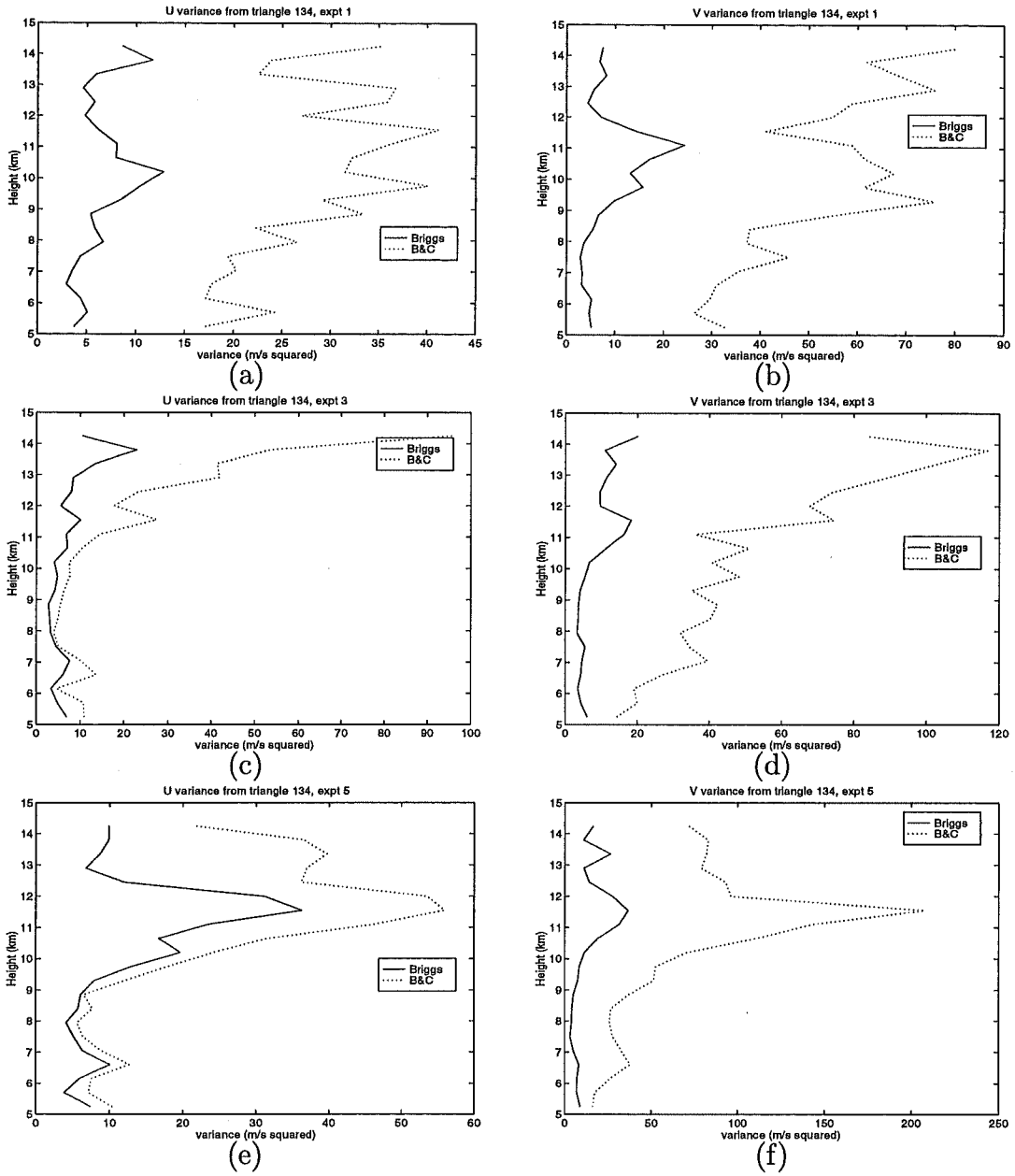

Figure 3.44. Comparison of zonal and meridional velocity variances calculated using the algorithms of Briggs [1984] and Brown and Chapman [1972]. The data shown includes all heights and runs runs from experiments 1, 3 and 5.

3.3.2.4 Conclusion

It has been shown that both the method of calculating the τ and τ' values and the particular FCA algorithm used can affect the velocities. The variation in the velocities presented in figure 3.36 and 3.37 is thus a combination of both these effects. The relationships between the velocity and the τ, τ' values in each algorithm are highly complicated and further work would be needed to determine the precise manner in which these two effects interact. In addition it has been shown that the

Brown and Chapman algorithm, as implemented here, has systematically smaller velocity magnitudes and larger variances than the Briggs method. There are also cases where the velocity directions obtained from the two methods are different.

It is suggested that these three effects are due to the fact that the implementation used here does not utilise all of the available information from the three receivers. In particular, only two of the three sides are used to obtain the true velocity. It should be noted that this is not a feature of the algorithm as proposed by Brown and Chapman [1972] but rather a historical artifact, as discussed earlier. Although it was not possible, due to the significant effort required, to implement an improved version of the algorithm there is every reason to believe that if this is done the agreement between these two FCA methods will be greatly improved. In its present form then the Briggs algorithm appears to offer significant advantages over the Brown and Chapman algorithm and the agreement between the two techniques, notwithstanding the comments made above, is further evidence that the FCA technique may be confidently applied to measure the wind profile.

3.3.3 Vertical velocities

Vertical velocities have been calculated and results for each of the six experiments are shown in figure 3.45 - 3.47. As discussed in section 2.2, calculation of radial velocities requires that a linear fit be made to the correlation function phases. This fitting has few failures, in contrast to the Gaussian fitting routines used to calculate the horizontal velocities. Thus, the radial velocities provide essentially complete coverage of the height and time regions observed in each data set. However it is necessary to correct the radial velocities for horizontal velocity contamination, as described in section 2.2, to give true vertical velocities. If these corrected velocities were shown then there would be few data from regions of either high or low-powered structure and thus only uncorrected velocities will be presented here.

The vertical velocities in figure 3.45 - 3.47 show little correspondence to the RTI plots of section 3.2.1. In particular, figure 3.45a and 3.45b show no horizontal layer structure of the type seen in the power RTI plots (figures 3.4a and 3.5a) for experiments 1 and 2. In addition, there are no features in any of the vertical velocity plots which clearly correspond to the high-power events. Note, however, that the

lack of similarity does not necessarily imply that the variables are independent. In fact useful information can be obtained by considering the covariance between the vertical and horizontal winds, as will be presented in section 3.5.

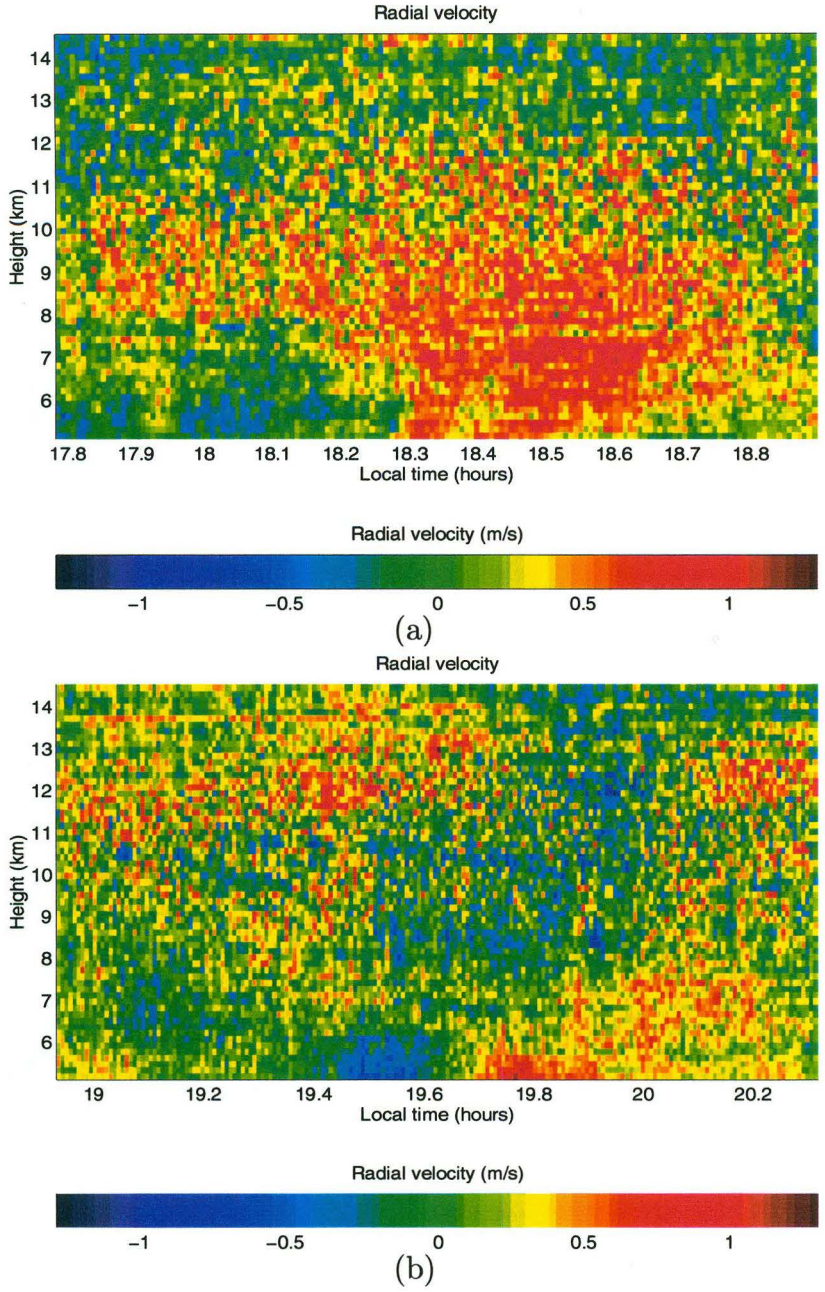

Figure 3.45. Radial velocities from (a) experiment 1 and (b) experiment 2. The magnitude of the velocity is shown as colour. The radial velocities have not been corrected for horizontal velocity contamination.

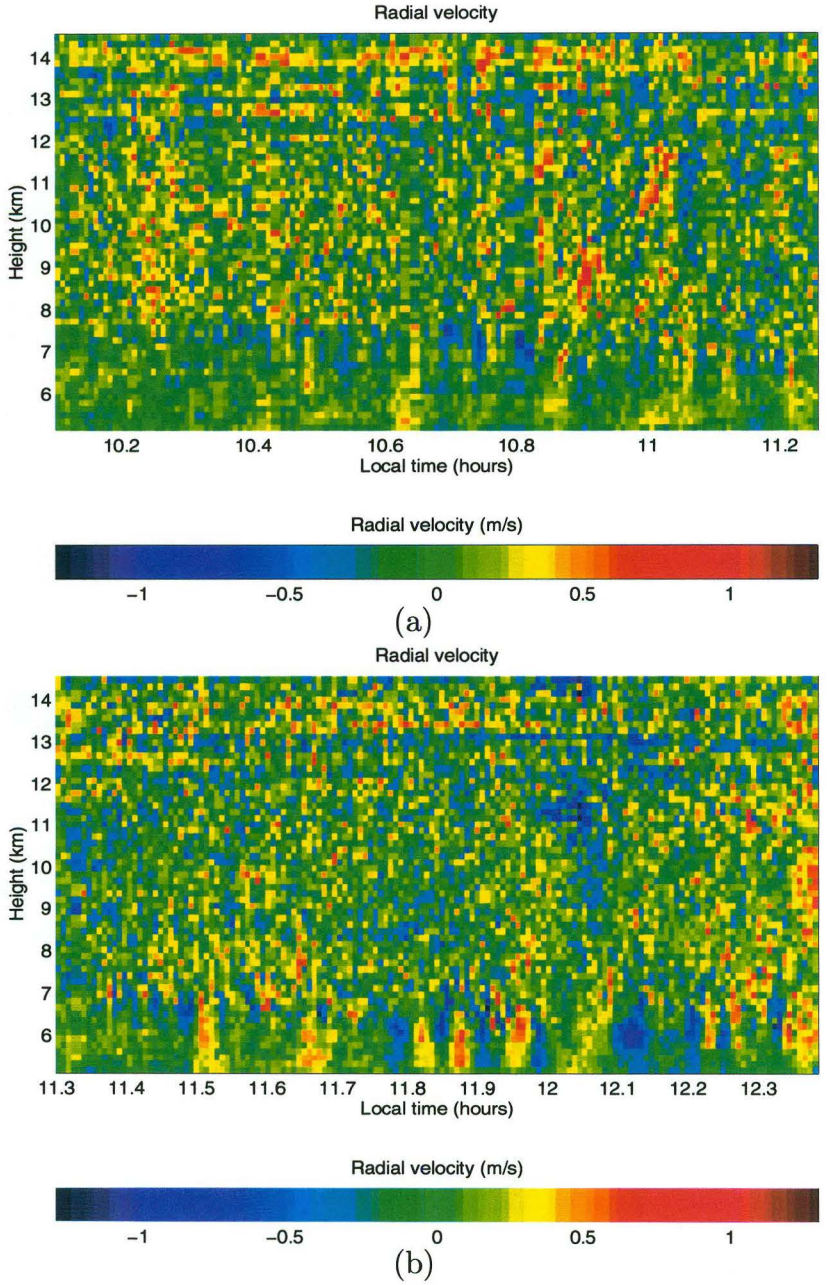

Figure 3.46. Radial velocities from (a) experiment 3 and (b) experiment 4. The magnitude of the velocity is shown as colour. The radial velocities have not been corrected for horizontal velocity contamination.

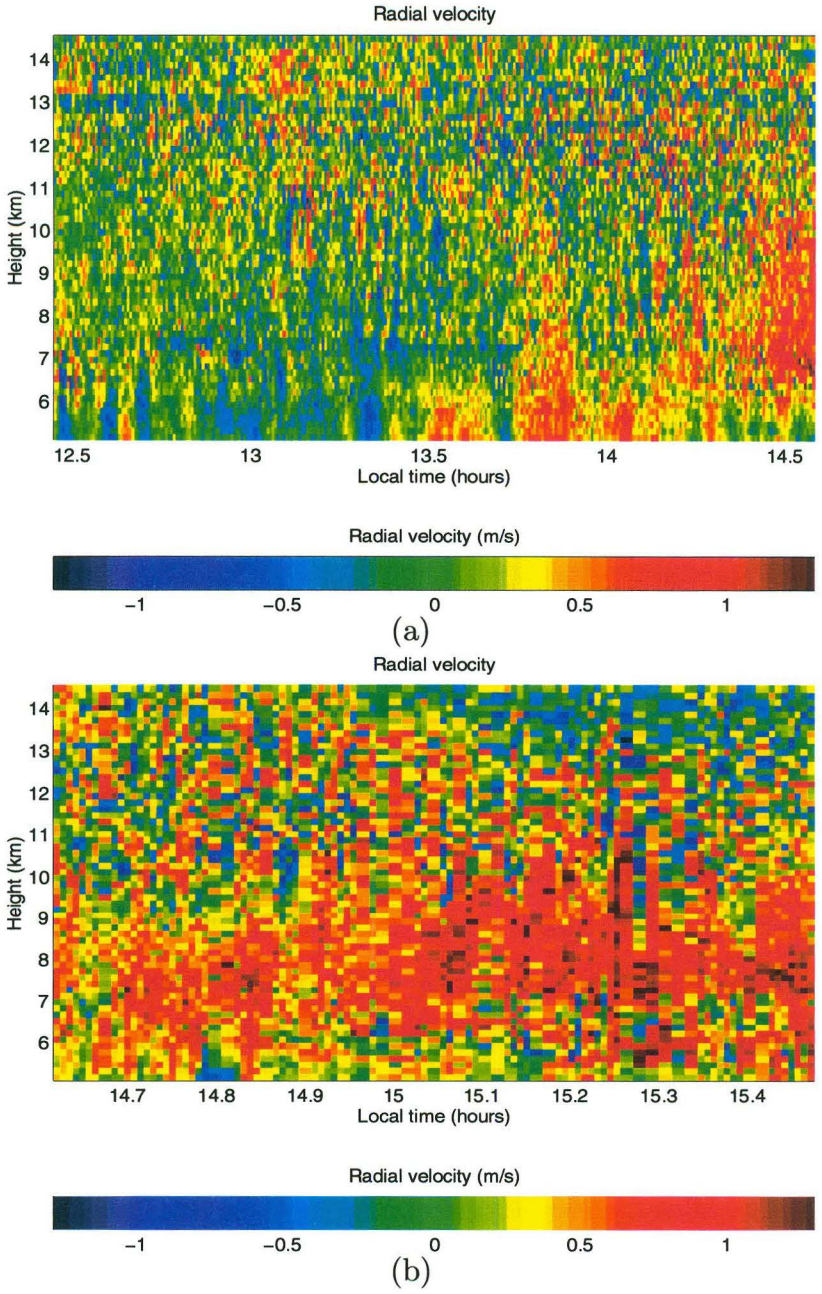

Figure 3.47. Radial velocities from (a) experiment 5 and (b) experiment 6. The magnitude of the velocity is shown as colour. The radial veloscities have not been corrected for horizontal velocity contamination.

3.4 Doppler beam swinging comparisons

Previous sections have discussed in depth the operation of the method of FCA and results will now be presented, on 10-min and 50-min timescales, of comparisons with the other major method of wind determination; Doppler beam swinging. Numerous comparisons between the two techniques have been made [e.g. Vincent et al., 1987; Larsen and Rottger, 1989; Van Baelen et al., 1990] and have found good agreement between the two methods.

3.4.1 Practical implementation

The DBS velocities used in this thesis were computed using a FORTRAN 77/C Unix programme supplied by Dr. W. Brown. The sole modifications made to the programme to enable it to run on the University of Canterbury Unix system were the removal of the non-portable graphics routines and outputting of the radial velocities in addition to the Cartesian components. The programme reads in the data files and, after performing checks on signal quality, uses the Doppler shift calculated on-line at the MU radar [Fukao et al., 1985b; Sato et al., 1985] to obtain radial velocities for each of the 5 beams. Linear interpolation is then used on the velocities from the oblique beams to produce values at heights corresponding to those from the vertical beam. Finally, the radial velocities are converted to u, v and w in the manner described in section 2.3.1.

3.4.2 Results

Results will now be presented showing comparisons between FCA and DBS velocities on 10-minute and 50-minute timescales. The calculation of FCA velocities is described in chapter 2.1. Note that, as can be seen in table 3.2, the FCA and DBS experiments to be discussed were sequential in time rather than parallel.

As there are no 'rejection criteria' for DBS velocities, analogous to those in section 2.1.3, it was necessary to develop a method of outlier rejection applicable to both data sets. Although it is possible to use a manual method of outlier rejection (e.g. Murphy [1990]) it is advisable to use some automatic scheme which has the advantages of greater objectivity and speed. The rejection method used first calculates the mean and standard deviation of the velocities at a particular height.

Data further than 2 standard deviations from the mean are removed and the process is then repeated once. This is a standard technique of outlier removal and has been used by several workers [e.g. Murphy, 1990; Brown, 1992; Worthington and Thomas, 1996]. This procedure is known as Chauvenet's criterion and statistical texts, [e.g. Young, 1962; Meyer, 1975], do not recommend its repeated use as, in the limit, it will remove every single data point. For the geophysical data being analysed here it is possible to have a small number of extreme outliers which substantially distort the calculated standard deviation and the first pass of the procedure is designed to remove these outlying outliers.

The DBS vertical velocities are calculated from the Doppler shift measured on the central beam in figure 3.6 and these are compared with FCA vertical velocities that have not had any correction made for off-zenith scatter, as described in section 2.2.1.

3.4.2.1 10 minute comparisons

To compare the two methods of velocity calculation it is instructive to concentrate on a small interval of time near the point of changeover from FCA to DBS or DBS to FCA as this allows effects due to changing wind velocities to be minimised. Too small an interval of time, however, will contain too few points for a reliable comparison. In this section profiles labelled 'FCA' are averages of 23 data runs ($\approx$ 10.05min), and those labelled 'DBS' are averages of 10 runs ($\approx$ 9.73min). Prior to averaging the data from each height were 'cleaned' by removing outlying points in the manner described above. In addition to temporal averaging the velocities used in this and subsequent comparisons in this section have been binned to a height resolution of 450m.

Figure 3.48a-l shows comparisons of the velocity components for each of the four occurrences of sequential DBS/FCA observations. All u, v, and w profiles are shown on the same horizontal axis for ease of comparison. There is good agreement between the two profiles with no appearance of any systematic over- or underestimation by either method. There is slightly more fluctuation in the FCA profiles despite these having been averaged over three height bins, as will be discussed further in section 3.5. The regions of insufficient or poor quality data near

10 – 12km in the FCA are due to regions of low signal power, discussed in section 3.2.3.

The differences, if any, between the two methods may be further investigated by assuming that any variations between the profiles in figure 3.48 are due only to linear changes in the wind velocity. By averaging the 10-min profiles in figure 3.48 and by averaging the profiles 20 – 10 min before the changeover with the profiles 10 – 20 min after and comparing these, it is possible to test this assumption. If the differences are due only to linear variations then these two profiles will be identical. Figure 3.49 shows the results of this process, where 'average A' denotes the average of those 10-min profiles closest to the changeover and 'average B' is the average of those next closest. The good agreement seen in this figure is thus further evidence of the reliability of the FCA method, in agreement with previous studies.

3.4.2.2 50 minute comparisons

Although the 10-min comparisons are useful it is more usual to compare slightly longer averages. Figure 3.50a-l shows 50-min averages for each of the four times of sequential DBS/FCA observations. All u, v, and w profiles are shown on the same horizontal axis for ease of comparison. Profiles labelled 'FCA' are averages of 111 data runs ($\approx$ 48.50 min) and those labelled 'DBS' are averages of 50 runs ($\approx$ 48.64 min). Outlier rejection was performed on the data in each height.

As expected, the averaging of more data points for each height has reduced the fluctuations in the FCA profiles and hence the effect of binning data from several heights would be less than for the 10-min profiles. There is still good agreement between the profiles even on this longer timescale, indicating that the two methods are, indeed, measuring essentially the same velocities. In fact most of the large differences, for example in figure 3.50k,l, are probably due to variations in the wind field as can be seen by comparison with the good agreement in figure 3.49.

3.4.3 Conclusion

During the course of the FCA experiments there were times for which sequential periods of DBS data were available and these have been analysed to provide comparisons with the FCA technique. Comparisons were made between FCA and

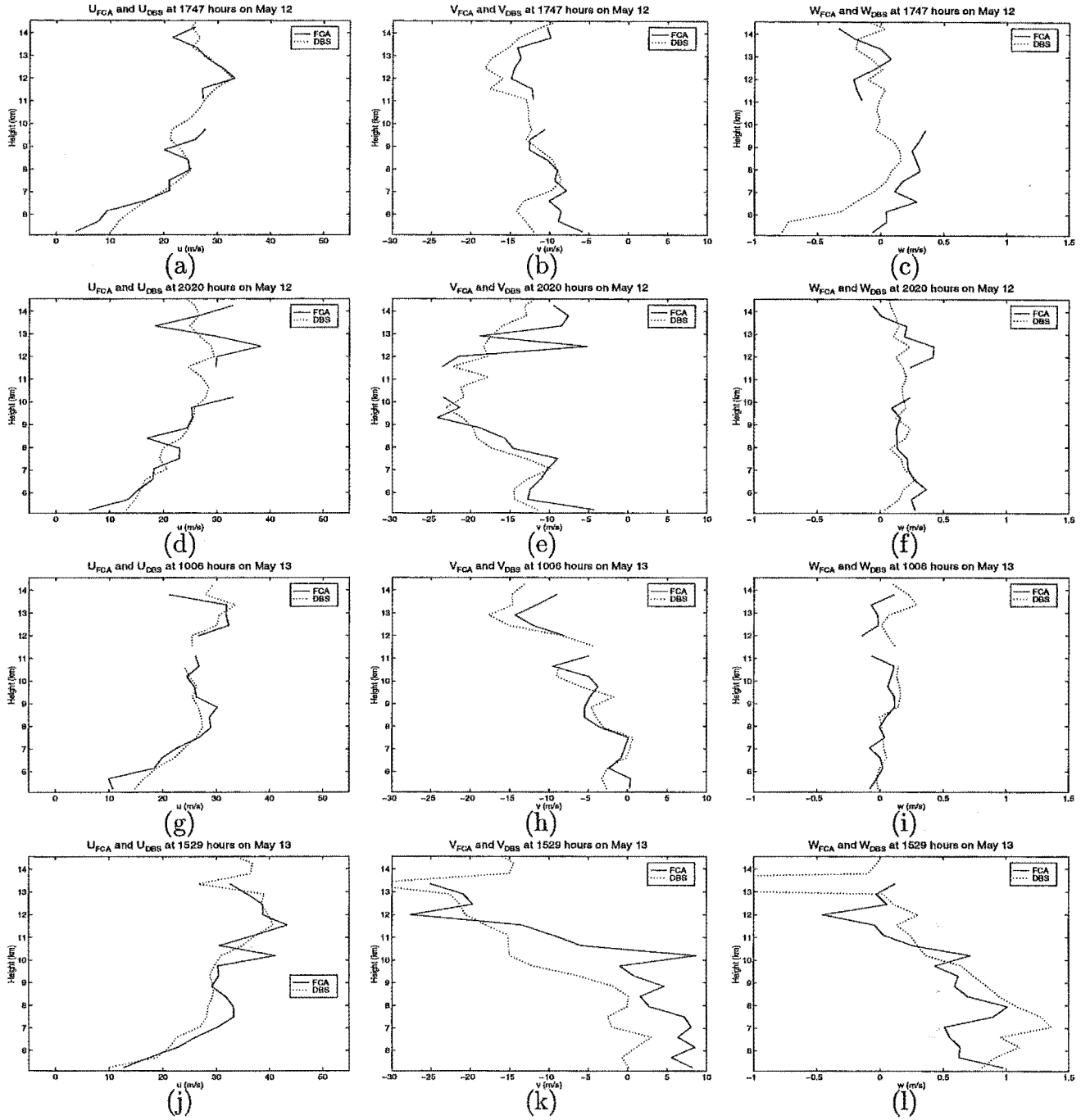

Figure 3.48. Comparisons of 10-minute profiles of FCA and DBS velocities. The time is given for the point of changeover between methods. Details of the analysis applied to the horizontal and vertical components may be found in the text.

DBS velocities on both 10- and 50-min timescales and show that in both cases the two methods are measuring similar average velocities, in agreement with previous work [e.g. Vincent et al., 1987], despite the fact that the observations were sequential in time rather than simultaneous. Averages of the data 10 minutes on either side of the FCA/DBS change and the average of data 10 to 20 minutes before and after the change were compared and showed that the primary cause of difference between

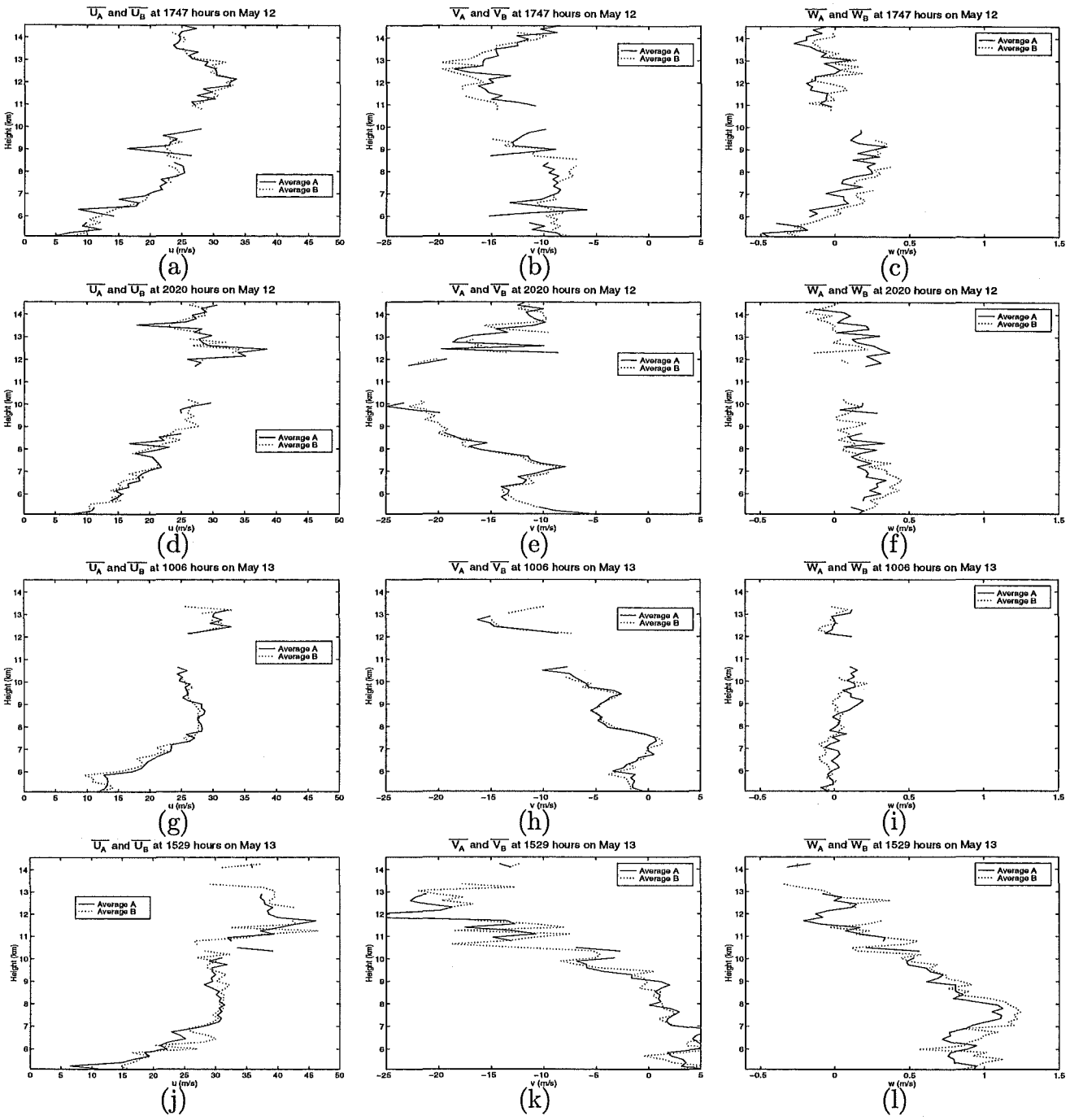

Figure 3.49. Comparison of FCA and DBS winds. Average A shows the average of the 10-min profiles before and after the changeover. Average B shows the average of the next closest 10-min profiles.

the 10- and 50-minute average FCA and DBS profiles was a linear change in the wind field. As a final point, it may be observed that the variation between the two methods is no larger than the variation found, using comparisons on similar timescales, between the FCA algorithms of section 3.3.2.

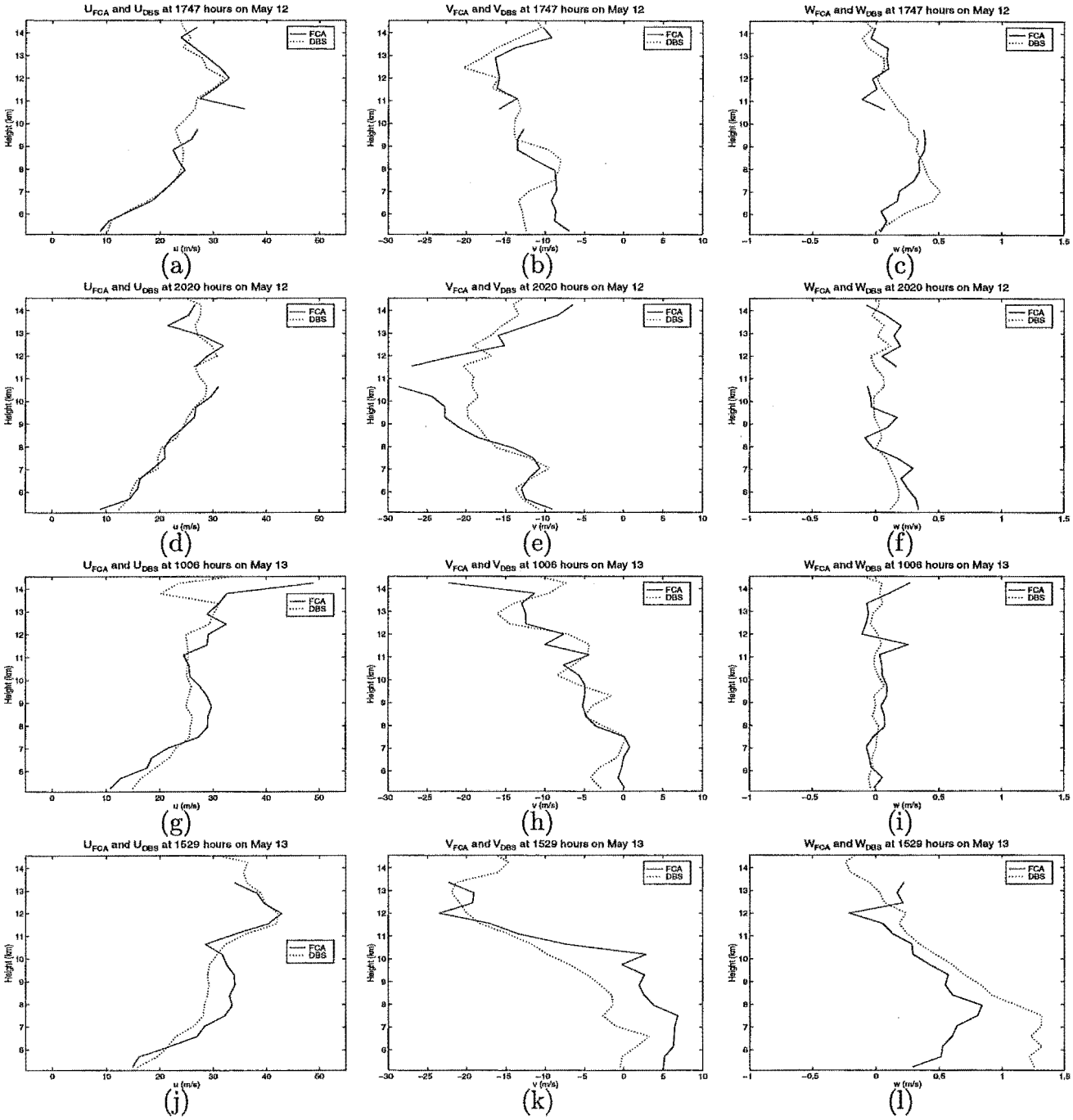

Figure 3.50. Comparisons of 50-minute profiles of FCA and DBS velocities. The time is given for the point of changeover between methods. Details of the analysis applied to the horizontal and vertical components may be found in the text.

3.5 Momentum flux comparisons

Studies of momentum flux using radar techniques have been made in both the mesosphere [e.g. Nakamura et al., 1993b; Murphy, 1990; Thorsen et al., 1997; Reid and Vincent, 1987; Tsuda et al., 1990] and the lower atmosphere [e.g. Fritts et al., 1990; Prichard and Thomas, 1993; McAfee et al., 1989; Chang et al., 1997;

Fukao et al., 1988; Vincent and Eckermann, 1990; Eckermann and Vincent, 1993]. This section presents the first comparisons between tropospheric momentum fluxes calculated using the FCA and DBS methods.

Measurements of $\overline{u'w'}$ and $\overline{v'w'}$ have generally used DBS radar systems and the symmetric beam analysis method of Vincent and Reid [1983]. Although FCA calculates only horizontal winds it is possible to use the phase of the correlation functions to obtain w and hence estimates of momentum fluxes. To date the only use of this method has been, in the mesosphere, with the University of Saskatchewan MF radar [Meek and Manson, 1989] and, in the troposphere and lower stratosphere, with the University of Adelaide VHF radar [Vincent and Eckermann, 1990; Eckermann and Vincent, 1993] and the Chung-Li radar, Taiwan [Pan et al., 1992].

Several studies have considered the symmetric beam technique in detail [e.g. Fritts et al., 1990; Nastrom and VanZandt, 1996; Reid and Vincent, 1987] and intercomparisons have been made with other DBS methods. These include the 'three beam' technique, which uses one vertical beam for w and a single off zenith beam for each of u and v, [Fukao et al., 1988; Worthington and Thomas, 1996] and a 'five beam' method, which uses a vertical beam for w and a pair of off zenith beams for each of the horizontal components, [Worthington and Thomas, 1996]. Among the few comparisons which have been made with non-DBS techniques, Nakamura et al. [1993a] have compared FCA mesospheric momentum fluxes obtained with the Saskatoon MF radar with symmetric beam results from the VHF MU radar and Thorsen et al. [1997] have compared zonal momentum fluxes using time domain interferometry and FCA on the Urbana MF radar. To date, the only comparison between the FCA and symmetric beam methods in the lower atmosphere has been done by Pan et al. [1992]. As the University of Canterbury VHF radar will be primarily a spaced-antenna system it is necessary to investigate any possible differences between these techniques of momentum flux measurement.

3.5.1 Data analysis

The velocity covariances, $u'w'$ and $v'w'$, depend on values which are deviations from a mean and thus outlier data points could easily outweigh the contribution from 'good' data points. This effect is not as important in the comparison of FCA and

DBS velocities of section 3.4.2 as these use mean values which will be less affected by outliers. The technique used in this thesis is to iteratively remove values which are a predetermined number of standard deviations away from the mean and is discussed in more detail in section 3.4.2.

Once any outlying data have been removed the variances required for momentum flux could be calculated using the mean value. For the approximately hour length data sets being considered here, however, it is more appropriate to calculate deviations from a line of best fit through the data at each height. This is because oscillations of period greater than one hour might affect the data, even though it is not possible to unambiguously detect them [Murphy, 1990]. If longer data sets were available then it may be necessary to fit for, and remove, longer period harmonics before calculating the straight line fit.

3.5.1.1 Analysing sparse data

It is possible to apply Fourier methods to the data to determine what periodicities exist and then to filter out those which are not wanted. There is, however, a major difficulty with this approach. This is a consequence of the fact that spectral techniques like the fast Fourier transform (FFT) assume that the data are evenly spaced. For many geophysical experiments this assumption is indefensible. Even a cursory glance at figures 3.4 to 3.9 shows that for the radar data presented here there is a significant amount of missing information. Add to this the knowledge that those graphs do not include values which subsequently failed the FCA selection criteria and clearly the situation is not ideal.

Figure 3.51a shows a profile of the percentage of accepted data from a typical FCA experiment. This percentage can be increased, at the expense of vertical resolution, by averaging over several heights. As the MU radar has a height resolution of 150m this is not a severe restriction. Figure 3.51b shows the effect of binning 4 heights (giving a resolution of 600m) and it can be seen that the average time resolution has been improved by a factor of about 3. To produce a set of points evenly spaced in time some form of interpolation could now be applied, however as Press et al. [1992] note the results 'are not encouraging'. As an example of the problems that can arise Lawrence et al. [1995], analysing mesospheric meridional

winds, shows that using linear interpolation can produce spurious power at low frequencies.

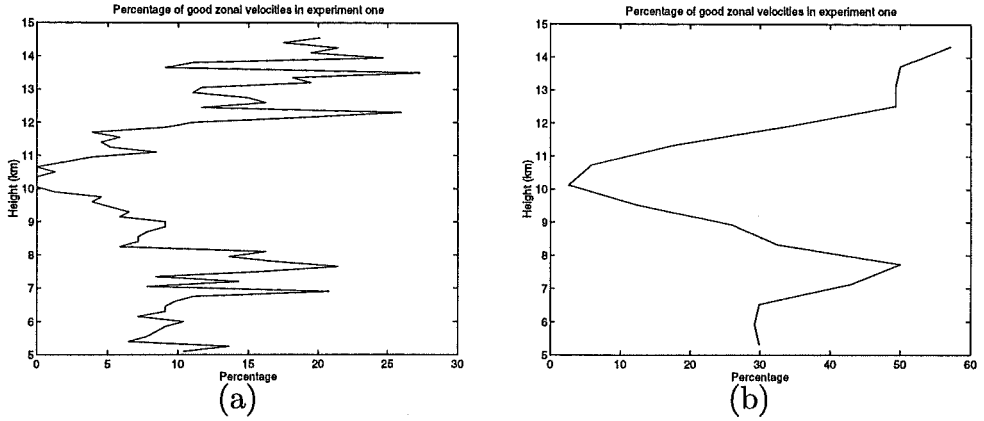

Figure 3.51. Profiles of the percentage of good data points from experiment one. Profile (a) shows the percentage of data which passed the FCA acceptance criteria and subsequent outlier removal. Profile (b) shows the percentage obtained by binning together 4 heights.

An alternative method of spectral analysis which does not require evenly spaced data, and hence interpolation, has been developed by Lomb [1976] and Scargle [1982] for determining periodicities, and their statistical significance, in astronomical data. A discussion of the technique can be found in Press et al. [1992]. The method used in this thesis is a modification, developed by Dr. R. Bennett and Mr. S. Marsh, which calculates amplitude and phase information. This is necessary for the filtering to be done here. The pertinent equations are reproduced below for completeness.

Consider a series of N data points $h_i \equiv h(t_i)$ sampled at irregular times t_i and let $\overline{h}$ be the mean of the values. Then for each angular frequency ω define τ by

$$\tan 2\omega\tau = \frac{\sum_{i=1}^{N} \sin 2\omega t_i}{\sum_{i=1}^{N} \cos 2\omega t_i}$$

The amplitude a and phase ϕ of the harmonic $a\cos(\omega t - \phi)$ which best fit the data (in a least-squares sense) are given by

$$a(\omega) = \sqrt{\left(\frac{\sum_{i=1}^{N}(h_i - \overline{h})\cos(\omega t_i - \phi)}{\sum_{i=1}^{N}\cos^2(\omega t_i - \phi)}\right)^2 + \left(\frac{\sum_{i=1}^{N}(h_i - \overline{h})\sin(\omega t_i - \phi)}{\sum_{i=1}^{N}\sin^2(\omega t_i - \phi)}\right)^2} \tag{3.5}$$

$$\phi(\omega) = \omega\tau - \tan^{-1}\left(\frac{\frac{\sum_{i=1}^{N}(h_i - \overline{h})\sin(\omega t_i - \phi)}{\sum_{i=1}^{N}\sin^2(\omega t_i - \phi)}}{\frac{\sum_{i=1}^{N}(h_i - \overline{h})\cos(\omega t_i - \phi)}{\sum_{i=1}^{N}\cos^2(\omega t_i - \phi)}}\right) \tag{3.6}$$

It is desirable to iteratively determine the frequencies of interest (S. Marsh pers com), as larger amplitude components can affect the amplitudes calculated for frequencies of smaller magnitude due to the non-orthogonality of the harmonic components. That is, determine $a(\omega)$ for all values of ω and then subtract the component of largest amplitude, ω_m say, from the data; thus $x \rightarrow x - a_m \cos(\omega_m t - \phi_m)$, where $a_m = a(\omega_m)$, $\phi_m = \phi(\omega_m)$. Repeating this process gives the second largest component and so on. This procedure gives the phases and amplitudes which best describe the data in a least-squares sense and will henceforth be designated as a least-squares frequency transform (LSFT).

3.5.2 Comparison of variance

As a preliminary to calculating momentum fluxes it is appropriate to study the variances of the velocities from which the fluxes are determined. Figure 3.52 shows a comparison of the variances of accepted FCA zonal velocities in experiment 1 and DBS velocities from the preceding run. Each profile is an average of 50 minutes data. The data have been grouped into 'bins' of 4 heights and have had the outliers in each bin removed prior to calculating the variance. The FCA velocities have a larger variance than do the DBS values and this trend is apparent in data from other experimental runs and also in the meridional velocities. The vertical velocity variances show less difference than the meridional and zonal values.

To investigate possible causes of the large variances in FCA wind it is useful to determine which frequencies are present in the data. Figure 3.53 shows the periodicities found in zonal data from a typical bin (4 heights) in experiment 1. One iteration over all frequencies was done to calculate $a(\omega)$ as per equation (3.5), rather than iterating through all frequencies as this was impractical. There is a large amount of power in periods less than about 6 minutes which is on the order of the Brunt-Vaisala period in the troposphere [Holton, 1979].

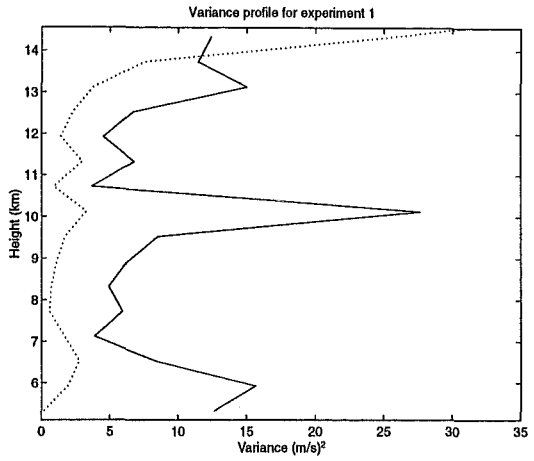

Figure 3.52. Comparison of variance of FCA (solid) and DBS (dashed) zonal velocities. The velocities are binned to give a resolution of 600m. FCA data is from experiment one and DBS data from the preceeding run.

Figure 3.53 does not appear to show the expected spectral reddening, i.e. lesser power at higher frequencies, as has been found in other studies [e.g. Larsen et al., 1982; Bemra et al., 1986; Rottger, 1986; May et al., 1995]. However it should be noted that the short data length available here only allow frequencies higher than about one hour to be calculated. Previous studies have generally analysed much longer data series and have typically only considered frequencies lower than the Brunt-Vaisala frequency. In addition, it appears that there is an increase in power at longer periods in figure 3.53 suggesting that the results obtained here are not in conflict with earlier work.

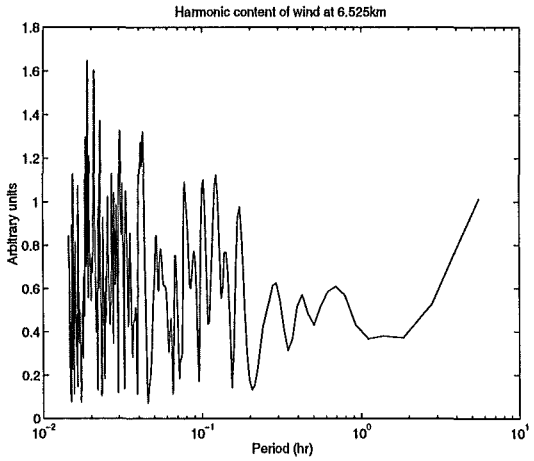

Figure 3.53. Harmonic content of FCA zonal velocities from a typical bin in experiment one as determined by the LSFT procedure.

Radiosonde flights are available for both days and thus it is possible to calculate the Brunt-Vaisala period during the experiment. The profile for May 12, averaged to 600m resolution, is shown in figure 3.54. The angular Brunt-Vaisala frequency is [Andrews et al., 1987]

$$\omega_{BV} = g\frac{\partial\theta}{\partial z}$$

where g is the mean gravitational acceleration at sea level, θ is potential temperature and z is height. Hence the Brunt-Vaisala period is

$$\tau_{BV} = \frac{2\pi}{\omega_{BV}}$$

From figure 3.54 an approximate value for τ_{BV}, which represents the fastest period

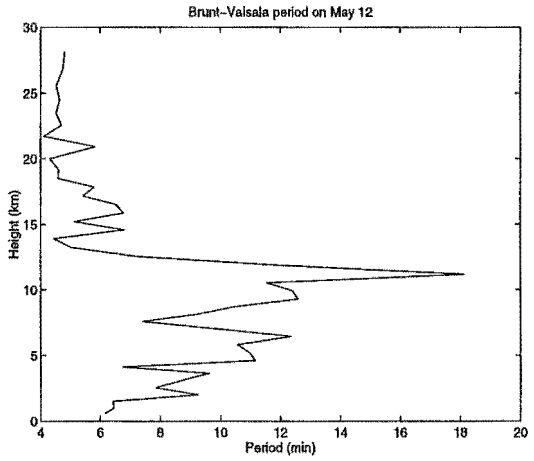

Figure 3.54. Profile of Brunt-Vaisala period for May 12 1994.

for buoyancy oscillations, would be on the order of 10 minutes in the troposphere. Periods faster than τ_{BV}, then, could not be due to gravity waves and this produces a motivation for filtering out these components from the velocities prior to calculation of momentum fluxes.

The procedure developed for this filtering is based on the LSFT technique described earlier. The data is first binned, outliers in each bin are removed and the mean value subtracted. Integer multiples of the fundamental frequency (equal to the inverse of the data length) are found up to the Brunt-Vaisala frequency and a LSFT of the data is calculated using this frequency set. Finally, using the phase and amplitude from the LSFT, a new 'filtered' data series is constructed by forming the

sum of the contributions from each harmonic and the previously subtracted mean value.

Typical results of this process are depicted in figure 3.55 which shows the variance of the data used in figure 3.52, now filtered with a low-pass cutoff period of 10 minutes. There is clearly a reduction in the variance of data which has had higher frequencies removed. The large variance at 10km in both figures 3.52 and 3.55 is caused by a lack of data at these heights as a result of low signal strength. Although, as expected, the variance after filtering is generally smaller, it is of some concern that the variance at 10km in figure 3.55 is substantially larger (being on the order of 1000) than that of figure 3.52. To probe further, consider figure 3.56a which shows the data and filtered reconstruction from a typical bin. Each data point is the average velocity over 4 heights. It can be seen that the technique appears to perform correctly. Figure 3.56b, however, shows the results from 10km. It is obvious that in this case there are simply too few data for the technique to provide a physically sensible reconstruction. Thus the unreasonably large variance in figure 3.55 is a result of trying to do too much with too little data.

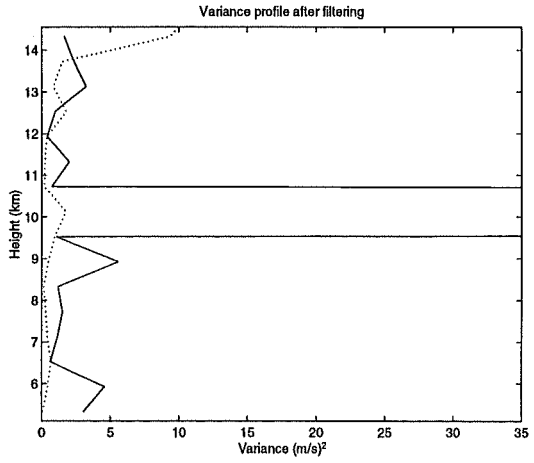

Figure 3.55. Comparison of variance of filtered FCA (solid) and DBS (dashed) zonal velocities using the data of figure 3.52. The velocities are binned to give a resolution of 600m and have had periods faster than 10 minutes removed as described in the text. The same scale as figure 3.52 is used for comparison.

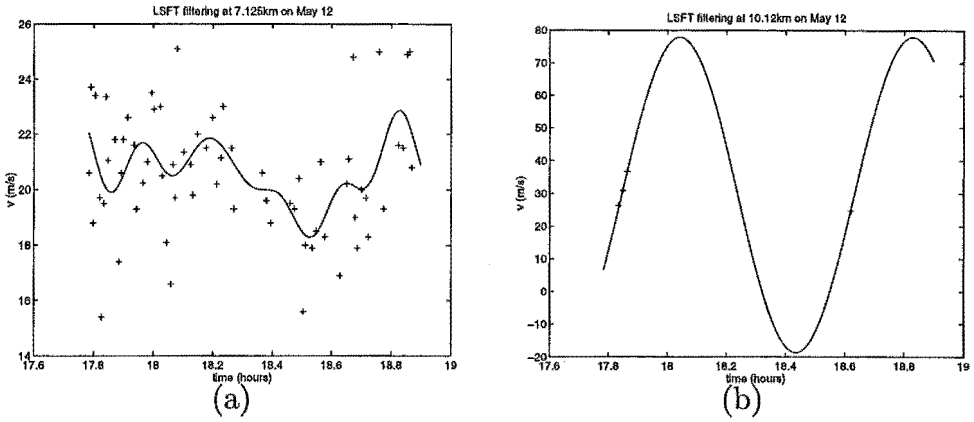

Figure 3.56. Examples of the fit obtained using LSFT to remove periods less than 10 minutes from accepted cleaned zonal velocities. (a) shows a typical fit at a height with a reasonable number of data points and (b) is an example of the situation that can arise with too few data points.

3.5.3 Comparison of hourly momentum fluxes

It now remains to combine the techniques developed above to obtain profiles of zonal and meridional momentum fluxes from the four times at which sequential FCA and DBS data exist. To summarise the procedure, first, the data are binned and the outliers in each bin removed. Next, a new velocity series for each bin is constructed containing only periods longer than a specified limit. Perturbation velocities are then calculated for 50 minutes either side of the FCA/DBS change as deviations from a straight line fit and finally, covariances of these perturbations are produced.

Figures 3.57-3.60 show the results of filtering out periods of less than 15 minutes and averaging over 4 heights. For comparison purposes the accepted FCA and DBS velocities, with outliers removed and averaged to the same resolution, are shown. All three methods are plotted; FCAW (red), 5-beam (green) and symmetric beam (blue). The two methods based on DBS velocities, 5-beam and symmetric beam, show good agreement throughout the height range while the FCAW fluxes do not agree as well with either of the DBS profiles. There are regions of good correlation (3.59d, 3.60e) and also heights where there is very little agreement (3.57d, 3.58d). It is interesting to note the region in figure 3.60d where the FCAW flux has opposite sign to the DBS fluxes. Although it is possible that the velocities are of opposite sign, figure 3.50 shows that this is not the case.

Also of interest are the large values (spikes) near the tropopause. It has been shown that for figure 3.57d this is due to the filtering procedure upon inadequate

data and since the acceptance criteria produce the same number of zonal and meridional values it is very probable that the spike in 3.57e is also due to the same process. In addition, comparison of the momentum fluxes of figures 3.58-3.59 with the corresponding velocity plots shows that at $\approx 10 - 12$km there are again regions of very sparse data and it is not unreasonable to assume that the sharp changes in momentum flux at these heights are due to the same mechanism as those of figure 3.57. It is difficult, however, to explain the large variations about 13km in both the FCAW and DBS profiles in figure 3.59 and in the FCAW profiles in figure 3.60 near 11km in this fashion. Here, inspection of u and v reveals large random temporal variations at these heights. Hence although the velocities and momentum fluxes are numerically consistent it is unlikely that either are physically meaningful.

By comparing the wind velocities over the observing period with the momentum flux profiles it possible to asses whether the latter are physically reasonable. The vertical gradient of the momentum flux represents a forcing term in the dynamical equations [e.g. Andrews et al., 1987] and hence, assuming the horizontal gradients in wind are negligible, a large change in the profiles should produce a corresponding systematic temporal variation in the wind. If this is not the case then the physical significance of the momentum flux values must be questioned. Examples of physically consistent profiles are the regions if small momentum flux in figure 3.59 which correspond, as expected with relatively constant winds. The difference between the large gradient of DBS momentum flux and the small FCAW flux in figure 3.57e can also be explained as the DBS meridional winds show a large temporal variation while the FCA winds do not. Thus, in this case at least, the observed difference in momentum flux is geophysical in origin rather than due to actual differences between the techniques.

Another method of removing short period components is by time averaging. This has been used by Eckermann and Vincent [1993] analysing tropospheric fluxes using an FCAW technique. The data were averaged in 15 minute blocks prior to the momentum flux analysis. As the DBS experiments were of 50 minute duration an 11-minute average was selected, giving a maximum of 4 points per height bin. Figure 3.61 show profiles using averages of 12 DBS runs (11.7 min) and 25 FCA runs (10.9 min) again applying 4 height binning. The profiles have the same general form as the corresponding graphs in figures 3.57-3.60, e.g. figures 3.60d and 3.61g,

and also exhibit fewer of the large spikes near 10km. This latter feature is probably due to the 11 minute averaging being less susceptible to the difficulties suffered by the filtering procedure in figure 3.56b. The spikes still visible in the FCAW profiles of figures 3.61g and h are due to the large fluctuations in velocity as noted earlier.

Based on such a small number of comparisons it is difficult to determine the level of agreement between FCAW and DBS momentum fluxes. The results suggest that the measurement of momentum fluxes of periods less than one hour is a non-trivial task. There is evidence, however, that the FCAW and DBS fluxes do agree occasionally and also that some of the differences may be geophysical in origin. The symmetric-beam and 5-beam profiles display good agreement in most cases. It would be desirable to make further comparisons of the three methods, particularly between the FCAW and either of the DBS techniques, based on several days data rather than the hourly sets presented here. Ideally such a data set would have a faster rate of switching between the FCA and DBS experiments and, as much as is practicable, identical configurations. It would then be possible to study in more detail the operation of the filtering and time averaging techniques and also to develop procedures for studying various frequency bands of momentum fluxes. Unfortunately such a data set was not available at the time of writing.

3.5.4 Conclusion

Momentum flux measurements have been made by combining the FCA horizontal winds with vertical winds calculated using the phase slopes of the correlation functions. These were compared with momentum fluxes calculated from the DBS data using the symmetric-beam method of Vincent and Reid [1983] and the 'five-beam' method of Worthington and Thomas [1996]. It was found that on the short timescales available here the SA method showed only moderate agreement with the two DBS techniques, which had good agreement with each other. It would be desirable to obtain more data to enable comparisons of momentum fluxes on longer timescales, however this was not possible at the time of writing. Thus, while the method of FCAW shows potential for the measurement of momentum flux profiles it is not possible, in the absence of further data, to draw firm conclusions about the agreement between this technique and the symmetric-beam or 5-beam methods on timescales longer than one hour. As discussed in section 4.4 it is desirable to be able

to make measurements of the sub-hour fluxes using the Canterbury VHF radar and thus it seems likely that some beam-swinging method will be needed. Although the Canterbury system will operate primarily in FCA mode proposed modifications to the transmitting array are described in section 4.4 to allow the radar to operate in a DBS-like fashion.

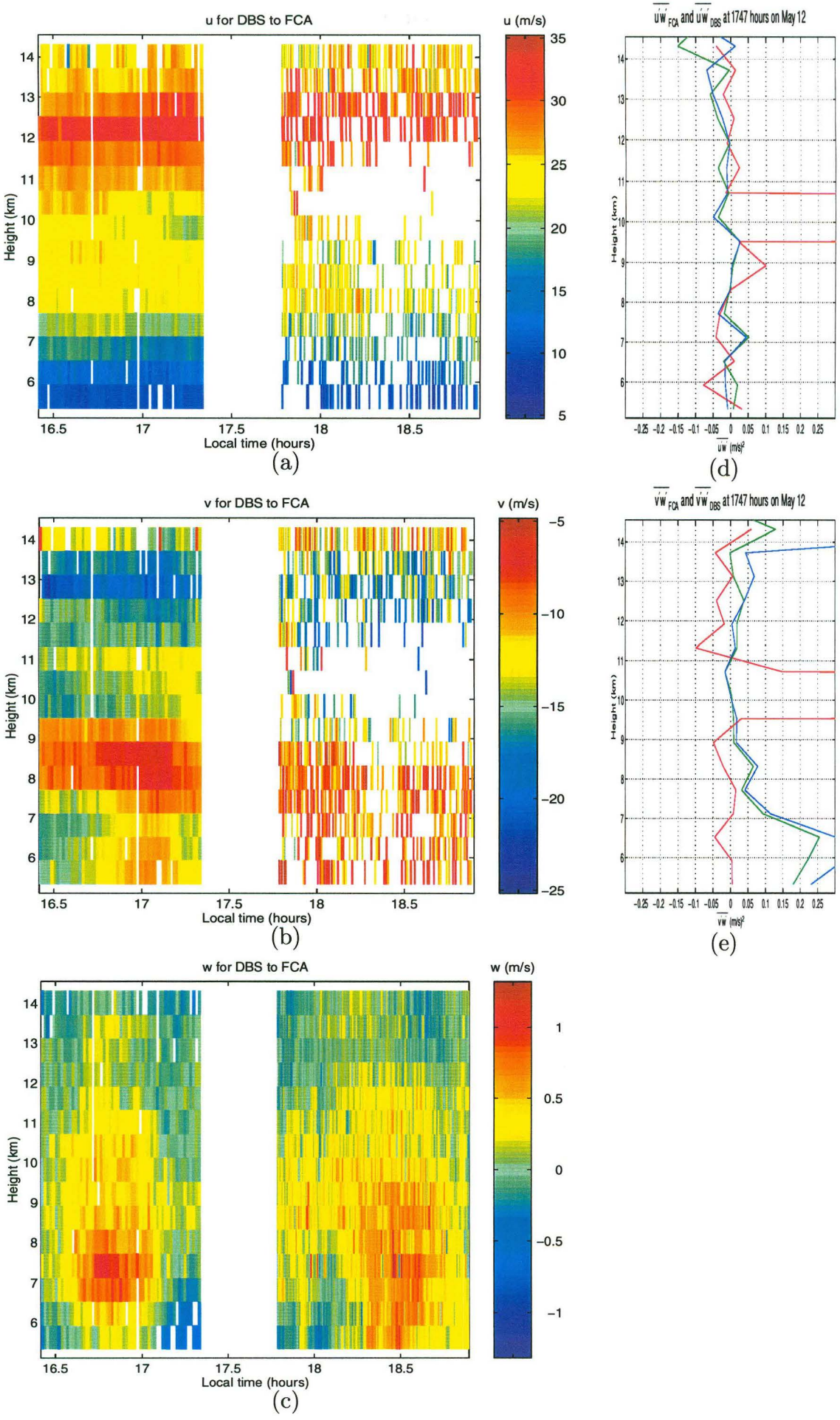

Figure 3.57. Profiles of hourly momentum flux from experiment 1 using the filtering procedure described in the text. Height-time plots of u, v and w are shown for comparison. The three lines show FCAW (red), 5-beam (green) and symmetric-beam (blue) methods.

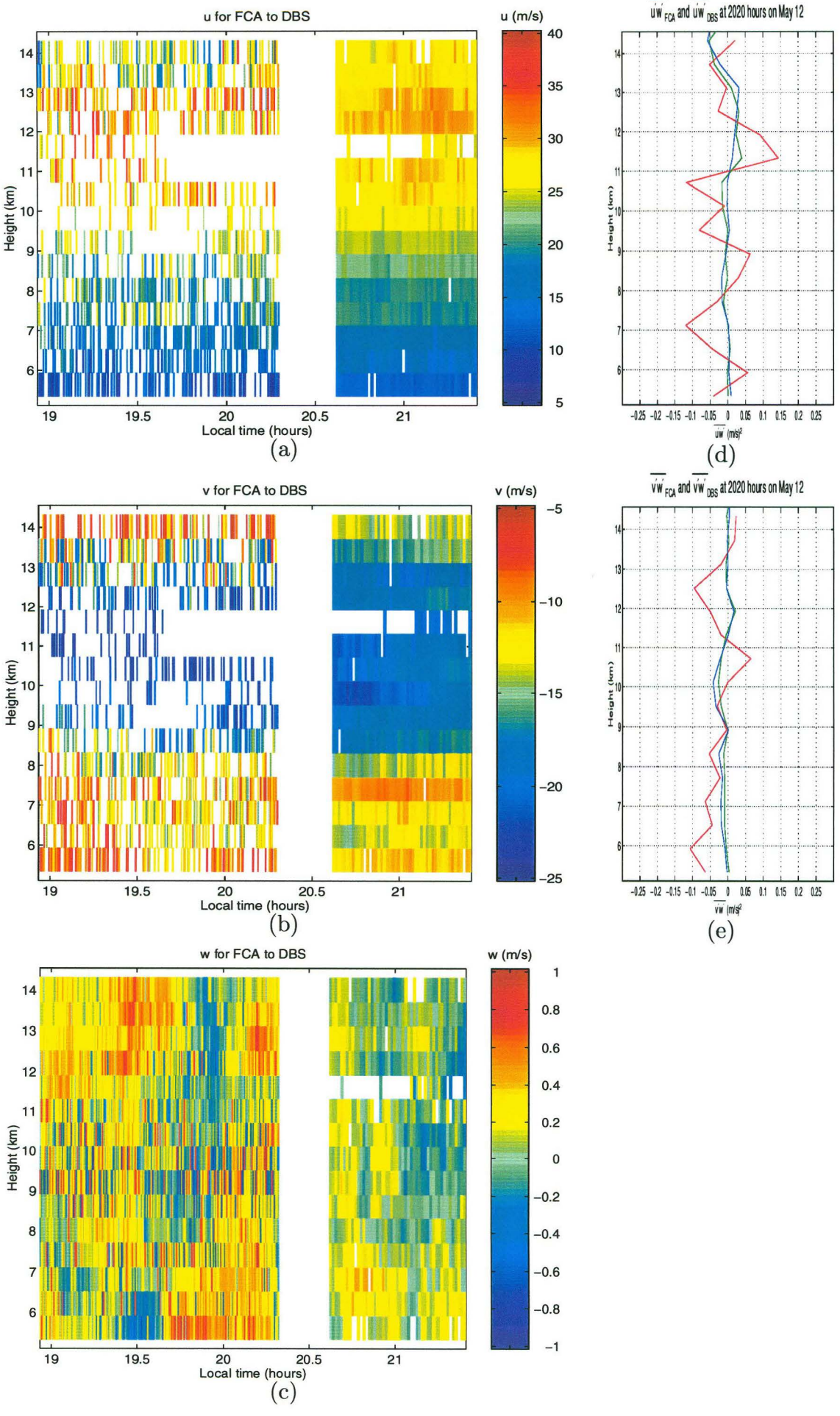

Figure 3.58. Profiles of hourly momentum flux from experiment 2 using the filtering procedure described in the text. Height-time plots of u, v and w are shown for comparison. The three lines show FCAW (red), 5-beam (green) and symmetric-beam (blue) methods.

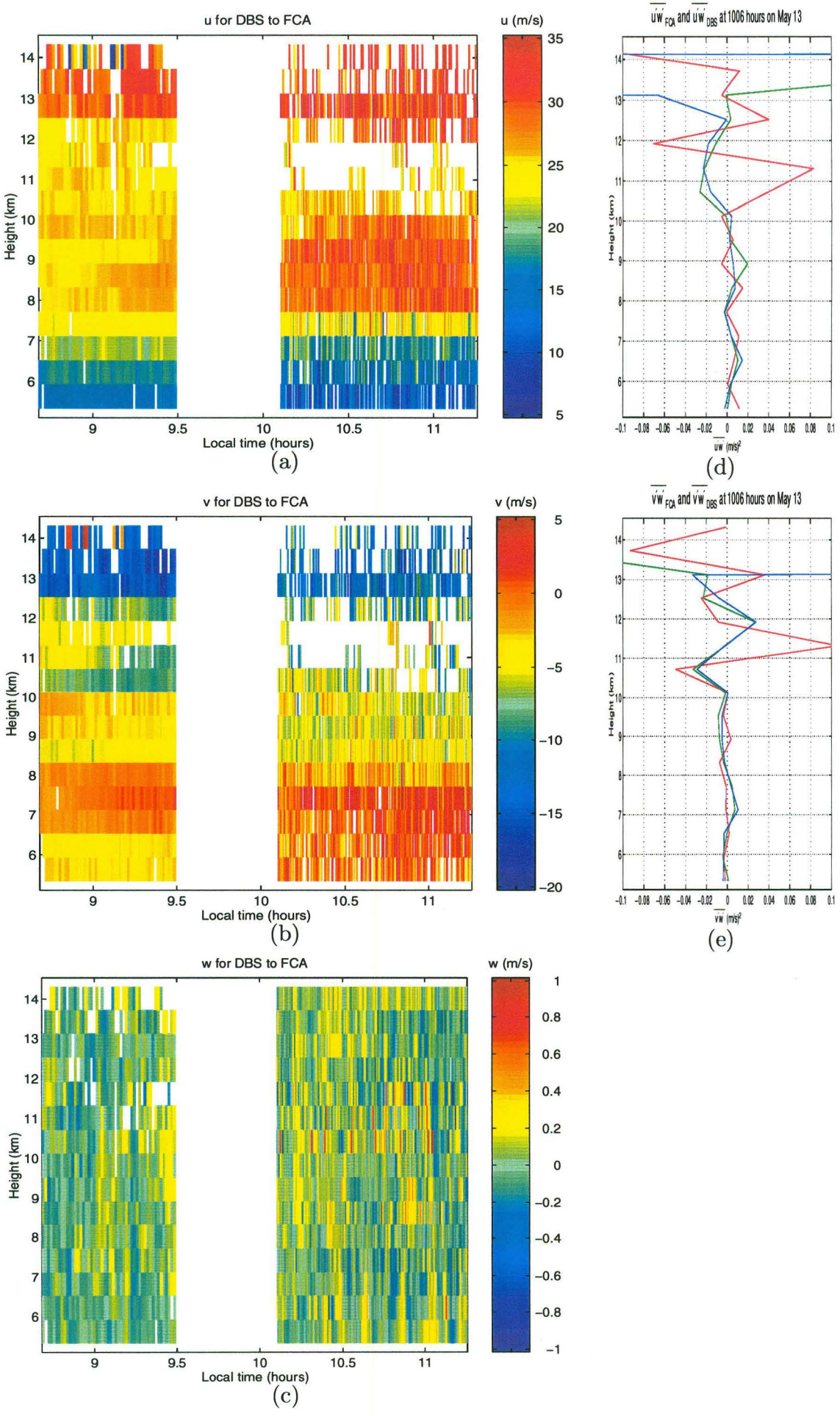

Figure 3.59. Profiles of hourly momentum flux from experiment 3 using the filtering procedure described in the text. Height-time plots of u, v and w are shown for comparison. The three lines show FCAW (red), 5-beam (green) and symmetric-beam (blue) methods.

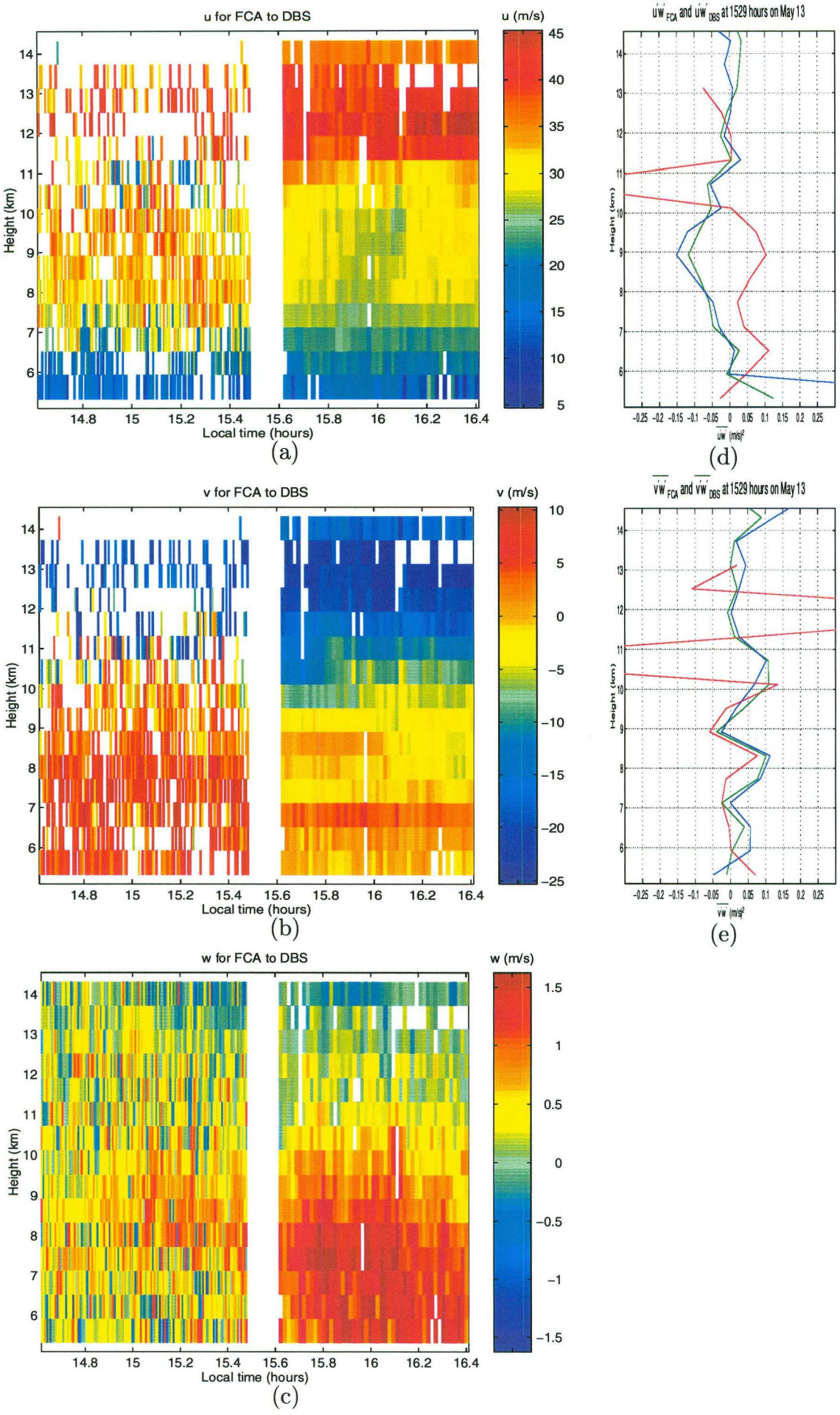

Figure 3.60. Profiles of hourly momentum flux from experiment 6 using the filtering procedure described in the text. Height-time plots of u, v and w are shown for comparison. The three lines show FCAW (red), 5-beam (green) and symmetric-beam (blue) methods.

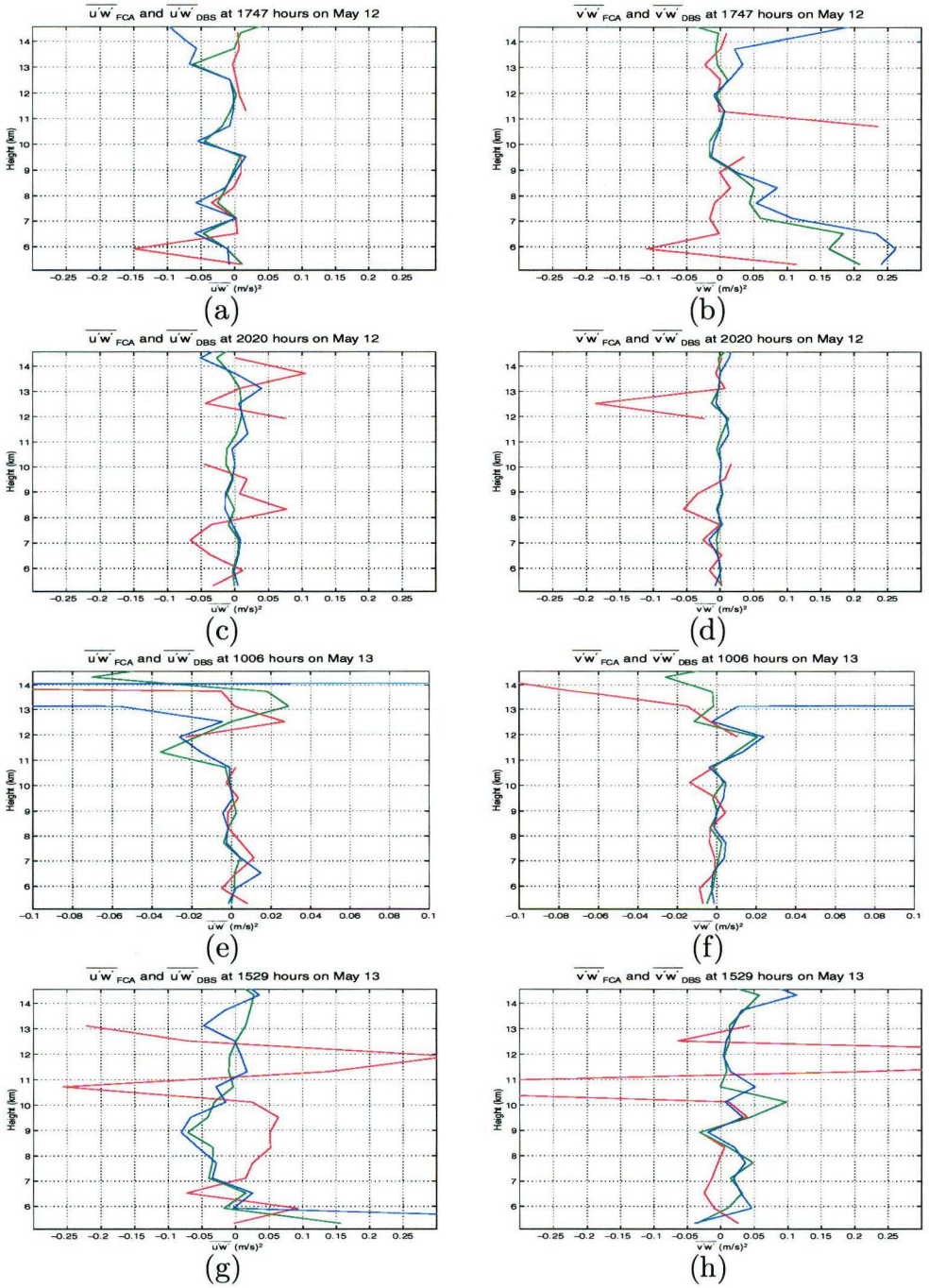

Figure 3.61. Profiles of hourly momentum fluxes using the time averaging procedure described in the text. The three lines show FCAW (red), 5-beam (green) and symmetric-beam (blue) methods.

Chapter 4
Canterbury VHF radar design

4.1 Introduction

This chapter will present work done during the course of this thesis on several aspects of the Canterbury University Atmospheric Radar Development (CUSTARD). Section 4.2 describes the operation of the radar controller and integrating analogue-to-digital converter hardware. Section 4.3 discusses the radar transmitting antenna array and outlines a proposal for testing the pointing angle using stellar radio sources. Finally, section 4.4 describes modifications to the antenna system to provide an alternative method of wind measurement to FCA.

4.2 Operation of an 8-channel integrating analogue-to-digital converter

An important part of the radar system is the ability to transfer the analogue data, consisting of a continuous range of values, from the receivers to the computer which performs the data analysis. Since computers store data in digital format, i.e. data may only have discrete values, some form of conversion will be needed for each of the channels of data to be analysed. For a radar with four quadrature receivers there will be eight channels; four 'in-phase' and four 'quadrature' channels. For an explanation of these terms see 1.3.1.2.

As discussed in section 1.3.2.1 it is desirable to perform coherent integration on the data. This involves the summation of consecutive radar echoes to improve the signal-to-noise ratio. Due to the rate of data acquisition this is best achieved using dedicated electronic hardware rather than the analysis software. Part of this thesis involved the extensive analysis of an eight-channel integrating analogue-to-digital (A/D) converter designed for use in a VHF radar under development at the University of Canterbury. In addition, software has been developed in both PASCAL and FORTRAN 77 to allow the operation of the A/D converter to be tested using standard pulse generators. The A/D converter was designed and constructed by Mr. Geoff Graham and Mr. Ross Ritchie of the electronics workshop of the Physics

and Astronomy department. The remainder of this section describes the operation of the integrating A/D converter, with particular reference to the digital hardware. Information on the actual digital components discussed may be found in data sheets or in any standard electronics text [e.g. Horowitz and Hill, 1989].

The A/D converter consists of eight identical integrating A/D boards and one radar controller (RC) board which is interfaced to the computer. The operation is as follows: The controlling computer specifies to the radar controller the number of height ranges, height resolution and number of coherent integrations to be used. The RC board then coordinates the required data collection and the results from the RAM chips on each board are in turn transferred to the computer by direct memory access (DMA). Schematics of the A/D and RC boards are shown in figures 4.1 and 4.2.

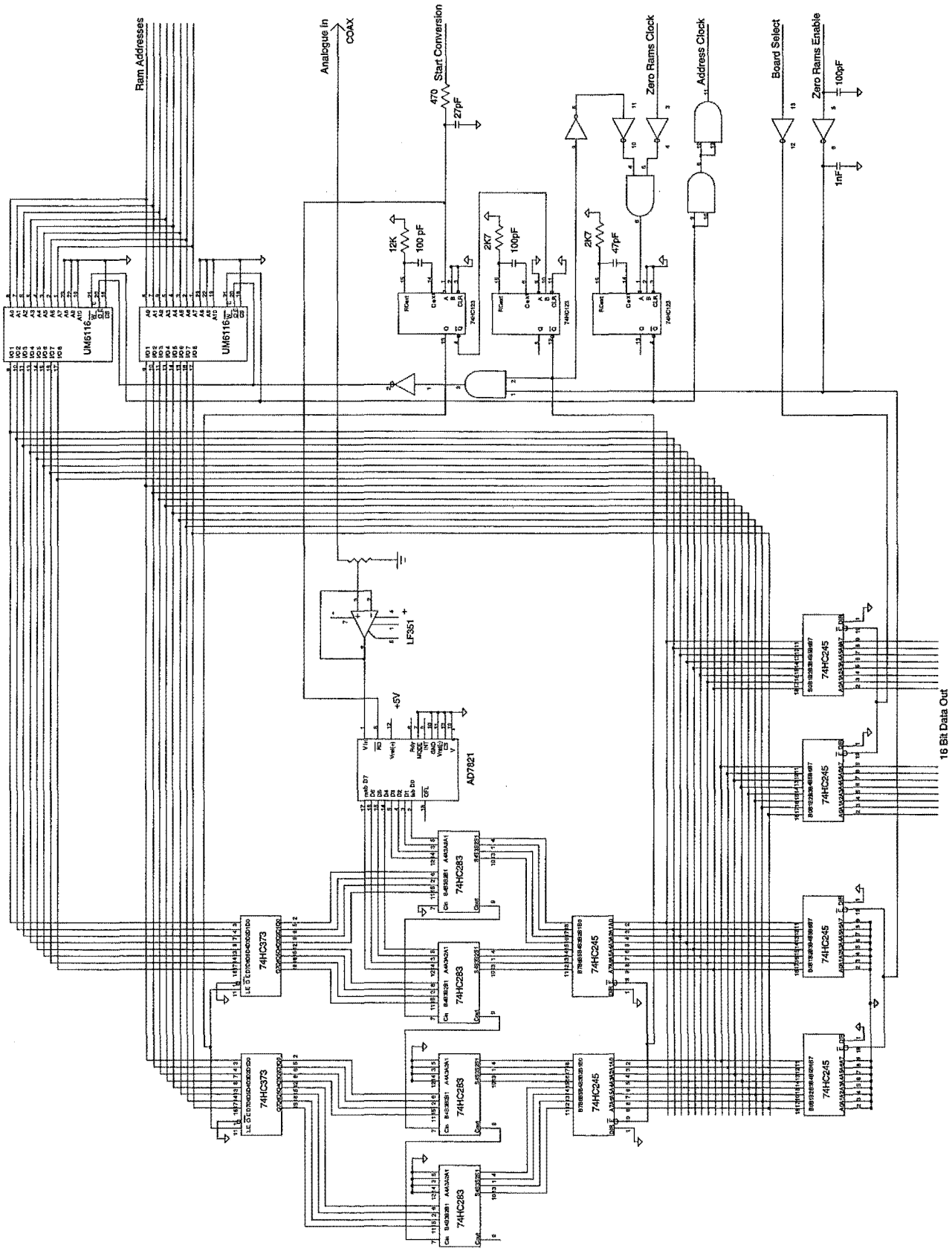

Figure 4.1. Integrating A/D board schematic.

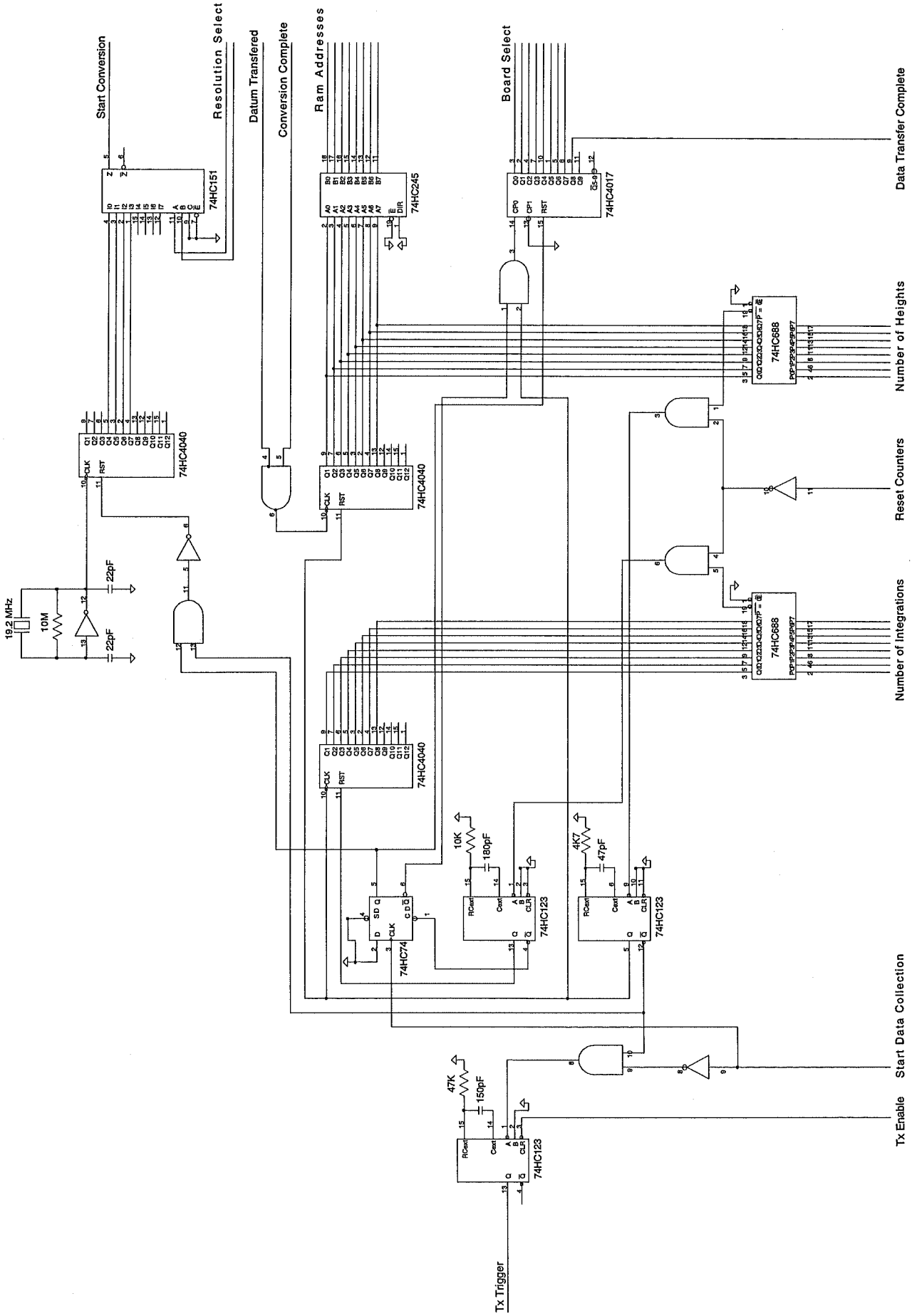

Figure 4.2. Radar controller board schematic.

4.2.1 System control

The RC board receives its instructions from the computer and must electronically implement the required functions. As mentioned above, the main operational parameters are the height resolution, number of heights and number of coherent integration. Although the electronics in figure 4.2 are complex they may be broken down into components that perform the various functions.

4.2.1.1 Height resolution

To provide a regularly spaced set of height data it is necessary for the RC board to produce a repetitive series of pulses to the A/D boards initiating sampling. The frequency of these pulses must be adjustable to allow for varying height resolutions. This is achieved through the circuit shown in figure 4.3. The oscillator circuit in the left of the figure produces a continuous series of pulses at 19.2MHz. This pulse train is used to drive a binary ripple counter (74HC4040 chip) the outputs of which are binary fractions of the input, i.e. $Q_i = \frac{input}{2^i}$ where Q_i are the output pin designators. Thus the available height resolutions for the Canterbury VHF radar are 500m and 1000m which correspond to sampling periods of $3\frac{1}{3}$ and $2\frac{2}{3}$ μs respectively.

A height resolution of 250m is also available although at present this would require a software workaround to fix a hardware bug in the integrator. This problem was discovered by the author during an analysis of the A/D converter based purely on the circuits of figures 4.1 and 4.2 and information from technical data-sheets and was subsequently shown to be present in the actual operation of the device. In brief, the extremely fast pulse rate at this range resolution causes the range address counter to be left in an incorrect state prior to the data being read into the computer. This causes the first range bin on channel one to have zero data and the second range bin contains the data from range one, the third range bin contains the data from range two and so on. It would be a straightforward task to then use software to shift all the data by one range index once it had been read into the computer.

The ripple counter can be reset via pin 11 at the start of data collection, at the end of each set of height samples and at the end of sampling prior to data transfer to the computer. To allow selection of various height resolutions a 8-input multiplexer

(74HC151 chip) is used to select one of the divided outputs from the ripple counter. This selection is under computer control.

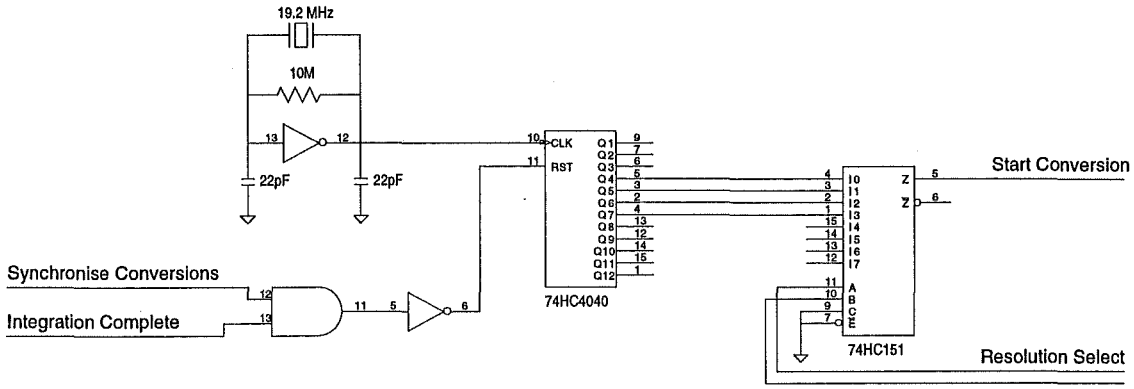

Figure 4.3. The timing circuit of the radar controller which allows the selection of a height resolution for data sampling. The height resolution is controlled by varying the frequency of conversions.

4.2.1.2 Number of heights

To allow the A/D cards to perform a given number of conversions, and hence a given number of height samples, it is necessary to count the number of conversions and compare this with the number requested. When these values are equal the specified number of conversions has been performed and appropriate action can be taken. This is done by the section of the RC board shown in figure 4.4.

Each time a conversion is done one of the A/D cards sends a pulse to the clock pin of a binary ripple counter. The output of this is used, via an 8 bit transceiver, to set the address registers in the ram chips on the A/D cards. The current number of conversions, as an 8 bit binary number, is compared with an 8 bit number from the computer interface using a comparator chip (74HC688) thus allowing a maximum of 256 heights to be sampled. When the values are equal the output pin (19) changes from high to low and this change causes a monostable (74HC123) to generate a pulse which initiates further necessary actions. During data transfer to the computer, after sampling is complete, it is also necessary to access all the memory registers on the ram chips sequentially and this is provided for by having an additional clock input from the computer. To allow for the two possible means of address incrementing, the two clock pulses are merged by a logical AND chip (74HC08) before parsing to the clock pin of the ripple counter.

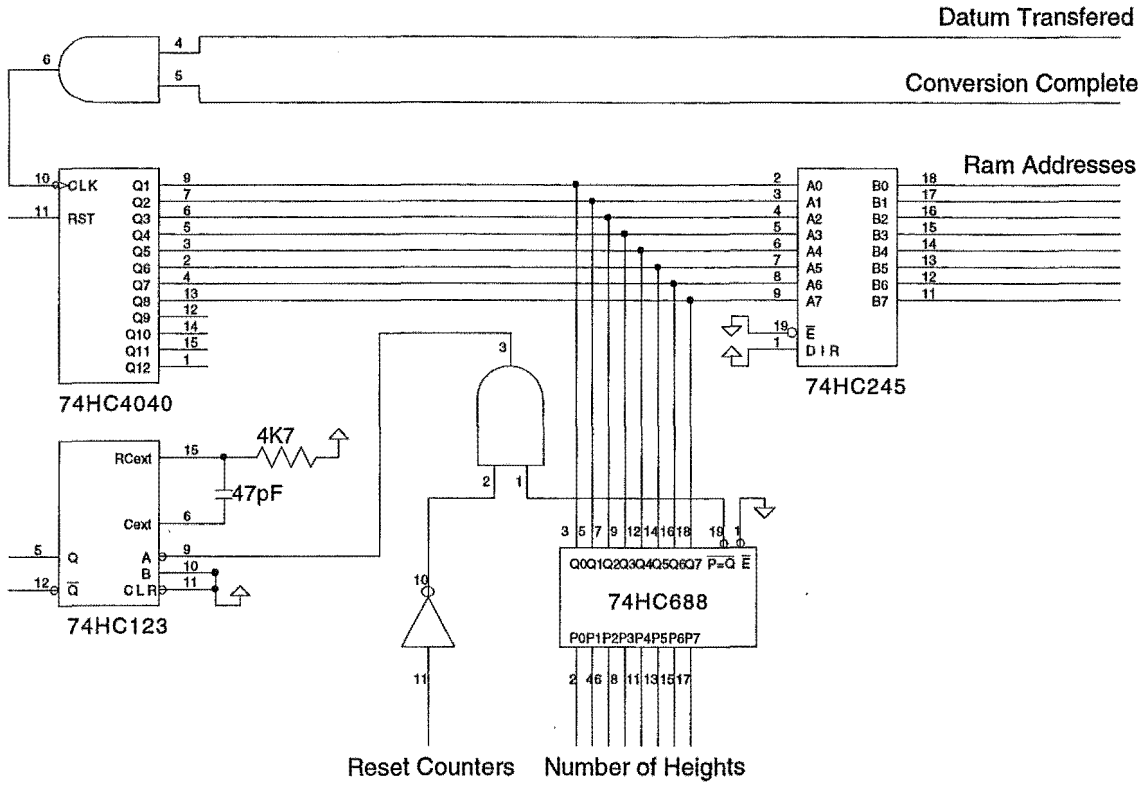

Figure 4.4. The portion of the radar controller used to count the number of conversions performed during one integration.

4.2.1.3 Number of coherent integrations

The circuit used to monitor the number of coherent integrations performed is similar to that used for the number of heights. The 8-bit output of a ripple counter is compared, using a comparator chip, to the value specified via the computer interface. As above, the 8 bits allow a maximum of 256 integrations to be performed. The completion of the required number of conversions, with associated addition of those conversions to previously stored totals, signifies that one coherent integration cycle has occurred and thus the output from the monostable in figure 4.4 is used as the clock input to the integration ripple counter. When the required number of integrations cycles is reached the output pin triggers a monostable as in figure 4.4. The ensemble is shown in figure 4.5.

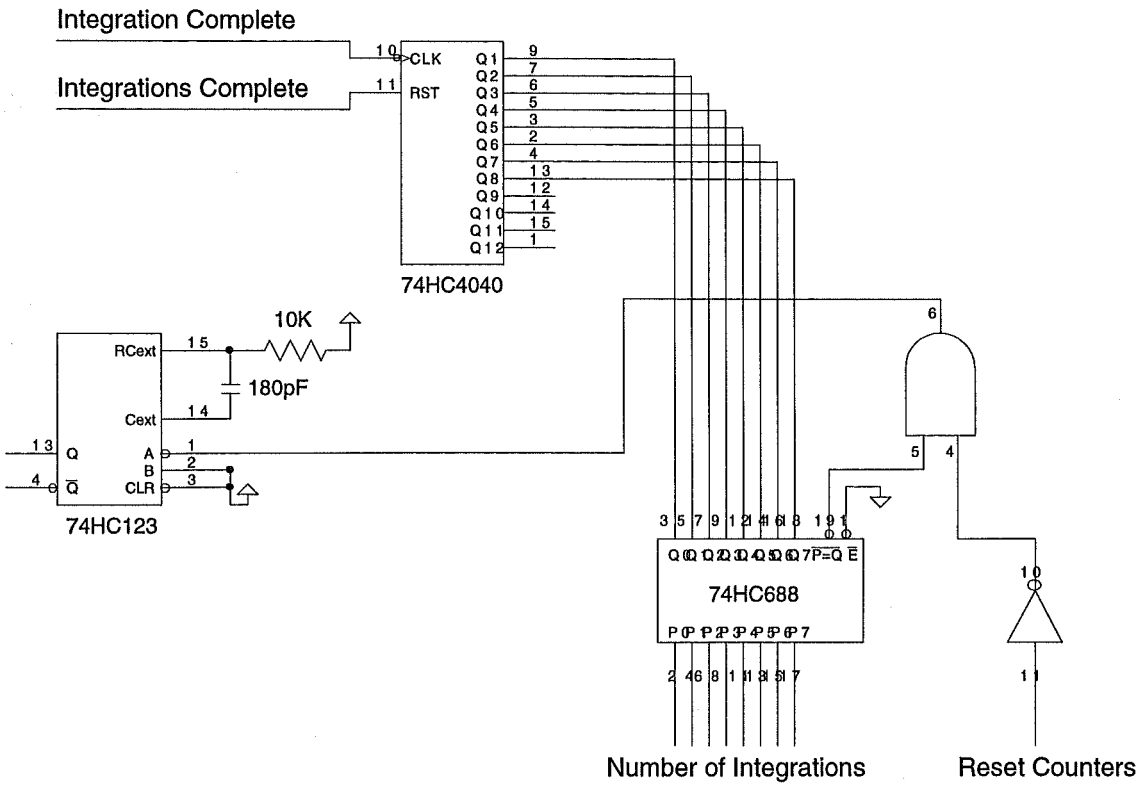

Figure 4.5. The portion of the radar controller that controls the number of coherent integrations performed.

4.2.1.4 Transmission control and data transfer

In addition to the functions described above there are other tasks which the radar controller must perform. It is advisable to signal the transmitter to pulse in synchrony with the start of conversion. For practical purposes it may be useful to slightly delay transmission relative to the start of sampling. This allows the 'true' height of a given A/D sample to be determined. These pulses, which are also useful when testing the interfacing of the RC board to the computer, are generated by the monostable shown centre-left in figure 4.2.

It is also necessary to be able to select the individual A/D boards during the data transfer to the computer. The results of the coherent integration from 8 A/D boards must be transferred to the computer in some logical fashion. This is done by taking each board in turn and sequentially transferring all the data from that board. Thus the first range datum from the first board, then the second range datum from the first board through to the last range datum from the last board are transferred

to the computer's memory. The board selection is done by a Johnson decade counter chip (74HC4017) which is shown at centre-right in figure 4.2.

4.2.2 The A/D boards

As mentioned in section 4.2 there are eight A/D boards operating in parallel; one such card is shown in figure 4.1. Each of these boards has the ability to perform the required number of A/D conversions and integrations and store the results prior to transfer to the computer. During the data-collection process data are stored in two 8-bit RAM chips (UM-6116) addressed in parallel from the 74HC245 of figure 4.2 via a bus. One 16-bit datum is stored between the two chips. Each of the addresses on the RAM chips corresponds to one height datum. The A/D conversion and integration process is identical for all heights.

Following the 'Start Conversion' pulse from the RC board an A/D sample is taken. Simultaneously the 16-bit datum, i.e. the sum of all previous conversions at that height, from the corresponding address on the ram chips is latched. These two quantities are then added and, after a small delay to allow for conversion, the result is transferred via two octal transceiver to the RAM chips. Following this process a pulse is sent back to the RC board to signify that the conversion has been performed and to update the address counter. The various processes are coordinated by pulses from three monostables.

4.2.2.1 Initialising the RAM chips

Prior to the A/D sampling and integration cycle it is necessary for all the RAM chip addresses to be storing the value zero. This is achieved by having two 74HC245 transceivers with their inputs grounded on the A/D board data bus. These can be seen at the lower left of figure 4.1. To zero a given address register a 'Zero Rams Clock' pulse from the computer causes the third monostable (centre right in figure 4.1) to generate a pulse which sets the RAM chips into write-mode, i.e. the addresses may be written to. With the outputs of the transceivers enabled, under computer control, the value written to the address is zero. The monostable output also informs the RC board that a value has been stored and thus the address counter is incremented in preparation for the next 'Zero Rams Clock' pulse.

4.2.2.2 A/D conversion

The A/D conversions are performed by the hardware shown in figure 4.6. The conversion is done by a AD7821 chip operating in unipolar mode, i.e. allowable voltages are in the range 0-5V. Analogue input is buffered through a LF351 operational amplifier and other unipolar voltage ranges may be obtained using a variable resistor voltage divider.

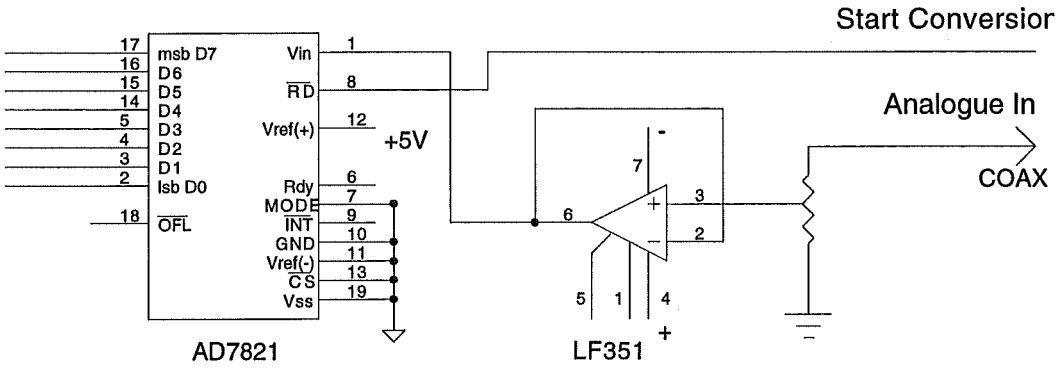

Figure 4.6. The hardware used for the analogue to digital conversion in the 8-channel integrating A/D converter.

4.2.2.3 Integration

When the 'Start Conversion' pulse triggers the first monostable a pulse is generated which causes two 8-bit latches (74HC373) to read a 16-bit datum from the preselected RAM address. This data remains on the latches until the next 'latch enable' pulse. Next a bank of four 4-bit adders (74HC283) perform the binary addition of the 16-bit datum and the 8-bit A/D sample from the current height. For the addition to be correct the carry bit (signifying overflow) from each adder must be passed along to the next highest order addition. Finally, the second monostable, which is triggered from the first monostable to give a small delay, sets the output enable on the two octal transceivers. This puts the new 16-bit datum onto the data bus where it can be re-written onto the RAM chips. The circuit is shown in figure 4.7.

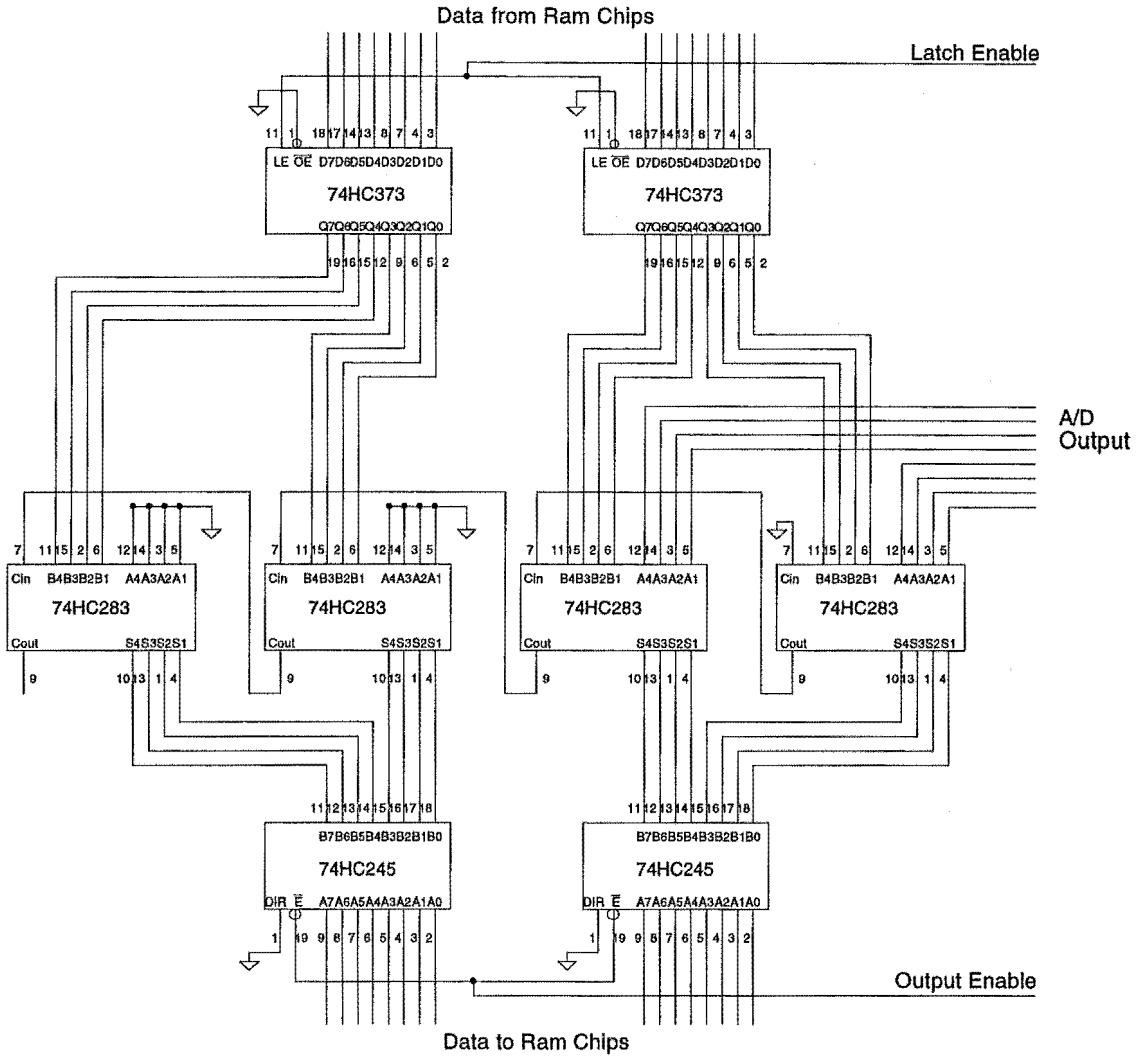

Figure 4.7. The hardware used to perform the coherent integrations in the 8-channel A/D converter.

4.2.3 Conclusion

This section has described the operation of the radar controller and integrating A/D converter that has been designed for the CUSTARD system. The main operational parameters are summarised in table 4.1. As was mentioned previously the height resolution of 250m is, at present, only available through a software workaround to fix a hardware bug in the integrator.

Parameter	Value
Maximun # of ranges	256
Maximum # of coherent integrations	256
Range resolution	250, 500, 1000m
A/D bits	8
A/D chip input range	$0-5$V

Table 4.1. Operational parameters of the CUSTARD integrating A/D converter.

4.3 Reverse radio astronomy

4.3.1 Introduction

In wind-profiling radar systems it is important to know precisely the angular distribution of power from an aerial. This, in turn, provides information on the pointing angle of the beam. When measuring vertical velocities it is assumed that the aerial is pointing vertically. If this is not the case then the measured 'vertical' velocity is, in fact, a radial velocity and corrections are necessary to obtain the true vertical component.

For a large dish aerial the beam pointing angle is readily determined, as it is simply the direction of the dish. For a fixed aerial array, commonly used with ST radars, the direction of the beam is controlled by adjusting the phase differences between the individual elements. In reverse radio astronomy point sources, or 'radio stars', are used to illuminate the aerial ensemble; which operates as a radio diffraction grating as in optics, and allow the determination of the angular power distribution [e.g. Guidice and Castelli, 1971]. Reverse radio astronomy has been used by Vincent et al. [1986] to measure the transmitting aerial pattern of the University of Adelaide VHF radar and by Chezechowsky et al. [1984] on the mobile SOUSY Doppler radar. It is also possible to use other types of radio sources to illuminate the aerials. Riddle [1986] has used the sun to monitor the pointing angle of the Ponape equatorial radar and Sato et al. [1986], using a technique similar to reverse radio astronomy, have used a receiver on board the OHZORA satellite to monitor the pattern of the MU radar during transmission. The MU radar array pattern has also been monitored using the moon as a radar reflector [Fukao et al., 1990].

In this section the theory of phase-switching radio interferometers and their application to the measurement of aerial patterns will be discussed. A overview

of basic astronomy and antenna theory, as relevant to these measurements, will be given. Some useful references on radio astronomy are Ryle [1950; 1952], Pawsey and Bracewell [1955] and Kraus [1966] and, for antenna theory, Wolff [1967], Kraus [1988] and Skolnik [1990]. This work is intended to provide a foundation for the measurement of the polar diagram of the transmitting array of the University of Canterbury ST radar, once the array is completed.

4.3.2 Positional astronomy

To gain some insight into the motion of the radio star across the aerial pattern it will be helpful to briefly discuss positional astronomy. A useful reference on general astronomy is Roy and Clarke [1982]. To an observer on earth stars appear fixed on a sphere of very large radius, centered on the earth, which rotates about the same axis as the earth with an opposite sense of rotation. Thus, an observer at either pole would see all the stars in their hemisphere following circular paths about a fixed point while an observer at the equator would see all the stars rising and setting. An observer at some middle latitude would see some stars rising and setting and some continuously visible; the latter are known as circumpolar stars.

To determine the motion of stellar objects some form of coordinate system is necessary. One which is readily visualised is the equatorial system which corresponds to latitude and longitude on earth. Imagine the earth's rotation is stopped and the 0° longitude meridian is aligned with the first point of Aires. Project the earth's lines of latitude and longitude onto the celestial sphere and then let the earth rotate. Now stars on the sphere have a unique 'latitude', known as declination (δ), and longitude, known as right ascension (RA). Declination is measured from 0 to $-90°$ in the southern hemisphere and right ascension is measured eastwards around the celestial sphere. During the course of a year the sun progresses eastwards around the celestial sphere on a path known as the ecliptic; the intersection of this path and the celestial 'equator' is the first point of Aires.

Another coordinate, related to RA, is hour angle (HA) which is measured westward from the observer's meridian. Thus, a star passing overhead, or through the zenith, has $HA = 0°$ and this hour angle increases as the star rotates. Due to

the apparent 24 hour rotation period of the stars it is convenient to express both HA and RA in units of time where 360° = 24hrs.

4.3.2.1 Astronomical time systems

To facilitate calculation of the time of rising and setting of a particular radio star it is first necessary to discuss some methods of measuring time. Measures of time may be based on either the diurnal motion of the sun, solar time, or on that of the stars, sidereal time. A 'day', the time between successive passages overhead of the sun or a star, is equivalent to a change in hour angle of 24hrs. However one solar day is approximately 4 minutes longer than a sidereal day as the earth must rotate by more than 360° for the sun to pass overhead again.

At the vernal equinox (approximately March 21) the local solar, t_{solar}, and sidereal, $t_{sidereal}$, times are exactly 12hrs different. Thus, approximately,

$$t_{sidereal} = t_{solar} + 12 + \frac{4}{60} N_{vernal} \tag{4.1}$$

where $t_{sidereal}$ and t_{solar} are in hours and N_{vernal} is the number of days since the vernal equinox.

Local sidereal time, $t_{sidereal}$ is also equal to the hour angle of the first point of Aires. Thus, since RA is defined from this point, the sidereal time that a star is at a given position is,

$$t_{sidereal} = RA + HA \tag{4.2}$$

Thus, given the hour angle and right ascension of a star it is possible to calculate the local solar time that the star is in that position.

To determine the hour angle at the setting of a southern hemisphere star consider the diagram of figure 4.8. By applying spherical trigonometry to triangle ZQX it can be shown that,

$$\cos \angle ZQX = \cos ZQ \cos QX + \sin ZQ \sin QX \cos HA$$

Substituting values gives

$$\cos \pi = \cos \pi - \phi \cos \pi - \delta + \sin \pi - \phi \sin \pi - \delta \cos HA$$

and thus, by rearranging,

$$\cos HA = -\tan\phi \tan\delta \tag{4.3}$$

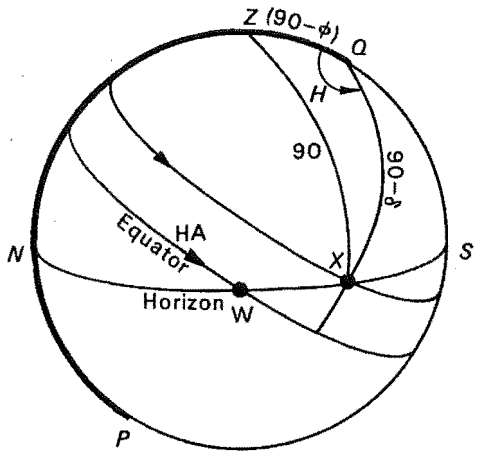

Figure 4.8. Diurnal motion of a southern hemisphere star. A star with declination δ°S is shown setting at X with an hour angle H as seen by an observer at lattitude ϕ°S.

Equation (4.3) gives the hour angle of a star with declination ϕ at setting for an observer at a latitude δ. It can be shown by the same argument that the hour angle of the star at rising is $HA = 360° - h$ where

$$\cos h = -\tan\phi \tan\delta \tag{4.4}$$

The rising or setting time is found by first using equation (4.4) or (4.3) to find the hour angle at rising or setting. The sidereal time can then be found from equation (4.2), and the solar time from equation (4.1).

4.3.3 Antenna theory

Before discussing the operation of the antennae as a radio interferometer it will be useful to consider the calculation of antenna patterns. Firstly some simple antenna systems will be discussed, followed by a more complex planar array similar to that intended for the University of Canterbury VHF radar.

4.3.3.1 Simple antenna systems

Consider firstly the case of a one dimensional antenna. The aperture distribution, $E(x)$, and the far field (Fraunhofer) distribution, $E(\theta)$, generated by that

aperture distribution are Fourier transforms of each other [Kraus, 1988]. Thus a radio version of Young's [1807] double slit experiment, with aperture width d and separation f, could be represented by

$$E(x) = \begin{cases} h & \left|x \pm \frac{f}{2}\right| < \frac{d}{2} \\ 0 & \left|x \pm \frac{f}{2}\right| > \frac{d}{2} \end{cases}$$

Thus, taking the transform,

$$\begin{aligned} E(\theta) &= \frac{1}{2\pi}\int_{-\infty}^{\infty} E(x)e^{-i2\pi\frac{x}{\lambda}\sin\theta}dx \\ &= \frac{dh}{2\pi}\frac{\sin\alpha}{\alpha}\cos\beta \end{aligned} \tag{4.5}$$

where $\alpha = \frac{dk}{2}\sin\theta$, $\beta = \frac{fk}{2}\sin\theta$ and $k = \frac{2\pi}{\lambda}$. This has the same form as the optical angular distribution given in elementary texts, e.g. Halliday et al. [1993]. Considering the situation where the apertures have different widths, a and b say, it can be shown that

$$\mathrm{Re}\left(E(\theta)\right) = \frac{h}{\pi k \sin\theta}\left(\sin\left(\frac{ka}{2}\sin\theta\right) + \sin\left(\frac{kb}{2}\sin\theta\right)\right)\cos\beta$$

Although a real antenna array is more complex than the simple cases discussed above, the Fourier relation is still applicable. The angular power distribution of an array can be obtained by multiplying the angular pattern of an array of point sources with the same geometry as the actual array by the pattern of a single array element. This technique, known as 'pattern multiplication', is covered in more detail in texts such as Kraus [1988] and will now be discussed with reference to two common arrangements.

A colinear array is a line of half-wave dipoles where the dipole axes are parallel to the array axis. Using pattern multiplication, the array pattern is the product of the angular distribution due to an single line of point sources and the pattern from a single half-wave dipole. From antenna theory the field for a line of n point sources is

$$E_{array}(\theta) = \frac{\sin\left(nkd\cos\frac{\theta}{2}\right)}{\sin\left(kd\cos\frac{\theta}{2}\right)} \tag{4.6}$$

where θ is the angle from the array axis and d is the source spacing. The field from a half-wave dipole is

$$E_{element}(\theta) = \frac{\cos\left(\frac{\pi}{2}\cos\theta\right)}{\sin\theta}$$

and thus the field from the total array is

$$E(\theta) = \frac{\sin\left(nkd\cos\frac{\theta}{2}\right)}{\sin\left(kd\cos\frac{\theta}{2}\right)}\frac{\cos\left(\frac{\pi}{2}\cos\theta\right)}{\sin\theta}$$

A broadside array, on the other hand, is a line of half-wave dipoles with the dipole axes perpendicular to the array axis. As before, the total pattern is the product of the 'point source' array and the element pattern. Now, however, the variation in field strength is not solely parallel to the array axis. The field from the line of point sources is still given by equation (4.6) but the dipole field is now

$$E_{element}(\phi) = \frac{\cos\left(\frac{\pi}{2}\cos\phi\right)}{\sin\phi}$$

where ϕ is the angle perpendicular to the array axis. Thus the total array pattern is

$$E(\theta) = \frac{\sin\left(nkd\cos\frac{\theta}{2}\right)}{\sin\left(kd\cos\frac{\theta}{2}\right)}\frac{\cos\left(\frac{\pi}{2}\cos\phi\right)}{\sin\phi}$$

which has variation in planes both parallel to and perpendicular to the array axis.

4.3.3.2 Two dimensional arrays

Although one-dimensional arrays of elements are used, e.g. the Advanced Meteor Orbit Radar (AMOR) at the University of Canterbury, it is more common for ST antennae to be two-dimensional arrays. The analysis of these arrays is more complex than the approach used above, although it is still possible to use pattern multiplication to obtain the total array pattern. First, however, the angular pattern of a two-dimensional array of point sources must be found. The method followed here is due to Wolff [1967]. The spherical coordinates pertinent to an analysis of a two-dimensional array in the yz plane are shown in figure 4.9.

From Maxwell's equations the far field at some point (r, θ, ϕ) due to the nth radiating element of a linear array along the z axis is

$$E_n(\theta, \phi) = f_n(\theta, \phi)\frac{e^{-ikr_n}}{r}$$

where r_n is the distance to the point from the element and f_n is the pattern of the nth element. Since r_n is large it can be approximated by $r_n \approx r - ns_z\cos\phi$ where s_z is the spacing of the elements. Assume that the elements have identical angular patterns $f_n = a_n E_{element}(\theta, \phi)$ where a_n is the complex current in the nth element

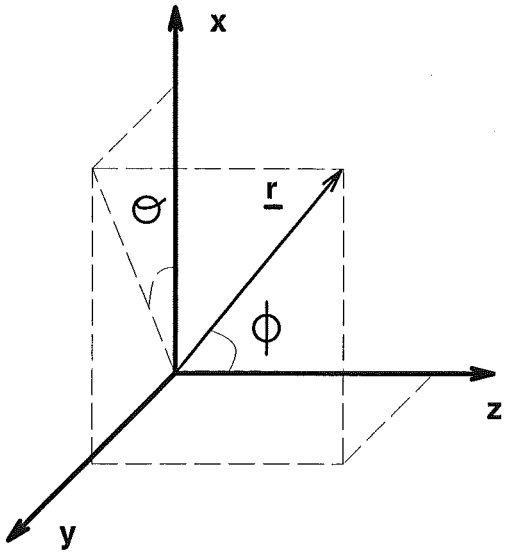

Figure 4.9. Geometry of spherical coordinates used in the analysis of a planar array.

and $E_{element}$ is the element pattern. Then, using superposition, the far field E_z of the total linear array is

$$E_z(\theta,\phi) = \frac{e^{-ikr}}{r} E_{element}(\theta,\phi) \sum_{n=-N}^{N} a_n e^{iknz_z \cos\phi} \tag{4.7}$$

Equation (4.7) can be used to construct the field equation for a two dimensional array by considering a linear array of elements along the y axis, where each element, rather than being a point source, is now a linear array parallel to the z axis. For the array of elements along the y axis the field f, neglecting variation in the r direction, is given by

$$f(\phi,\beta) = \sum_{m=-M}^{M} f_m(\phi,\beta)\, e^{ikms_y \cos\beta} \tag{4.8}$$

where s_y is the spacing between elements in the y direction and β is the angle from the y axis to the far field point. Note that $\cos\beta = \sin\theta \sin\phi$ from spherical coordinates. The coefficients f_m which express the radiation pattern of each element are, from equation (4.7) and neglecting variation in r,

$$f_m(\phi,\beta) = E_{element}(\theta,\phi) \sum_{n=-N}^{N} a_{mn} e^{iknz_z \cos\phi} \tag{4.9}$$

since each element is now a linear array in the z direction. Combining equations (4.8) and (4.9) gives

$$f(\theta,\phi) = E_{element}(\theta,\phi) \sum_{m=-M}^{M} \sum_{n=-N}^{N} a_{mn} e^{ik(ns_z \cos\phi + ms_y \sin\theta \sin\phi)} \tag{4.10}$$

for a two dimensional array of equal elements.

An example of the use of equation (4.10) is the calculation of the theoretical antenna pattern of the University of Canterbury VHF radar transmitting array designed by Dr. R. Bennett. A diagram of the array showing the position of the elements is shown in figure 4.10.

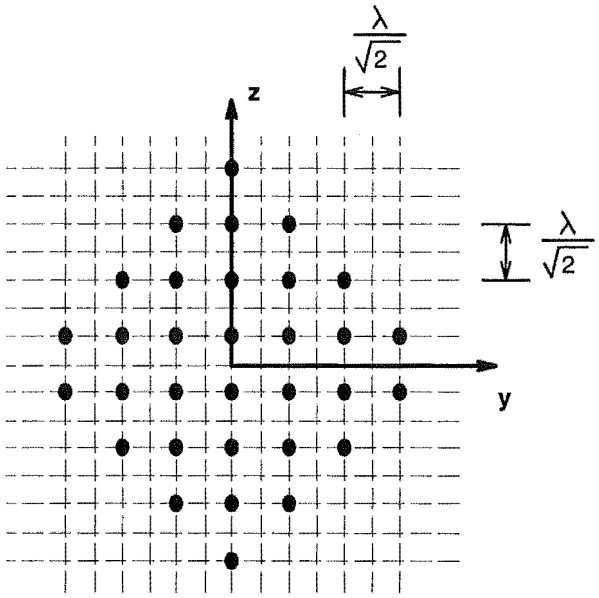

Figure 4.10. Transmitting array geometry for the University of Canterbury VHF radar. Each dot represents one array element which will be half-wave dipoles.

Before applying equation (4.10) it is necessary to consider the effect of re-radiation by the ground. The method of images used here assumes a perfectly conducting ground plane and substitutes an image of the real antenna for the ground. This approximation means that all the power radiated below the array is reflected producing a unidirectional polar diagram. It is also necessary to determine the polar pattern of the array elements. In this case the elements are half wave dipoles and hence the polar diagram is given by

$$E_{element} = \frac{\cos\left(\frac{\pi}{2}\sin\theta\sin\phi\right)}{\sin\left(\cos^{-1}\left(\sin\theta\sin\phi\right)\right)}$$

for elements along the y axis or

$$E_{element} = \frac{\cos\left(\frac{\pi}{2}\cos\phi\right)}{\sin\phi}$$

for elements along the z axis. Putting all this together gives, after some manipulation,

$$E(\theta,\phi) = 2E_{element}(\theta,\phi)\sum_{n=1}^{4}\sum_{m=-(4-n)}^{4-n}\cos\left(kd\left((2n-1)\cos\phi + 2m\sin\theta\sin\phi\right)\right) \tag{4.11}$$

where $d = \frac{\lambda}{2\sqrt{2}}$, for the total polar diagram.

Figure 4.11 shows vertical polar diagrams along the y and z axes and in the yz plane for the case where the array elements are point sources, i.e. $E_{element}(\theta,\phi) = 1$. If half-wave dipoles are used, as is intended, the polar diagram is not modified substantially; the major difference being in the size of some of the side lobes. This can be seen in figure 4.12 which shows corresponding polar diagrams to those in figure 4.11 for the case of half-wave dipoles aligned along the y axis. In the horizontal plane the transmitted energy is reduced in a direction along the dipole axis, as shown in figure 4.12a, allowing the array to be rotated to reduce radiation in a particular direction. This could be used to reduce backscatter from nearby cliffs or to reduce radio interference to dwellings in the vicinity of the array. In the vertical planes the major effect of using dipole elements is the reduction of sidelobes along the dipole axis as shown in figure 4.12b. Due to the toroidal shape of the dipole field there is negligible difference in the sidelobes perpendicular to the dipole axis, i.e. along the z axis, as can be seen in figure 4.12c.

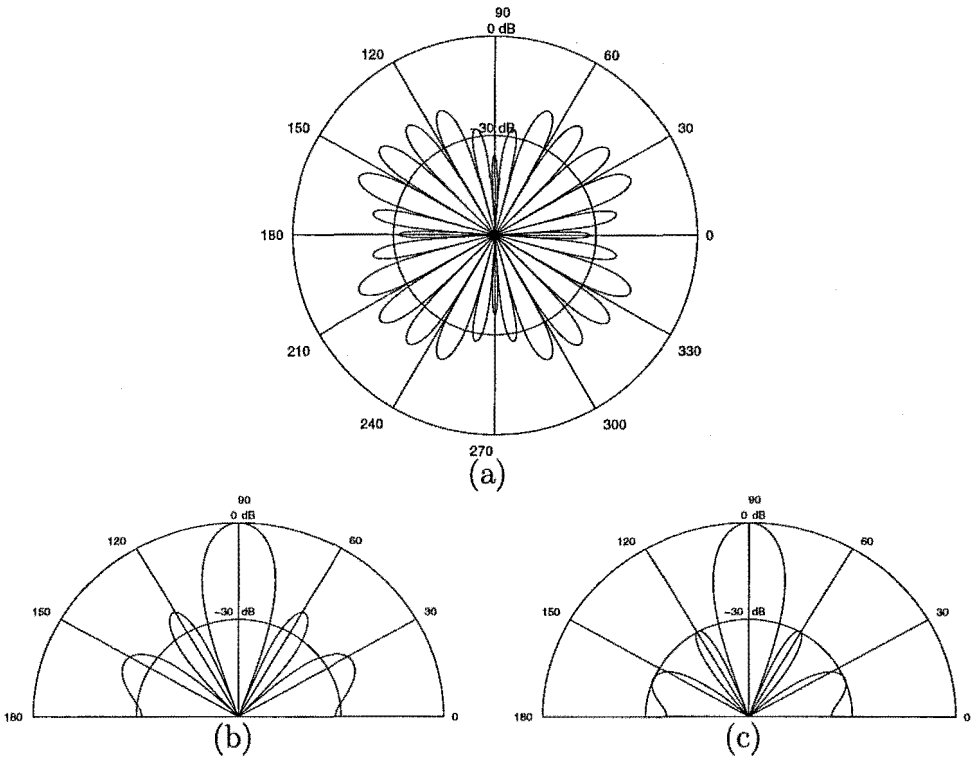

Figure 4.11. Polar diagrams of a planar array of point sources. The array geometry is shown in figure 4.10. Figure (a) shows the field in the horizontal plane and (b) and (c) show vertical sections along the y and z axes.

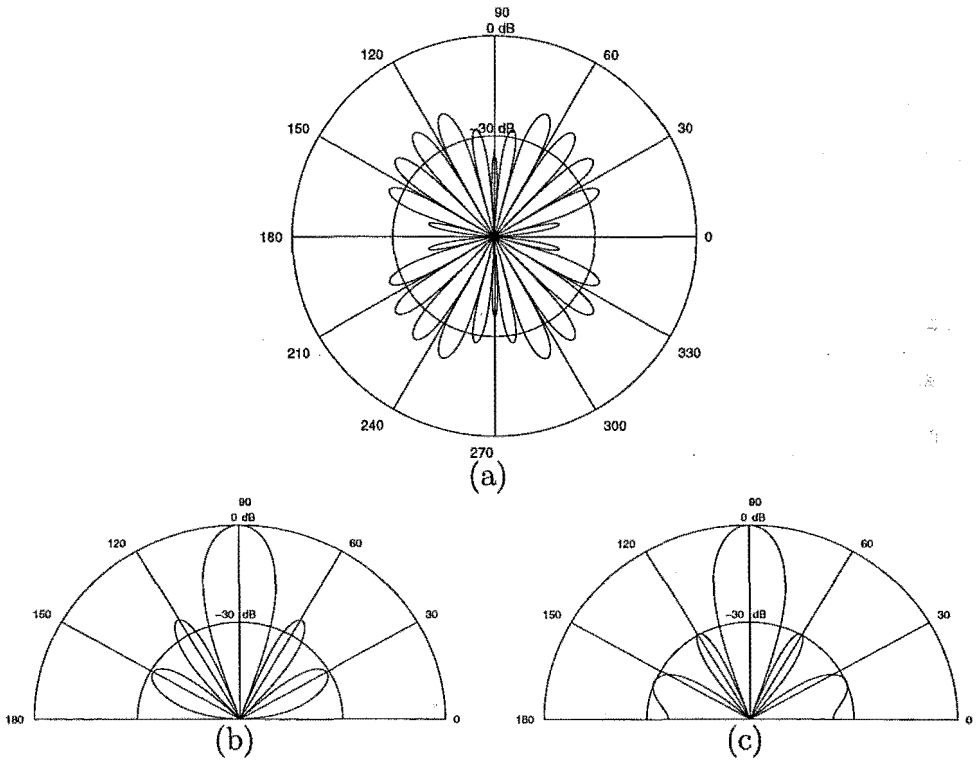

Figure 4.12. Polar diagrams of a planar array of half-wave dipoles. The array geometry is shown in figure 4.10 and the dipoles are aligned along the y axis. Figure (a) shows the field in the horizontal plane and (b) and (c) show vertical sections along the y and z axes.

4.3.4 Radio interferometry

Having considered the movement of radio stars and the theoretical angular power distribution from antennae it remains to show how these combine to allow the determination of the actual polar diagram. This is achieved by employing two spatially-separated antennae as a radio interferometer.

Following Jansky [1932; 1933; 1935], who reported the apparent extraterrestrial origin of certain types of radio noise, Reber [1944] published the first comprehensive maps of the radio sky. It was quickly realised that higher resolution maps would require antennae of greater angular discrimination. Unfortunately as discussed in section 1.3.1.1 this requires, for a given aerial, a larger size. Although large single dish radio telescopes have been constructed, e.g. Arecibo, Parkes and Jodrell Bank, it was the development of the two-aerial interferometer that provided a solution to this problem.

Interferometers are the radio equivalent of Thomas Young's [1807] double slit experiment in optics, with the spatially separated aerials corresponding to Young's slits. Although the fringes of the diffraction pattern are not visible, as in the optical case, it is possible to map out the pattern by using the interferometer to receive rather than transmit. When the aerial combination is used in reception the power received from a point source is proportional, by the reciprocity principle, to the intensity of the fringe that would be observed at the location of the source had the aerial been used in transmission. Thus, a moving point source can delineate the *spatial* features of the directional diagram as *temporal* variations of received power [Pawsey and Bracewell, 1955].

In this section the theory of two radio interferometers will be briefly discussed. Further details may be found in Kraus [1966] and Ryle [1952]. Firstly the simple two-element interferometer, which is a direct analogue of Young's experiment, and secondly the phase-switching interferometer (PSI), which is a refinement of the former. Finally some typical results from various works will be presented and the proposed setup of the Canterbury VHF system will be outlined.

4.3.4.1 The two-element interferometer

Consider the arrangement depicted in figure 4.13 which shows two aerials, spaced a distance f apart, with uniform aperture distribution of width d. From equation (4.5) the normalised far field pattern of the array is

$$E(\theta) = \frac{\sin\alpha}{\alpha}\cos\beta$$

and hence the normalised power pattern is

$$P(\theta) = E^2(\theta) = \frac{\sin^2\alpha}{\alpha^2}(1+\cos 2\beta)$$

Figure 4.14 shows the receiver output as a radio star of very small angular size passes overhead. The outer envelope is twice the polar diagram of a single element. This

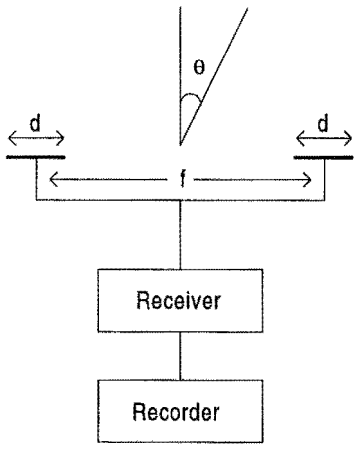

Figure 4.13. Block diagram of a simple two-element interferometer.

configuration is also known as a 'total power' system and was historically the first type of radio interferometer used to study stellar radio sources.

4.3.4.2 The phase switching interferometer

A refinement of the two-element interferometer, first used by Ryle [1952], is shown in figure 4.15. The configuration is identical except that an extra $\frac{1}{2}\lambda$ length of cable, where λ is the wavelength that the antenna and receivers are tuned to, can be switched in or out of one antenna path. As before the normalised in-phase far

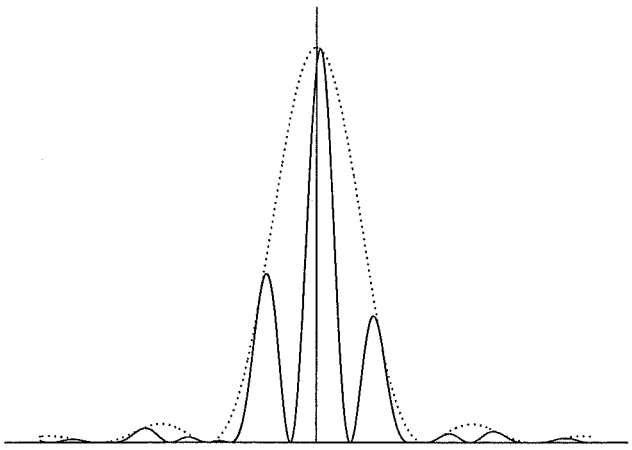

Figure 4.14. The detector output of a simple two element-interferometer as a radio star pases overhead.

field pattern is just

$$E_i(\theta) = \frac{\sin\alpha}{\alpha}\cos\beta$$

and the out of phase far field, i.e. with the $\frac{1}{2}\lambda$ cable inserted, is

$$E_o(\theta) = \frac{\sin\alpha}{\alpha}\sin\beta$$

Now let the system be switched rapidly, relative to the fringe period, between the in and out of phase conditions and the polarity of the receiver switched in synchronism. The net effect is to produce an output which is the difference of the two cases, thus

$$\begin{aligned} P(\theta) &= E_i^2(\theta) - E_o^2(\theta) \\ &= \frac{\sin^2\alpha}{\alpha^2}\cos 2\beta \end{aligned}$$

If the elements are not identical then it can be shown that, provided the individual element patterns are symmetrical, the detector output is [Kraus, 1966]

$$P(\theta) = E_1^2 E_2^2 \cos 2\beta \tag{4.12}$$

where $E_1(\theta)$ and $E_2(\theta)$ are the directional patterns of the individual elements. For the identical elements of figure 4.15 the output of the detector during the transit of a radio star of small angular size is shown in figure 4.16.

The phase-switching interferometer has many desirable characteristics. Although similar information can be obtained, in theory, from the simple two-element system in practice the PSI is far less susceptible to both man-made interference and

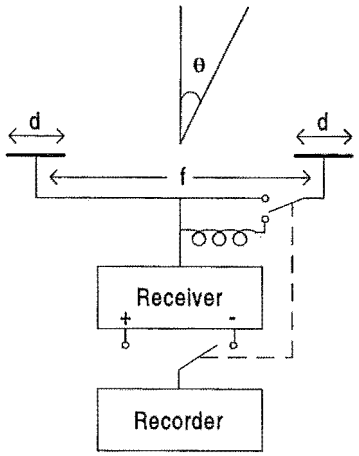

Figure 4.15. Block diagram of a phase-switching interferometer.

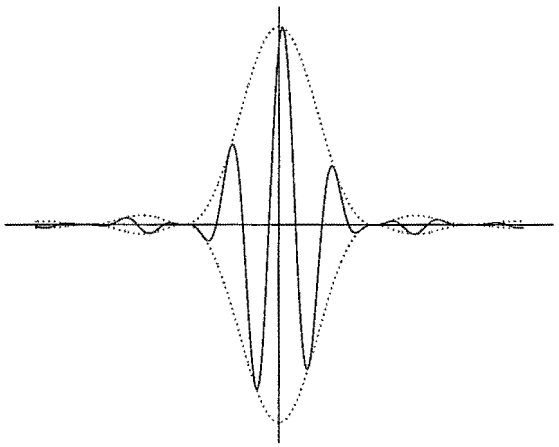

Figure 4.16. Output of a phase-switching interferometer.

cosmic background radiation. This latter would be a serious problem in measuring the envelope in figure 4.14 as the fringes would be barely visible if the point radio source had much weaker strength than the background.

4.3.4.3 The Canterbury VHF system

As mentioned previously the purpose of this section is to provide a foundation for the measurement of the polar diagram of the Canterbury University VHF radar transmitting array. Although the array itself is still under construction, other components necessary for the reverse radio astronomy have been produced and some details will be discussed here. These hardware components are based on a series of articles by Dr. G. Swenson [1978a; 1978b; 1978c; 1978d; 1978e; 1978f] and comprise

a phase switch, which inserts or removes the $\frac{1}{2}\lambda$ cable and a control module. The control module generates the switching pulses to switch phase and reverse polarity, and incorporates the amplifier/detector stages used to drive the recorder. Various outputs are available to facilitate system testing. It is also possible to operate the unit in 'total power' mode, i.e. as a simple two-element interferometer with no phase switching. For circuit diagrams and detailed information on the construction of these components refer to the aforementioned articles.

It is obvious from the discussion on interferometers that two spaced antennae are required and hence it is necessary to decide on a second aerial to use in conjunction with the VHF transmitting array. Since the measurement of the array polar diagram is the intended result, rather than measuring properties of stellar objects, the second aerial must have a minimal effect on the envelope of figure 4.16.

From equation (4.12) it can be seen that the fringe envelope is the product of the polar patterns of the two antennae. Thus if an isotropic radiator were used as the second element of the interferometer the resulting envelope would be just the pattern of the transmitting array. In practice it is difficult to obtain an isotropic radiating aerial however by using one with a very wide polar diagram, such as a half-wave dipole it is possible for the second aerial to have a negligible effect.

4.3.4.4 Expected typical results

It now remains to show how the interferometer output is used to obtain antenna pointing angles. First, however, an envelope must be fitted to the measured fringes. Figure 4.17 (from Ryle [1952]) shows a record made using both total power and phase switching methods. It can be seen that, in the presence of broad background noise (in this case solar), the PSI system gives superior results in terms of obtaining the precise envelope shape.

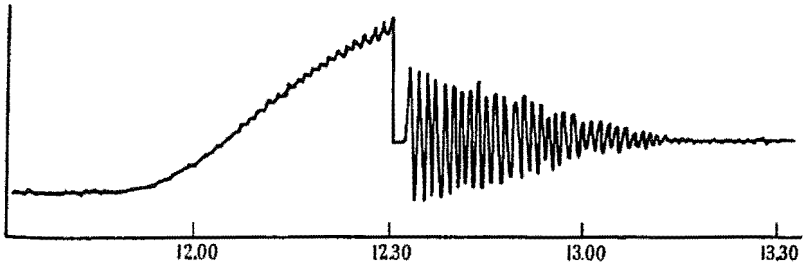

Figure 4.17. Example of an interferometer record showing both total power and phase switching modes. The left-hand section of the record shows the detector output in total power mode and the right-hand section shows the output in phase-switching mode. From Ryle [1952].

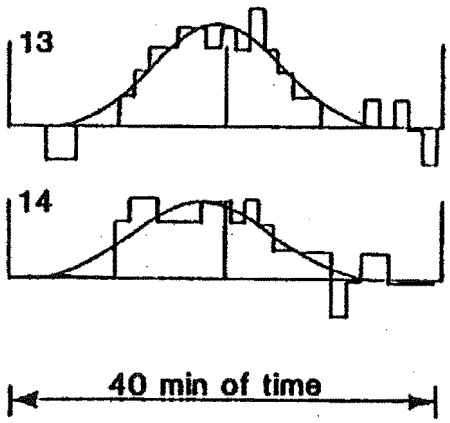

Figure 4.18. Fitting a Gaussian shape to a total power interferometer record. From Riddle [1986]

When fitting to the fringe envelope either a functional form such as a parabola must be used or, alternatively, the expression derived for the theoretical array shape may be employed. Riddle [1986], using the sun as a radio source, has used a Gaussian shape to fit to total power data; some examples are shown in figure 4.18. In either case only the main lobe need be fitted to.

Having done this it is possible to estimate the time at which the radio source appears to be directly over head. This will correspond to the peak of the main envelope lobe. By comparing this with the actual time, calculated using the theory of section 4.3.2, the deviation (if any) of the main aerial lobe from the vertical may be found. At present this method is currently being tested on the Canterbury University AMOR antennae.

4.3.5 Conclusion

This section has discussed the theory of phase-switching radio interferometers and their application to the measurement of aerial patterns. Some basic antenna theory was also introduced and this was extended to the two-dimensional case to derive expressions for the polar diagram for the CUSTARD transmitting array. Finally some expected typical results were presented and an outline of how the pointing angle of the transmitting aerial may be determined using stellar radio sources was given.

4.4 Design for DBS operation

As discussed in section 3.5 it appears, based on the data currently available, that there are difficulties with measuring short period momentum fluxes using the spaced antenna method (FCAW). The short-period fluxes are of interest as it would appear that these have the most important dynamic effects at high altitudes (B. Lawrence pers com). Consequently it is highly desirable that the CUSTARD system be able to measure them. This motivates the modification of the transmitting array (section 4.3.3.2) to allow a dual-beam DBS-like mode of operation. This would also permit intercomparisons with FCA velocities, which would be a useful validation of the system.

A full DBS implementation would progressively change the phase of each element across the array to tilt the main beam off-zenith. For the CUSTARD array this would be prohibitively expensive and is outside the design concept of the system which is to be low cost and non-complex. A novel solution is proposed which divides the array of figure 4.10 into four equal segments each of which could be individually phased; all elements within a given section having the same phase. In this section it will be shown that such a configuration can be operated to give a pseudo-DBS method of wind measurement.

There has been relatively little work done using such a simultaneous beam array, not least because of the inability to determine the wind direction unambiguously. Rastogi and Bowhill [1976] using the Jicamarca radar in a mesospheric study used a simultaneous beam configuration by segmenting the main array. However

their system also utilised separate receiving channels for each subgroup and thus is in essence two collocated single-beam radars. Brun et al. [1986] using the Provence radar have used a true dual-beam system. However as they note it is still necessary to determine the wind direction by some other technique. The design proposed here circumvents this requirement whilst still using a dual-beam system.

4.4.1 Measuring $|u|$

Consider figure 4.19 which shows the VHF array depicted in figure 4.10 divided in to 4 quadrants. Phasing all the solid circle elements at 0° (+) and all the open circle elements at 180° (−) will produce a field with a null in the vertical direction and with two off-zenith beams. This result can be derived qualitatively by considering a simplified array which has point sources of + or − phase located at the centre of each quadrant, i.e. on the corners of a square of side length 2λ. In the vertical direction, waves from the in-phase and anti-phase sources travel the same path length and hence will destructively interfere to produce a null. In the plane defined by the line at −45° to the y axis in figure 4.19 and the z axis the path length to any point from the + and − sources is again equal, thus producing no signal. In the plane defined by the line at +45° to the y axis and the z axis, however, there will be some angles of elevation at which the additional path length travelled by one of the waves is π, or equivalently $\lambda/2$, which will now make the wave trains interfere constructively, thus producing off-zenith beams. Application of simple trigonometry to this situation would produce the expression

$$\cos\theta = \frac{\frac{1}{2}\lambda + n\lambda}{2\lambda}$$

where $n = 0, 1, 2, ...$, for the angle of elevation θ which has the solutions $\theta = 76°, 41°$.

To determine the actual pattern of the array it is necessary to turn to the theory of section 4.3.3.2 for planar arrays of point sources. Using this theory it can be shown, again through some manipulation, that the field of the array of point sources is now given by

$$\begin{aligned} E(\theta,\phi) &= 4\Bigg\{\cos(kdc_\phi)\sum_{m=1}^{3}\sin(2ms_{\theta\phi}) + \cos(3kdc_\phi)\sin(4kds_{\theta\phi}) \\ &\quad + \cos(2kds_{\theta\phi})\sum_{n=2}^{3}\sin(kd(2n-1)c_\phi)\Bigg\} \end{aligned}$$

$$+2\sum_{n=1}^{4}\sin\left(kd\left(2n-1\right)c_{\phi}\right) \tag{4.13}$$

where $c_{\phi} = \cos\phi$ and $s_{\theta\phi} = \sin\theta\sin\phi$ and k, d are as for equation (4.11). Similar expressions can also be derived for the cases where the segments are phased with different combinations of + and −. These beam configurations are largely identical except for having the off-zenith beams in different planes.

Polar diagrams of sections through the pattern represented by equation (4.13) are shown in figure 4.20, for comparison with figure 4.11, where the elements are all in phase, the pattern is normalised to the strength of the main vertical lobe of figure 4.11. In the plane at +45° to the y axis there are now two beams displaced symmetrically off vertical at 79°, as was derived qualitatively above, while in the perpendicular plane (−45° to the y axis) there is essentially no radiated power.

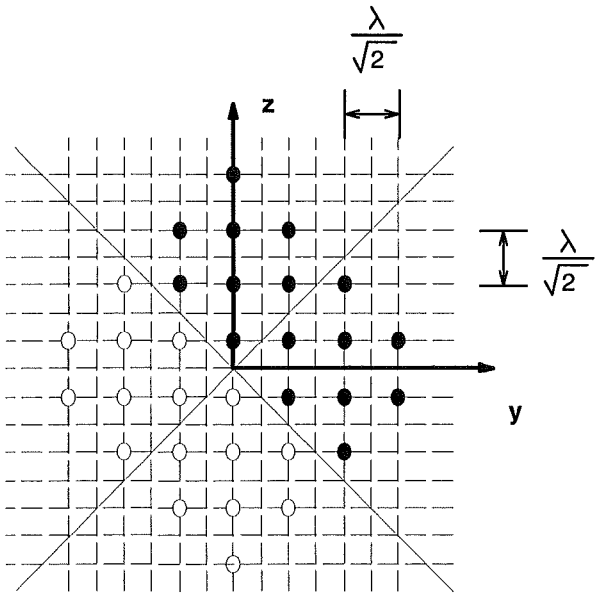

Figure 4.19. Transmitting array geometry for a dual-beam system. The array is divided into quadrants shown by the solid lines and each filled or open circle represents one array element. All elements within a quadrant have the same phase.

To show how this beam arrangement will allow measurement of the magnitude of the horizontal velocity consider figure 4.21 which shows a wind vector V incident on the dual-beam system. Each beam will separately produce a Doppler shifted signal corresponding to the radial velocity in the beam. Thus if $\cos 2\pi f_o t$ represents

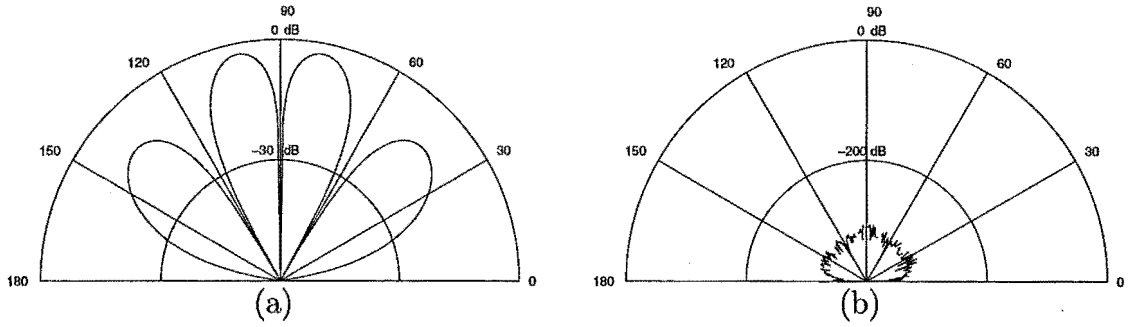

Figure 4.20. Polar diagrams of a planar array of point sources phased at 0° and 180°. The array geometry is shown in figure 4.19. Figures (a) and (b) show the field sectioned along lines at +45° and −45° to the y axis.

the transmitted wave then the signal voltages from each beam are

$$\begin{aligned} v_1 &= \cos 2\pi \left(xf_0 - f_x + f_z\right) t \\ v_2 &= \cos 2\pi \left(xf_0 + f_x + f_z\right) t \end{aligned}$$

where f_o is the operating frequency and f_x, f_z are the Doppler shifts from the horizontal and vertical components of V. The outputs of the two beams combine as $v_T = v_1 + v_2$ and to proceed further it is necessary to take a Fourier transform of v_T.

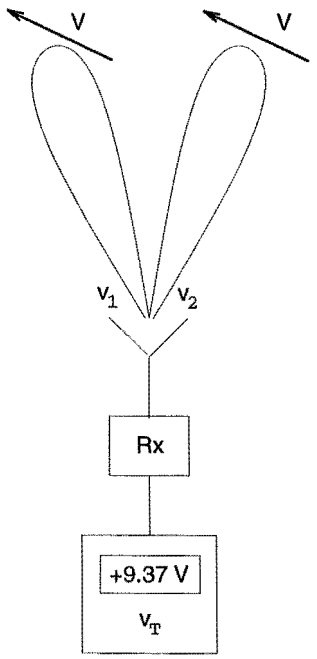

Figure 4.21. Schematic of a dual-beam system for measuring the magnitude of u. Each beam produces a Doppler shifted voltage, which combine to give a total voltage v_T.

Figure 4.22 shows the Fourier transform of v_T, for simplicity $f_0 \equiv 0$ and signals from each beam are shown as single frequencies. The distance between the two lines is $2f_x$ and, from section 2.2, this is equal to $\frac{4|u|}{\lambda}$.

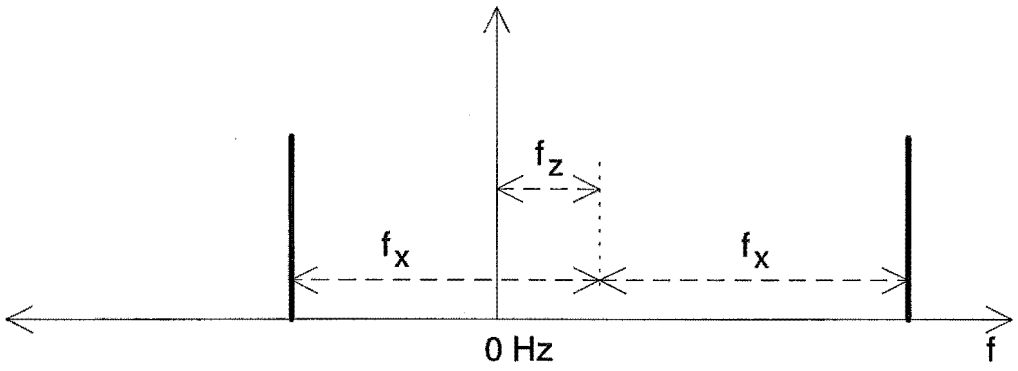

Figure 4.22. Fourier transform of the signal v_T in figure 4.21 from a dual-beam array with elements phased at 0° and 180°.

4.4.2 Measuring the sign of u

The technique described previously allows the magnitude of u to be determined but not the sign. This could be obtained by switching to the FCA mode of operation, measuring u, and assuming that the wind field remains unchanged between the two measurements. This solution whilst feasible is clearly unsatisfactory if the purpose of the method is to provide an independent technique to FCA. In a DBS system which has only one off-zenith beam as compared to the dual beams of figure 4.20 the sign of the velocity is simply obtained from the sign of the Doppler shift. For the dual-beam system, however, as there are equal and opposite shifts from each of the off-zenith beams it is not possible to determine the direction of the horizontal wind. The solution proposed here is to utilise a phasing configuration of the array which, whilst not producing a single beam, gives beams of unequal strength and thus allows an unambiguous determination of the sign of u.

Consider now the segmented array of figure 4.19 where the open circle elements are phased at $-45°$ and the solid elements are phased at $+45°$. In this case a most useful beam pattern is produced, with off zenith beams of unequal intensities. As before, using the theory of section 4.3.3.2, it can be shown that

$$E(\theta,\phi) = 4\left\{\cos(kdc_\phi)\sum_{m=1}^{3}\cos\left(2ms_{\theta\phi}+\frac{\pi}{4}\right)+\cos(3kdc_\phi)\cos\left(4kds_{\theta\phi}+\frac{\pi}{4}\right)\right.$$

$$+\cos\left(2kds_{\theta\phi}\right)\sum_{n=2}^{3}\sin\left(kd\left(2n-1\right)c_{\phi}+\frac{\pi}{4}\right)\Bigg\}$$
$$+2\sum_{n=1}^{4}\sin\left(kd\left(2n-1\right)c_{\phi}+\frac{\pi}{4}\right) \tag{4.14}$$

which has sections as depicted in figure 4.23. Relative to figure 4.20 it can be seen that the lobes of figure 4.23a have moved closer to the zenith and are now not symmetric in strength. There is again no important structure in the vertical plane, the apparent vertical lobe in figure 4.23b is due to the larger lobe of figure 4.23a having a finite angular width.

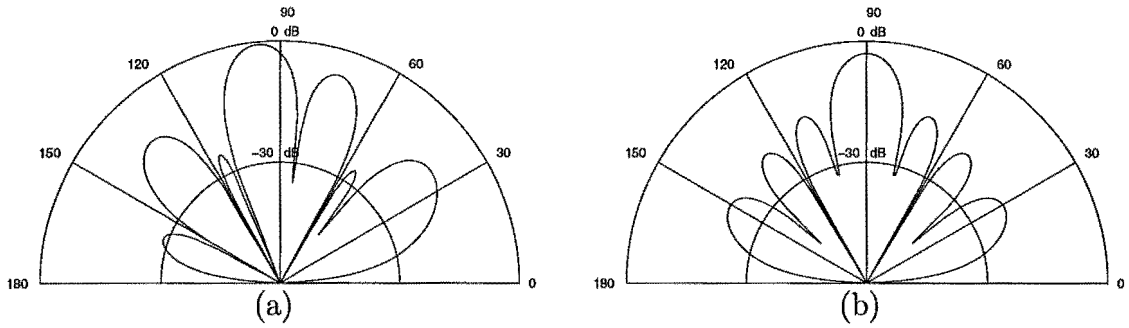

Figure 4.23. Polar diagrams of array of point sources phased at +45° and −45°. The array geometry is shown in figure 4.19. Figures (a) and (b) show the field sectioned along lines at +45° and −45° to the y axis.

To show how figure 4.23a can be used to find the sign of u consider the output v_T in the presence of the same velocity V as in figure 4.21. A Fourier transform of v_T will still show two distinct peaks (shifted by different amounts due to the different beam angles) however one component will be of larger magnitude than the other. The transform for this new configuration is shown in figure 4.24. By finding the Doppler shift, positive or negative, of the larger Fourier component and combining this with a knowledge of the pointing direction of the stronger lobe of figure 4.23a it is thus possible to obtain the sign of u.

4.4.3 Practical considerations

One of the primary motivating influences in the development of this new method has been the need to obtain a low-cost alternative to FCA. One of the major costs associated with a DBS system is the necessary cabling, controllers and switches which allow phasing of each element, or small subgroups, of the array. It is

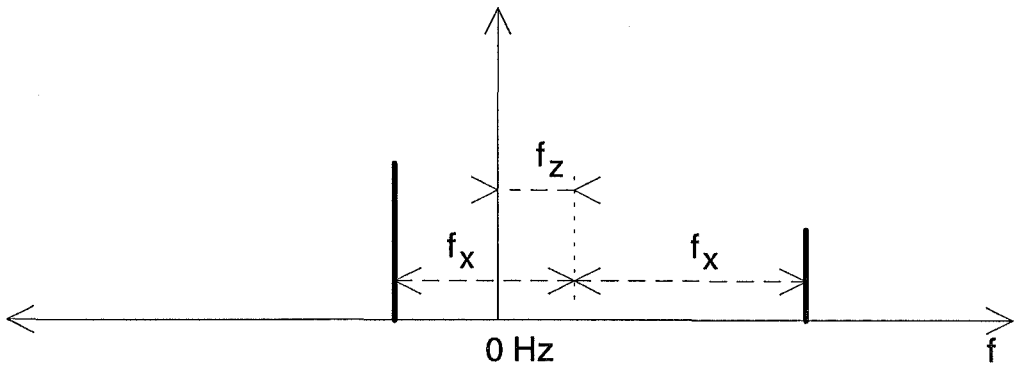

Figure 4.24. Fourier transform of signal v_T from an array with elements phased at +45° and −45°.

possible that in the future the basic transmitting array of figure 4.10 will be scaled up in size by the addition of more elements. If this is done then the pointing angles of the beams in figures 4.20 and 4.23 will change (becoming closer to the vertical) and this may necessitate phasing the array in smaller segments. This would, in effect, mean changing the array to full DBS operation with all the associated costs. Although this is not an issue with the current design it may need to be considered at some later stage.

The feeding of the transmitting array in quadrants has a number of desirable consequences. The first is that it is not significantly more expensive than feeding from a single central feed point and could be done irrespective of the implementation of the system described above. It would be advisable to commission the system for operation in spaced antenna mode and to perform measurements in this mode for some time to gain a thorough understanding of the radar's capabilities. If at some later date it is necessary to implement some alternative form of wind measurement then this could be carried out, providing that the array had been fed as described. An additional advantage of feeding the array in segments is that this reduces the tapering, i.e. antennas at the edges of the array receiving less power than those closer to the central feed, that would occur if a central feed point were to be used.

Another sophistication which should be mentioned is that the Fourier components represented as single frequencies in figures 4.22 and 4.24 are, in fact, broadened by the finite width of the beams. It may be that small Doppler shifts will be difficult to determine accurately due to the spread of the Doppler spectrum caused by the

finite angular width of the beams. Thus it is possible that small, on the order of a few ms^{-1}, winds may be difficult to measure with this system.

To determine the minimum resolvable magnitude consider the case where the two lines of figure 4.22 are represented by Gaussian peaks. The spectral power from each beam, denoted p_1 and p_2, are given by

$$\begin{aligned} p_1 &= a_1 e^{-\left(\frac{f-b_1}{2c_1}\right)^2} \\ p_2 &= a_2 e^{-\left(\frac{f-b_2}{2c_2}\right)^2} \end{aligned}$$

Since the beams are identical and point in opposite directions it can be assumed that $a = a_1 = a_2$, $c = c_1 = c_2$ and, by setting the frequency origin midway between the peaks, $\Delta b = -b_1 = b_2$. If the spectral amplitude has an uncertainty given by Δa then a criteria for detection is that the minimum amplitude $(a - \Delta a)$ is equal to the spectral power at the frequency where the two Gaussians first become distinct. This occurs midway between the two peaks, at $f = 0$, and thus

$$a - \Delta a = a e^{-\left(\frac{\Delta b}{2c}\right)^2}$$

or equivalently

$$\Delta b = 2c\sqrt{-\ln\left(1 - \frac{\Delta a}{a}\right)} \tag{4.15}$$

The fractional error in the spectral estimate can be decreased by averaging, both coherent and incoherent. If n_c and n_i are the number of coherent and incoherent averages then [Tsuda, 1988]

$$\frac{\Delta a}{a} = \frac{1}{n_c\sqrt{n_i}} \tag{4.16}$$

To determine the spectral width, c, it will be assumed that only random turbulent motions and beam broadening are important. For narrow beams the spectral half-power half-width, f_b, due to beam broadening is [Hocking, 1988]

$$f_b = \frac{2}{\lambda}(1.0)\,|\mathbf{V}|\,\theta'_{\frac{1}{2}}$$

where $\mathbf{V}$ is the total wind vector and $\theta'_{\frac{1}{2}}$ is the two-way half-power half-width. In terms of the equivalent Gaussian width, c_b, this becomes

$$c_b = \frac{f_b}{2\sqrt{\ln 2}} = \frac{2\,(1.0)\,|\mathbf{V}|\,\theta_{\frac{1}{2}}}{2\sqrt{\ln 2}\lambda\sqrt{2}}$$

where $\theta_{\frac{1}{2}}$ is the one-way half-power half-width. Assume that the contribution to spectral width from velocity fluctuations is

$$c_f = \frac{2}{\lambda} v_{rms}$$

where v_{rms} is the random velocity fluctuation and hence

$$c = \frac{2}{\lambda}\left(v_{rms} + \frac{(1.0)\,|\mathbf{V}|\,\theta_{\frac{1}{2}}}{2\sqrt{2\ln 2}}\right) \tag{4.17}$$

Combining equations (4.16) and (4.17) with equation (4.15) gives

$$\Delta b = \frac{2\,|v_{\min}|}{\lambda} = 2\frac{2}{\lambda}\left(v_{rms} + \frac{(1.0)\,|\mathbf{V}|\,\theta_{\frac{1}{2}}}{2\sqrt{2\ln 2}}\right)\sqrt{-\ln\left(1 - \frac{1}{n_c\sqrt{n_i}}\right)}$$

and assuming $v_{\min} = |\mathbf{V}|$ this allows $v_{\min}$ to be calculated. Taking $v_{rms} = 0.5$m/s [Holdsworth and Reid, 1995], $n_c = 16$, $n_i = 6$ and $\theta_{\frac{1}{2}} = 8°$ give $v_{\min} = 0.2$m/s which is an acceptable minimum detectable velocity.

For a conventional DBS system which has a single beam and hence only a single spectral peak it is not necessary to be able to distinguish individual peaks and the criteria for detectability is based on the signal-to-noise ratio. Another problem associated with this finite beam width is the 'effective pointing angle' which, in the presence of anisotropic scatter, will be different to the actual pointing angle of the beam [Hocking, 1997b].

Finally the rate of switching between the various modes of operation must be discussed. It has been shown that by switching between figures 4.20 and 4.23 u may be determined. By switching the array segment phases so that the off-zenith beams are pointed in the north-south plane, rather than the east-west plane, v could be measured and, by having all segments in phase, w could be obtained. This last configuration would also allow the system to be operated in FCA mode.

Given that the pulse repetition frequency of the CUSTARD transmitter is 2kHz it is conceivable that the system be switched between the various modes at this rate. There are two major arguments against such an approach. Firstly although transmit-receive switches can handle this rate, the cost of relays capable of switching phases at this frequency and at the high power levels output from the transmitter are expensive. If the CUSTARD system had used several lower level transmitters each feeding a subgroup of the array then cheaper low-power fast switching relays could

have been utilised. However the transmitter, which has already been constructed, is not of this design. Secondly even if switching at this rate were possible it is necessary to perform coherent integrations as discussed in section 1.3.2.1. Although these integrations could be done in software, switching between beam configurations after every pulse and storing signals from each of the operating modes, the integration hardware is already available (section 4.2) and it is more sensible to use it, thus requiring a lower rate of switching.

To estimate the total time required to perform all the required wind measurements it is necessary to choose some operational parameters. For an experiment taking 256 samples at each of 128 height bins with a resolution of 500m and using 256 coherent integrations a single beam configuration run would take $256 \times 128 \times 3\frac{1}{3}\mu s \times 256 = 27.9s$. Given that two configurations are needed to determine each horizontal component with the dual-beam system described here and that in FCA mode (beam vertical) it is also possible to measure w as well as the horizontal components then the whole procedure would take approximately 1min during which time it is reasonable to expect the statistical properties of the atmosphere to remain unchanged. This value of estimated temporal resolution is not atypical of other radar systems [e.g. Rottger, 1988; Doviak and Zrnic, 1993]. Although taking 128 heights may appear excessive it is necessary to avoid range aliasing ambiguities and it would seem advisable to do as many coherent integrations as possible. The large number of samples, 256 in this scenario, is necessary to allow the computation of correlation functions or Fourier transforms from the coherently integrated data in each range bin. Note that none of the numbers in this example are fixed as they can all be changed under software control once the radar is operational.

4.4.4 Conclusion

This section has described a modification to the CUSTARD transmitting array which would allow the system to measure both components of the horizontal wind in a manner similar to DBS. While there will undoubtedly be practical difficulties involved in implementing both the hardware and software required for this technique it has been proved that the method is applicable to the CUSTARD system and does not require a large degree of modification of the original design.

Chapter 5
Conclusion

This thesis has described the design of several components of a proposed VHF radar system for the Department of Physics and Astronomy of the University of Canterbury, New Zealand. A suite of software for implementing the full correlation analysis of Briggs [1984] has been developed and its operation tested using data from the MU radar of the University of Kyoto. This chapter summarises the results of this analysis and presents recommendations for the CUSTARD system.

The variation in the signal power with height and time was investigated and found to contain two distinct types of features which were studied in detail. Firstly, regions of very high power were found to correspond to regions in which the FCA was unable to calculate a velocity. It was found that the computed correlation functions often took the form of a large spike at the origin with smaller side lobes at higher and lower time shifts. The frequency power spectra often showed considerable aliasing. The echo power during several of these events was also studied and showed that the high power was not due to a single spike nor to a constant high power throughout the entire run, but rather gave the appearance of an object of high reflectivity passing through the aerial beam. Several other runs were studied, all of which showed similar characteristics.

It was hypothesised that these events might be caused either by aircraft or by range-aliased meteors. The characteristics of the reflected power are not of the expected form for a meteor echo, which should show a linear increase up to some maximum value and then an exponential decrease as the ionisation trail diffused away. Also the 'meteors' appear to occur between $70-85$km, after allowing for range aliasing, which is somewhat lower than the height of maximum meteor occurrence (≈ 95km). Thus the aircraft hypothesis was considered to be more plausible.

The second feature observed in the signal power was the presence of thin horizontally stratified regions of very low power which, again, corresponded to areas where the FCA method failed. The correlation functions showed similar characteristics to those which would be obtained from either random noise or uncorrelated

signal. Suggestions were made as to a method of determination of the true signal-to-noise ratio, which would allow discrimination between these two cases.

To investigate the cause of the low signal power, profiles of potential refractive index squared, which is proportional to the reflected echo power, were calculated from radiosonde data. Although the times of the radiosonde flights were not coincident with radar observations these profiles also showed layered structure, which matched the heights of the layers in the radar data.

In addition to the signal characteristics, horizontal and vertical velocities were calculated. The vertical velocities were compared with the regions of high and low power and showed no corresponding features. Horizontal velocities were found to depend on both the triangle of receivers used and also the method of analysis used to calculate the velocity. A spectral analysis of the FCA velocities suggested that there were significant spurious high frequency components and this, combined with the large amount of missing data, indicate that it will be difficult to study the short period velocity components with this technique.

Analysis of data recorded on four receivers was analysed using various triangle combinations. The analysis was found to underestimate the wind velocity when the wind direction was perpendicular to the longest side of the triangle. Failure to exclude the zero-lag point value of the covariance data prior to fitting led to a larger difference between velocities calculated using different receiving triangles, a manifestation of the 'triangle size effect', in agreement with the modelling results of Holdsworth and Reid [1995].

Differences were also observed which were insensitive to the inclusion of the zero lag data, i.e. the exclusion of this data produced no reduction in the velocity difference between triangles. This effect was attributed to anisotropies in the ground diffraction pattern as evidenced by systematic differences observed in the correlation functions from parallel pairs of receivers. A possible explanation for this was found in considering the high power events, which in several of the cases studied appeared to suggest anisotropies in the aerial pattern.

Secondly, a comparison was made of velocities from two different FCA methods. One, implemented by the author, follows that of Briggs [1984], and the other, implemented by Dr. G. Fraser, is that of Brown and Chapman [1972]. A difference

was found between the velocities calculated using the two methods, with the magnitudes obtained by the author being larger than the magnitudes found by Fraser. There are two possible sources of difference in the calculation of these velocities. The first is in the method used to determine the τ and τ' values, while the second is in the particular algorithm which uses those values to compute a velocity. These effects were investigated separately and it was found that the method of calculating the τ, τ' values used by the author gave smaller velocities than those based on τ, τ' values calculated by Fraser. In addition to this it was found that velocities calculated using the algorithm of Briggs were larger than those calculated, using the same τ, τ' values, by the algorithm of Brown and Chapman. In the comparison of the velocities of the author with those of Fraser both of these effects were present.

Variances of the velocity components were also calculated and these showed that the implementation of Brown and Chapman used here produces larger variances than does the algorithm of Briggs. It was suggested that this difference, and also the slight differences in direction observed, were due to the different amounts of averaging used by each method to obtain the velocity. In short, the Brown and Chapman implementation does not utilise all of the available information from the three sides of the receiving triangle whereas the Briggs method does. It was noted that in their paper Brown and Chapman [1972] suggest using all possible information. However, for historical reasons, this was not done in Fraser's implementation of the Brown and Chapman analysis.

Consecutive hour-long periods of FCA and DBS were available and these were used to investigate the FCA technique further. Comparisons were made between FCA and DBS velocities on both 10- and 50-min timescales and show that in both cases the two methods are measuring similar average velocities, despite the fact that the observations were sequential in time rather than simultaneous. Momentum flux comparisons were also made by combining the FCA horizontal winds with vertical winds calculated using the phase slopes of the correlation functions. These were compared with momentum fluxes calculated from the DBS data using the symmetric-beam method of Vincent and Reid [1983] and the 'five-beam' method of Worthington and Thomas [1996]. It was found that on the short timescales available here the SA method showed only moderate agreement with the two DBS techniques, which

had good agreement with each other. It would be desirable to obtain more data to investigate this further and also to compare momentum fluxes on longer timescales.

Several components of the radar system have been described in detail both as a reference for future workers and to gain an understanding of their operation. A thorough analysis has been made of the radar controller and integrating A/D converter and a procedure has been developed for measuring the pointing angle of the transmitting array using cosmic radio sources. In addition, modifications to the transmitting array have been described which would allow the radar to measure winds in a manner similar to Doppler beam-swinging thus providing an alternative to the spaced-antenna mode of operation.

In summary it has been found that the atmosphere exhibits a variety of phenomena which may be studied using radar and FCA techniques. As can be seen from the results presented here, the observations made may depend on the measurement and analysis techniques employed. To quote Fraser, 'Our equipment and methods of analysis are the rose-tinted spectacles through which we view the world around us'. Thus without a knowledge of the idiosyncracies of our observation system, we can but behold the atmosphere 'as in a mirror dimly'.

References

Andrews, D. G., Holton, J. R. and Leovy, C. B., [1987]. *Middle atmosphere dynamics*. Academic Press.

Atkins, P. W., [1988]. *Physical Chemistry*, p. 141. Oxford University Press, 3rd edn.

Awe, O., [1964]. Errors in correlation between time series. *Journal of Atmospheric and Terrestrial Physics*, 26:1239–1255.

Barber, N., [1957]. Timing errors in an equilateral array of receivers. *Journal of Atmospheric and Terrestrial Physics*, 11:299–300.

Bemra, R. S., Rastogi, P. K. and Balsley, B. B., [1986]. A study of gravity-wave spectra in the troposphere and stratosphere at 5-min to 5-day periods with the Poker Flat MST radar. In *Handbook for MAP, Volume 20*, pp. 216–224. ICSU.

Berenson, M. L., Levine, D. M. and Rindskopf, D., [1988]. *Applied Statistics: A first course*. Prentice Hall.

Beynon, W. J. G. and Wright, J. C., [1969]. The analysis of ionospheric drift data in the closely spaced receiver method. *Journal of Atmospheric and Terrestrial Physics*, 31:593–596.

Bowhill, S. A., [1986]. The Tukey algorithm for enhancing MST radar data. In *Handbook for MAP, Volume 20*, pp. 486–488. ICSU.

Bracewell, R., [1965]. *The Fourier transform and its applications.*. McGraw-Hill.

Briggs, B. H., [1977]. Ionospheric drifts. *Journal of Atmospheric and Terrestrial Physics*, 39:1023–1033.

Briggs, B. H., [1980]. Radar observations of atmospheric winds and turbulence: a comparison of techniques. *Journal of Atmospheric and Terrestrial Physics*, 42:823–833.

Briggs, B. H., [1984]. The analysis of spaced sensor records by correlation techniques. In *Handbook for MAP, Volume 13*, pp. 166–186. ICSU.

Briggs, B. H., [1992]. Determination of mean direction of arrival and vertical velocity from the phases of the correlation functions: 2-D case. In *Workshop on Multiple Receiver Radar Techniques*.

Briggs, B. H. and Vincent, R. A., [1992]. Spaced-antenna analysis in the frequency domain. *Radio Science*, 27:117–129.

Briggs, B. H., Phillips, G. J. and Shinn, D. H., [1950]. The analysis of observations on spaced receivers of the fading of radio signals. *Proceedings of the Physical Society, London*, B63:106–121.

Briggs, B. H., Elford, W. G., Felgate, D. G., Golley, M. G., Rossiter, D. E. and Smith, J. W., [1969]. Buckland Park aerial array. *Nature*, 223:1321–1325.

Brown, G. M. and Chapman, J. W., [1972]. Full correlation ionospheric drift analysis for a general observing triangle. *Annales Geophysicae*, 28:349–356.

Brown, W. O. J., [1992]. *MF radar interferometry*. Ph.D. thesis, Department of Physics, University of Canterbury.

Brown, W. O. J., Fraser, G. J., Fukao, S. and Yamamoto, M., [1995a]. Spaced antenna and interferometric velocity measurements with MF and VHF radars. *Radio Science*, 30:1281–1291.

Brown, W. O. J., Fukao, S., Yamamoto, M. and Fraser, G. J., [1995b]. Spaced antenna scattering scale and orientation measurements of the upper troposphere on the MU radar. *Journal of Geomagnetism and Geoelectricity*, 47:1231–1235.

Brun, E., Crochet, M. and Ecklund, W. L., [1986]. Simultaneous multibeam sounding of wind and turbulence. In *Handbook for MAP, Volume 20*, pp. 402–408. ICSU.

Burke, M. J., [1987]. Moving random surfaces and correlation analysis. *Radio Science*, 22:607–624.

Carter, D. A., [1983]. Discrimination against interfering signals at the Poker Flat MST radar. In *Handbook for MAP, Volume 9*, pp. 120–121. ISCU.

Cervera, M. A. and Reid, I. M., [1995]. Comparison of simultaneous wind measurements using colocated VHF meteor radar and MF spaced antenna radar systems. *Radio Science*, 30:1245–1261.

Chandra, H. and Briggs, B. H., [1978]. The effect of filtering on ionospheric drift parameters determined by full correlation analysis. *Journal of Atmospheric and Terrestrial Physics*, 40:541–548.

Chang, J. L., Avery, S. K., Riddle, A. C., Palo, S. E. and Gage, K. S., [1997]. First results of tropospheric gravity wave momentum flux measurements over Christmas Island. *Radio Science*, 32:727–748.

Chang, J. Y., Larsen, M. F., Palmer, R. D., Fukao, S., Yamamoto, M., Nakamura, T. and Tsuda, T., [1993]. Comparison of multiple receiver techniques for estimating horizontal winds: A case study of the triangle orientation effect. In *Proceedings of the Sixth Workshop on Technical and Scientific Aspects of MST Radar*.

Chezechowsky, P., Schmidt, G. and Ruster, R., [1984]. The mobile SOUSY Doppler radar: Technical design and first results. *Radio Science*, 19:441–450.

Chu, Y. H., Hsu, T. S., Chen, L. H. and Chao, J. K., [1990]. A study of the characteristics of VHF radar echo power in the Taiwan area. *Radio Science*, 25:527–538.

Costa, E., Basu, S. U. and Basu, S., [1992]. Application of cross correlation techniques to

spaced receiver data. *Journal of Atmospheric and Terrestrial Physics*, 54:1257–1263.

Devara, P. C. S., Raj, P. E., Panithurai, G. and Dani, K. K., [1997]. Tropical atmospheric stability and wind structures as inferred from the Indian MST radar observations. *Meteorology and Atmospheric Physics*, 64:173–186.

Doviak, R. J. and Zrnic, D. S., [1993]. *Doppler radar and weather observations*. Academic Press, 2nd edn.

Doviak, R. J., Lataitis, R. J. and Holloway, C. L., [1996]. Cross correlations and cross spectra for spaced antenna wind profilers, 1, Theoretical analysis. *Radio Science*, 31:157–180.

Eckermann, S. D. and Vincent, R. A., [1993]. VHF radar observations of gravity wave production by cold fronts over Southern Australia. *Journal of the Atmospheric Sciences*, 50:785–806.

Farley, D. T., Ierkic, H. M. and Fejer, B. J., [1981]. Radar Interferometry: A new technique for studying plasma turbulence in the ionosphere. *Journal of Geophysical Research*, 86:1467–1472.

Fedor, L. S. and Plywaski, W., [1972]. The interpretation of ionospheric radio drift measurements - IV. the effects of signal coupling among spaced sensor channels. *Journal of Atmospheric and Terrestrial Physics*, 34:1825–1303.

Fooks, G. F., [1965]. Ionospheric drift measurements using correlation analysis; methods of computation and interpretation of results. *Journal of Atmospheric and Terrestrial Physics*, 27:979–989.

Fritts, D. C., Tsuda, T., VanZandt, T. E., Smith, S. A., Sato, T., Fukao, S. and Kato, S., [1990]. Studies of velocity fluctuations in the lower atmosphere using the MU radar II: Momentum fluxes and energy densities. *Journal of the Atmospheric Sciences*, 47:51–66.

Fukao, S., Sato, T., Tsuda, T., Kato, S., Wakasugi, K. and Makihira, T., [1985a]. The MU radar with an active phased array system 1. Antenna and power amplifiers. *Radio Science*, 20:1155–1168.

Fukao, S., Tsuda, T., Sato, T., Kato, S., Wakasugi, K. and Makihira, T., [1985b]. The MU radar with an active phased array system 2. In-house equipment. *Radio Science*, 20:1169–1176.

Fukao, S., Sato, T., Tsuda, T., Kato, S., Inaba, M. and Kimura, I., [1988]. VHF Doppler radar determination of the momentum flux in the upper troposphere and lower stratosphere: Comparison between the three- and four-beam methods. *Journal of Atmospheric and Oceanic Technology*, 5:57–69.

Fukao, S., Sato, T., Tsuda, T., Yamamoto, M., Yamanaka, M. D. and Kato, S., [1990]. MU radar: New capabilities and system calibrations. *Radio Science*, 25:447–485.

Gage, K. S. and Green, J. L., [1979]. Tropopause detection by partial specular reflection with very-high-frequency radar. *Science*, 203:1238–1240.

Gardner, F. F. and Pawsey, J. L., [1953]. Study of the ionospheric D-region using partial reflections. *Journal of Atmospheric and Terrestrial Physics*, 3:321–344.

Golley, M. G. and Rossiter, D. E., [1970]. Some tests of methods of analysis of ionospheric drift records using an array of 89 aerials. *Journal of Atmospheric and Terrestrial Physics*, 32:1215–1233.

Golley, M. G. and Rossiter, D. E., [1971]. Some aspects of ionospheric drifts using partial and total reflections from the lower ionosphere. *Journal of Atmospheric and Terrestrial Physics*, 33:701–714.

Green, J. L. and Gage, K. S., [1980]. Observations of stable layers in the troposphere and stratosphere using VHF radar. *Radio Science*, 15:395–405.

Guidice, D. A. and Castelli, J. P., [1971]. The use of extraterrestrial radio sources in the measurement of antenna parameters. *IEEE Transactions*, AES7:226–234.

Halliday, D., Resnick, R. and Walker, J., [1993]. *Fundamentals of physics*. John Wiley and Sons, 4th edn.

Hildebrand, P. H. and Sekhon, R. S., [1974]. Objective determination of the noise level in Doppler spectra. *Journal of Applied Meteorology*, 13:808–811.

Hocking, W. K., [1988]. Target parameter estimation. In *International School of Atmospheric Radar*.

Hocking, W. K., [1993]. The University of Western Ontario VHF atmospheric radar. In *Proceedings of the Sixth Workshop on Technical and Scientific Aspects of MST Radar*.

Hocking, W. K., [1997a]. Recent advances in radar instrumentation and techniques for studies of the mesosphere, stratosphere, and troposphere. *Radio Science*, 32:2241–2270.

Hocking, W. K., [1997b]. Strengths and limitations of MST radar measurements of middle atmosphere winds. *Annales Geophysicae*, 15:1111–1122.

Hocking, W. K., [1997c]. System design, signal processing and preliminary results for the Canadian (London, Ontario) VHF atmospheric radar. *Radio Science*, 32:687–706.

Hocking, W. K. and Thayaparan, T., [1997]. Simultaneous and colocated observation of winds and tides by MF and meteor radars over London, Canada, (43°N, 81°W), during 1994-1996. *Radio Science*, 32:833–865.

Hocking, W. K., May, P. T. and Rottger, J., [1989]. Interpretation, reliability and accuracy of parameters deduced by the spaced antenna method in middle atmosphere applications. *Pure and Applied Geophysics*, 130:571–604.

Holdsworth, D. A., [1997]. An investigation of biases in the full spectral analysis technique. *Radio Science*, 32:769–782.

Holdsworth, D. A. and Reid, I. M., [1995]. A simple model of atmospheric radar backscatter: Description and application to the full correlation analysis of spaced antenna data. *Radio Science*, 30:1263–1280.

Holdsworth, D. A., Vincent, R. A. and Briggs, B. H., [1992]. Further work on frequency domain analysis. In *Workshop on Multiple Receiver Radar Techniques*, p. 46.

Holloway, C. L., Doviak, R. J., Cohn, S. A., Lataitis, R. J. and Van Baelen, J. S., [1997]. Cross correlation and cross spectra for spaced antenna wind profilers, 2, Algorithms to estimate wind and turbulence. *Radio Science*, 32:967–982.

Holton, J. R., [1979]. *An introduction to dynamic meteorology*. Academic Press, 2nd edn.

Hooper, D. A. and Thomas, L., [1998]. Complementary criteria for identifying regions of intense atmospheric turbulence using lower VHF radar. *Journal of Atmospheric and Terrestrial Physics*, 60:49–61.

Horowitz, P. and Hill, W., [1989]. *The art of electronics*. Cambridge University Press, 2nd edn.

Houghton, J. T., [1977]. *The physics of atmospheres*. Cambridge University Press.

Jansky, K. G., [1932]. Directional studies of atmospherics at high frequencies. *Proceedings of the Institute of Radio Engineers*, 20:1920–1932.

Jansky, K. G., [1933]. Electrical disturbances apparently of extraterrestrial origin. *Proceedings of the Institute of Radio Engineers*, 21:1387–1398.

Jansky, K. G., [1935]. A note on the source of interstellar interference. *Proceedings of the Institute of Radio Engineers*, 23:1158–1163.

Kelleher, R. F., [1966]. Some statistical properties of the ground diffraction patterns of vertically reflected radio waves. *Journal of Atmospheric and Terrestrial Physics*, 28:213–223.

Kraus, J. D., [1966]. *Radio Astronomy*. McGraw-Hill.

Kraus, J. D., [1988]. *Antennas*. McGraw-Hill, 2nd edn.

Kumar, K., Singh, S., Mahajan, K. K. and Sethi, N. K., [1994]. A study of tropopause and stable layers in lower atmosphere using the Indian MST radar. *Indian Journal of Radio and Space Physics*, 23:71–74.

Larsen, M. F., [1988]. Applications of MST radars: Meteorological applications. In *International School of Atmospheric Radar*.

Larsen, M. F. and Rottger, J., [1989]. The spaced antenna technique for radar wind profiling. *Journal of Atmospheric and Oceanic Technology*, 6:920–938.

Larsen, M. F., Kelly, M. C. and Gage, K. S., [1982]. Turbulence spectra in the upper troposphere and lower stratosphere at periods between 2 hours and 40 days. *Journal of the Atmospheric Sciences*, 39:1035–1041.

Lataitis, R. J., Clifford, S. F. and Holloway, C. L., [1995]. An alternative method for inferring winds from spaced antenna radar measurements. *Radio Science*, 30:463–474.

Lawrence, B. N., [1990]. *The southern hemisphere middle atmosphere: Climatology and waves*. Ph.D. thesis, Department of Physics, University of Canterbury.

Lawrence, B. N., Fraser, G. J., Phillips, A. and Vincent, R., [1995]. The four-day wave in the Antarctic mesosphere. *Journal of Geophysical Research*, 100D:18899–18908.

Liu, C. H. and Pan, C. L., [1993]. New observational techniques for studying the dynamics of the middle atmosphere using the Chung Li VHF radar. *Journal of Atmospheric and Terrestrial Physics*, 55:1055–1066.

Liu, C. H., Rottger, J., Pan, C. J. and Franke, S. J., [1990]. A model for spaced antenna observational mode for MST radars. *Radio Science*, 25:551–563.

Liu, C. H., Rottger, J., Dester, G., Franke, S. J. and Pan, C. J., [1991]. The oblique spaced antenna method for measuring the atmospheric wind field. *Journal of Atmospheric and Oceanic Technology*, 8:247–258.

Lomb, N. R., [1976]. Least-squares frequency analysis of unequally spaced data. *Astrophysics and Space Science*, 39:447–462.

May, P. T., [1988]. Statistical errors in the determination of wind velocities by the spaced antenna technique. *Journal of Atmospheric and Terrestrial Physics*, 50:21–32.

May, P. T., [1990]. Spaced antenna versus Doppler radars: A comparison of techniques revisited. *Radio Science*, 25:1111–1119.

May, P. T., Ecklund, W. L. and Hess, G. D., [1995]. Spectral and bispectral characteristics of wind variability at Darwin, Australia observed by a VHF radar wind profiler. *Quarterly Journal of the Royal Meteorological Society*, 121:527–544.

McAfee, J. R., Balsley, B. B. and Gage, K. S., [1989]. Momentum flux measurements over mountains: Problems associated with the symmetrical two beam radar technique. *Journal of Atmospheric and Oceanic Technology*, 6:500–508.

McIntyre, M. E., [1993]. On the role of wave propagation and wave breaking in atmosphere-ocean dynamics. In J. Singer, A. Solan, S. Bodner and Z. Hashin, eds., *Proceedings of the 18th International Conference in Theoretical and Applied Mechanics*, pp. 281–304. Elsevier.

Meek, C. E., [1980]. An efficient method for analysing ionospheric drifts. *Journal of Atmospheric and Terrestrial Physics*, 42:835–839.

Meek, C. E., [1990]. Triangle size effect in spaced antenna wind measurements. *Radio Science*, 25:641–648.

Meek, C. E. and Manson, A. H., [1989]. Vertical motions in the upper middle atmosphere from the Saskatoon (52°N,107°W) MF radar. *Journal of the Atmospheric Sciences*, 46:849–858.

Meyer, S. L., [1975]. *Data analysis for scientist and engineers*, chap. 6, pp. 17–18. John Wily and Sons.

Mitra, S. N., [1949]. A radio method of measuring winds in the ionosphere. *Proceedings I.E.E.*, 96:441–446.

Murphy, D. J., [1990]. *Measurements of energy and momentum flux in the mesosphere*. Ph.D. thesis, Department of Physics and Mathematical Physics, University of Adelaide.

Nakamura, T., Tsuda, T., Fukao, S., Kato, S., Manson, A. H. and Meek, C. E., [1993a]. Comaparative observations of short period gravity waves (10-100 min) in the mesosphere in 1989 by Saskatoon MF radar (52°N), Canada, and the MU radar (35°N), Japan. *Radio Science*, 28:729–746.

Nakamura, T., Tsuda, T., Yamamoto, M., Fukao, S. and Kato, S., [1993b]. Characteristics of gravity waves in the mesosphere observed with the MU radar I: Momentum flux. *Journal of Geophysical Research*, 98:8899–8910.

Nastrom, G. D. and VanZandt, T. E., [1996]. Biases due to gravity waves in wind profiler measurements of winds. *Journal of Applied Meteorology*, 35:243–257.

Nastrom, G. D., Green, J. L., Peterson, M. R. and Gage, K. S., [1989]. Tropopause folding and the variability of tropopause height as seen by Flatland VHF radar. *Journal of Applied Meteorology*, 28:1271–1281.

Pan, C. J. and Liu, C. H., [1992]. A model for oblique spaced antenna technique for mesosphere, stratosphere, troposphere radars and its applications. *Radio Science*, 27:131–144.

Pan, C. J., Liu, C. H. and Rottger, J., [1992]. Momentum flux measurements in the troposphere: Comparison of DBS and spaced-receiver method. In *Proceedings of the Fifth Workshop on Technical and Scientific Aspects of MST Radar*.

Pawsey, J. L., [1935]. Further investigations of the amplitude variations of downcoming wireless waves. *Proceedings of the Cambridge Philosophical Society*, 31:125–144.

Pawsey, J. L. and Bracewell, R. N., [1955]. *Radio Astronomy*. Oxford University Press.

Pfister, W., [1971]. The wave-like nature of inhomogeneities in the E region. *Journal of*

Atmospheric and Terrestrial Physics, 33:999–1025.

Phillips, G. J. and Spencer, M., [1955]. The effects of anisometric amplitude patterns in the measurement of ionospheric drifts. *Proceedings of the Physical Society, London*, B68:481–492.

Press, W. H., Teukolsky, S. A., Vetterling, W. T. and Flannery, B. P., [1992]. *Numerical Recipes in FORTRAN: The art of scientific computing*. Cambridge University Press, 2nd edn.

Prichard, I. T. and Thomas, L., [1993]. Radar observations of gravity wave momentum fluxes in the troposphere and lower stratosphere. *Annales Geophysicae*, 11:1075–1083.

Rao, Y. J., Jain, A. R., Anandan, V. K. and Rao, P. B., [1994]. Some observations of tropical tropopause using ST mode of the Indian MST radar: Multiple stable layer structure. *Indian Journal of Radio and Space Physics*, 23:75–85.

Rastogi, P. K., [1986]. An overview of data acquisition, signal coding and data analysis techniques for MST radars. In *Handbook for MAP, Volume 20*, pp. 431–440. ICSU.

Rastogi, P. K. and Bowhill, S. A., [1976]. Gravity waves in the equatorial mesosphere. *Journal of Atmospheric and Terrestrial Physics*, 38:51–60.

Ratcliffe, J. A., [1956]. Some aspects of diffraction theory and their application to the ionosphere. *Reports on Progress in Physics*, 19:188–267.

Ratcliffe, J. A. and Pawsey, J. L., [1933]. A study of the intensity of downcoming wireless waves. *Proceedings of the Cambridge Philosophical Society*, 29:301–318.

Reber, G., [1944]. Cosmic static. *Astrophysics Journal*, 100:279–287.

Reid, I. M. and Vincent, R. A., [1987]. Measurements of mesospheric gravity wave momentum fluxes and mean flow accelerations at Adelaide, Australia. *Journal of Atmospheric and Terrestrial Physics*, 49:443–460.

Riddle, A. C., [1986]. Use of the sun to determine pointing of ST radar beams. In *Handbook for MAP, Volume 20*, pp. 410–413. ICSU.

Rottger, J., [1983]. Interpretation of radar returns from clear air - discrimination against clutter. In *Handbook for MAP, Volume 9*, pp. 114–119. ICSU.

Rottger, J., [1986]. On the varying slope of velocity spectra. In *Handbook for MAP, Volume 20*, pp. 225–227. ICSU.

Rottger, J., [1988]. The instrumental principles of MST radars and incoherent scatter radars and the configuration of radar system hardware. In *International School of Atmospheric Radar*.

Rottger, J. and Ierkic, H. M., [1985]. Postset beam steering and interferometer applica-

tions of VHF radars to study winds, waves and turbulence in the lower and middle atmosphere. *Radio Science*, 20:1461–1480.

Rottger, J. and Vincent, R. A., [1978]. VHF radar studies of tropospheric velocities and irregularities using spaced antenna techniques. *Geophysical Research Letters*, 5:917–920.

Roy, A. E. and Clarke, D., [1982]. *Astronomy: Principles and practice*. Adam Hilger Ltd., 2nd edn.

Royrvik, O., [1983]. Spaced antenna drift. In *Handbook for MAP, Volume 9*, pp. 187–191. ICSU.

Ryle, M., [1950]. Radio astronomy. *Reports on Progress in Physics*, 13:184–246.

Ryle, M., [1952]. A new radio interferometer and its application to the observation of weak radio stars. *Proceedings of the Royal Society, London A*, 211:351–375.

Sastri, J. H. and Rao, B. M., [1971]. Dependence of horizontal drift and anisotropy of irregularities on the relative spacing of the aerials. *Journal of Atmospheric and Terrestrial Physics*, 33:507–510.

Sato, T., [1988]. Radar Principles. In *International School on Atmospheric Radar*.

Sato, T., Tsuda, T., Kato, S., Morimoto, S., Fukao, S. and Kimura, I., [1985]. High resolution MST observations of turbulence by using the MU radar. *Radio Science*, 20:1452–1460.

Sato, T., Inooka, Y., Fukao, S. and Kato, S., [1986]. Monitoring of the MU radar antenna pattern by satellite OHZORA (EXOS-C). In *Handbook for MAP, Volume 20*, pp. 414–418. ICSU.

Scargle, J. D., [1982]. Studies in astronomical time series analysis II. Statistical aspects of spectral analysis of unevenly spaced data. *The Astrophysical Journal*, 263:835–853.

Sheppard, E. L., Larsen, M. F., Palmer, R. D., Fukao, S., Yamamoto, M., Tsuda, T. and Kato, S., [1993]. A statistical comparison of spaced antenna and spatial interferometry wind estimation. *Radio Science*, 28:585–593.

Skolnik, M. I., [1990]. *Radar Handbook*. McGraw-Hill, 2nd edn.

Slack, M., [1945]. The probability distributions of sinusoidal oscillations combined in random phase. *The Journal of the Institution of Electrical Engineers*, 93:76–86.

Stubbs, T. J. and Vincent, R. A., [1973]. Studies of D-region drifts during the winters of 1970-1972. *Australian Journal of Physics*, 26:645–660.

Sulzer, M. P. and Woodman, R. F., [1986]. Optimum coding techniques for MST radars. In *Handbook for MAP, Volume 20*, pp. 441–447. ICSU.

Swenson, G. W., [1978a]. An amateur radio telescope - I. *Sky and Telescope*, 55:385–390.

Swenson, G. W., [1978b]. An amateur radio telescope - II. *Sky and Telescope*, 55:475–479.

Swenson, G. W., [1978c]. An amateur radio telescope - III. *Sky and Telescope*, 56:28–33.

Swenson, G. W., [1978d]. An amateur radio telescope - IV. *Sky and Telescope*, 56:114–120.

Swenson, G. W., [1978e]. An amateur radio telescope - V. *Sky and Telescope*, 56:201–205.

Swenson, G. W., [1978f]. An amateur radio telescope - VI. *Sky and Telescope*, 56:290–293.

Tahara, Y., Yamamoto, M. and Fukao, S., [1997]. Wind estimation errors of the spaced antenna technique studied with simulations and observations: A case study for the MU radar. *Radio Science*, 32:1193–1201.

Thorsen, D., Franke, S. J. and Kudeki, E., [1997]. A new approach to MF radar interferometry for estimating mean winds and momentum flux. *Radio Science*, 32:707–726.

Tsuda, T., [1988]. Data acquisition and processing. In *International School of Atmospheric Radar*.

Tsuda, T., May, P. T., Sato, T., Kato, S. and Fukao, S., [1988]. Simultaneous observations of reflection echos and refractive index gradient in the troposphere and lower stratosphere. *Radio Science*, 23:655–665.

Tsuda, T., Murayama, Y., Yamamoto, M., Kato, S. and Fukao, S., [1990]. Seasonal variation of momentum flux in the mesosphere observed with the MU radar. *Geophysical Research Letters*, 17:725–728.

Valentic, T. A., Avery, J. D., Avery, S. K. and Vincent, R. A., [1997]. A comparison of winds measured by meteor radar systems and an MF radar at Buckland Park. *Radio Science*, 32:867–874.

Van Baelen, J. S., Richmond, A. D., Avery, S., Tsuda, T., Kato, S. and Fukao, S., [1989]. SAD and interferometry analysis with the MU radar. In *Handbook for MAP*, vol. 28, pp. 416–423. ISCU.

Van Baelen, J. S., Tsuda, T., Richmond, A. D., Avery, S. K., Kato, S., Fukao, S. and Yamamoto, M., [1990]. Comparison of VHF Doppler beam swinging and spaced antenna observations with the MU radar: First results. *Radio Science*, 25:629–640.

Vaughan, G., Howells, A. and Price, J. D., [1995]. Use of MST radar to probe the mesoscale structure of the tropopause. *Tellus*, 47:759–765.

Vincent, R. A. and Eckermann, S. D., [1990]. VHF radar observations of mesoscale

motions in the troposphere: Evidence for gravity wave Doppler shifting. *Radio Science*, 25:1019–1037.

Vincent, R. A. and Reid, I. M., [1983]. HF Doppler measurements of mesospheric gravity wave momentum fluxes. *Journal of the Atmospheric Sciences*, 40:1321–1333.

Vincent, R. A. and Rottger, J., [1980]. Spaced antenna VHF radar observations of tropospheric velocities and irregularities. *Radio Science*, 15:319–335.

Vincent, R. A., Candy, B. and Briggs, B. H., [1986]. Measurements of antenna polar diagrams and efficiencies using a phase-switched interferometer. In *Handbook for MAP, Volume 20*, p. 409. ISCU.

Vincent, R. A., May, P. T., Hocking, W. K., Elford, W. G., Candy, B. H. and Briggs, B. H., [1987]. First results of the Adelaide VHF radar: spaced antenna studies of tropospheric winds. *Journal of Atmospheric and Terrestrial Physics*, 20:353–366.

Washington, W. M. and Parkinson, C. L., [1986]. *An introduction to three dimensional climate modelling*, chap. 3, pp. 109–110. Oxford University Press.

Wolff, E. A., [1967]. *Antenna Analysis*. John Wiley and Sons.

Woodman, R. F., [1988]. Statistical characteristics of MST radar echos and its interpretation. In *International School of Atmospheric Radar*.

Woodman, R. F. and Guillen, A., [1974]. Radar observations of winds and turbulence in the stratosphere and mesosphere. *Journal of the Atmospheric Sciences*, 31:493–505.

Woodman, R. F., Sulzer, M. P. and Farley, D. T., [1984]. Binary pulse compression techniques for MST radars. In *Handbook for MAP, Volume 13*, pp. 155–165. ICSU.

Worthington, R. M. and Thomas, L., [1996]. The measurement of gravity wave momentum flux in the lower atmosphere using VHF radar. *Radio Science*, 31:1501–1517.

Young, H. D., [1962]. *Statistical treatment of experimental data*, chap. 3, pp. 78–80. McGraw-Hill.

Young, T., [1807]. *A course of lectures on natural philosophy and the mechanical arts*, vol. 1, p. 464. London.